

https://dspace.org/

Foreign atoms on the three low index diamond surfaces

Makau, Nicolas W

2008-04-08T10:18:20Z
http://hdl.handle.net/10539/4742

Downloaded from a DSpace repository. https://dspace.org/

FOREIGN ATOMS ON THE THREE LOW INDEX DIAMOND SURFACES

By

Nicholas W. Makau

A thesis submitted to the Faculty of Science, University of the Witwatersrand, Johannesburg, in fulfilment of the requirements for the degree of Doctor of Philosophy.

Johannesburg, 2006.

Declaration

I declare that this thesis is my own unaided work. It is being submitted for the degree of Doctor of Philosophy in the University of the Witwatersrand, Johannesburg. It has not been submitted before for any degree or examination in any other university.

_____

(Signature of candidate)

_____day of_____2006

VOLUME I

This volume presents results of the experimental work that was conducted in this study. It includes results obtained from the X-ray Photoelectron Spectroscopy (XPS), Nuclear Reaction Analysis (NRA), Optical microscopy and the Atomic force microscopy studies.

Abstract

The topmost atom layers of any surface often play very crucial roles regarding the surface properties, in addition to facilitating the interaction of materials with their external environment. They form substrates for both homo and hetero-epitaxial growth of thin films used in semiconducting device fabrication and in other cases act as heterogeneous catalysts used to induce and steer a given chemical reaction. They are the key players in many surface processes such as bonding, wettability, surface conductivity, lubrication, optical absorption and corrosion among many others.

Some of these processes can be affected quite significantly by the foreign atoms residing on the surfaces, which may be introduced onto the surfaces either intentionally or through alien means. It is therefore extremely important when studying surface properties to pay keen interest towards their nature and where necessary the foreign atoms residing on them, their bonding sites and also the bonds that they form, as well as their proportions.

Foreign atoms on diamond surfaces have already been shown to alter its surface properties in a way that makes it quite useful in various technological applications and in other cases less attractive. Among the many foreign atoms that may bond onto polished diamond surfaces, oxygen has so far been shown to be among the main adsorbate on diamond surfaces prepared through mechanical polishing and then cleaned in an acid mixture, followed by rinsing in deionised water.

This was confirmed by our XPS studies which further established that the optimum oxygen coverage on clean diamond surfaces was 0.5monolayers on the (100) surface, and 0.3monolayers on both the (110) and (111) surfaces. The oxygen atoms were further bonded in various oxidation states, sometimes forming C-O or C=O bonds and in other cases C-OH bonds. The C=O bond

was found to be the most stable configuration on the (111) surfaces, while the C-O-C and C-OH dominated on the (100) surfaces. The (110) surface had four major functional groups, which included the C-OH, C-O-C, C=O and COOH groups, with none of them showing any outright dominance. Few cases were nonetheless considered on this surface, and the absence of any specific group being the most stable was attributed to the nature of the surface. Some minor groups such as O-C-O, O-C=O, C-O-C=O and H-C=O were also observed occasionally on the three surfaces, and these were believed to reside at suitable sites with more dangling bonds such as steps, edges etc.

This study also investigated quite extensively the transfer of ^{13}C atoms onto polished diamond surfaces. The source of the ^{13}C atoms was the polishing olive oil (principally olein), labelled with 99% ^{13}C atoms, since olive oil is normally used to polish diamond surfaces. It therefore doubles as a lubricant and in other cases as a source of the hydrogen atoms that terminate the polished diamond surfaces. By using nuclear reaction analysis and the 550keV ^{13}C(p,γ)^{14}N resonant nuclear reaction, it was found that when diamond surfaces were polished with this labelled oil, a full monolayer of ^{13}C atoms was always found bonded on to each of the three diamond surfaces. This was quite a high coverage, and at the same time also an interesting result, because the possibility of being able to transfer atoms from the polishing lubricant to the surface had key implications. Among them, novel surfaces could perhaps be prepared in the manner suggested in this work, while labelling of surfaces for identification could also be a possible application.

By analyzing the gamma rays emitted from the nuclear reaction as a function of the exciting proton's energy, the nuclear reaction's width was found to be 25$\pm$1keV, which was in excellent agreement with other studies. This value of the width was nonetheless narrower than the most recently quoted value of 32.5keV, which is composed of both s and p-waves. Due to the geometry of our detector, the value of 25keV was believed to be due to contributions from the isotropic s-wave only. Our results further showed that it was unlikely that clumping would occur on strongly covalent surfaces, while previous works indicated that there was no exchange of labelled carbon atoms at a diamond surface. As such, a distribution in depth was clearly ruled out. The narrow

width of the nuclear reaction confirmed that the ^{13}C surface layer was indeed very thin, and possibly the thinnest layer that can be formed, thereby being better than most supported thin targets. This was yet another way of preparing thin targets for nuclear reaction applications.

This work was based primarily on the study of diamond surfaces that are polished mechanically. Mechanical polishing is the earliest and also the most well developed method for preparing well characterised diamond surfaces. Diamond surfaces prepared through mechanical polishing are known to be bulk-like, and also terminated with a layer of hydrogen. Exposure of these to air adds a monolayer of oxygen and/or hydroxyl groups as observed in the XPS studies. When given an extra 30 or more minutes of manual polishing, these surfaces are believed to be very flat, but their degree of roughness has not been investigated directly up until now. The manual polishing exposes a new surface, which is probably different from that achieved after the mechanical polishing. By using atomic force microscopy and optical microscopy within the Nomarski interference mode, it was found that both the mechanically and manually polished diamond surfaces were composed of a series of parallel polishing lines. They all had very small roughnesses, with the manually polished surfaces being smoother. Some of the polishing grooves were wider and also deeper, while others were shallower and much smaller and these were found to be residing inside the larger ones. The AFM results in particular revealed that the amount of surface roughness on the three low index polished diamond surfaces was varied, albeit in a small way, and also depending on whether the surfaces were polished only mechanically, or if they were given the extra manual polishing. Details of the actual roughnesses on each face after the mechanical and manual polishing stages are given in the thesis.

Annealing these surfaces under vacuum conditions of better than 10^{-6} Torr, up to temperatures of 250 and 750°C, revealed that the 250°C anneal did not change the surface roughness much from what it was before the annealing. It was thus believed that if any changes occurred, these resulted only in the desorption of the physisorbed species. However, annealing the surfaces to 750°C under vacuum resulted in some changes in the overall surface roughness of all the the three low index faces, which were not observed at the 250°C anneal.

This was therefore believed to lead to surface etching and in some instances smoothing of the surfaces, as the surface-bonded species got desorbed as C-O groups. Lack of severe etching was attributed to the fact that not all the adsorbates got desorbed by the 750°C anneal.

The role of oxygen atoms and hydroxyl groups on diamond surfaces has been a subject of debate for a while now. Their stable sites, how they are bonded and their proportions (i.e. monolayers) under various conditions are issues that are yet to be fully resolved. Using density functional theory, this study sought to establish the preferred bonding sites and configurations of the oxygen atoms and the hydroxyl groups on the single-dangling-bond (111) (1×1) and (2×1) diamond surfaces. This was intended to complement the experimental work done in the XPS studies, and also other works reported in literature. It was realized by computing the adsorption energies of oxygen atoms and hydroxyl groups from first principles at various sites and for varying monolayer coverages. Among the sites investigated were the ONTOP, bridge, hexagonal close packed (HCP) and the face centred cubic (FCC) sites. The coverages were varied between the full, half, third and quarter monolayers. By comparing the adsorption energies as well as the total minimum energies of the different systems, it was found that the ONTOP site was overall the most stable bonding site on diamond (111)-(1×1) surfaces, while the third monolayer coverage was the most preferred one. The half monolayer bridge site bonded with oxygen atoms was found to be the most stable site and coverage on the (2×1) reconstructed surface.

In addition, while the bond lengths and angles were preserved close to the experimental values of 1.54Å for the C-C bonds and 109.4° respectively within the bulk, those in the topmost bilayer of carbon atoms were not. They were found to elongate by as much as 10% and others contracted by as much as -6%. The bond angles varied predominantly between 101 and 112°. Some of the surface bond length changes were attributed to the presence of the adsorbates, while others were due to the strong rehybridization within these layers, especially between the 2nd and 3rd carbon atom layers of the C(111)-(1×1) surfaces. Bond lengths within the bulk regions varied by less than ±1% of the bulk bond length for both the (1×1) and (2×1) surfaces. Very small buckling and no dimerization of the surface bonds was observed on the clean (2×1) reconstructed

C(111) surfaces, but some considerable buckling of the upper π-bonded surface layer was observed after the adsorption of oxygen atoms or hydroxyl groups.

The computed bulk properties of diamond such as the bulk modulus (4.16Mbar), the cohesive energy (7.89eV/atom) and the lattice constant of 3.563Å were all well within the expected theoretical and experimental ranges. The same applied to the bulk properties of the free oxygen molecule and the hydroxyl group. Their bond lengths were 1.21 and 0.978Å for the oxygen molecule and the hydroxyl group respectively, while the binding energy and vibrational frequency of the free oxygen molecule were 3.31eV/atom and 1550cm^{-1} respectively.

Both the O atoms and OH groups were also found to affect not only the electronic density of states of diamond, but also the work function. Oxygen atoms led to an increase of the work function, while the hydroxyl group's adsorption resulted in decreasing of the work function, owing to the resulting surface dipoles, which in turn makes the surfaces to posses negative electron affinity. An average valence band width for bulk diamond of $\sim$21eV was obtained and both surface states due to the oxygen atoms and the carbon atoms were established at different energies.

The half monolayer coverages of oxygen atoms at the ONTOP and bridge sites were found to be insufficient for lifting the (2×1) surface reconstruction, while all the full monolayer coverages and the hydroxyl terminations resulted in the lifting of the surface reconstruction to the unreconstructed (1×1) surface. The inability of the half monolayers coverages with oxygen atoms to break the (2×1) surface reconstruction was attributed to an activation barrier of going from oxygen on a (2×1) to oxygen on a (1×1) surface. It was further found that on the C(111)-(1×1) surface, repulsion between the oxygen adsorbates started at coverages greater than 0.33monolayers, while for the hydroxyl termination, it was not until coverages greater than 0.5monolayers that the systems got less stable due to the OH-OH repulsions.

Much of this work has been published in various journal, and also presented in both international and local conferences as shown in Appendix A. Some more publications and conference presentations are also planned for.

To my wife Rosemary M. Muange and our children
Mercy Mueni and Stacy Ngenyi.

Acknowledgements

I would like to express my sincere gratitude to my supervisor, Prof. T. E. Derry who was always available for me all the time during the studies. His expertise, encouragement and support were extremely motivating. Without his guidance, wisdom and foresight, this work would not have been completed.

I am also highly indebted to prof.C. Stampfl of the School of Physics, University of Sydney, Australia for her guidance and unrelenting support with the density functional theory calculations. She was always at hand to help with any questions at any time of the day.

The contribution of the academic and technical staff of the former Schonland Research Institute (now iThemba LABS (Gauteng)) is highly acknowledged. In particular, I would like to thank Trevor Hollander and Richard Chirwa for their help with the electronics problems at the "Christine"accelerator and also the Ultra High Vacuum (UHV) machine. Eric Rood and Marius Labuschagne of the metal workshop, as well as Osborn malinga and Molefe Mabitsela of the environmental isotope group, are all thanked for their help.

I would also like to thank all the new staff members of the iThemba LABS (Gauteng) whom I collaborated with quite closely, Poke Mashita, Ella Kungoane, Mpho and Khaya Rabebe and the director, Dr. I Machi.

The secretaries at the School of Physics, University of the Witwatersrand and iThemba LABS (Gauteng), C. Chinane and D. Monyamane respectively are especially thanked for their help with stationary, phone calls and many enquiries. The former librarian of iThemba LABS (Gauteng) C. Hlatshayo is also thanked for her help with getting books and journals, together with Paul Kalushi of the Biology and Physical Sciences library of the University of the Witwatersrand.

To all my friends and fellow students who were always a source of inspiration, especially when things were not working alright. I would like to express my sincere thanks especially to George Amolo, Mary Assiamah and Godfrey Sauti for the many useful discussions that we had, as well as Ian Korir who was

extremely helpful with some computer programs. Emmanuel Nshingabigwi, Ronald Machaka, Morgan Madhuku, Thomas Sibiya, Lucky Mkhonza, Christopher Machio, A. da Costa, C. Ogola and Dr. C. Chiteme are also thanked for their help. Mervin Naidoo is especially thanked for his help in explaining the use of the XPS, Auger and LEED techniques of the UHV system.

Staff at the school of Physics, University of the Witwatersrand are all thanked for their help at different stages of the work, which assisted in shaping up the thesis. Prof. J. Carter, Prof. D. Joubert, Dr. Elias Sideras-haddad and Sanjiv Shrivashtava are highly thanked for showing a lot of interest in this work. I would also like to thank Joseph Dikgale the driver/technician at the school of Physics and Lebang Mathlandisha of the former Schonland Research Institute, both of whom were always more than willing to drive me to the University of Pretoria and CSIR on many occasions to carry out some experiments. Mik Rebak of the former Schonland Research Institute is highly thanked for the mechanical polishing of the diamond surfaces in an extremely expert way. All the technical staff of the School of Physics who were always quite keen in knowing my progress and all the well wishers are thanked for their concern.

Some of the work has been done out of the University of the Witwatersrand, and in this regard I would like to thank the CSIR, the University of Pretoria and iThemba LABS (Gauteng) for allowing me to use their facilities. I would like to thank Dr. Nic van der Berg of the University of Pretoria for his unwavering support with the Atomic Force Microscopy measurements at their University.

Special gratitude is given to the Fritz Haber, Max Plank Institute at Berlin, German for allowing me to use their computers and programs to carry out the density functional theory calculations. I am also highly indebted to all the staff and students at this institute, especially Alexey Dick, with whom I shared an office when I visited the institute, the head of the theory department, Prof. Dr. Mathias Scheffler and Prof. Dr. Peter Kratzer who was always quite helpful with numerous computer problems.

The financial support given to me by the DAAD, the Department of Science/National Research Foundation-Centre of Excellence in Strong Materials at Wits University and also the University of the Witwatersrand is also highly acknowledged.

Finally, I would like to thank all authors of free software, since a great part of this work was done using such software.

Nicholas W. Makau, Johannesburg, 2006.

Preface

This thesis is divided in two volumes. The first volume (volume I) deals with the experimental work, while the second, (volume II) covers the theoretical work dealing with the computational studies.

There are four chapters in volume I. Chapter 1 gives a general review of surfaces, the theory of diamond and its surfaces, and finally the mechanical polishing of diamond.

Chapter 2 deals with the X-ray photoelectron spectroscopy (XPS) studies of the three low index diamond surfaces after mechanical and manual polishing. The preferred bonding configurations of oxygen atoms and hydroxyl groups on polished diamond surfaces, their binding energies and their proportions in terms of monolayer coverages are determined.

Chapter 3 investigates the transfer of ^{13}C atoms on to the three low index diamond surfaces after mechanical and manual polishing. Olive oil (principally Olein) labelled with 99% ^{13}C atoms was used as the polishing lubricant, together with diamond pastes of 0.25 and 0.1μm which achieved the manual polishing. The 550keV ^{13}C(p,γ)^{1}4N resonant nuclear reaction was used to determine the number of ^{13}C atoms transferred after the polishing and repolishing, and its full width at half maximum was also remeasured.

Chapter 4 deals with the surface smoothness of the three low index diamond surfaces after both mechanical and manual polishing, using optical microscopy. Laue X-ray images were initially obtained to establish how close the diamond surfaces were polished, relative to their true orientation.

Chapter 5 outlines the Atomic Force Microscopy (AFM) investigations of diamond surfaces polished both mechanically and manually. The samples were also annealed under vacuum conditions of better than 10^{-6}Torr, up to 250°C and 750°C for about 10 minutes at each temperature regime, and then cooled down under similar vacuum conditions to room temperature. New AFM images

were then taken and analyzed to establish if there were any differences after the annealing.

Volume II is constituted of one chapter, that considers in detail the role of oxygen atoms and hydroxyl groups adsorbed on the single-dangling-bond bulk terminated (1×1) diamond surfaces, as well as on the (2×1) reconstructed surfaces from first principles. This is considered as a function of the site and coverage, with the coverages being varied from full, half, third and quarter monolayers and the sites of interest being the ONTOP, bridge, hexagonal close packed and the face centred cubic sites.

Contents

Declaration **i**

ii

Abstract **iii**

Acknowledgements **iii**

Preface **v**

List of Figures **x**

List of Tables **xxiii**

1 Surface Description and Review of Diamond Properties. **1**
1.1 The definition of a surface. 1
1.2 Surface features 3
1.3 The Diamond. 4
1.4 Mechanical polishing of diamond surfaces. 10

2 X-Ray Photoelectron Spectroscopy (XPS) Studies of Oxygen Adsorption on the Three Low Index Diamond Surfaces. **20**
2.1 Chapter layout 20
2.2 Introduction 20
2.3 Experimental 28
2.4 Results 35
2.5 Discussion 52
2.5.1 Wide scans 52
2.5.2 C1s and O1s narrow scans 54
2.6 Surface states 69
2.7 Conclusion 74
2.8 Recommendation 76

3 Carbon Atom Exchange Between The Lubricant And The Diamond Surfaces During Polishing. 77
3.1 Chapter layout . . . 77
3.2 Introduction . . . 77
3.3 Nuclear reactions . . . 80
3.4 Particle-gamma nuclear reactions $^{x}A(p,\gamma)^{y}B$ . . . 80
3.5 Reaction cross-section . . . 82
3.6 Resonant nuclear reactions. . . . 85
3.7 Stopping power of protons (H^{+}) in diamond . . . 88
3.8 The 550 keV $^{13}C(p,\gamma)^{14}N$ nuclear reaction . . . 89
3.9 The oleic acid molecule. . . . 92
3.10 Interaction of incident gamma rays with the NaI(Tl) detector's active material. . . . 93
3.11 Experimental Procedure . . . 96
3.11.1 Sample Preparation . . . 96
3.11.2 Experimental set up . . . 98
3.12 Gamma ray background minimization and sample irradiation analysis. . . . 101
3.13 Detector calibration . . . 104
3.14 Quantification of the adsorbed ^{13}C atoms on diamond surfaces. . 108
3.15 Results . . . 116
3.15.1 Number of ^{13}C atoms transferred onto the polished diamond surfaces. . . . 123
3.16 Discussion . . . 130
3.16.1 Full Width At Half Maximum (FWHM) of the 550keV $^{13}C(p,\gamma)^{14}N$ resonant nuclear reaction. . . . 138
3.17 Stereo-chemical bonding of the oil molecule with the diamond surface. . . . 140
3.18 Conclusion . . . 145
3.19 Recommendations . . . 149

4 Optical Microscopy studies of the three low index polished diamond surfaces obtained using the Nomarski interference technique. 150
4.1 Layout of the chapter. . . . 150
4.2 Introduction. . . . 151
4.3 Discussions. . . . 155
4.4 Conclusions . . . 158

5 Atomic Force Microscopy investigations of the three low index polished diamond surfaces. 160
5.1 Introduction . . . 160
5.2 Experimental . . . 162
5.3 Results . . . 164

5.3.1 2D and 3D AFM images, together with their line profiles and the corresponding power spectra. 164
5.3.2 Ratios of real areas to the projected ones, and the root mean square roughnesses. 179
5.4 Discussions 185
5.4.1 The (100) surface 185
5.4.2 The (111) surface 188
5.4.3 The (110) surface 191
5.4.4 Annealed surfaces 194
5.4.5 Root mean square roughnesses of the polished surfaces and ratios of the real area to the scan size; for unannealed and annealed surfaces. 210
5.5 Conclusions 218

A **229**
A.1 Papers published in refereed journals. 229
A.2 Paper to be submitted to a refereed journal. 229
A.3 Papers presented at international conferences 230
A.4 Papers presented at local conferences 230

B **231**
B.1 Correction for XPS oxygen monolayer coverage. 231
B.1.1 Contribution from oxygen on the molybdenum (Mo) sample holder, for spectra obtained using the VG Scientific spectrometer. 231
B.1.2 Oxygen atoms coverage σ, per cm^2 on polished diamond surfaces. 232
B.1.3 Oxygen monolayer coverage 232

C **234**

References **256**

List of Figures

1.1 Various surface features. 1. Adatom 2. Dimer 3. Trimer 4. Kink edge 5. Step 6. Terrace vacancy neighbour 7. Terrace 8. Step adatom 9. Step vacancy 10. Terrace vacancy [6] 4

1.2 A photograph of the diamond samples used in this study. The top row starting from the LHS shows a (111) surface [sample kc5], and a (100) surface [sample kc3]. The middle row starting from the LHS shows a (111) surface [sample kc11], a (100) surface [sample kc8], and the RHS one a (111) surface [sample kc9]. The bottom row starting from the LHS shows a (111) surface [sample kf4], and a (110) surface [sample kk7]. 5

1.3 Crystal lattice of diamond.(After A. K. Ramdas [9]). 6

1.4 A diamond surface sliding over diamond grit that has embedded itself into the cast iron scaife due to high pressures developed at the point of contact, as well as temperature (Adapted from [65, 54]). Diamond is quite resistant to plastic deformation except at high temperatures ($> 1600°C$) [60], although Hird *et al.* [54], appear to suggest that this can occur even at lower temperatures. 15

1.5 A schematic diagram of a simplified set up used for the mechanical polishing of diamond surfaces. 15

2.1 Photoemission of a core level electron. (After J.C. Vickerman [1]). 26

2.2 The XPS process. (After J.C. Vickerman [1]). 27

2.3 An illustration of the twin anode X-ray gun. (After VG Scientific company [114]) 27

2.4 Schematic diagram of the XPS process using a Phi Quantum 2000 spectrometer [115]. 32

2.5 Schematic diagram of the CLAM 100 VG scientific spectrometer [120]. 33
2.6 Wide survey scan for a (100) face. [Sample (kc8)] 36
2.7 Narrow scans for a (100) face. Top panel represents the C1s while the bottom one is the O1s scan.[Sample (kc8] 37
2.8 Wide survey scan for a (111) face. (Sample kc11) 38
2.9 Narrow scans for a (111) face. Top panel represents the C1s peak, while the bottom one is the O1s peak.[Sample (kc11] 39
2.10 Wide survey scan for a (111) face. (Sample kc9) 40
2.11 Narrow scans for a (111) face. Top panel represents the C1s peak, while the bottom one is the O1s peak.[Sample (kc9] 41
2.12 Wide survey scan for a (111) face. (Sample kf4) 42
2.13 Narrow scans for a (111) face. Top panel represents the C1s peak, while the bottom one is the O1s peak.[Sample (kf4] 43
2.14 Wide survey scan for a (110) face. (Sample kk7) 44
2.15 Narrow scans for a (110) face. Top panel represents the C1s peak, while the bottom one is the O1s peak.[Sample (kk7] 45
2.16 Wide survey scan for a (110) face. (Sample kk7) 46
2.17 Narrow scans for a (110) face. Top panel represents the C1s peak, while the bottom one is the O1s peak.[Sample kk7] 47
2.18 XPS total (valence) density of states for the three low index diamond surfaces. 51
2.19 Functional groups on the three low index polished diamond surfaces 65

3.1 Dangling bonds on the three low index diamond surfaces. First panel represents a (111) face, the second a (110) and the last a (100) face. [After Hansen *et al.* [94]] 79
3.2 A proton of radius R_1 interacting with a target atom of radius R_2. b is the impact parameter. 81
3.3 A 3 dimensional illustration of a beam of particles I_o hitting a target and producing scattered gamma rays, with some being emitted in an element of a solid angle $d\Omega$. Adapted from G.R. Satchler [155] 84

3.4 Nuclear reaction cross-section, σ as a function of exciting energy. E_r is the resonance energy, and D is the nuclear level spacing . . 86
3.5 Stopping cross-sections of protons incident on diamond at various energies. [Adapted from [154]] 89
3.6 Nuclear energy transitions for the production of the 8.06MeV gamma rays from the ^{14}N energy level diagram. (After F. Ajzenberg-Selove [163]). 91
3.7 The chemical structure of the oleic acid molecule. The green balls are the labelled carbon-13 atoms, the grey ones the hydrogens, and the red ones the oxygen atoms. After [164]. 92
3.8 Various interaction mechanisms that occur when incident gamma rays interact with the detector's active material. 93
3.9 Detector interaction response as a function of the incident gamma ray's energy for a 76x76mm NaI(Tl) detector. (After [166]) . . . 94
3.10 Illustrations of the atomic arrangement at each of the three low index diamond faces. The left hand side panel shows a (100) face, the middle a (111) face and the right hand side one, a (110) face. Note the large channels within the (110) face. 96
3.11 Operating principle of the Cockcroft-Walton high voltage Power supply. (After D.B. Rebuli [167]) 99
3.12 Schematic diagram of the 1.4 MV Cockcroft-Walton Proton accelerator. (After R.A. Spits [168]) 99
3.13 Sample - detector - readout arrangement. The dimensions are not drawn to scale. 102
3.14 Detector calibration peaks using ^{137}Cs and ^{60}Co standard sources. 107
3.15 Three gamma ray peaks obtained at a specific proton energy, fitted with a Gaussian distribution. The area under them is taken between channels x and y. 109
3.16 A step function illustrating the background spectrum from the 1.11% ^{13}C atoms contained within the bulk of all natural diamond samples. These data were obtained from sample kc5, which was a (111) face. 111
3.17 A typical ^{13}C peak riding on the background spectrum. 113

3.18 An extracted surface peak fitted with the Breit-Wigner distribution. 113
3.19 Gamma ray profile from sample kc5, which was a (111) surface that was not treated with the ^{13}C-labelled oil. It shows the step function yield of the 1.11% ^{13}C atoms contained in all natural diamonds. 117
3.20 Gamma ray profile from sample kc9 which was a (111) surface that was untreated with the ^{13}C-labelled oil. This yield profile corresponds to the 1.11% ^{13}C atoms contained in all natural diamonds. 117
3.21 A plot of the gamma ray yield profile from sample kc3, which was a (100) surface treated with ^{13}C. 118
3.22 Gamma ray yield from sample kc8, which was a another (100) surface treated with ^{13}C. 118
3.23 Gamma ray yield from sample kc5, which was a (111) surface treated with ^{13}C. 119
3.24 Gamma ray yield profile from sample kc11, which was a second (111) surface treated with ^{13}C. 119
3.25 Gamma ray yield from sample kf4, which was yet another (111) surface treated with ^{13}C. 120
3.26 Gamma ray yield from sample kk7, which was a (110) surface treated with ^{13}C. 120
3.27 Gamma ray yield profile from the opposite side of the (110) surface whose profile is shown in figure 3.26, which was also treated with ^{13}C. 121
3.28 Gamma ray yield from the same (110) surface as in figure 3.27 which was treated with ^{13}C, but with the face slightly tilted relative to the proton beam axis. 121
3.29 Some examples of the three gamma ray peaks obtained as the proton energy was progressively increased. Note the difference in the vertical scale. 122
3.30 Carbon -13 surface peak for a (100) surface, extracted from figure 3.21. 125

3.31 Carbon -13 surface peak for a (100) surface, extracted from figure 3.22. 125
3.32 Carbon -13 surface peak for a (111) surface, obtained from figure 3.23. 126
3.33 Carbon -13 surface peak for a (111) surface, obtained from figure 3.24. 126
3.34 Carbon -13 surface peak for a (111) surface, extracted from figure 3.25. 127
3.35 Carbon -13 surface peak for a (110) surface, obtained from figure 3.26. 127
3.36 Carbon -13 surface peak for a (110) surface, obtained from figure 3.27. 128
3.37 Carbon -13 surface peak for a (110) surface, obtained from figure 3.28. 128
3.38 Gamma ray detector geometry. 139
3.39 Process by which the oil molecule may bond with the diamond surface. 140

4.1 Laue x-ray image of a (100) diamond surface polished manually. 151
4.2 Laue x-ray image for a (110) diamond surface polished manually. 152
4.3 Laue x-ray image for a (111) diamond surface polished manually. 152
4.4 Optical microscopy image of a manually polished (100) diamond surface for sample kc3, obtained at a magnification of 1000 times. 153
4.5 Optical microscopy image of a manually polished (110) diamond surface for sample kk7, obtained at magnification of 1000 times. 153
4.6 Optical microscopy image of another manually polished (110) diamond surface (sample kk7). The image was taken at a magnification of 1000 times. 154
4.7 Optical microscopy image of a manually polished (111) diamond surface (sample kc11) obtained at a magnification of 1000 times. 154
4.8 Optical microscopy image of another (111) diamond surface polished manually (sample kc11), obtained at a magnification of 1000 times. 155

5.1 Schematic diagram of the AFM equipment showing the cantilever, the tip, photo-detector, laser beam and the sample. On the right hand side is an SEM image of the tip fabricated from Si_3N_4. Note the possible wear and contamination on the tip. . . 162
5.2 Schematic diagram of the AFM tip scanning over a thick sample. 164
5.3 Three and two dimensional atomic force microscopy images of a (100) surface polished mechanically (sample kc8), measuring 7×7 μm. Note the dark line used as a guide for the eye to show where data inside the polishing grooves were obtained. 170
5.4 Three and two dimensional atomic force microscopy images of a (100) surface polished manually (sample kc8), measuring 2×2 μm.170
5.5 Line profiles and power spectra obtained from figure 5.3. These are for a (100) surface (sample kc8) polished mechanically. Graph (a) shows the line profile obtained perpendicular to the polishing grooves, (b) its power spectrum, (c) the line profile obtained inside the polishing grooves, and (d) its corresponding power spectrum. The vertical scale of the power spectra is capped at $2nm^2$ since we wanted to amplify and pick out the smaller roughnesses that were caused by the manual polishing. 171
5.6 Line profiles and power spectra for a (100) surface polished manually, whose AFM image is shown in figure 5.4. Note the shallowing, smoothing and narrowing of the polishing grooves after the manual polishing compared to those of the mechanically polished surfaces (figure 5.5), and also the loss of some high and low frequency Fourier components. Graphs (a), (b), (c) and (d) have similar meanings as those shown in figure 5.5. 172
5.7 Three and two dimensional atomic force microscopy images of a (110) surface polished mechanically (sample kk7), measuring 3.7×6.7 μm. 173
5.8 Three and two dimensional atomic force microscopy images of a (110) surface polished manually (sample kk7), measuring 4×6.5 μm. 173

5.9 Line profiles and power spectra obtained from a mechanically (110) surface, whose AFM image is shown in figure 5.7. Graphs (a), (b), (c) and (d) have similar meanings as those shown in figure 5.5. 174
5.10 Line profile and power spectra for a (110) surface polished manually, whose AFM image is shown in figure 5.8. Note the disappearance of the high frequency components below 0.1μm (graphs (b) and (d)) and the prominence of those above 0.2μm for the spectra obtained perpendicular to the grooves. This is accompanied by the smoothing of the grooves but no noticeable shallowing, compared to the mechanically polished ones. Graphs (a), (b), (c) and (d) have similar meanings as those shown in figure 5.5. 175
5.11 Three and two dimensional atomic force microscopy images of a (111) surface polished mechanically (sample kc11). 176
5.12 Three and two dimensional atomic force microscopy images of a (111) surface polished manually (sample kc11). 176
5.13 Line profiles and power spectra obtained from a mechanically polished (111) surface whose AFM image is shown in figure 5.11. Graphs (a), (b), (c) and (d) have similar meanings as those shown in figure 5.5. 177
5.14 Line profiles and power spectra obtained from a manually polished (111) surface, whose AFM image is shown in figure 5.12. Note the disappearance of the high frequency Fourier components in the power spectra, and also those around 0.2μm and the accompanying prominence of the peaks after the manual polishing. The intensity of most components within the polishing grooves is also greatly diminished. Graphs (a), (b), (c) and (d) have similar meanings as those shown in figure 5.5. 178
5.15 Ratio of the real area to the scan size for the three low index diamond surfaces polished both mechanically and manually. Graph (a) includes data for a synthetic diamond sample while (b) doesn't. 181

5.16 Root mean square roughness plotted against the scan sizes. Panels (a) and (b) are for the large scan regions while (c) and (d) are for the smaller ones below 1x1μm. Panel (a) includes data for a mechanically polished (100) synthetic diamond sample. 182
5.17 Ratio of the true area to the projected one, plotted separately against the scan size for each of the three low index diamond surfaces polished mechanically and manually. 183
5.18 Root mean square roughnesses of the three low index diamond surfaces, plotted separately against the scan size. These were polished both mechanically and manually. 184
5.19 Three and two dimensional atomic force microscopy images of a (100) surface annealed to 250°C after manual polishing (sample kc8). 195
5.20 Three and two dimensional atomic force microscopy images of a (100) surface annealed to 750°C after manual polishing (sample kc8). The bar on the RHS shows a marginal decrease of 2nm in the peak-to-valley distance after the 750°C anneal compared to the 250°C anneal shown in figure 5.19. 195
5.21 Line profiles and power spectra for the (100) surface whose AFM image is shown in figure 5.19. This was polished manually, and then annealed in vacuum upto 250°C. Graph (a) shows the line profile obtained perpendicular to the polishing grooves, while (b) is its corresponding power spectra. Graph (c) is the line profile obtained inside the polishing grooves, while (d) is its power spectra. 196
5.22 Line profiles and power spectra for the (100) surface whose AFM image is shown in figure 5.20. This surface was polished manually and then annealed upto 750°C. Graphs (a), (b), (c) and (d) are similar to those described in figure 5.21. Note the marginal shallowing after the 750°C anneal (figures 5.21 (a) and 5.22 (a) obtained from AFM images of almost equal size). 197
5.23 Three and two dimensional atomic force microscopy images of a (111) surface annealed to 250°C after manual polishing (sample kc11). 198

5.24 Three and two dimensional atomic force microscopy images of a (111) surface annealed to 750°C after manual polishing (sample kc11). 198
5.25 Line profiles and power spectra for the (111) surface whose AFM image is shown in figure 5.23. This was polished manually and then annealed under vacuum upto 250°C. Graphs (a), (b), (c) and (d) are similar to those described in figure 5.21. 199
5.26 Line profiles and power spectra for the (111) surface whose AFM image is shown in figure 5.24, which was polished manually and then annealed upto 750°C. Graphs (a), (b), (c) and (d) are similar to those described in figure 5.21. Note the loss of some roughnesses and the deepening of the grooves after the 750°C anneal (figures 5.25 (a) and 5.26 (a)), which is corroborated by the power spectra where components above 0.27μm became fairly prominent and more intense. 200
5.27 Three and two dimensional atomic force microscopy images of a (110) surface annealed to 250°C after manual polishing (sample kk7). 201
5.28 Three and two dimensional atomic force microscopy images of a (110) surface annealed to 750°C after manual polishing (sample kk7). 201
5.29 Line profiles and power spectra for the (110) surface whose AFM image is shown in figure 5.27. This surface was polished manually and then annealed under vacuum upto 250°C. Graphs (a), (b), (c) and (d) are similar to those described in figure 5.21. 202
5.30 Line profile and power spectra for the (110) surface whose AFM image is shown in figure 5.28. The surface was polished manually and then annealed upto 750°C. Graphs (a), (b), (c) and (d) are similar to those described in figure 5.21. Note the prominence of the grooves after the 750°C anneal (figures 5.29 (a) and 5.30 (a)), just like in the AFM images themselves (figures 5.27 and 5.28), accompanied by shallowing and narrowing of the grooves. 203

5.31 Ratios of the real area to the scan size as well as the corresponding RMS roughness for diamond surfaces annealed up to 250 and 750°C (panels (c) and (d)) and those of surfaces polished manually for about an hour (panels (a) and (b)). 212

C.1 Three and two dimensional atomic force microscopy images of a (100) surface polished mechanically (sample kc8), measuring 7×7μm. 235

C.2 Three and two dimensional atomic force microscopy images of a (100) surface polished manually (sample kc8), measuring 3×3μm. 235

C.3 Line profiles and power spectra for a (100) surface polished mechanically, which were obtained from the AFM image shown in figure C.1. Graph (a) shows the line profile obtained perpendicular to the polishing grooves, (b) its power spectra, (c) the line profile obtained inside the polishing grooves, and (d) its corresponding power spectra. 236

C.4 Line profiles and power spectra for the (100) surface polished manually, which was obtained from the AFM image shown in figure C.2. Graphs (a), (b), (c) and (d) are as described in figure C.3. 237

C.5 Three and two dimensional atomic force microscopy images of a (110) surface polished mechanically (sample kk7), measuring 7×3.5μm. 238

C.6 Three and two dimensional atomic force microscopy images measuring 1×1μm, for a (110) surface polished manually (sample kk7).238

C.7 Line profiles and power spectra for a (110) surface polished mechanically, which were obtained from the AFM image shown in figure C.5. Graphs (a), (b), (c) and (d) are as described in figure C.3. 239

C.8 Line profiles and power spectra for a (110) surface polished manually, which were obtained from the AFM image shown in figure C.6. Graphs (a), (b), (c) and (d) are as described in figure C.3. 240

C.9 Three and two dimensional atomic force microscopy images of a (111) surface polished mechanically (sample kc11). 241

C.10 Three and two dimensional atomic force microscopy images of a (111) surface polished manually (sample kc11). 241
C.11 Line profiles and power spectra for a (111) surface polished mechanically, that were obtained from the AFM image shown in figure C.9. Graphs (a), (b), (c) and (d) are as described in figure C.3. 242
C.12 Line profiles and power spectra for a (111) surface polished manually, which were obtained from the AFM image shown in figure C.10. Graphs (a), (b), (c) and (d) are as described in figure C.3. 243
C.13 Three and two dimensional atomic force microscopy images of a (100) surface annealed up to 250°C after manual polishing (sample kc8). 244
C.14 Three and two dimensional atomic force microscopy images of a (100) surface annealed up to 750°C after manual polishing (sample kc8). 244
C.15 Three and two dimensional atomic force microscopy images of a (100) surface annealed up to 750°C after manual polishing (sample kc8). 244
C.16 Line profiles and power spectra for a (100) surface annealed to 250°C after manual polishing, which were obtained from the AFM image shown in figure C.13. Graphs (a), (b), (c) and (d) are as described in figure C.3. 245
C.17 Line profiles and power spectra for a (100) surface annealed to 750°C after manual polishing, which were obtained from the AFM image shown in figure C.14. Graphs (a), (b), (c) and (d) are as described in figure C.3. 246
C.18 Line profiles and power spectra for a (100) surface annealed to 750°C after manual polishing, which were obtained from the AFM image shown in figure C.15. Graphs (a), (b), (c) and (d) are as described in figure C.3. 247
C.19 Three and two dimensional atomic force microscopy images of a (111) surface annealed to 250°C after manual polishing (sample kc11). 248

C.20 Three and two dimensional atomic force microscopy images of a (111) surface annealed to 750°C after manual polishing (sample kc11). 248
C.21 Line profiles and power spectra for a (111) surface annealed to 250°C after manual polishing, that were obtained from the AFM image shown in figure C.19. Graphs (a), (b), (c) and (d) are as described in figure C.3. 249
C.22 Line profiles and power spectra for a (111) surface annealed to 750° after manual polishing, which were obtained from the AFM image shown in figure C.20. Graphs (a), (b), (c) and (d) are as described in figure C.3. 250
C.23 Three and two dimensional atomic force microscopy images of a (100) surface polished manually (sample kc8), measuring 3×3μm. 251
C.24 Three and two dimensional atomic force microscopy images of another (100) surface polished manually (sample kc8), measuring 3×3μm. 251
C.25 Three and two dimensional atomic force microscopy images of a (100) surface polished mechanically for sample kc8, measuring 2×2μm. 251
C.26 Three and two dimensional atomic force microscopy images of a (100) surface polished manually (sample kc8), measuring 2×2μm. 252
C.27 Three and two dimensional atomic force microscopy images of a (100) surface polished manually (sample kc8), measuring 1×1μm. 252
C.28 Three and two dimensional atomic force microscopy images of a (100) surface polished manually (sample kc8), measuring 400×420 nanometers. 252
C.29 Three and two dimensional atomic force microscopy images of a (110) surface polished mechanically (sample kk7), measuring 7×7μm. 253
C.30 Three and two dimensional atomic force microscopy images of a (110) surface polished mechanically (sample kk7), measuring 3×3μm. 253
C.31 Three and two dimensional atomic force microscopy images of a (110) surface polished manually (sample kk7), measuring 2×2μm. 253

C.32 Three dimensional atomic force microscopy images of (110) surfaces polished mechanically (sample kk7). The images show different but small sizes of scan areas, all expressed in nanometers in order to amplify the polishing grooves. 254
C.33 Three and two dimensional atomic force microscopy images of a (110) surface polished manually (sample kk7), measuring $1\times1\mu$m. 254
C.34 Three and two dimensional atomic force microscopy images of a (110) surface annealed to 750°C after manual polishing (sample kk7). 254
C.35 Three and two dimensional atomic force microscopy images of a (110) surface annealed to 250°C after manual polishing (sample kk7). 255
C.36 Three and two dimensional atomic force microscopy images of a (110) surface annealed to 750°C after manual polishing (sample kk7). 255
C.37 Three and two dimensional atomic force microscopy images of a (110) surface annealed to 750°C after manual polishing (sample kk7). 255

List of Tables

1.1 Properties of Diamond 7

2.1 Functional groups on "clean" polished diamond surfaces and their binding energies from the carbon peak. The binding energies are for photoelectrons coming from the underlined and bolded carbon atom, and these values have errors of about ±0.2eV. 49

2.2 Functional groups on "clean" polished diamond surfaces and their binding energies from the oxygen peak. The binding energies shown are for photoelectrons coming from the underlined and bolded oxygen atom, and these have errors of about ±0.2eV. . . 49

2.3 Fractional oxygen monolayer coverages on "clean" polished diamond surfaces. 50

3.1 ^{13}C atom coverages on clean diamond surfaces expressed as areal densities and monolayer coverages. 124

3.2 Full width at half maximum (FWHM) values for the 550 keV ^{13}C(p,γ)^{14}N resonant nuclear reaction. 130

5.1 Surface roughness due to the polishing grooves on the three low index diamond surfaces after mechanical and manual polishing. 186

5.2 Smaller surface roughnesses on the three low index faces after mechanical and manual polish. 187

5.3 Surface roughness due to polishing grooves on the three low index faces polished manually and then annealed to 250° and 750°C. . 205

B.1 Functional groups on the respective diamond faces investigated together with their corresponding binding energies (eV). 233

Chapter 1

Surface Description and Review of Diamond Properties.

1.1 The definition of a surface.

A surface is described as not only the very top layer of atoms, but as the boundary layer between one phase at the interface with another. For this reason, it is usually said to be constituted of at least the top 1-10 atom layers or say a depth of 0.25-3nm [1], with most solids having surface areal densities of the order of 10^{15} atoms/cm^2 [2]. The depth concept of a surface which would otherwise refer to the near-surface-region arise from the fact that the structure and chemistry of the topmost atom layer is influenced by the atoms immediately below it.

Surfaces often play crucial roles in facilitating the interaction of materials with their external environment, by virtue of the fact that surfaces are constituted of the very top atom layers. As a result, the description of a surface is to a large extent governed by the use for which it is intended, making the study of solid surfaces to be a rather intriguing field of basic research. They are the substrates for both homo and hetero-epitaxial growth of thin films used in semiconducting device fabrication and in other cases act as heterogeneous catalysts used to induce and steer a given chemical reaction, because such processes take

place at the surfaces. Therefore, there isn't a single universal definition that can describe a surface adequately, without making reference to its application. This can be appreciated when one considers the fact that, for surface processes such as bonding and wettability to take place or even catalysis as mentioned before, surface thicknesses close to a monolayer, or equivalently surface layers of less than 1nm are usually involved. On the other hand, surface conductivity and lubrication occur in surface layers of the order of 5nm in thickness, while passive surface films, corrosion and optical absorption involve surface layers whose thicknesses range between 10 and 50nm [3]. This suggests that the distinction between a surface and a thin film sometimes becomes very arbitrary, depending on how one looks at the surface.

Due to the lack of neighbouring atoms on one side of the very topmost layer, surfaces are generally said to be unbalanced and because of this, they are often referred to as being major bulk defects. This arises from the breakdown of the 3 dimensional bulk periodic potential/symmetry. Not only do surface atoms have fewer neighbours than the bulk ones, but the neighbouring atoms may be distributed anisotropically. Such a scenario renders them susceptible to foreign atom contamination because of the surface free energy that they possess, together with the prevailing surface thermodynamics. The availability of dangling bonds that are created during their preparation makes surfaces active and favourable sites for bonding with foreign atoms. If the surface formed is clean, that is, no adsorbates, the surface layer atoms tend to move to new equilibrium positions where they have minimum energy, leading to the phenomenon of surface reconstruction, where every atom tries to optimize its coordination. Such movement of surface atoms can also be triggered by an adsorbate attaching itself onto the surface, in such a way that the surface atoms readjust their positions to accommodate it [4].

Surface processes, their phenomena as well as key properties very often involve small concentrations of the participating atom species especially the adsorbates, which may be in the order of few parts per million of the underlying substrate atoms' areal density. This therefore requires the techniques probing them to be not only sensitive, but also to be surface specific. Such techniques include mainly the spectroscopic and microscopic ones. In addition to the techniques being surface specific, high vacuum is often required when investigating surfaces or interfacial phenomena, partly to avoid contaminating the surfaces, and also to enable the spectroscopic techniques probing them to access the surfaces unhindered by atom species other than those being investigated.

1.2 Surface features

A real surface will often contain varying amounts of surface features that may arise from its preparation processes. These include terraces, steps, slopes, kinks, step edge vacancies, edge dislocations, step edge adatoms, vacancies, screw dislocations and sometimes grooves [5]. Some of these features are illustrated in figure 1.1.

A combination of all these features or part of them can affect a surface in various ways, depending on its application. Some applications such as the electronic and optical ones require well characterized flat surfaces with minimum features, while mechanical processes such as adhesion may require surfaces having a slightly different topography. This also applies to surface processes involving corrosion and catalysis, where a surface that provides maximum surface area for the interaction process is required. It therefore becomes important to emphasize that, as with the depth of a surface, its application also determines the quality of a surface. Often cracks develop on surfaces during their preparation and these may accelerate their rate of erosion, especially if they are

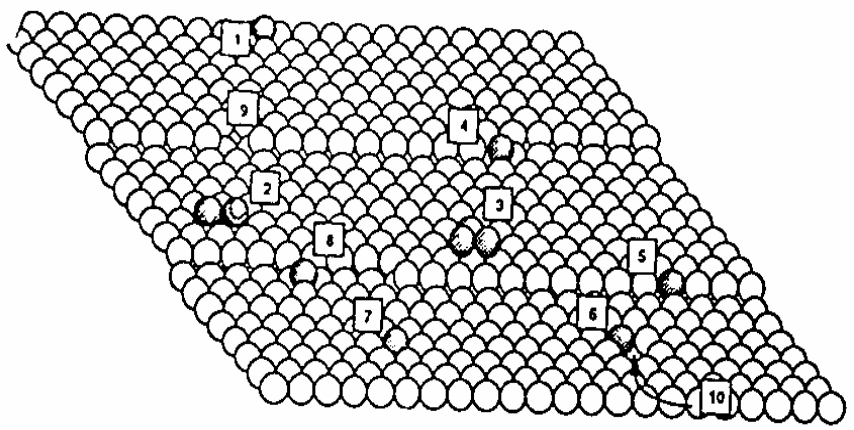


Figure 1.1: Various surface features. 1. Adatom 2. Dimer 3. Trimer 4. Kink edge 5. Step 6. Terrace vacancy neighbour 7. Terrace 8. Step adatom 9. Step vacancy 10. Terrace vacancy [6]

used in harsh environments. A plausible theory on crack formation at surfaces proposed by Somorjai *et al.* [4] is that at steps, clustering of atoms near the edge can occur, and these clustered atoms then move away from the step, in the process opening up atomic channels into the bulk, which in turn may lead to crack formation or propagation if an external force is applied.

1.3 The Diamond.

This work involved mainly the study of natural diamond surfaces polished mechanically in the three principal orientations; the cuboid {100}, the dodecahedral {110} and the octahedral {111}, and this therefore makes it quite important to discuss the key material properties of diamond initially. The study of the three principal orientations was especially important because most applications involving diamond tend to use some of them, as opposed to the higher index planes. The three crystal orientations were initially determined by x-ray diffraction measurements and a photograph of the actual polished diamond samples that were used in this study is shown in figure 1.2. More details regarding some

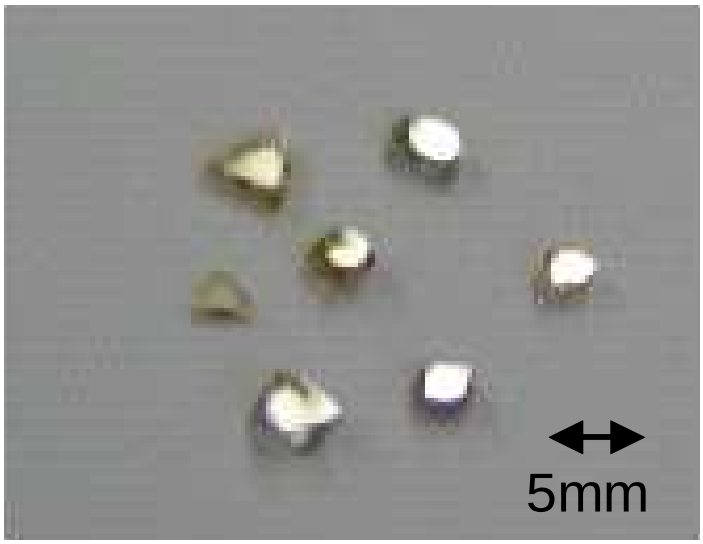


Figure 1.2: A photograph of the diamond samples used in this study. The top row starting from the LHS shows a (111) surface [sample kc5], and a (100) surface [sample kc3]. The middle row starting from the LHS shows a (111) surface [sample kc11], a (100) surface [sample kc8], and the RHS one a (111) surface [sample kc9]. The bottom row starting from the LHS shows a (111) surface [sample kf4], and a (110) surface [sample kk7].

of these samples are given in ref [7].

Diamond is an allotrope of carbon, made up almost entirely of carbon atoms bonded in a tetrahedral structure. This means that every carbon atom is surrounded by four others at angles of about 109.47° to each other. It occurs in the isometric cubic form of crystalline carbon as shown in figure 1.3 and it is the high-pressure polymorph of carbon, which is metastable at room temperature [8]. The carbon atoms in diamond are bonded covalently through the hybridization of the 2s orbitals of carbon ($1s^2 2s^2 2p^2$) and the three 2p orbitals, to form the strong sp^3 hybridization that is characteristic of diamond. The four valence electrons thus formed become equally distributed among the sp^3 orbitals with each orbital pointing to one of the four corners of the tetrahedron. As such, diamond exhibits close packing of the carbon atoms, with the highly directed charge density giving rise to its strength (hardness) and chemical stability. This

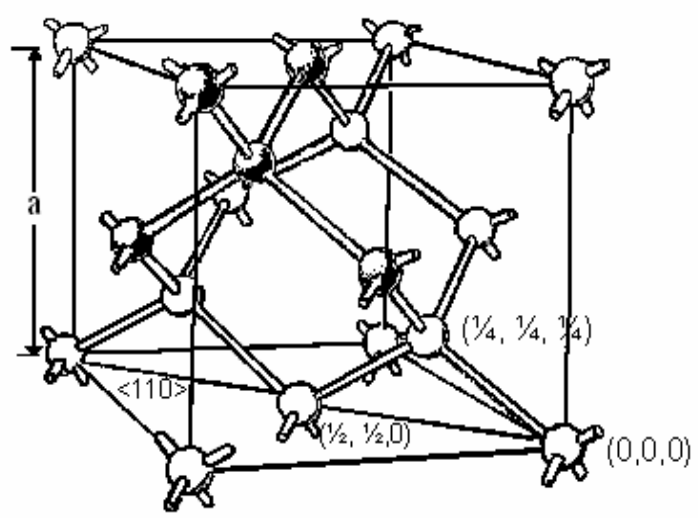


Figure 1.3: Crystal lattice of diamond.(After A. K. Ramdas [9]).

property causes diamonds to be the hardest of all known natural materials, with a bulk modulus of about 4.42Gpa [10, 8, 11] and a hardness ranging between 55-62GPa for type I diamond and 75-113GPa for type II diamond on the Knoop scale [12, 13, 14].

Due to its structure and composition, diamond is a material that possesses extreme properties which make it very useful in various technological applications. Some of these properties are listed in Table 1.1.

In addition to these properties, recent discoveries have shown that certain adsorbates on diamond surfaces have the ability to alter significantly their electron affinities and therefore their electrical properties [22], making diamond an extremely sought after material for those applications that exploit the said phenomena such as cold cathodes [23], LEDs [24] and other optoelectronic devices [25].

Furthermore, the unique properties of diamond cause it to be widely used in the gem industry, as well as in technological applications. The main difference between diamonds used in various technological applications and those meant

Table 1.1: Properties of Diamond

Material property	Value
Lattice constant (RT) (Å)	3.5668 [12]
Atomic concentration (cm^{-3})	1.763x10^{-23} [7]
Mass density($g.cm^{-3}$)	3.5154 [15]
Linear Expansion coefficient (K^{-1})	1.05x10^{-6} [15]
Thermal conductivity(RT) ($W.cm^{-1}.K^{-1}$)(Type IIa)	25 (6 × Cu) [16]
Melting point (K)	3773
Debye Temperature (K)	2230 [17]
Breakdown field ($V.cm^{-1}$)	10^7 [18]
Resistivity (Ω.cm) (Type IIa)	10^{16} [19]
Cohesive energy (eV/atom)	7.37 [10]
Energy Gap (eV)	5.49 [20]
Refractive index (over the visible spectrum)	2.418 (for sodium light) [21]
Vickers hardness (kg/mm^2)	9000-10000 [8]

for gem quality applications is the level of imperfection and impurity contained [26]. If imperfections are undetectable with an optical lens having a magnification of X10, and the diamond has good brilliance, sparkle, colour and of appreciable size, then it is said to be 'eye clean'or flawless, and hence of gem quality.

For industrial applications, natural diamonds remain an expensive option, and hence the need to synthesize these for such applications. In this regard, major breakthroughs have been made in synthesizing good quality diamonds for both industrial and gem quality applications, as outlined in [27, 28, 29, 30, 31, 32]. The level of the sophistication of the techniques used to fabricate both high quality single crystal and polycrystalline synthetic diamonds has developed quite dramatically since the first artificial synthesis of diamond in the early 1950s [33]. However, the most commonly used techniques still remain the High Pressure High Temperature (HPHT) technique, and the Chemical Vapour Deposition (CVD), with the HPHT diamonds starting to infiltrate the gem diamond market [26], thereby causing some uncertainties in the diamond trade. Synthetic diamonds currently account for more than 90% of industrial diamonds, and their yearly output stands at about 80 tons [26]. In addition,

for the 100 tons of diamond now produced annually, 80% is manufactured by the HPHT routine [27].

Most natural diamonds are colourless stones, with some yellowish ones also being found [34, 26]. The colour in natural diamonds is widely attributed to lattice defects or optical centres rather than trace elements but in certain cases the amount of single substitutional nitrogen and hydrogen have been found to play some role [20]. However, although this seems to be the generally accepted view regarding the origins of colour in diamonds, debate still rages on regarding the origin of some of the colours especially the brown diamonds [35, 36]. Those that appear naturally pink are thought to be due to strong plastic deformation leading to a broad UV-VIS-NIR absorption band at 550nm [34], together with an increasing absorption towards shorter wavelengths, while the yellow colour in diamonds is attributed to minute amounts of nitrogen close to 1ppm (parts per million) that replace carbon in the lattice.

Generally, most natural diamonds contain small amounts of nitrogen, hydrogen and occasionally boron as trace elements, and these enable them to be categorized as either type I or II. Those diamonds that contain nitrogen as the main impurity are classified as type I diamonds [8]. If the nitrogen exists in clusters, it has been shown not to affect the colour of diamond, and these type of diamonds are referred to as type Ia. These clusters may be constituted of about 10 atoms [37], with typical concentrations rising up to 500ppm and sometimes as high as 2500ppm [38]. Most natural diamonds are of this type. If the nitrogen appears in dispersed positions throughout the crystal lattice such as in isolated substitutional sites [39] at concentrations of between 40 to 100ppm [20] with utmost concentrations of up to $5\text{x}10^{19}\text{cm}^{-3}$, these are referred to as type Ib, and sometimes they appear yellow. They are very rare in nature but almost all synthetic diamonds are of this type.

Type II diamonds have a very small concentration of nitrogen impurities

[20]. Within this category, if the diamonds contain nitrogen concentrations of the order of 10^{18}cm^{-3} [40], these are known as Type IIa diamonds and they constitute the purest form of all natural diamonds. They are also very rare in nature, and their electronic mobility at room temperature ranges between 2000 and 2800 cm^{2}V^{-1}s^{-1} [41], compared to 1500 cm^{2}V^{-1}s^{-1} in silicon, while their hole mobility is between 1800 and 2100 cm^{2}V^{-1}s^{-1}. Compared with recently developed synthentic diamonds, the un-doped single-crystal chemically vapour deposited diamonds have been reported to have very high drift mobility of between 4500 and 3800 cm^{2}V^{-1}s^{-1} [33] for electrons and holes respectively.

When considered against the pure diamond's bandgap of 5.5eV, the donor level due to isolated substitutional nitrogen lies relatively deep at 1.7eV [42]. However, without the nitrogen donor levels, diamond is an indirect wide bandgap material especially when compared to other group IV elements such as silicon which has a narrow band gap of 1.12eV. This implies that the donor levels of the incorporated nitrogen makes it act as a shallow dopant. If the diamonds contain traces of boron of the order of 10^{17}cm^{-3} or less than 1ppm, within the crystal matrix, they are characterized as type IIb and they appear as blue. These types of diamond are extremely rare in nature, and they are semiconducting, with an activation energy of 0.37eV [18]. Their hole mobility measured at room temperature is 1500 cm^{2}V^{-1}s^{-1}, compared to silicon's 450 cm^{2}V^{-1}s^{-1}. Apart from being an impurity or a shallow dopant in diamond, nitrogen has also been found to influence considerably the mechanical strength of diamond in such a way that synthetic diamonds with increased concentration of carbon defects in the form of dispersed nitrogen have lower mechanical strength. This has also been attributed to the metal inclusions in such diamonds. In particular, Nassau [43] observes that diamonds with a high concentration of dispersed nitrogen above 1000ppm may be considerably weak, an observation that agrees quite well with the earlier findings of Field *et al.* [14].

Those diamonds that show a predominantly hydrogen related absorption line at around 2900cm^{-1} [44], are classified as type IIc, and they are also very rare in nature.

Diamond stones are normally weighed in carats, with 1carat being equal to 200 milligrams [14].

1.4 Mechanical polishing of diamond surfaces.

In order to be able to make any economical use of diamond surfaces, relatively large flat areas often need to be exposed, and one way of doing this is through cutting and polishing. Various polishing techniques have so far been developed as reported in literature [45, 46, 47, 48, 49, 50] but the most widely used and well developed is still the mechanical polishing. However, before any form of polishing commences, the rough diamonds are first cleaved or sawed, in order to expose larger faces of the required orientations. The cleaving process is the preferred way of creating the (111) faces due to the fact that it's the plane of lowest strength [51, 52] while the (110) and (100) faces are more easily formed by sawing along the {110} and {100} faces. This is done by pressing the single crystal diamond onto a phosphor-bronze wheel impregnated with a mixture of diamond powder and oil at the edges. The process is however generally slow, and it takes about 10 hours to traverse a 1 carat diamond [51]. The choice of the sawing direction is also very critical in the sense that choosing the wrong direction could lead to breakage of the blade. Laser cutting of diamonds has also been used quite extensively lately, and this has made the cutting process not only more flexible, but also much faster.

After cleaving, laser cutting or sawing, the diamond surfaces are then polished mechanically by pressing them onto a rotating cast iron scaife charged with different sizes of diamond grit, with average pressures of about 10 to 25

kg/mm^2 [53]. Exceeding this value has been reported to lead to rough polishing or grinding. More details of scaife preparation are given in [54]. The wheel, which measures about 30cm in diameter and 2cm in thickness, rotates at a speed of about 2800rpm, and the material removal rate is linearly proportional to the speed [45]. This means that the material removal is proportional to the number of revolutions of the scaife irrespective of its speed, implying that the every revolution of the wheel results in the same amount of material removal [55]. This agrees fairly well with the slow manual polishing technique which is applied in this work, where the polishing is achieved by rubbing the diamond back and forth on a metal block loaded with diamond paste and olive oil. The manual polishing follows the mechanical polishing as outlined later on in the experimental section of the XPS chapter.

As the grit particles interact with the diamond surface asperities, the polishing is believed to proceed in two dominant ways; mechanical and chemical wear, with three forms of mechanical wear being proposed in the literature. These include fracture at the highest loads, plastic grooving at intermediate loads and attrition of the surface involving the removal of individual atoms or small groups of atoms at low loads [56]. The size of the grit particles has also been reported to affect the removal rate of material, with large-sized grains leading to higher removal rates and therefore to a larger affected layer such as more pronounced crack patterns. Many studies have also shown that the material removal rate on diamond surfaces through mechanical polishing depends very strongly on the crystallographic orientation of the polished plane, [47] as well as the direction of polishing. This finding leads to what are commonly referred to as the easy (soft) and hard polishing directions, meaning that material removal is different in each direction, depending on the orientation being polished. Thus, although any surface may be polished in any given direction, the polishing proceeds differently depending on whether it is done in an easy or hard direction, implying

that the mechanisms governing material removal are also different.

The <100> is the soft polishing direction for both the {110} and {100} orientations, while the <110> direction is the hard polishing one for the same faces. The {100} planes have four directions of maximum wear in the cube <100> directions, while the {110} planes have two 'soft'<100> polishing directions [57]. The {111} orientation is resistant to wear and therefore hard to polish in all directions [51], although it shows a slightly three fold symmetry [54]. As such, polishing of this plane is only achieved by tilting the face slightly off the principal plane, say by 1 or 2° [58]. Polishing in the soft directions has been shown to result in formation of grooves with very smooth bottoms [56], and the surface shows no fractures or generation of dislocations, an observation that has been attributed to the removal process occurring at stress levels under the critical value of the applied load. However, the grooves are absent when polishing is done in a hard direction. The earlier work of Hitchiner *et al.* [59] showed that ratios greater than 10:1 for material removal rate between the soft <001> and the hard <110> polishing directions were realized for the (110) face, showing quite clearly that the choice of the correct polishing direction is critical as to how the polishing proceeds. More recently, it has been shown in other related studies that material removal rate is so different between polishing in the soft or hard directions for both the {110} and {100} orientations, that variations of 2 to 3 orders of magnitude higher for the soft <100> abrasion direction as compared to the hard <110> direction are typically reported [51]. This confirms Thornton *et al's* [60] earlier findings that the rates at which polishing proceeds in different directions on different crystallographic faces may differ by more than two orders of magnitude.

Environments rich in hydrogen and oxygen have also been reported to increase the rates of polishing, with similar effects in both the soft and hard directions, an observation attributed to oxidation processes aiding in the polishing,

in the presence of H_2 [61]. Such an observation was also made by Thornton and Wilks [62] where they established that scratch marks produced by normal polishing process may be removed by rubbing on a cast iron lap in the presence of an oxidizing agent such as potassium nitrate. Although Field [55] reported earlier that abrasion resistance is not thermally activated, heating of the scaife upto 100°C has been reported to result in higher removal rates, with further temperature increases reducing the polishing rate [53]. According to Yarnitsky *et al.* [57], heating the scaife to say 145°C allows the grit particles to get embedded into the cast iron scaife, thereby achieving faster polishing rates. However, heating the scaife further makes it soft, and in the process the grit particles sink completely into the cast iron, and hence no further polishing is realized. On the contrary, heating the diamond itself does not achieve any improvement in polishing, a factor that has been attributed to the yield stress of diamond not decreasing appreciably below 1900K. This means that the number of diamond-grit contacts remain unchanged below this temperature, and hence the rate of material removal. Furthermore, Hird *et al.* [54] observed that the grit particles tend to orient themselves to positions that facilitate polishing in the easy directions. Efforts to determine the exact temperature at the point of contact of the surface asperity and the scaife are currently going on, with a view to establishing its real effects on the polishing process [54].

Various explanations have been presented regarding the exact wear processes of diamond when the diamond grit interacts with a surface, especially those involving the microscopic and atomic scales. In their work on diamond polishing, Grillo *et al.* [49] found that the polishing of diamond in the soft direction proceeds via a process in which diamond transforms to less dense forms of carbon, after which the transformed material detaches, possibly as graphitic debris. Similarly, Couto *et al.* [56, 63] established that a form of plastic nanogrooving develops while polishing in the soft directions [64]. These suggestions

seem to be driven by the general understanding that when two solids slide over each other, very high pressures(10^8 - 10^{10} Pa) develop at the point of contact with a surface asperity or a grit particle, on application of normal loads (several Newtons). At such pressures, local sites on the surface are drastically deformed and get displaced from their equilibrium positions, giving rise to an atomically disordered interface [65] as illustrated in figure 1.4, while figure 1.5 shows a schematic diagram of the actual set up used in the mechanical polishing. The argument of the local site becoming deformed under high pressure and high polishing velocities, becomes even more convincing when considers the fact that the indentation hardness of cast-iron (used in making the polishing wheel) is equivalent to 30 kilobars, which is the pressure onset of diamond-stable region [66]. Therefore, as the diamond surface being polished slides over the diamond grit particles, they sink into the iron as shown in figure 1.4 until this pressure is present over the indentation area, with the pressure that the top of the particle is exerting on the diamond being usually higher (depending on shape) and hence well within the diamond-stable region. A momentary 'cold weld'can then be expected to form, with the subsequent fracture possibly occurring in a different place, and hence the diamond surface getting gradually eroded, partly as individual atoms or as quite small groups of atoms. Frictional sliding at high contact pressures has been reported to produce plastic deformation in diamond, which implies that transformation to lower-order carbon structure occurs [54], and in the process severe surface damage takes place too.

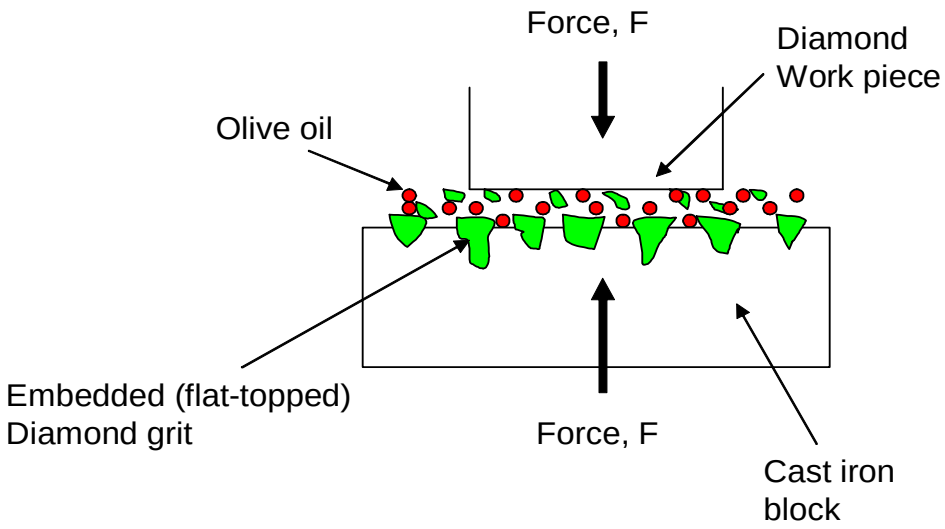


Figure 1.4: A diamond surface sliding over diamond grit that has embedded itself into the cast iron scaife due to high pressures developed at the point of contact, as well as temperature (Adapted from [65, 54]). Diamond is quite resistant to plastic deformation except at high temperatures ($> 1600°C$) [60], although Hird *et al.* [54], appear to suggest that this can occur even at lower temperatures.

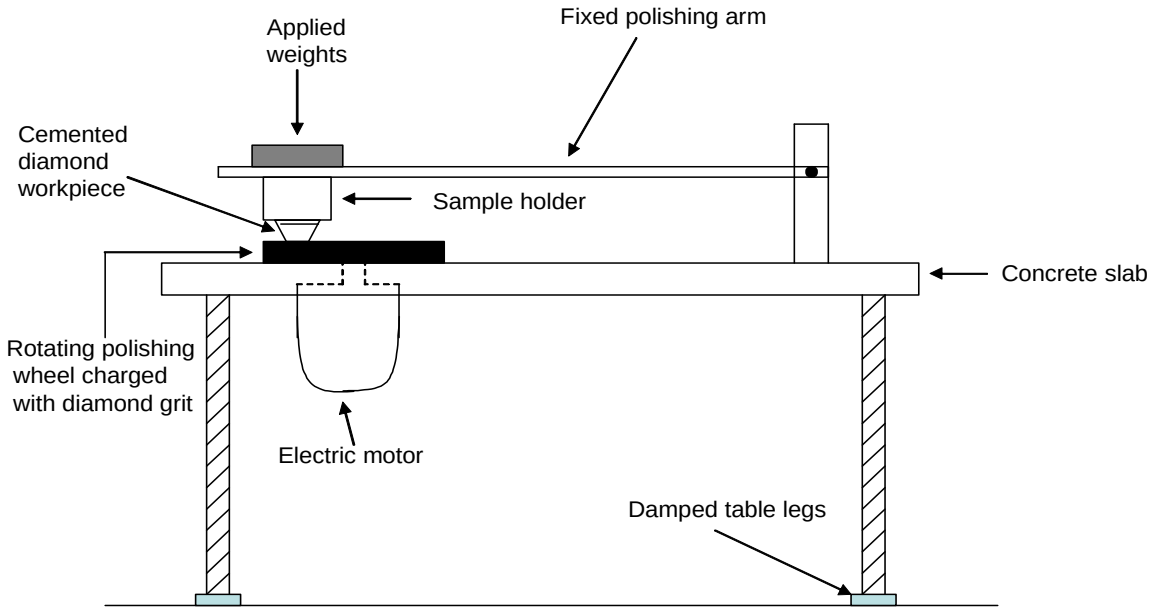


Figure 1.5: A schematic diagram of a simplified set up used for the mechanical polishing of diamond surfaces.

Using Rutherford Backscattering Spectrometry (RBS), it was shown that a large number of atoms is displaced in the subsurface layer during polishing [67]. However, the term large is rather relative here, since for the mechanically polished surfaces, this has been shown to corresponded to 1.2×10^{17}atoms/cm^2 or a depth of about 200nm down to which damage occurs, although not the whole of it is disordered [67]. For the tribochemically polished surface, a damaged region of 1.2nm or 1.2×10^{16}atoms/cm^2 near the surface region of the top 20nm was observed. Reflection Electron Energy Loss spectroscopy further showed that no diffraction pattern occurred for the polished {110} surface, whereas a cleaved {111} face showed a pattern of perfectly crystalline structure. These observations were interpreted to mean that during frictional contact of diamonds, the surface of the diamond degrades towards a structure that is amorphous to some extent and containing sp^2 bonded carbon [49]. Derry *et al.* [68] using RBS together with ion channelling found very little damage being propagated into the bulk by mechanical polishing, with only one or two atom layers being disordered. This follows early experiments on subsurface damage carried out by Casey *et al.* [69] using the cathodoluminescence mode of the electron microscope. They found some traces of surface damage of mechanically polished diamond surfaces, but they did not indicate its extent in terms of the depth.

Computer simulations have also been helpful in complementing the experimental findings regarding the mechanical polishing of diamond surfaces. By applying principally the *ab initio* quantum mechanical simulations to the wear processes on the (110) diamond surface, Jarvis *et al.* [70] showed that mechanical processes involving the atomistic mechanism of nano-grooving earlier proposed by Couto *et al.* [56] were responsible for polishing on this surface in the soft direction. In the hard direction, they proposed that nano-grooving may play some role in the wear of diamond, but the process is significantly

difficult. They further established that the surface deformation in the soft polishing direction was local while it was nonlocal in the hard direction since the stress was distributed over a large number of diamond bonds, leading to extensive subsurface damage and the likelihood of the polishing residue being amorphous. Their observations agree fairly well with the RBS and channelling findings mentioned earlier as far as the displacement of the subsurface atoms during polishing is concerned. Recent findings by Bouwelen *et al.* [47] suggest that a form of mechanically induced degradation of diamond by bond bending weakens the material and allows removal by harder material. In particular, they suggest that non-degraded diamond, may actually be responsible for the removal of material during polishing in the soft directions.

As more efforts continue to be invested towards the understanding of the mechanisms by which diamond polishing proceeds, new and more accurate methods have progressively been developed for both natural and synthetic diamonds [71, 45, 72, 59, 48, 73, 74] and [49], but most of the workers agree that the microcleavage mechanism initially proposed by Tolkowsky [45, 8] and further developed by Wilks and Wilks [75] is the most likely process of material removal only in the hard polishing directions. These were complemented by both the early and recent works of Ford [76], Feng *et al.* [77], Thornton *et al.* [60], Casey *et al.* [78], Hird *et al.* [79], Grillo *et al.* [80] and Tolansky *et al.* [81] which spans a period of more than 5 decades.

The study of the topography of various polished diamond surfaces has also helped a great deal in understanding the underlying mechanisms of diamond polishing. In this regard, while studying the topography of polished diamond surfaces, Couto *et al.* [82] found that diamond polishing along the soft direction is produced by disruption of atomic bonds under high shear stress. Through this process, they suggested that individual atoms or groups of atoms were removed

from the diamond interface, reorganizing into carbonaceous debris. They further established that the topography of surfaces polished in the easy direction (e.g. the {100} plane in the <100> direction) exhibits smooth grooves often free from indications of fracture [49]. However, when the same surface is polished in the direction of difficult abrasion, it shows a rough array of grooves suggesting that the mechanism of material removal is one of fracture on a nanometre scale. In addition, when the (100) face is polished in the easy polishing direction <100>, there is a fourfold symmetry in friction, the lowest value being observed along the hard polishing direction <011>, while the highest is registered in the easy <100> polishing direction, commonly referred to as the cube edge direction. Such an observation was also made by Yarnitsky et al [57].

Friction of diamond surfaces also plays a significant role when diamond surfaces are polished, through the abrasive wear. This was initially established by the pioneering work of Tabor [83], with further developments being made by E. M. Wilks and J. Wilks [84] and later on by Tabor and J.E. Field [85] all of whom showed that the friction depended on the crystal face as well as the orientation. They also found that friction is always low on the (111) face with a coefficient close to 0.1 being reported for diamond on diamond [65] and there is no anisotropy on this face, which agrees with the findings of Mingyoung *et al.* [86]. Furthermore, friction, wear and lubrication of diamond surfaces is closely intertwined with their applications in industry, as well as their polishing process [87], [56], [77], [88], [89], [78].

Due to the strong dependence of mechanical polishing of diamond surfaces on the orientations and the polishing directions, certain difficulties may be encountered when polishing polycrystalline diamonds using this process, an observation also made by Bouwelen *et al.* [50]. Instead, other techniques as discussed in [74, 90, 91] as well as the ion polishing technique explained by Koslowski *et al.* [48] may be appropriate. These may be complemented by other new techniques

for preparing smooth surfaces such as the lift-off technique [92]. This technique is achieved through ion irradiation, resulting in a buried damaged layer. A smooth surface is then obtained by 'lifting-off'the top layer after annealing.

The aforementioned discussion summarizes the polishing of diamond surfaces, and although it only touches on the key aspects, it seems to suggest quite strongly some sort of consensus with regard to the actual processes involving the mechanical polishing of diamond at the atomic level. However, some debate still remains, and the exact combination of factors responsible for the wear mechanism during polishing remain elusive as alluded to by Hird *et al.* [79, 54]. This means that further work is still needed to give a better understanding of the wear mechanisms developed over 600 years, when diamond surfaces are prepared through mechanical polishing.

Chapter 2

X-Ray Photoelectron Spectroscopy (XPS) Studies of Oxygen Adsorption on the Three Low Index Diamond Surfaces.

2.1 Chapter layout

This chapter deals specifically with the x-ray photoelectron spectroscopy studies of the adsorbed oxygen and hydroxyl groups on the three low index diamond surfaces. XPS is the technique of choice in this case because of its high energy resolution and surface sensitivity (0.5% of an atom layer), which make it possible to establish not only the atomic species adsorbed on the polished surfaces and the responsible amounts (monolayer coverages), but also their binding energies. These findings, their role and possible effects on the applications of diamond surfaces, are indicated. Further details are given in Appendix B.

2.2 Introduction

As mentioned before, the first few atom layers that constitute a surface are crucial to the behaviour and properties of surfaces. These are the atoms that interact with the environment, participate in surface modifications and bond

with other materials to form interfaces. The adsorbates on them also play a crucial role with regard to the surface applications. In any surface, the top-most layer of atoms are generally unbalanced because they have matter on one side and not the other, meaning that the electron distributions around them are asymmetrical with respect to the positive ion cores. Although not always desirable, foreign atoms may therefore be introduced onto "clean"surfaces either through alien sources or intentionally, depending on the environment in which the surface is prepared or is within. Foreign atoms adsorbed on surfaces have an advantage that they contribute towards the lowering of surface energies, making such surfaces to be more stable.

There has been a great deal of interest lately to use diamond in various technological applications where it has various advantages over other materials owing to its unique properties. Interestingly, many of these applications depend mainly on its surface properties and therefore, establishing the identity and nature of the foreign atoms on polished diamond surfaces holds the key towards the realization of these objectives. Over the last few years, tremendous efforts have been committed towards the investigation of particularly oxygen on polished diamond surfaces, a task which seems to present some challenges even up to now. Theoretical models using various approaches such as the local density approximation (LDA), quantum *ab initio* calculations and molecular dynamics methods have been developed [93]. Such efforts have benefited immensely through the numerous experimental investigations that have been conducted to verify these models, and also to get an idea of the actual bonding on the real surfaces, with the spectroscopic techniques being mainly used. But in spite of all this, different theories continue to be suggested, indicating a need to investigate these surfaces further, and more thoroughly.

Oxygen has so far been established to be the main foreign atom on "clean"polished diamond surfaces [94], apart from hydrogen [95, 96]. It has also been shown to

play some key role in the technological applications of "clean"polished diamond surfaces, especially at the surface interfaces with other materials, such as semiconductors. An earlier investigation by Derry *et al.* [94] using RBS revealed a sub monolayer of oxygen coverage on the three low index diamond faces, with the (100) face showing higher oxygen coverages. Such varying oxygen coverages were attributed partly to the fact that the (100) face has two dangling bonds per surface carbon atom while the other two have one each. This coverage has further been confirmed by Rebuli *et al.* [97] using RBS and nuclear reaction analysis, who in addition found that the oxygen coverage depends on the vacuum level of the target chamber as well as the cleaning technique used. Oxygen atoms on diamond surfaces have also been suggested to have hydroxyl (OH) groups on the (111) surface and C-O-C bridges or C=O groups on the (100) surface [98]. Perhson *et al.* [99] however report that the oxygen chemistry of the smooth C(100) faces is hardly understood. They further indicated that although carboxyl (C=O), bridge (C-O-C) and hydroxyl groups on polished diamond surfaces have been observed, specific groups were not attributable to specific faces. A similar observation was earlier made by Wang *et al.* [100], but they point out that the bridge chemisorption of oxygen monolayer dominates at temperatures below 400°C, while the ONTOP chemisorption becomes favourable at 500°C. Baumann *et al.* [101] on the other hand observed that in addition to the two bonding configurations for oxygen terminated surfaces, i.e. C=O and C-O-C observed by Rebuli *et al.* [98] and Perhson *et al.* [99], oxygen termination on the C(100) leads to a (1×1) structure. First principle calculations of Rutter *et al.* [102] showed that standard chemical bond energies favoured the double bonded structure over the bridge bonded one on an ideal C(100) surface, while Perhson *et al.* [99] indicated that similar calculations suggested that atomic oxygen adsorption energies at the ONTOP and bridge sites were nearly identical, showing clearly a need for further clarification to reconcile

the two hypotheses. The presence of adsorbed oxygen atoms on polished diamond surfaces has also been shown to yield surface states which gives further insights about the bonding environments, as well as the strength of the bonds. Most of the previous work on the surface density of states of diamond has tended to concentrate more on the effects of hydrogen [103, 104, 105, 106, 107, 101], because of its ability to yield negative electron affinity on diamond surfaces, with little work being done on oxygen [108, 109, 110, 111, 112]. A great deal of it has also involved mainly theoretical modelling. The available works in literature show that oxygen leads to positive electron affinity on diamond surfaces and therefore its adsorption on these surfaces can lead to modifications of such surfaces for electronic purposes.

In most cases, Ultraviolet photoelectron spectroscopy (UPS) or electron energy loss spectroscopy (EELS) have been the techniques of choice to probe the surface density of states, but with improved energy and spatial resolutions offered by modern XPS systems, they are now routinely being used to probe the valence band spectra. The importance of the valence spectra is rooted in the fact that valence electrons are the ones involved directly in the bonding process, and so the intensity and energy of the valence band peaks depend on the bonding environment. According to the chemistry of bond formation, when an adsorbate forms on a solid surface, it either donates an electron to the conduction band of the substrate, or electron transfer to the adsorbate may occur. In either case, when the adatom gets adsorbed, charge can accumulate at a surface in positions between atomic planes, and this charge could reduce the surface energy because the s-like states which concentrate at the ion cores have higher energy than the p-like states of electrons collecting between the atoms [2]. Somorjai *et al.* [113] reports that adsorbates tend to fill up first the strongly bonding surface states before the weaker bonding sites become occupied as the coverage increases. With regard to oxygen adsorption, Baumann *et al.* [101]

indicated that the lone pair orbitals of oxygen extending from the surface are expected to increase the work function of the surface, possibly leading to the reported positive electron affinity associated with adsorbed oxygen on diamond surfaces.

Theoretically, surface states are solutions to the Schrödinger equation in the region near the surface where the potential varies periodically in only two dimensions. In the case of diamond, electrons may be regarded as being tightly bound to the ion cores, since it exhibits a wide band gap and therefore the tight binding electron theory is normally used. For some cases, the solutions of the Schrödinger equations at a surface can have eigenfunctions whose energy corresponds to a band gap but which are localized at the surface, and such are the kind of surface states one expects in an environment where there are broken bonds. If charge is situated in these surface states it will result in electrostatic fields penetrating into the solid, and thus a varying electrostatic potential on passing from the surface to the interior [2]. This varying potential distorts the band structure of the bulk solid, leading to band bending because the charge associated with these states is different from the bulk charge distribution. Surface states will thus inevitably affect the electronic properties of the surfaces by acting as either sources or sinks of electrons. Due to the fact that only the electrons in the valence shells (and not the core level ones) of all the ions constituting the oxidation states of oxygen on diamond are directly involved in the bonding, the structure of the oxygen layer on diamond (valence band) VB is very sensitive to changes in short and/or long range ordering of the ions in the oxygen layer.

When XPS is used to obtain the valence band spectra, the kinetic energy of the valence photoelectrons is such that the final states may lack structure due to the high energy of the exciting x-rays, though this may not be the case always,especially with the new spectrometers that have added features

as explained previously. Thus, we can confidently allude to the fact that the observed density of states closely reflects the initial filled density of states. Furthermore, due to the depth of the photoelectrons, it is very likely that the XPS would also yield some bulk states. Additionally, the cross-sections of the photoelectron emission from the valence levels are much lower than for core levels, giving rise to low intensities in general.

In this work, we present XPS (X-ray photoelectron spectrometry) results for adsorbed oxygen and its nature (configurations) on the polished "clean" diamond surfaces. Since its early development throughout the 1950's and 1960's by Siegbahn *et al.* [1], XPS has become one of the preferred tools for surface analysis, owing to its high surface sensitivity of the order of 0.5% of an atom layer, as well as its superior energy and spatial resolutions. Its popularity is further enhanced by its high information content, its ability to address a wide variety of samples, and its sound theoretical basis. It is important to note that, while the X-rays may travel deep into the material, the detected photoelectrons come from only within a few atom layers below the surface. The distance below the surface from which the photoelectrons come, is determined by the inelastic mean free path (IMFP) λ , which is a function of the energy of the photoelectron, and from this, the mean escape depth of the photoelectrons which is expressed as $\lambda\cos\theta$ (θ is the emission angle) can be determined. The probability of detecting the photoelectrons in the XPS spectrometer therefore depends primarily on the distance of the emitting atom below the surface and not how deep the exciting X-rays travel within the materials' bulk. This probability is normally expressed as

$$p(d) = exp(-\frac{d}{\lambda}) \tag{2.2.1}$$

Where $\lambda = \lambda(\mathrm{E})$ is the inelastic mean free path of the photoelectron and d = the photo-emitting atom's perpendicular distance below the surface.

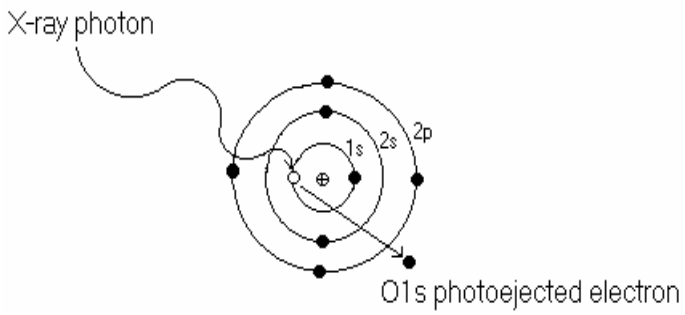


Figure 2.1: Photoemission of a core level electron. (After J.C. Vickerman [1]).

When an X-ray photon impinges on a target atom, it may transfer all its energy to an atomic orbital electron, thus leading to the emission of the electron from the atom into the vacuum. This process which forms the basis of XPS can be summarized by Einstein's equation that

$$h\nu = KE + BE + \phi \tag{2.2.2}$$

Where, hν= kinetic energy of the X-ray source, KE=energy of the emitted photoelectron, BE=binding energy of the electron in the atom, and ϕ = work function of diamond. However, the work function is normally a small value compared to the other terms in equation 2.2.2, and thus the expression reduces to,

$$BE = h\nu - KE \tag{2.2.3}$$

It is the value of the binding energy in equation 2.2.3 that gives the signature of the photo-emitting atom. This process is illustrated in figures 2.1 and 2.2.

Figure 2.3 shows a typical Mg and Al dual anode X-ray gun. Unlike the earlier versions of XPS spectrometers, the modern ones are now fitted with monochromators, which are capable of giving spatial resolutions of down to 20μm, while at the same time the X-ray beam scans and rasters over the specimen surface [115]. Energy resolutions of between 0.1 and 0.2eV are possible

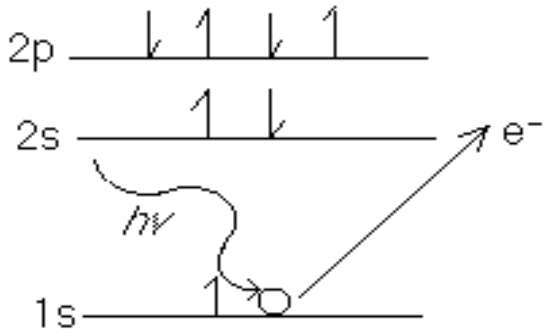


Figure 2.2: The XPS process. (After J.C. Vickerman [1]).

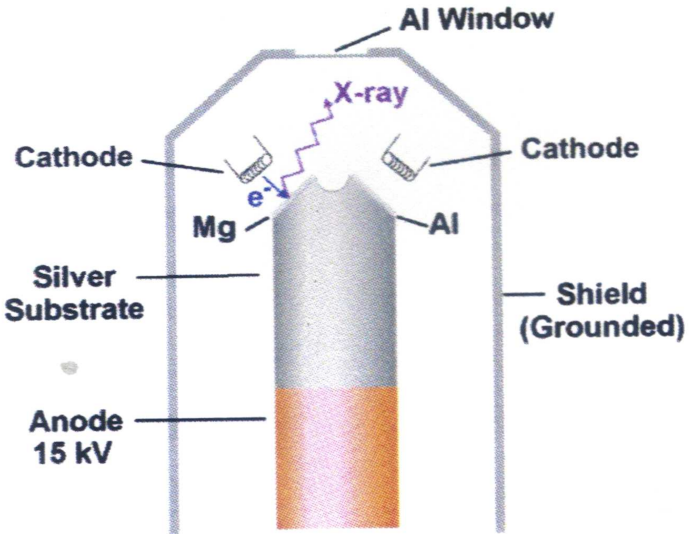


Figure 2.3: An illustration of the twin anode X-ray gun. (After VG Scientific company [114])

today, and the surface sensitivity can even be improved further by carrying out angle resolved XPS analysis, which decreases the distance perpendicular to the sample surface, which the photoelectrons have to travel.

The advantages offered by modern XPS equipment are therefore fully exploited in this work to investigate oxygen adsorption on polished diamond surfaces, as well as their associated surface density of states.

2.3 Experimental

Six natural type Ia diamond samples and one synthetic of different sizes and thickness ranging between 3mm x 3mm x 2mm and 5mm x 4mm x 3mm were used. The actual sizes of these are shown in figure 1.2. They were initially polished mechanically by pressing onto a cast iron disk (scaife) rotating at about 2800 revolutions per minute. Diamond powder of the order of 1μm was initially used, and the polishing is thought to proceed through cleavage of tiny diamond fragments when the diamond particles in the powder hit the surface asperities [50], at least for the hard polishing directions. Recent studies suggest that other mechanisms such as transformation of diamond into other phases under shear stress may be responsible for polishing in the easy directions as outlined in the introduction chapter. The polishing was done in air, where the environmental conditions were not controlled. The polished surfaces were then cleaned by boiling for 30 minutes in an acid mixture of 1 part HNO_3 (nitric) acid, 3 parts $HClO_4$ (perchloric) acid and 4 parts H_2SO_4 (sulphuric) acid in order to remove any impurities (such as metal and other loosely bound particles or debris) which may attach themselves on the faces during the polishing process. This was followed by a 3 times rinsing process in double distilled deionised water.

After the surface preparation procedure discussed above, each surface was

further polished manually by pressing it on a highly polished metal block using normal (hand) force. The metal blocks used in our laboratory are made of mild steel, cast iron and tin. The diamonds were held on a cork, where the preferred polishing directions were already marked. To achieve the desired polishing, $1/4\mu$m and $1/10\mu$m diamond pastes were used as the abrasive medium, together with olive oil which acted as the lubricant. Apart from being the lubricant, the oil was also believed to have provided the hydrogen atoms required to terminate some of the broken (dangling) diamond-carbon bonds, especially in view of the fact that most dangling bonds have been established to be terminated preferentially by hydrogen [116]. The principal aim of the manual polishing was to achieve a much smoother (flat) surface as opposed to the mechanically-polished ones where diamond grit particles of the order of 6μm down to a $1/4\mu$m were used. Additionally, it was very likely that the $1/4\mu$m or even the $1/10\mu$m diamond particles would break down into smaller fragments during the polishing procedure, thus achieving even smoother surfaces. It has already been established that the mechanical polishing is a 3 body process where both the diamond workpiece as well as the diamond grit particles get polished in a reciprocal manner [54].

As a measure of achieving better polishing, all the polishing marks evident from the mechanical polishing (as observed using an optical microscope) were expected to become relatively smaller or any loosely bound diamond or non-diamond particles swept away, since a finer grade of diamond paste was used. In the process, much smoother and cleaner surfaces were expected to be achieved. Such a hypothesis is thoroughly investigated in the Atomic force microscopy work presented in chapter 5, by studying the nature and size of the polishing lines/grooves, before and after the manual polishing. Through the slow speed and low contact pressures of the manual polishing, rearrangement of the surface carbon atoms was expected to proceed via the breaking of some surface bonds

together with the associated atoms or groups of atoms, in a manner similar to the one described earlier. Through this, much improved surfaces were to be realized [117]. It is important to also note that, before the hand polishing procedure commenced, the easier polishing directions were first identified, and these were established to be the same directions as used in the mechanical polishing. This was realized through the identification of the polishing marks on each face before starting the manual polishing process using an optical microscope. The manual polishing procedure lasted for about 30 minutes on every face. Each surface was then cleaned separately in a solution of "Contrad"(a surface cleaning detergent also sold under the name "Decon 90") and deionised water in ratios of 1:4, so as to remove any metal impurities as well as any non-diamond carbon atoms. This was followed by a three times ultrasonic rinsing in deionized water over different durations of time, to ensure thorough and non-contaminating rinsing. A Pyrex beaker was used during all the rinsing stages.

Although diamond surfaces are generally hydrophobic [94], a few water droplets were seen on the surfaces after the rinsing process, probably due to the presence of polar surface oxygen groups. These were nonetheless eliminated by blowing dry nitrogen gas over the surfaces, and the dried samples were stored in 'polythene'bags to avoid further contamination, while awaiting the analysis. Plastic gloves were worn in order to avoid surface contamination with body oils during the manual polishing process, and plastic tweezers were used, to avoid scratching the surfaces, lest one introduces some further surface contamination.

The cleaned samples were analyzed using both a Phi quantum 2000 spectrometer and a VG scientific ESCALAB III Spectrometer fitted with a CLAM 100 dual anode (Al and Mg) x-ray gun source. From these two, both wide and narrow survey scans for each sample were obtained, while the valence band spectra were obtained using only the Phi quantum 2000 spectrometer, due to its high energy resolution and its ability to focus and tune the x-ray beam. This

spectrometer also enabled us to carry out small sample area scans of about 100μm owing to the added features that were capable of yielding relatively monochromatised X-rays that could be focused, as shown in figure 2.4.

Charge compensation for spectra obtained using the phi Quantum 2000 spectrometer was achieved by depositing a thin gold film on each sample after taking the C and O spectra, followed by the acquisition of the XPS spectrum containing the Au_{4f} peak. The peak thus obtained was then shifted to the expected binding energy (BE) value, which was 84eV [1, 118], although Vincent C. [119] gives it as 83.98eV, which is practically a negligible difference compared to the former value. The difference in the amount of energy shift was then applied to the observed carbon and oxygen peaks of the respective faces, so as to obtain the expected peak locations independent of charging. Instead on relying on only one sample, the thin gold film was deposited on one of each of the three low index diamond faces for consistency, which was a desired requirement so as to cancel out any effects arising from possible individual differences on the respective faces. The amount of shift that was obtained gave a precise reference for locating the peak positions, and thus identifying the specific atomic species as well as the bonding configurations corresponding to them. Through this, it was possible to assign the peaks not only to the atoms where the photoelectrons originated, but also the respective orbitals, thereby establishing the foreign atoms thereon unambiguously.

Since relatively thick insulating diamond samples ranging from about 2 to 4mm were used, the loss in the intensity of the photon flux and the loss of the bremsstrahlung of X-rays arising from monochromatising the X-ray beam led to an appreciable decrease in the amount of the scattered low energy electrons in the vicinity of the sample and consequently, static charge builds up. This static charge was minimized, by using an electron flood gun producing an electron beam of low energy ($\leq$ 1eV) with respect to the vacuum chamber at earth,

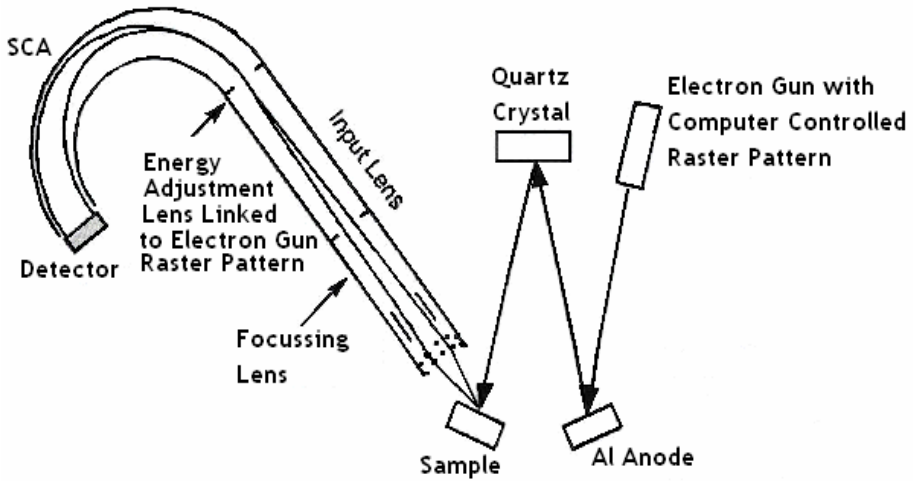


Figure 2.4: Schematic diagram of the XPS process using a Phi Quantum 2000 spectrometer [115].

from a source that was positioned very close to the specimen.

In the case of the VG Scientific spectrometer whose schematic diagram is shown in figure 2.5, charge compensation was achieved by first obtaining the spectra of a thin gold foil, and then shifting the observed $Au4f_{7/2}$ doublet peaks to the positions where they were expected to occur at 87.63 and 83.95eV in the standard reference [119]. The amount of shift in the BE was noted and then applied to each subsequent carbon and oxygen peak obtained thereafter on the respective diamond samples. This gave the locations of the peaks' BEs and therefore their atomic identities too.

Additionally, although UPS (Ultraviolet Photoelectron Spectroscopy) is commonly used to obtain the VB spectra, due to the small line width of the UV sources (HeI and II) compared to the line width of X-ray sources, in this investigation, determination of the VB spectra by XPS was preferred. This arose from the fact that, the line width for this spectrometer was also small, and the relatively higher energy of X-ray radiation (as opposed to the UV radiation), meant that the valence band spectra obtained using XPS corresponded more closely to the actual electron density of states of the VB of the solid. This way,

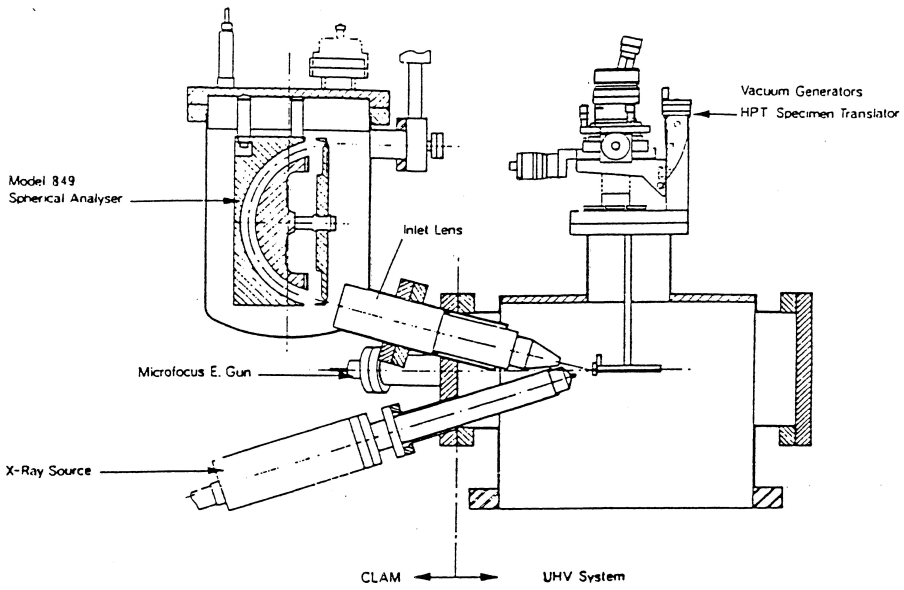


Figure 2.5: Schematic diagram of the CLAM 100 VG scientific spectrometer [120].

it would be possible to identify the surface density of states due to the adsorbed oxygen as well as those due to the underlying surface and bulk carbon atoms.

The Phi quantum 2000 spectrometer had a better energy resolution of about 0.45eV and this enabled us to deconvolve the observed carbon and oxygen peaks, while the relatively low energy resolution of the VG Scientific spectrometer ($\cong$2.0eV) did not make deconvolution of the carbon and oxygen peaks worthwhile, because it would not distinguish between peaks which were much closer than this. Besides, due to the large size of the X-ray beam ($\approx$10mm) [121], the entire sample was always illuminated and it sometimes fell onto the sample holder. This could in a way give incorrect information on the spectra regarding the actual species coming from the sample itself, and those from the holder, and in the process making their quantification troublesome. The beam spot was not entirely circular as expected, but rather oval due to the design of the twin anode x-ray gun source. Additionally, with the intensity of the x-ray beam dropping as $1/r^2$, where r is the distance between the x-ray gun and the sample,

(which in this case was ≈10mm), the sample holder was not expected to be a key contributing factor regarding the spectra obtained, since it was located a bit further than the sample surface, owing to its thickness. The problem of a significant amount of the beam falling on the sample holder was resolved by optimizing the counts of the carbon peak via the manipulator set-up in such a way that the most intense carbon peak possible was obtained. A high carbon peak meant that most of the scanning X-ray beam was falling onto the diamond and not the holder. Under these circumstances, very little contribution from the molybdenum holder was expected and sometimes none at all, especially on the bigger samples. This setting was then used to obtain all the subsequent spectra for that particular sample.

Whenever a new sample was introduced into the UHV chamber, another optimized setting was always obtained, in a similar manner as described above, before commencing with the scanning, due to the varying thicknesses of the samples. The samples were introduced into the UHV chamber of the VG Scientific Spectrometer using a transfer rod, and since they were coming from atmospheric pressure, the pumping had to be done differentially in three stages. This was achieved by first using a mechanical pump, then a turbo molecular pump, and finally a diffusion pump to obtain the required UHV pressures of better than 10^{-11} Torr.

In the case of the Phi Quantum 2000 spectrometer, all the samples were introduced into the UHV chamber at once. This was made possible by the use of a facility (carousel) that was in cooperated into it, which could accommodate all the samples simultaneously, while each sample was introduced and analyzed separately in the VG Scientific UHV system because it could only handle one sample at a time. This meant that some samples stayed relatively longer within the Phi quantum 2000 UHV chamber, than others, before being analyzed. Samples were also deliberately allowed to stay for longer periods of time within the

UHV chamber of the system containing the VG Scientific spectrometer, so as to investigate the role of ambient pressure conditions on the adsorbates. Repetitive scans were obtained in both cases so as to improve the signal to noise ratio, and particularly in the case of the VG Scientific spectrometer, since its X-ray beam was not focussed, as mentioned earlier. This procedure was expected to improve the signal and reduce the noise level because the signal to noise ratio S/N increases as $t^{1/2}$, where t is the scan time [1], thus yielding less background. AlKα X-rays at 1486.6eV were used for the analysis in both cases.

2.4 Results

Figures 2.6, 2.8, 2.10, 2.12, 2.14 and 2.16 show the wide survey scans of the X-ray photoelectron spectra obtained from the samples that were investigated, while figures 2.7, 2.9, 2.11, 2.13, 2.17 and 2.15 show the corresponding carbon (C 1s) and oxygen (O 1s) narrow scans.

The wide scans for each face were taken within the binding energy range of 0eV to 1300eV and from these, the narrow scans were extracted. The carbon and oxygen narrow scans that were obtained using the Phi quantum 2000 spectrometer were deconvolved after a linear background subtraction, since all had a FWHM greater than the energy resolution of the spectrometer. A linear background subtraction was the most appropriate choice because the lower and higher binding energy sides of every peak were almost at the same level. The deconvolved peaks that are shown in figures 2.7, 2.9, 2.11, 2.13, 2.15 and 2.17, gave the various sub-peaks which corresponded to different oxidation states on the "clean"polished diamond surfaces. Identity of all the functional groups attached to these polished faces were thus established by comparing the observed binding energies from the respective sub-peaks with the standard references [1], [122], [119]. Tables 2.1 and 2.2 gives a summary of the observed functional

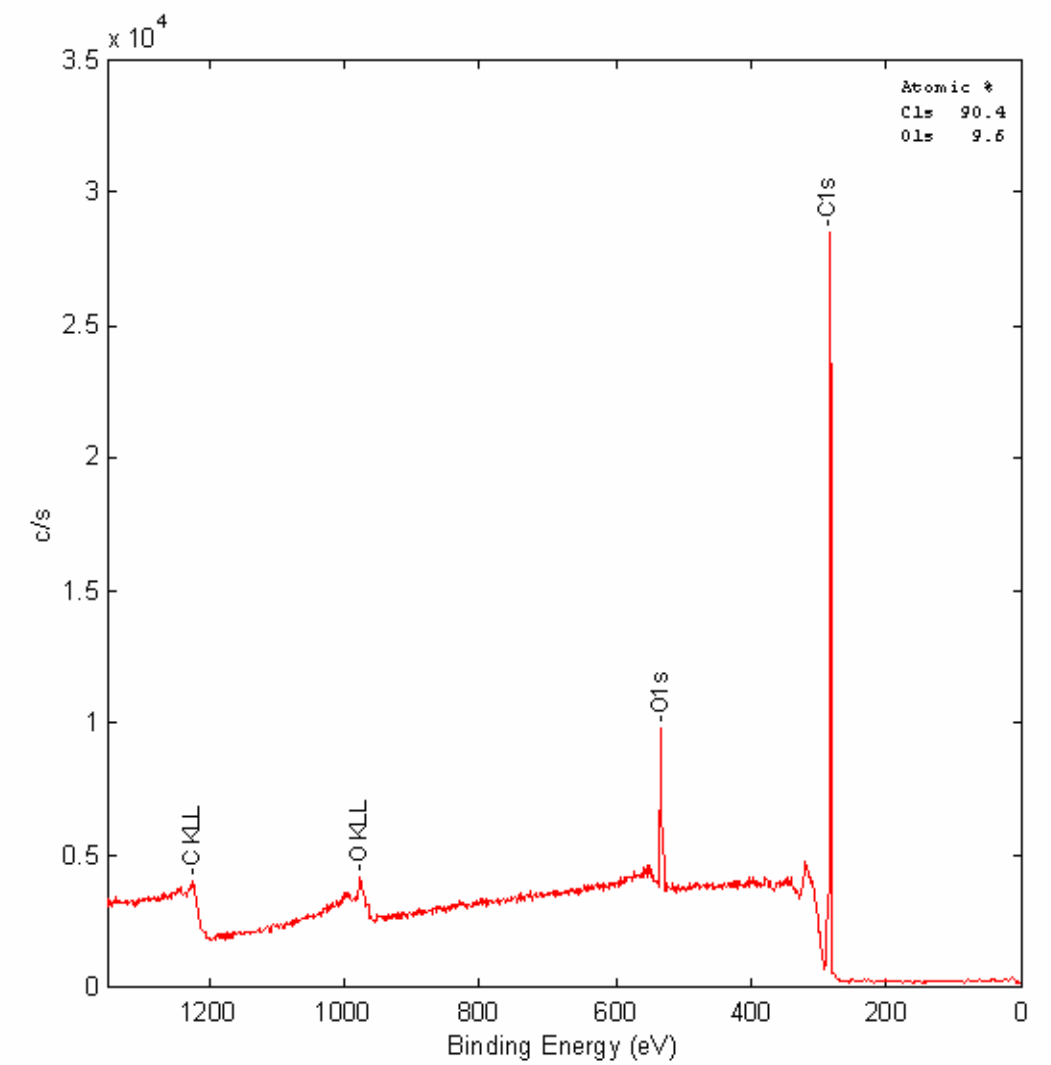


Figure 2.6: Wide survey scan for a (100) face. [Sample (kc8)]

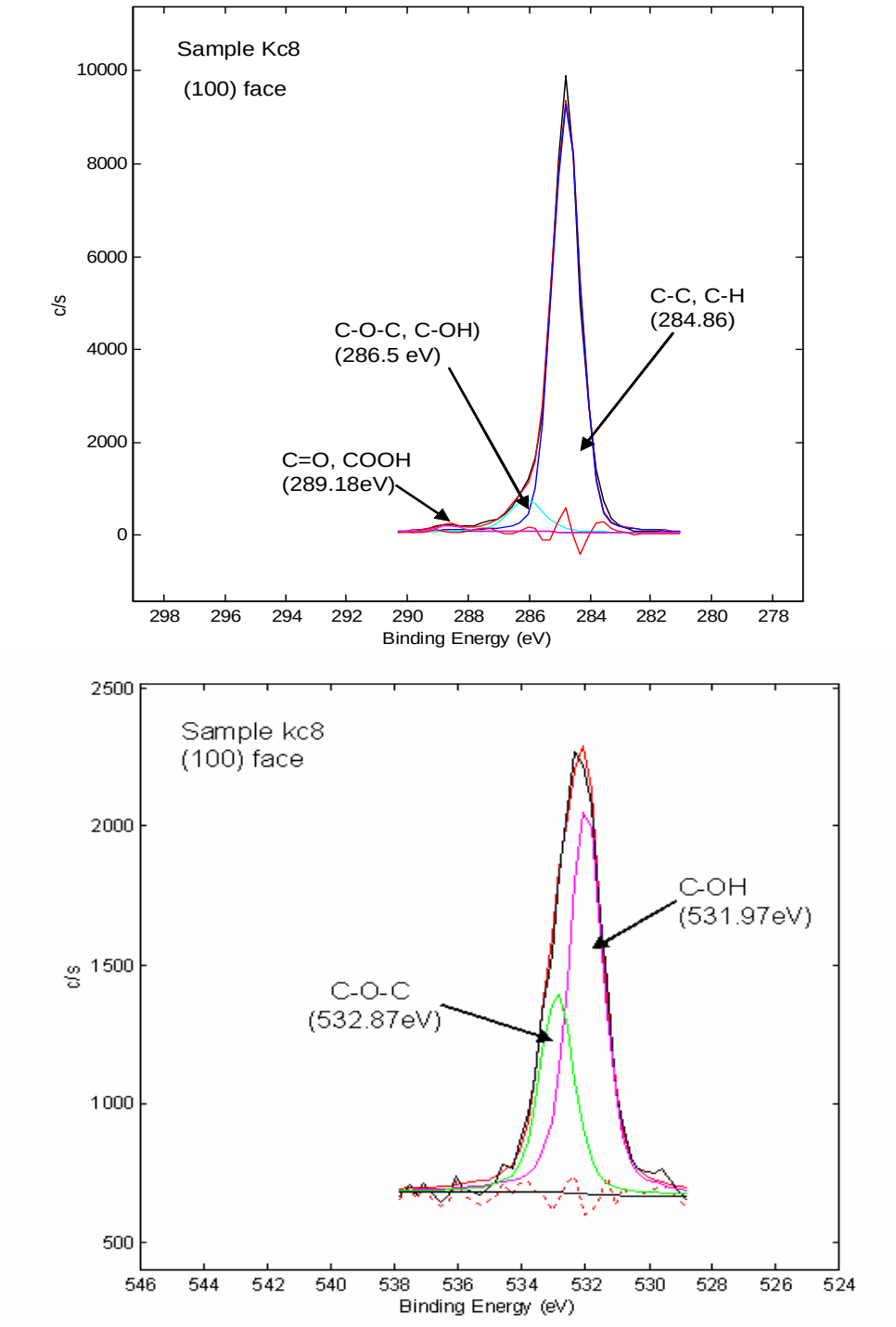


Figure 2.7: Narrow scans for a (100) face. Top panel represents the C1s while the bottom one is the O1s scan.[Sample (kc8]

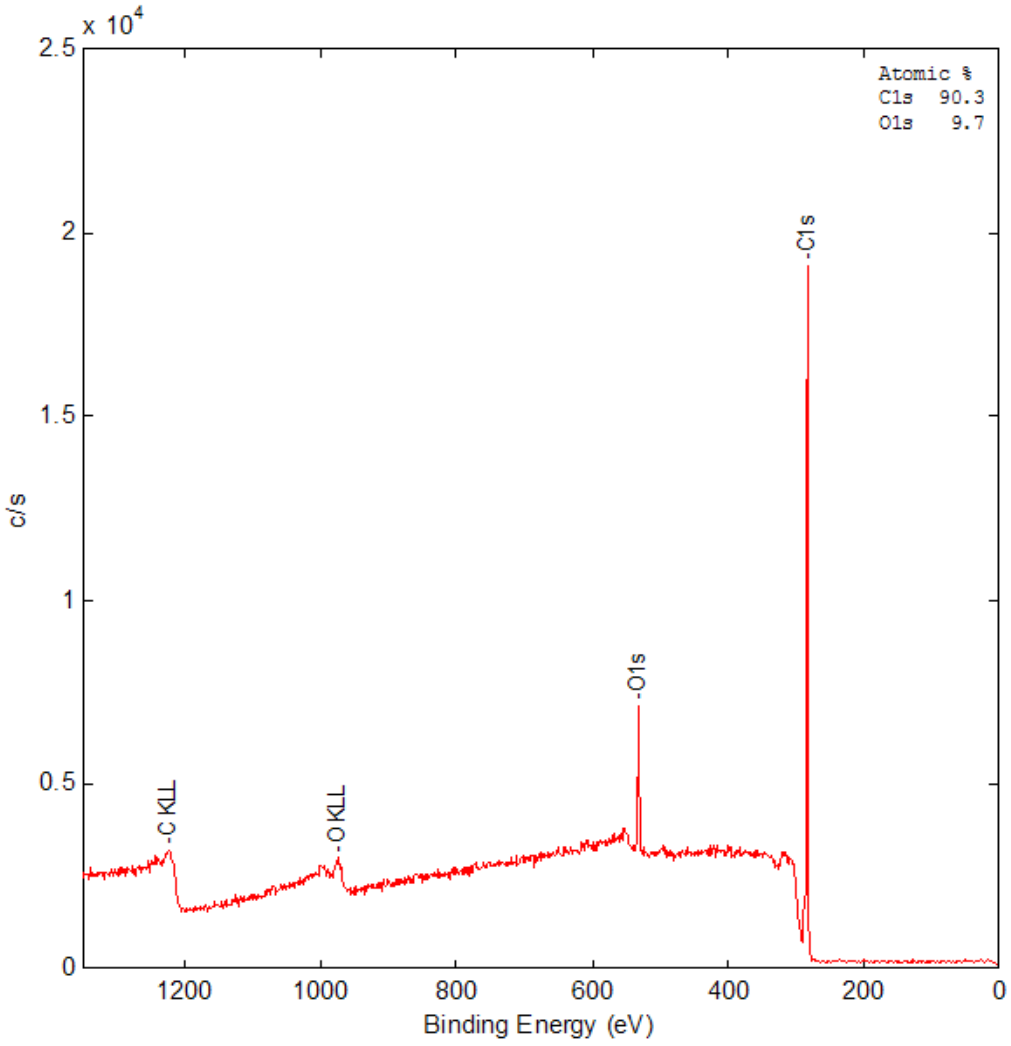


Figure 2.8: Wide survey scan for a (111) face. (Sample kc11)

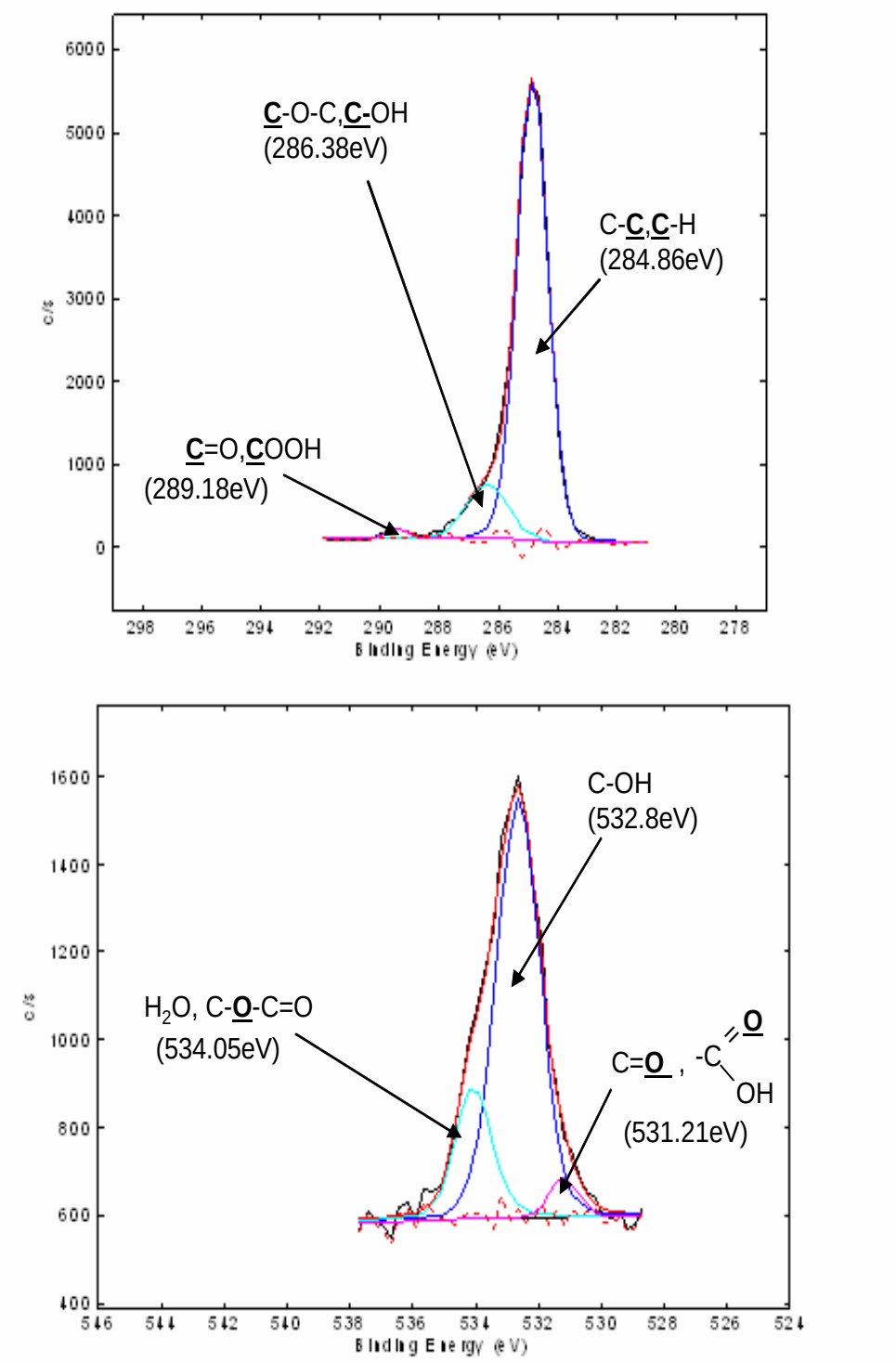


Figure 2.9: Narrow scans for a (111) face. Top panel represents the C1s peak, while the bottom one is the O1s peak.[Sample (kc11]

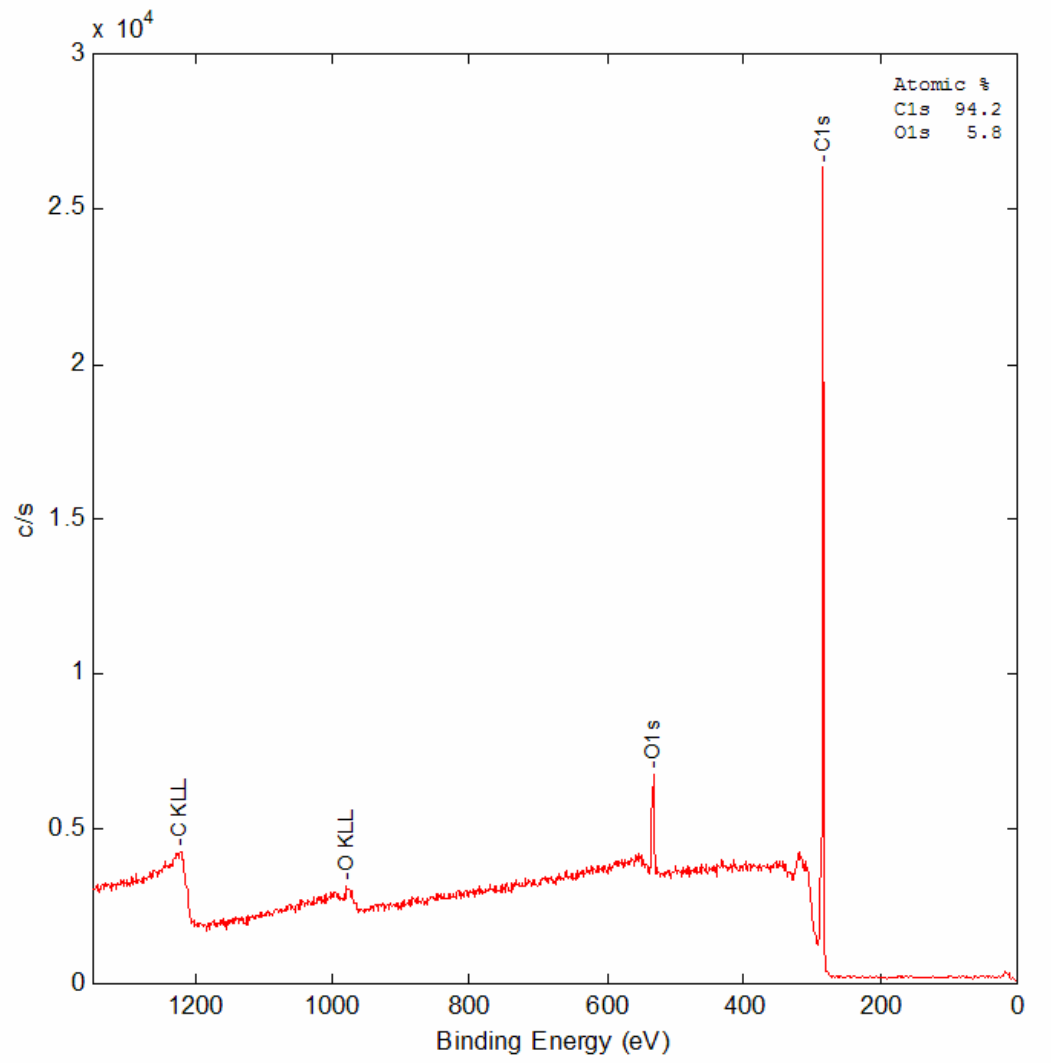


Figure 2.10: Wide survey scan for a (111) face. (Sample kc9)

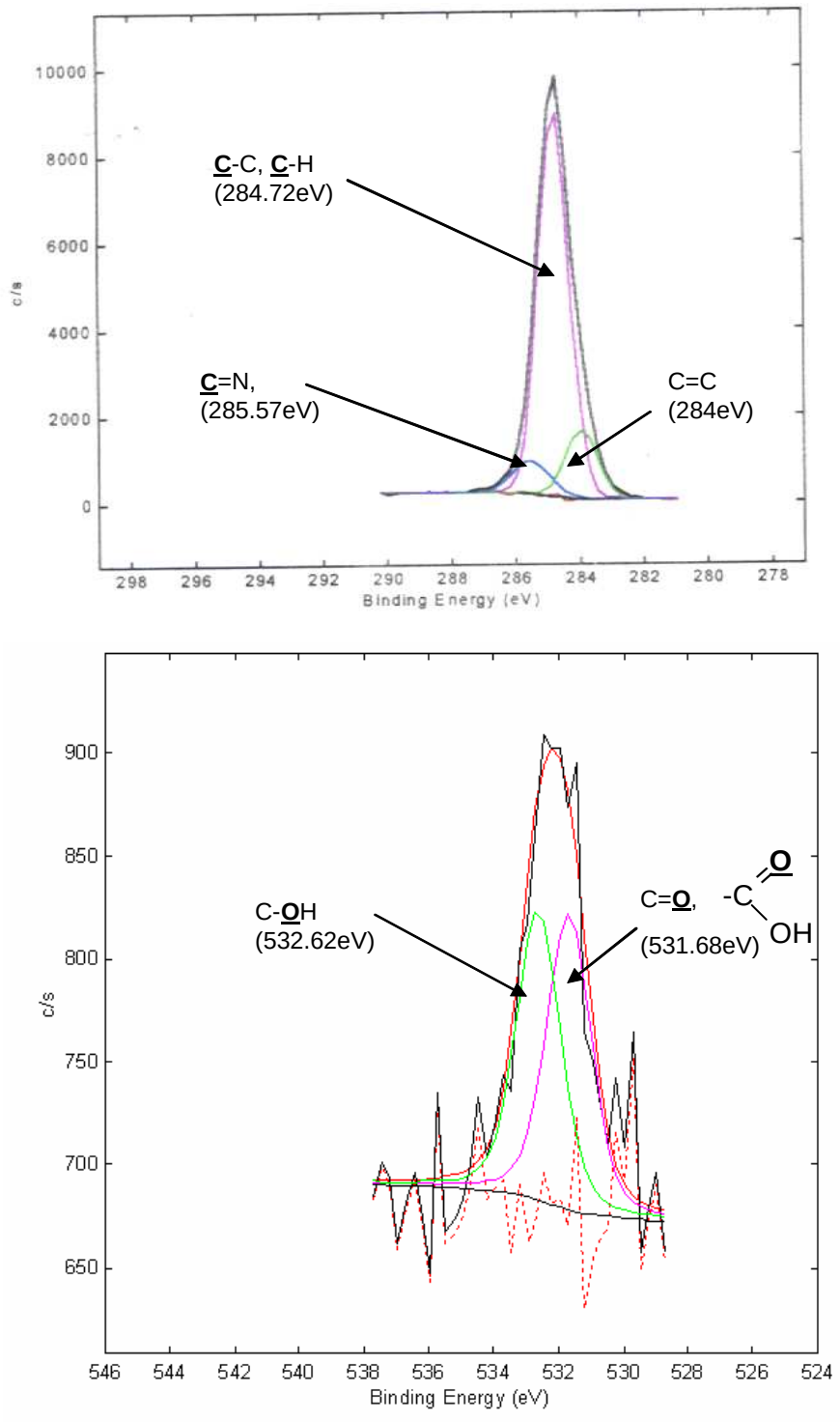


Figure 2.11: Narrow scans for a (111) face. Top panel represents the C1s peak, while the bottom one is the O1s peak.[Sample (kc9]

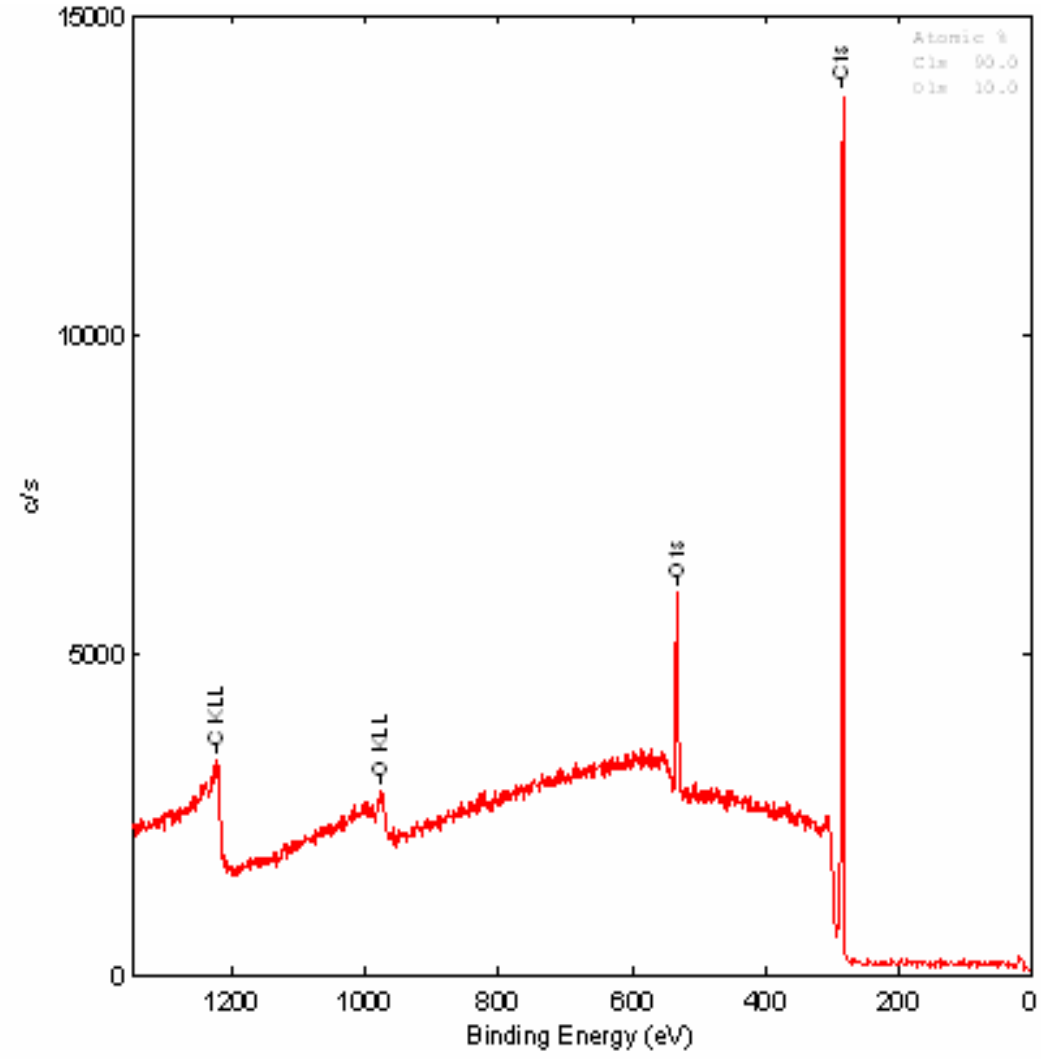


Figure 2.12: Wide survey scan for a (111) face. (Sample kf4)

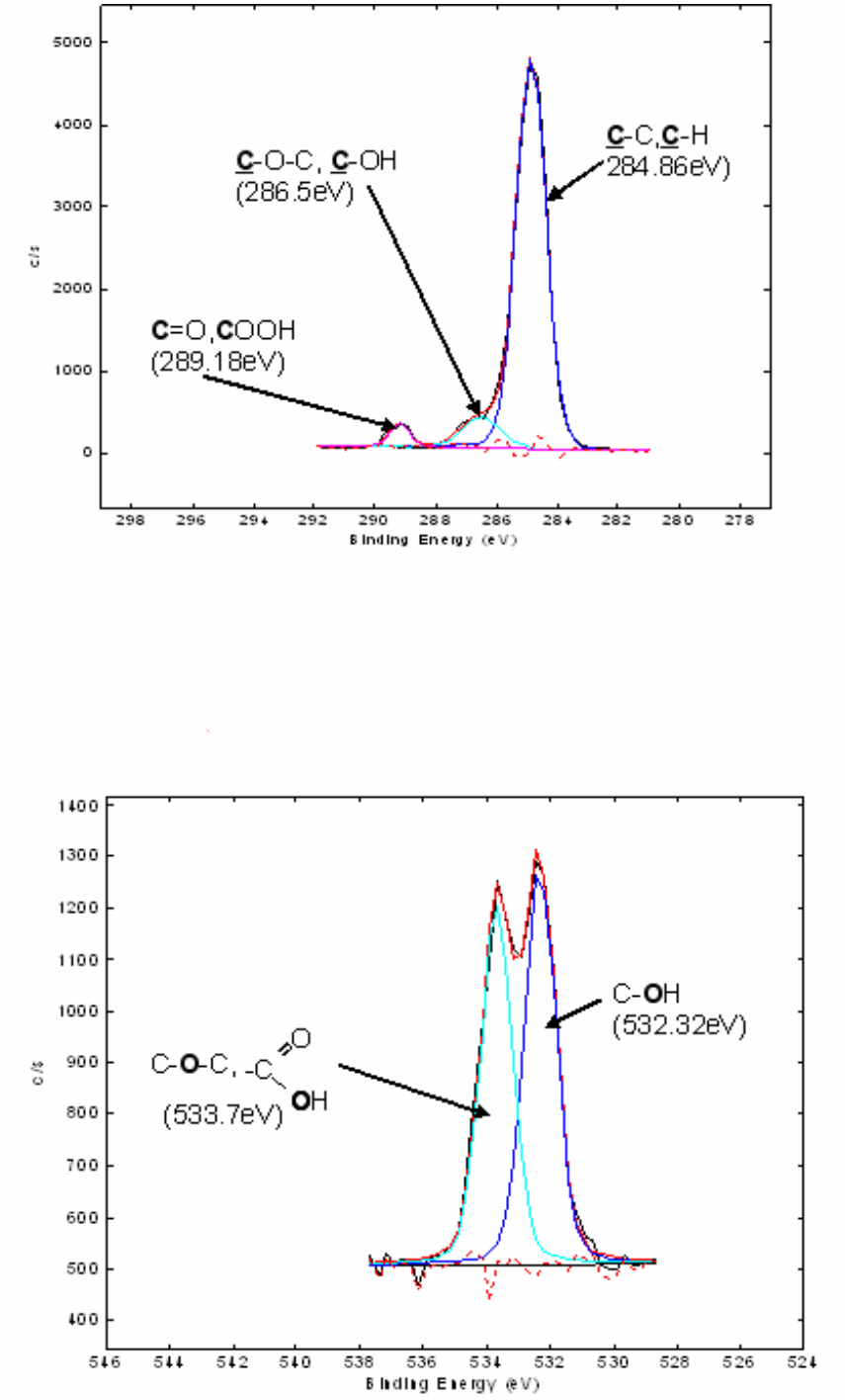


Figure 2.13: Narrow scans for a (111) face. Top panel represents the C1s peak, while the bottom one is the O1s peak.[Sample (kf4]

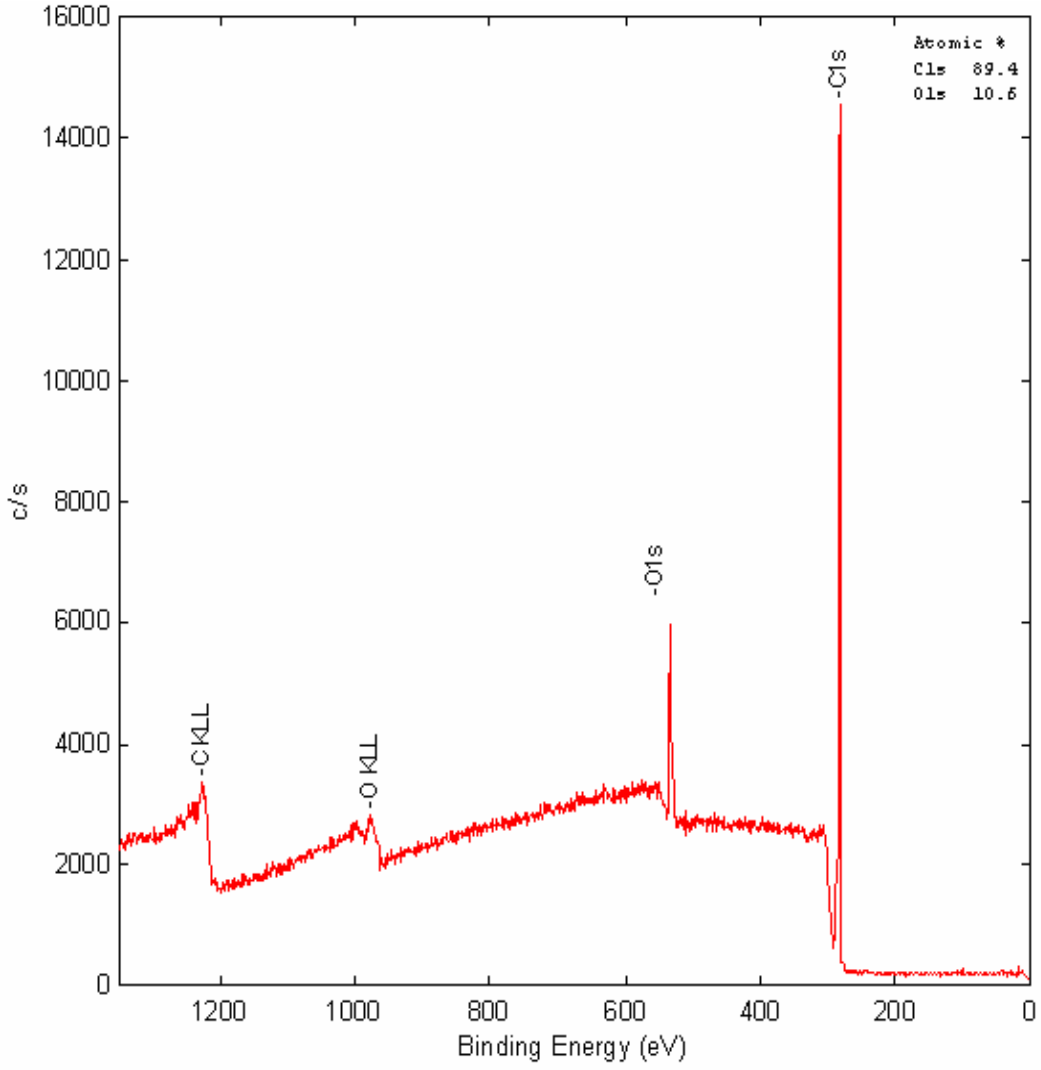


Figure 2.14: Wide survey scan for a (110) face. (Sample kk7)

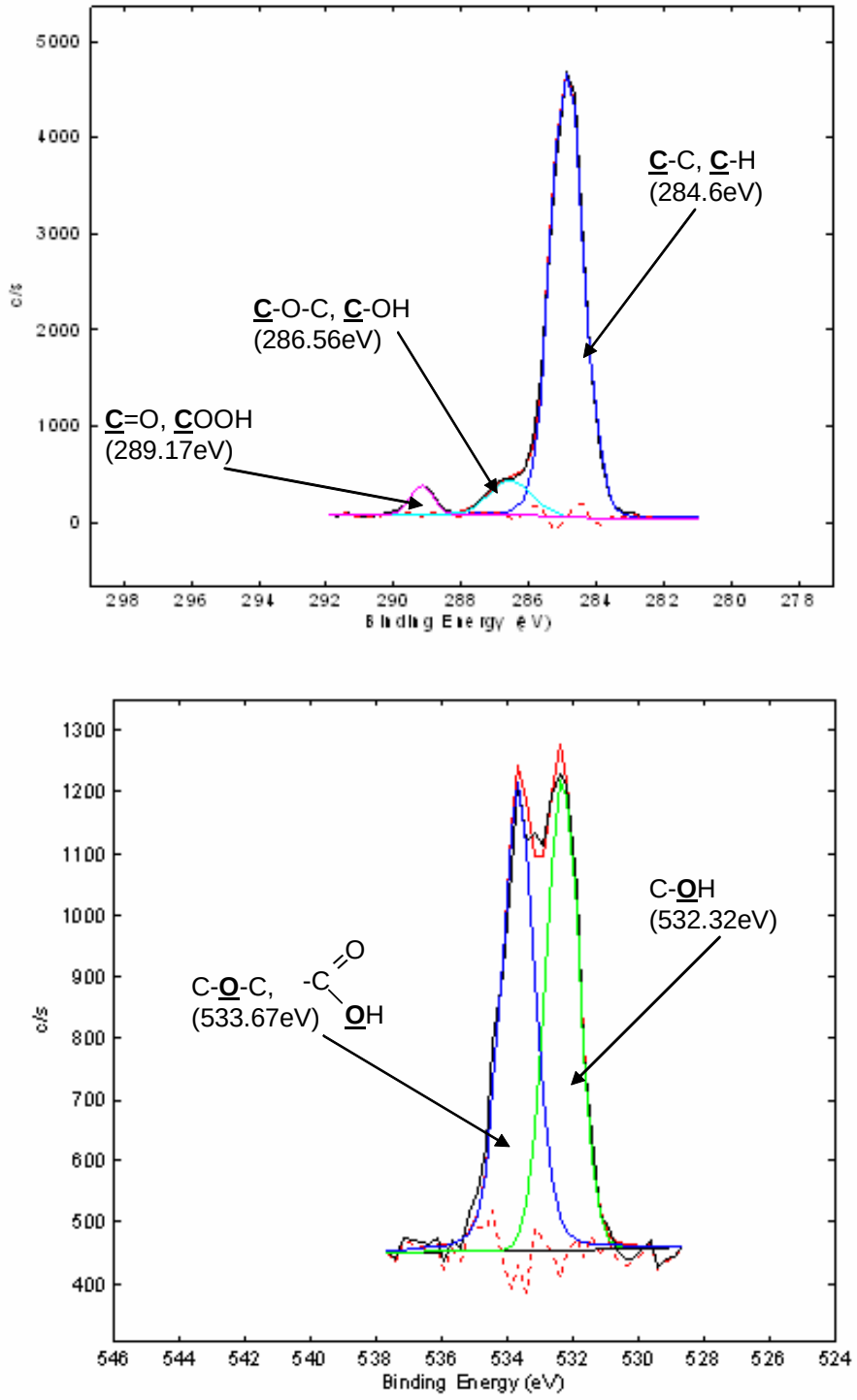


Figure 2.15: Narrow scans for a (110) face. Top panel represents the C1s peak, while the bottom one is the O1s peak.[Sample (kk7]

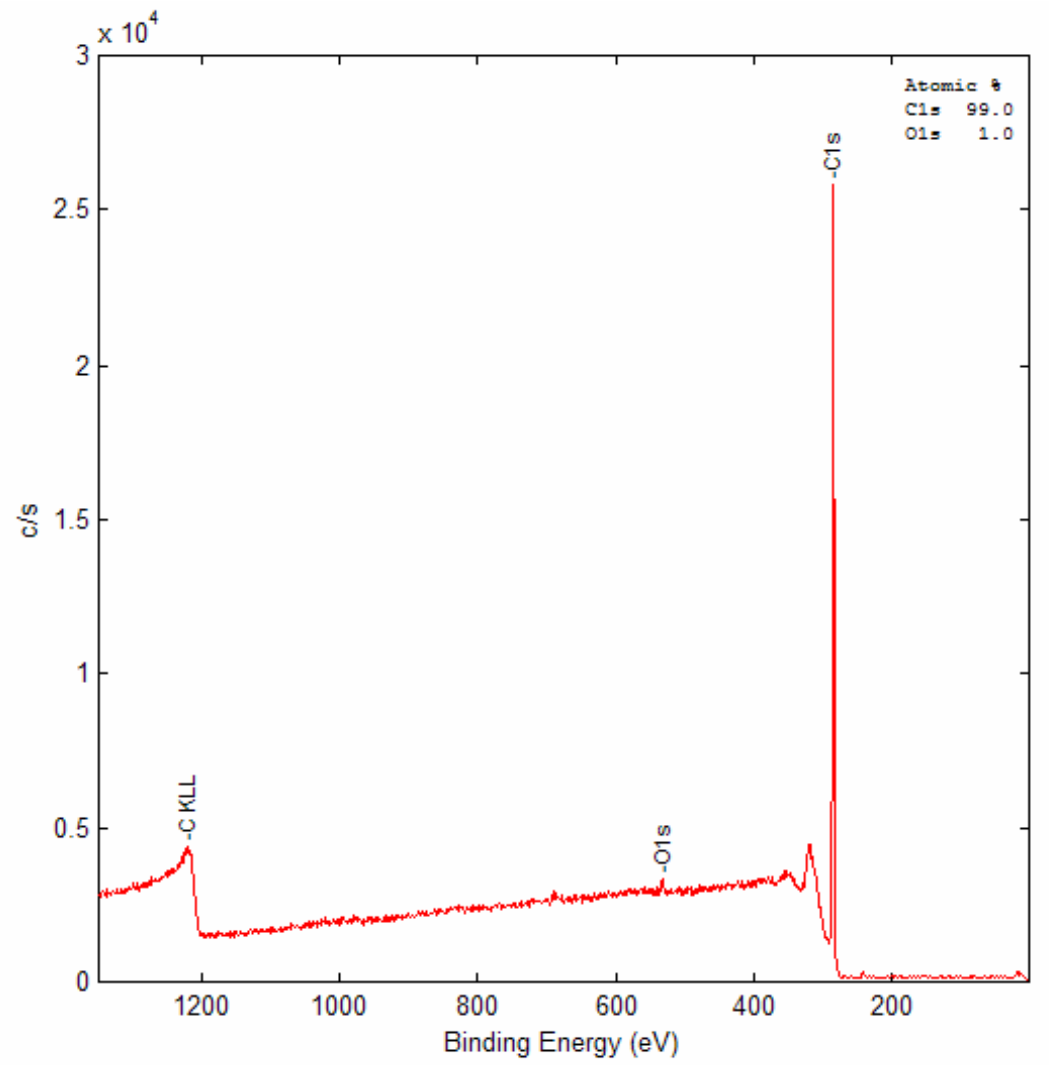


Figure 2.16: Wide survey scan for a (110) face. (Sample kk7)

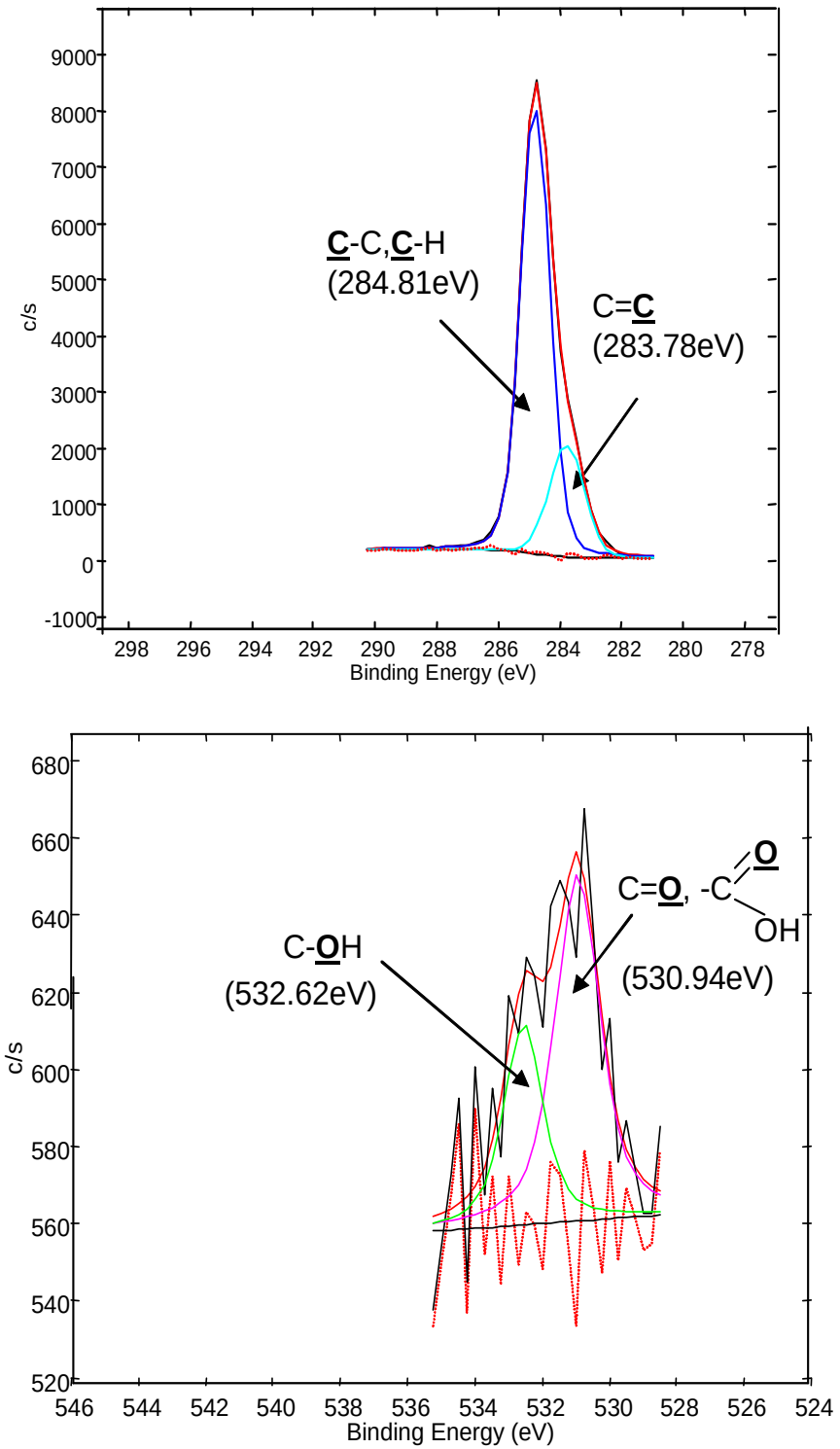


Figure 2.17: Narrow scans for a (110) face. Top panel represents the C1s peak, while the bottom one is the O1s peak.[Sample kk7]

groups due to the adsorbed oxygen on the three low index polished diamond surfaces, together with their corresponding binding energies. In particular, Table 2.1 shows the oxidation states associated with the carbon atom, while Table 2.2 shows those associated with the oxygen atom.

Using the integrated areas under the C1s and O1s peaks, the number σ, of oxygen atoms per cm^2 on a given face was obtained from the expression quoted by M.W. Roberts [123] for atomic coverages viz.

$$\sigma = \frac{Y_O}{Y_C} \frac{N_A \cos\theta \mu_C \rho_C \lambda}{\mu_O M_C} \tag{2.4.1}$$

Where Y_O= Integrated peak area of adsorbed oxygen

Y_C =Integrated peak area of the substrate carbon

N_A = Avogadro's number

θ= Emission angle (25° for the VG Scientific and 45° for the quantum 2000 spectrometer).

μ_O= Photoionisation cross-section of the adsorbed oxygen = 2.92

μ_C =Photoionisation cross-section of the substrate carbon = 1.0

M_C = Atomic mass of carbon = 12.01amu

ρ_C = Density of diamond = 3.52g/cm^3

λ= Photoelectron mean free path in diamond = 10x10^{-8}cm. [122]

After correcting for the respective spectrometer atomic sensitivity factors (as shown in the Appendix B), the corresponding number of oxygen monolayer coverages on each of the faces were obtained. These were calculated from the computed number of oxygen atoms per cm^2 according to equation 2.4.1, together with the number of carbon atoms on each of the three low index faces. The procedure used is summarized in equation 2.4.2, and the computed oxygen monolayer coverages are presented in Table 2.3, as averages of the data obtained from all the samples considered for each respective face using the two

Table 2.1: Functional groups on "clean"polished diamond surfaces and their binding energies from the carbon peak. The binding energies are for photoelectrons coming from the underlined and bolded carbon atom, and these values have errors of about ±0.2eV.

Face	Groups(From the Carbon peak)	BEs(eV)-(C1s)
{100}	**C**-C,**C**-H	284.8
	C-OH,**C**-O-C	286.3
	C=O,**C**OOH	288.7
{110}	**C**-C,**C**-H	284.7
	C-OH,**C**-O-C	286.6
	C=O,**C**OOH	289.2
{111}	**C**-C,**C**-H	284.8
	C-OH,**C**-O-C	286.6
	C=O,**C**OOH	289.1

Table 2.2: Functional groups on "clean"polished diamond surfaces and their binding energies from the oxygen peak. The binding energies shown are for photoelectrons coming from the underlined and bolded oxygen atom, and these have errors of about ±0.2eV.

Face	Groups(From the Oxygen peak)	BEs(eV)-(O1s)
{100}	**O**=C,**O**=C-OH	531.5
	C-**O**-C,H**O**-C=O	533.1
	H**O**-C	532.2
	H_2**O**	534.9
{110}	C=**O**,**O**=C-OH	531.3
	C-**O**-C,H**O**-C=O	533.4
	C-**O**H	532.4
{111}	C=**O**,**O**=C-OH	531.4
	C-**O**-C,H**O**-C=O	533.5
	C-**O**H	532.3
	H_2**O**	534.7

Table 2.3: Fractional oxygen monolayer coverages on "clean"polished diamond surfaces.

Face	Oxygen Monolayers
{100}	0.47±0.10
{110}	0.33±0.10
{111}	0.33±0.10

spectrometers. (See Appendix B for more details)

$$\gamma_{hkl} = \frac{\sigma_{hkl}}{\xi_{hkl}} \tag{2.4.2}$$

σ_{hkl} = Number of atoms per cm^2 for face (hkl) obtained from equation 2.4.1 and,

ξ_{hkl} = Number of atoms per cm^2 for a face (hkl) as shown in Johansen *et al.* [94], i.e 1.82×10^{15} for (111), 2.22×10^{15} for (110), and 1.57×10^{15} for the (100) face.

γ_{hkl} = Fractional oxygen monolayer coverage for face (hkl)

Data obtained from the VG scientific spectrometer, was subjected to a further correction to eliminate the C1s and O1s contributions from the sample holder as mentioned earlier. This correction was necessary because the x-ray beam was approximately of the order of 10mm in diameter, whereas the sample sizes were much smaller, indicating an obvious contribution from the sample holder, which was not desirable. (See Appendix B for more details)

In addition to the wide and narrow XPS scans, valence band spectra were also obtained from the three low index polished diamond faces as shown in figure 2.18. These were obtained over an energy interval of -7eV to 32.5eV at a step size of 0.2eV, dwell time of 2.4s and a pass energy of 23.5eV, although they were not compensated for energy shifts arising from sample charging. A longer dwell time was important so as to improve on the statistics of the spectra, and hence be able to pick out the weaker hidden surface state features, particularly those due to the adsorbed oxygen. However, due to the high energy of the X-ray beam used for the analysis, it was possible to obtain both bulk and surface

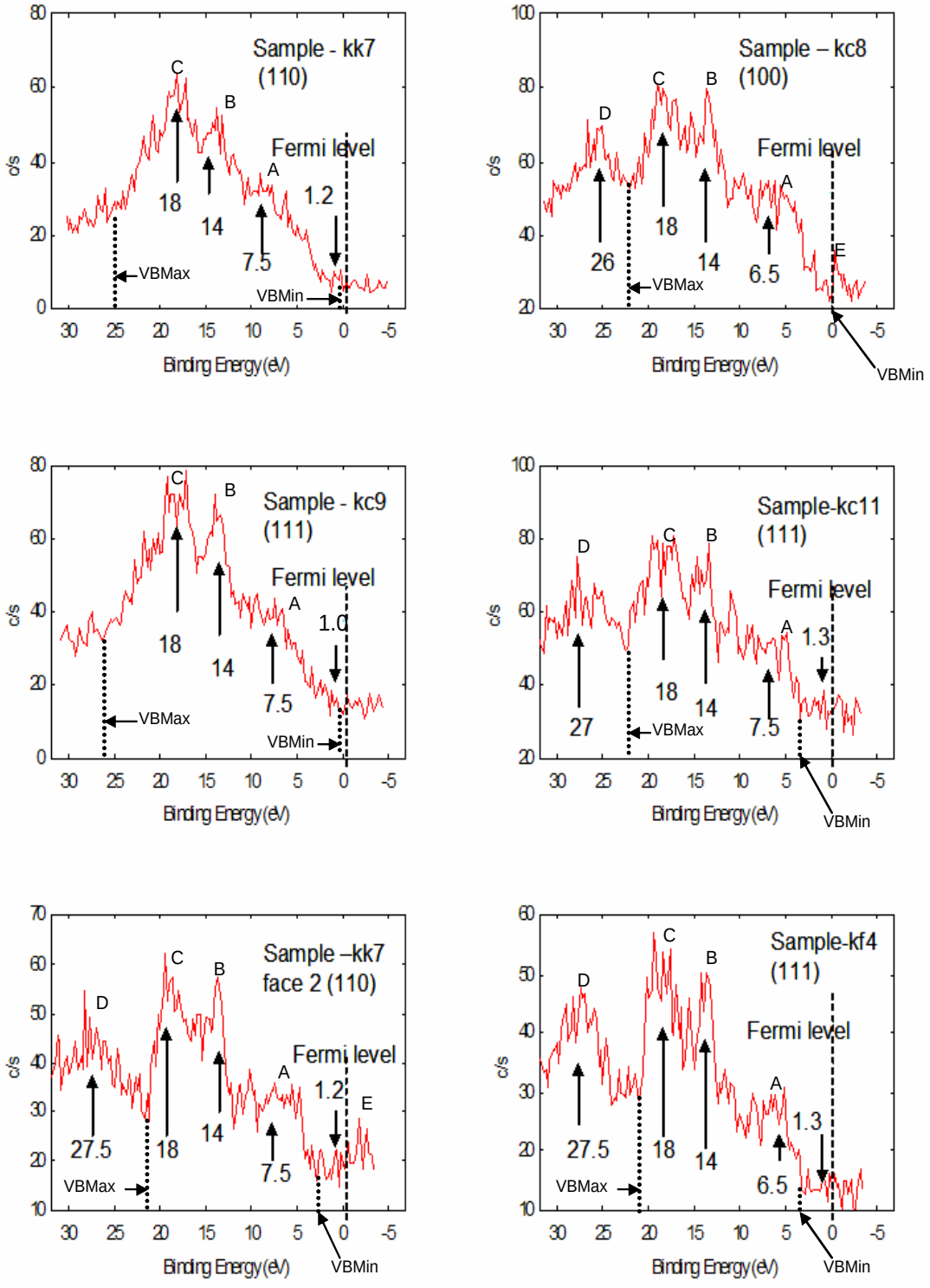


Figure 2.18: XPS total (valence) density of states for the three low index diamond surfaces.

states.

2.5 Discussion

2.5.1 Wide scans

All the XPS wide or survey scans showed clear evidence of oxygen as a major foreign atom on all the three low index polished diamond surfaces. This was found to exist as either adsorbed oxygen atoms or hydroxyl groups. Together with oxygen and its derivatives, previous studies have shown that hydrogen is also a key termination of the polished diamond surfaces [95, 96, 94]. This means that oxygen and hydrogen adsorbates co-exist on the polished "clean" diamond surfaces. Unfortunately, the presence of hydrogen cannot be detected by XPS, but rather it is inferred through the observation of hydrogen containing functional groups, especially from mass spectrometry experiments of the desorption products. As pointed out previously, the initial surface cleaning procedure involved boiling the samples in strong oxidizing acid mixtures. Boiling in such acids has the effect of oxidizing the surfaces, a step that was nonetheless done deliberately to get rid of the undesired graphitic carbon. In fact, Pehrsson *et al.* [99] points out that immersing polished diamonds in boiling acids could lead to re-oxidation of such surfaces.

In addition to achieving much smoother diamond surfaces, the manual polishing procedure that was used in this study was intended to expose a fresh surface, onto which the only oxygen atoms would come from the aqueous cleaning medium, or the atmosphere. As such, most of the oxygen atoms that were derived from the previously strong oxidizing acids were expected to be eliminated through the manual polish. However, while most of the adsorbed oxygen atoms on the "clean" manually-polished diamond surfaces comes from the two

sources mentioned above, further oxygen contamination may also come from other sources such as residual gases within the UHV chamber, as well as other contaminations coming from the x-ray gun window or casing in close proximity to the sample. However, the contribution of these is expected to be quite small. To minimise these, extreme care was taken during the surface preparation of the samples. Some of these measures included not keeping the samples for too long before being analyzed, as well as flushing the chamber occasionally with a titanium sublimation pump so as to improve the vacuum conditions, and thus eliminate some of the contaminants within the chamber.

Based on the above observations, it is quite obvious that the surface preparation procedure as well as the environment in which the surface is prepared plays a key role towards the amount of oxygen adsorbed, or even other adsorbates on the surfaces. It is nevertheless important to note that diamond surfaces are generally inert, but this does not necessarily exclude totally contaminations from unlikely sources such as smearing during the polishing process, an observation that has already been reported [124] on metal surfaces. However, with good care coupled with our excellent surface cleaning procedures, these effects were completely eliminated or at worst kept at bare minimum, which explains why no other adsorbed species were observed from the wide scans, except oxygen and of course diamond carbon. However, while doing initial calibration of the VG Scientific Spectrometer using heated teflon (tetrafluoroethylene - $F_2C{=}C_2F$), some fluorine deposits were found on the diamond surfaces which were apparently transferred from the sample holder to the diamond surfaces. These were nevertheless successfully removed through repetitive manual polishing. Davidson *et al.*[104] indicates that using total-energy tight binding method on the relaxation of a stepped (111) diamond surface, they found the clean surface to be sp^2 bonded near the step, suggesting a form of graphitic transformation.

However, our experiments showed that our surface preparation procedure eliminates not only all non-diamond carbon including the sp^2 bonding reported by Davidson *et al.*[104], but also any metal impurities on the polished diamond surfaces.

The adsorbed oxygen species may be thought of being randomly arranged on the respective faces, although some may be ordered on the large flat terraces where similar oxidation states could exist. This is quite feasible, especially after balancing most of the competing effects such as atom sizes and their locations, adsorbate-adsorbate, adsorbate-substrate interactions as well as steric repulsions. In addition, no conclusive evidence of clear LEED patterns for the adsorbed oxygen atoms on all the three low index diamond surfaces have been reported so far, except the pioneering work of Bobrov *et al.* [125] on molecular oxygen adsorption and desorption from single crystal (111) and (110) surfaces. Although van der Weide *et al.* [126] also report that oxygen termination on the (100) surface leads to a (1×1) structure, the available literature shows quite clearly that comprehensive LEED studies on diamond surfaces are still needed. It is also worth mentioning that, failure to observe other elements apart from diamond carbon, oxygen atoms and hydroxyl groups illustrates quite convincingly that the surface preparation procedure presented in this work was not only capable of yielding more flat and fairly smoother surfaces, but was also quite effective in removing any other atomic species on the polished diamond surface. In addition, the observations made in this study suggest very strongly that oxygen adsorbs on the polished diamond surfaces through bonding at suitable sites during the surface preparation.

2.5.2 C1s and O1s narrow scans

The high intensities observed in the C1s peaks were a clear testimony that the photoelectrons originated from a few atom layers below the diamond surface,

while the presence of O1s peaks implied an appreciable amount of oxygen adsorption on the surfaces. The narrow scans from the C1s and O1s orbitals were obtained over an energy range of 20eV spanning from 278eV to 298eV and 525eV to 545eV respectively. A step size of 0.2eV and a pass energy of 23.5eV was used in both cases. In all the surfaces that were investigated, the carbon peak was found to contain relatively more information than the oxygen one. In addition, both the raw C1s and O1s peaks were found to be rather broad, suggesting that they were constituted of more than one oxygen species. The specific atom species were obtained by deconvolving, both the C1s and O1s peaks shown in figures 2.7, 2.9, 2.13, 2.17 and 2.15 into a number of sub-peaks. Each of the sub-peaks corresponded to a specific oxygen termination, thereby confirming the existence of several oxygen bonding configurations on each of the three low index diamond surfaces that were studied.

It is worth mentioning that a number of attempts have been made previously regarding the study of oxygen adsorption on polished diamond surfaces as outlined in the introductory and later sections of this chapter, but before this study, not much comprehensive work had been done on all the three low index faces, leaving a number of questions unanswered. For example, it had not been established conclusively which oxidation states dominated the respective three low index faces under various pressure and temperature conditions, as well as their expected binding energies. A large proportion of the previous work has also involved a bit of theoretical modelling of oxygen adsorption on either the (100) [127, 128, 112] and the (111) faces [108, 109], and very little attention on the (110) face. As such, building on previous studies, this work sought to shed some light on the vital details of the specific oxidation states on all the three low index polished diamond orientations, as well as the corresponding monolayer coverages.

While it may not be entirely possible to assign any specific oxygen-containing

groups to any one face, our study revealed that some groups were more abundant on certain faces than others. In particular, we observed mainly the C-OH, C-O-C, C=O and COOH groups on all the three low index polished diamond faces, with other minor groups such as H-C=O, O-C-O, O-C=O and C-O-C=O being observed occasionally. These observations are summarized in Tables 2.1 and 2.2 as well as on the individual sub-peaks, and they all show quite clearly the existence of different oxygen functional groups on any given face. Ando *et al.* [129] reports finding both single and double CO bonds as well as carboxylic anhydride groups on diamond surfaces.

Our results further revealed that the C-O-C and C-OH groups as the most favoured oxidation states on the (100) face. They had almost equal occurrence probabilities, followed quite closely by those of the C=O and COOH (carboxyl) groups. However, out of the two carboxyl groups, the **O**=**C**-OH species was found to be the more favoured oxidation state than the O=**C**-**O**H group. This result was in agreement with the findings of Petrick and Benndorf [130] on their acid-treated (100) face. If one therefore considers only the C=O bonding state in the carboxyl group together with the already established C=O bonding state, it becomes almost clear that the C=O group was the dominant one on the (100) face. Water molecules were also found on the (100) face, occurring at a BE of 534.9eV. Our results agree quite well with the findings of Perhsson *et al.* [99], who reported observing ether, carbonyl and hydroxyl groups on the (100) face. Our study therefore not only establishes the most stable bonding configurations on the (100) face, but also complements the findings of other workers with regard to oxygen adsorption on the (100) surface. Perhsson *et al.* [99] further found that after introducing small doses of oxygen on hydrogenated surfaces, equal amounts of hydroxyl and carbonyl groups were observed, while increasing the oxygen dose resulted in only carbonyl groups.

Based on our findings, such a transformation would be clearly driven by

the preferential development of the double bond on the more stable and energetically favoured carboxylic group that we observe on the (100) face, over the purely hydroxyl groups. Our results were in good agreement with those of Perhsson *et al.* [99], especially before they deliberately oxidized the surfaces. Our surfaces represented typically those that are used in many day-to-day applications where they are rarely oxidized deliberately, but instead only pick up the oxygen from the atmosphere or environment in which they are prepared. As such, our observations are hardly surprising, especially in view of this argument. The transformation of the hydroxyl groups to carboxylic ones would initially appear to contradict the widely accepted view that hydrogen can displace adsorbed oxygen from diamond surfaces, while oxygen cannot displace adsorbed hydrogen. However, a closer look at the process reveals that no hydrogen atoms get displaced, but only the bonding configuration changes with the initial number of hydrogen atoms being preserved.

Nemanich *et al.* [131] observed that oxygen bonds most strongly on the (100) surface, where it forms strong bonds with the top layer of atoms on the unreconstructed (100) diamond surfaces. The strong bonds arise from the formation of two bonds to the atoms beneath it while the other two are free. In addition, they also established that oxygen was most weakly bonded onto the C(111) surface, and the strong bonding of oxygen on the (100) surface was attributed to be responsible for the reasons why it took long to discover negative electron affinity on the (100) surface.

Regarding the strength of the bonded oxygen, Bobrov *et al.* [125] established that molecular oxygen was easily bonded to polished diamond surfaces at room temperature, and upon thermal desorption, carbon monoxide was the only product from both the C(111) and C(110) surfaces. On the other hand, Thomas *et al.* [132] reported that oxygen was attached more easily to the (100) diamond surface, forming (ether) bridge bond between two carbon atoms or a

double bond with one carbon atom. These deductions were made on the basis of the temperatures needed to remove oxygen from the three low index diamond surfaces. It follows from their experimental findings that the temperature necessary to remove oxygen from the C(100) surface was higher than that of the other surfaces, being 900°C. Meanwhile, assuming a bulk truncated C(110) surface, the temperature necessary to induce NEA (Negative electron affinity) on this surface was found to be 700°C, which was quite close to that of the C(111) surface of 600°C, since both have a single dangling bond termination.

At the same time, the role of the adsorbed oxygen atoms on polished diamond surfaces is clearly captured with regard to the electronic properties of the interfaces thus formed. This becomes even more vital when making ohmic contacts on the respective surfaces. In particular, the Schottky barrier for metals on oxygen terminated diamond surfaces has been found to be nearly constant, except for Ti and Zr, since these two are highly reactive, and hence they would displace the oxygen from the metal-diamond interface to react with the diamond directly [133]. This is one of the reasons why the two metals are often used when making ohmic contacts on diamond surfaces.

Using Temperature programmed desorption (TPD), Klauser *et al.* [134], established that the major desorption components from diamond surfaces were CO and CO_2 groups, with the CO being the main component and CO_2 constituting only ∼5%. They further showed that the activation energy of CO desorption from O/C(111) surface was 67kcal mol^{-1}, which was higher than that for the O/C(100) system as shown by Thomas *et al.* [132] and Frenklach *et al.* [135]. Previous theoretical calculations have further showed quite convincingly that there is a difference between the chemisorption behaviour of O on all the three low index diamond surfaces. On the reconstructed C(111) surfaces, the H/O/C(111) spectrum showed similar features to those of H/C(111) surface[134] which was also similar to the observations made by J.C. van der

Weide [116]. These observations could explain why both hydrogen and hydroxyl terminated surfaces exhibited negative electron affinity.

Furthermore, oxygen terminated diamond surfaces are generally bulk terminated (i.e. have (1×1) structures), while annealing up to 900-1000°C leads to a (2×1) reconstruction, which is similar to (2×1):H terminated surface. Clean (110) diamond surfaces have also been reported to exhibit a bulk terminated (1×1) structure [95, 136]. On the contrary, annealing the C(111) up to 950°C drives away the adsorbed oxygen, and in the process leads to (2×1) reconstruction and consequently a positive electron affinity is observed [101]. The LEED and TPD studies of atomic and molecular oxygen chemisorption on the (2×1) reconstructed diamond (100) face by Thomas *et al.* [132] further showed oxygen adsorption could convert the surface structure into a bulk terminated (1×1) phase and that CO was the dominating desorption product after annealing.

On the (110) face, our results showed that all the four groups (C-OH, C-O-C, C=O and COOH) had almost equal chances of occurrence, although fewer samples were considered for this surface. This unique behaviour which was apparently exhibited only by the (110) face could be attributed to a number of factors, among them the possible difficulties associated with its preparation. As such, the inability to establish clearly the dominant oxygen containing species on this face could imply that the surface topography was possibly different from that of the others, or instead its quality may not have been entirely perfect. In particular, our Atomic Force Microscopy measurements established that the (110) face had relatively larger but fewer grooves per given area than all the others, which obviously brings out some subtle differences between the three low index faces.

No water molecules were found on the (110) face, unlike in the case of the (100) surface. Previous work by Sappok *et al.* [137] found an ether-like bridge-bonding on both C(111) and (110) faces and carbonyl groups on the C(100)

face, while Ando *et al.* [129] reported finding C=O and C-O-C structures on the surfaces of oxidized powders. However, powders present all possible faces and therefore it was hard to attribute the observed group by Ando *et al.* [129] to any one face. After performing Temperature Programmed Desorption (TPD), they found that the main desorption components were CO and CO_2 which was in agreement with the observations of Bobrov *et al.* [125] and Loh *et al.* [138]. Once again, since powders generally present all sorts of orientations, it becomes difficult to establish the face from which the desorption products reported by Ando *et al.* came [129]. Clearly, very few studies of oxygen adsorption have been done on the (110) surface.

Our results of oxygen adsorption on the (111) diamond surface showed the C=O group being the most favoured oxidation state. We also established the **O**=C-OH carboxyl group, the C-OH group, the C-O-C, as well as O=C-**O**H oxidation states as the other favoured bonding species on a (111) face, in that order. At times, the occurrence probabilities of these oxidation states were so close to each other that it became a bit hard to distinguish clearly between the other most stable bonding states, except the dominant C=O group. This was exacerbated, by the errors associated with them. This sort of behaviour where the oxidation states were hard to distinguish between the most and least preferred ones was also reported elsewhere using first principle calculations [139], as well as in our very own *Ab Initio* DFT calculations. In particular, we found that the adsorption energies of various functional groups varied very slightly at times, thus making it somewhat difficult to establish outrightly the order of their stability.

The observation of hydroxyl, anhydride and generally hydrogen containing groups on all the three low index diamond faces gave a clear indication that there was a certain amount of hydrogen terminating them. In principle, groups of the form C_xH_y would occur at the same binding energy as the diamond's C-C

bonds, since XPS cannot detect the presence of hydrogen explicitly. However, whilst most of the hydroxyl groups were believed to be due to bonding of the adsorbed oxygen atoms together with the hydrogen terminating the diamond surfaces, some hydroxyl groups could also originate from the deionised water used in the rinsing of the surfaces. At the same time, some hydrogen atoms could also be derived from the olive oil used in the polishing, although with its double bond (unsaturated) it may be hard for it to lose any hydrogens as discussed in the chapter 3 dealing with atomic transfer. It is nevertheless to be expected that, if by some means all the adsorbed hydrogen atoms were to be completely eliminated from the "clean"polished diamond surfaces and be replaced by total oxygen adsorption, then we would find that all the hydrogen containing groups such as hydroxyl and anhydride groups would disappear too. As a result, the most favoured oxidation states discussed earlier on each of the three low index diamond faces would most likely change, due to the disappearance of the previously oxygen-bonded hydroxyl and anhydride groups transforming themselves into states that contain no hydrogen such as the single or double CO bonds. Coupled with their high affinity for hydrogen termination and the previous explanation of hydrogen displacing adsorbed oxygen, it seems almost inevitable that hydrogen-containing groups would always exist on polished diamond surfaces.

The relatively low values of oxygen monolayer coverages shown in Table 2.3 are indicative of the fact that functional groups having more oxygen atoms such as O-C-O, O-C=O and C-O-C=O were less likely on polished diamond surfaces. Besides, groups with more oxygen atoms attached to the carbon atoms were even more unlikely because the two valence electrons on the oxygen atoms have to be saturated by bonding with either a hydrogen atom to form groups such as O=C-O-H, or remain in the charged state. We did not however establish any evidence of the charged oxygen states and hence the only permissible

configurations are those where the oxygen bond is fully saturated by bonding with either a carbon atom or terminated by hydrogen. If we were to have a case where more oxygen atoms were bonded to a carbon atom as implied by species such as O-C-O and O-C=O, then the monolayer coverages would be large, which was not the case in this study. We therefore conclude that the only possible atomic oxygen arrangements that match the observed fractional monolayers are those that have an oxygen atom on every alternate carbon atom and not those with an oxygen atom on every carbon atom. This argument ties in well with the observed fractional monolayer coverages, although [140] report observing 0.75 monolayers (where 1ML$\approx$1.6$\times$10^{15} atoms/cm^2) of fluorine atoms on diamond (100) surface, in spite of the fact that the fluorine atoms have a larger van der Waals radius than oxygen. Their surfaces were however fluorinated deliberately under varying temperatures in a UHV chamber with atomic and molecular fluorine. They further indicated that the accommodation of the fluorine molecules was limited by the number of reactive sites and not thermally driven dissociation. The DFT calculations of Zheng *et al.* [139] appear to suggest that the optimum oxygen coverage on diamond (111) surface would be a full monolayer, but our density functional theory calculations as well as the findings of this work, those of Rebuli *et al.* [98] and Derry *et al.* [94] for surfaces prepared following the procedure described in this work totally refute these claims. Besides, through their wettability studies, Derry *et al.* [94] found out that their surfaces was neither strongly hydrophobic as might be expected of a surface terminated by hydrogen, nor strongly hydrophilic as might be expected in the case of a monolayer oxygen coverage. Our calculations further revealed that the third monolayer oxygen coverage at the ONTOP site was the most stable oxidation state on the (111) diamond surface, after testing for various coverages ranging from a quarter to full monolayer at different adsorption sites. This result confirms the findings of this work where the C=O bond was

found to be the dominant oxidation state at the ONTOP site and at a 0.33 monolayer coverage.

Based on the previous discussions, it was quite evident that the carbonyl, ether, hydroxyl and carboxyl groups were the most favoured oxidation states, and hence, likely to be found on polished diamond surfaces that are prepared under normal atmospheric conditions, as described in the experimental section. We do not however rule out entirely the existence of groups such as O-C=O or O-C-O, especially at those regions of the surface where certain features such as steps with an excess of dangling bonds would favour them.

As a result, the occurrence of these minor groups was attributed mainly to the existence of surface features such as steps intersecting the flat terraces, edges and/or kinks among other suitable surface features as shown in figure 1.1. These are the sites which often tend to have extra dangling bonds. However, the same features should be quite few on properly prepared surfaces as is evident from the Atomic Force Microscopy work reported in this study, and hence those functional groups existing around them would be minimal. As a result, these groups are hereunto referred to as minor groups. The step-terrace arrangement is expected to be ordered and to exhibit high thermal stability until the surface is heated to high temperatures. Our observation of mainly C-O-C and C=O functional groups on all the faces, and particularly the (100) face was further confirmed by the *ab initio* DFT calculations, of Rutter *et al.* [102, 22] and Skokov *et al.* [127]. Rutter *et al.* [102, 22] in particular further found that the bridging configuration was more stable by about 0.5eV per surface carbon atom. This, they said, contradicted theoretical studies of Whitten *et al.* [141] who found the ketone configuration to be lower in energy by 0.18eV and also the prediction of chemical bond energies which gave the C=O bond a higher energy than the two C-O bonds.

The observation of the C-OH oxidation state in our studies was further a

manifestation of the existence of the hydrogen atom that terminates polished diamond surfaces [95]. They were either bonded onto the adsorbed oxygen atoms, or instead the surface carbon atoms thereby forming different organic groups. Earlier work of Rebuli *et al.* [97], Derry *et al.* [94], Perhson *et al.* [99, 111] and Beerling *et al.* [142] showed that the ether, C-O-C and carbonyl, C=O to be the most favoured functional groupings on the (100) face, observations which are in good agreement with our XPS results. Wang *et al.* [100] further reported that the bridge chemisorption of the oxygen monolayer dominated at temperatures below 400°C whereas the "on-top"chemisorption became favourable at 500°C. Perhson *et al.* [99] on the other hand, indicated that atomic oxygen adsorption energies at the on-top and bridge-bonded sites were identical, which again agrees with our DFT calculations where it was observed that the adsorption energies of some of the species were very close to each other, making it rather difficult to establish which among them was the most stable.

One of the surfaces showed an unknown peak centred at around 283.78eV, which was thought to be close to the one observed by Bobrov *et al.* [143] at -283.8eV. They attributed this to π-bonded dangling bonds of a clean surface dimer on a (2×1) reconstructed (100) diamond surface, and although in our case it was established on a (110) surface we also predict that the peak at 283.78eV (in figure 2.17) was due to a surface dimer too, although our surface may not have necessarily undergone any reconstruction. In another surface, a peak was observed at 284eV (in figure 2.11) and this was also associated with the same surface dimer observed by Bobrov *et al.* [143], especially due to the closeness in their energies, and more so when the error of 0.2eV associated with their binding energies was considered. This was in fairly good agreement with the findings of Perhson *et al.* [111] who observed that while oxidising heated diamond (100) surfaces (twice at 540°C), the surface became apparently roughened, creating edge sites for sp^2-bonded C=C dimers and C=O groups. Yet another peak

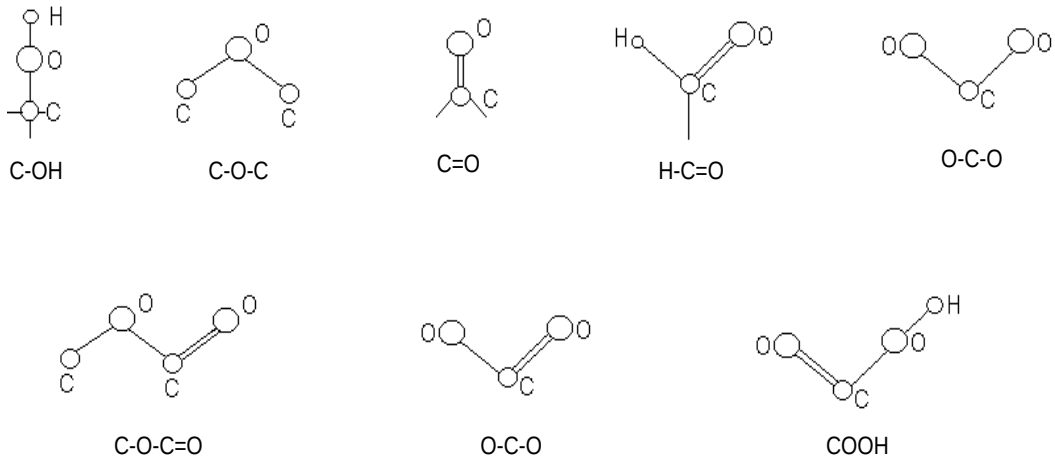


Figure 2.19: Functional groups on the three low index polished diamond surfaces

which was assigned to the C=N double bond was observed on the same surface at 285.57eV (in figure 2.11). This was hardly suprising because nitrogen is a known defect in diamond, albeit in small quantities.

On the basis of our results, we concluded that the most likely bonding configurations of adsorbed oxygen on the three low index polished diamond surfaces are those shown in figure 2.19. However, these narrow down to C-OH, C-O-C, C=O, COOH and H-C=O as the most stable oxidation states on diamond surfaces that are prepared according to the procedure described previously in this work.

The occurrence of similar groups such as C-O-C, C=O and C-OH on all the three low index faces indicated that, although one was analyzing either a (110) or a (100) face, on a microscopic scale, these faces may actually be composed of many tiny facets of similar orientation, at different places. This may not be unexpected because during the polishing procedure discussed previously, some (111) facets may be created on either the (100) and (110) faces, since the fracture of diamond is highly directional and heavily dominated by cleavage in the (111) plane. However, our polishing was done mainly along the easy directions where

the process of material erosion was different from that in the hard direction, therefore excluding the creation of most of the facets, especially if they are formed through cleavage. In fact, very low concentrations of oxygen coverage were particularly observed in one case involving the (110) face, which possibly indicated the surface was somewhat different from the others microscopically. Such a surface was thought to have been either generally smooth or flat, and therefore devoid of many surface features (defects) such as steps, etc., that could act as suitable sites for a large amount of oxygen to adsorb there, or alternatively the surface quality was not too good. In line with the argument of other facets being created on different faces, Kern *et al.* [107] reported that at steps on the (111) and (100) surfaces, facets with the (110) orientations also appear. These they indicated played a pivotal role in the model of layer-by-layer artificial growth of diamond. Indeed, from a practical point of view, it is extremely difficult to have an ideally flat surface, but instead what one expects from the polishing process are surfaces with generally large and flat terraces, having a few surface features such as steps, kinks etc., and probably full of arrays of polishing grooves. A "clean" polished diamond surface possessing these features will therefore undoubtedly show the existence of various types of oxidation states, as confirmed by the findings of this study.

With regard to the varying amounts of adsorbate coverages, Somorjai *et al.* [4] observed that, when the adsorbate coverage increases so that the mean adsorbate distance decreases to about 5-10Å, the mutual interactions often strongly influence the adsorbate ordering, thus favouring certain adsorbate configurations over others. On this basis, we propose that the dominant configurations of oxygen atoms on polished diamond surfaces were mainly those found on the large flat areas, thus depicting what one would expect on a real face, while the minor ones were to be found at suitable surface features such as on the steps and

the edges as mentioned earlier. The sizes of the steps on properly prepared polished diamond surfaces were however expected to be quite small, and in many instances being of the order of one atom or a few atom layers in height, and their ordering would probably be due to an excess of electron charge at those sites. The adsorbate-adsorbate forces have been reported to be weaker than the adsorbate-substrate binding forces, and it was thus believed that the optimum adsorbate locations or sites were determined by the optimum adsorbate-substrate bonding, although the adsorbate-adsorbate interactions among the adsorbates themselves, often dominate the long-range ordering of the overlayer. These surface thermodynamic processes as well as the adsorbate properties will definitely influence the oxygen ordering on polished diamond surfaces and hence dictate which oxidation states are to be expected on a particular surface and site.

We observed from the binding energies of the oxidation states of carbon that oxygen on polished diamond surfaces induces shifts to higher binding energies by about 1.5eV per C-O bond. As a result, the O-C-O and C=O groups give similar BE, while O-C=O has a binding energy shift of almost three times that of a single C-O bond. Our experimental findings further showed that various oxidation states on polished diamond surfaces led to a range of about 2.25eV centred about the main diamond carbon peak at 284.8eV. Similarly, the binding energy of the oxygen peak was found to fall within a narrow energy range of almost 1.3eV about the major oxygen peak at 532eV.

The very low oxygen coverages observed especially in the (110) face appeared to suggest that the carbon atom bonds were instead saturated by a species that could not be detected by XPS, and this was probably adsorbed hydrogen, although this is only speculative. This was therefore thought to leave the oxygen and its derivatives to occupy only very few sites, and thus the reason for the low oxygen monolayer coverages as observed. However, although not necessarily in

all cases, this was often observed from those samples that were kept for relatively longer periods of time within the UHV chamber (more than 12 hours) before being analyzed. This therefore suggested that there was a possibility of some weakly bound oxygen species being lost while the sample was in the UHV chamber, an observation made earlier by Rebuli *et al.* [97] who pointed out that the oxygen coverage on the various "clean"polished diamond surfaces was a function of the pressure in the vacuum chamber, and not necessarily the cleaning methods. Although this was observed mainly on the (110) faces (incidentally because they were the only ones that were left in the analysis chamber for long), there was no reason not to imagine that the same could also occur on any of the other two low index faces if they were left for long (enough) periods of time within the UHV chamber.

The UHV chamber was operated at pressures of better than 10^{-10} Torr. Our earlier observations indicated that oxygen has been shown to be most strongly bonded onto the (100) face [131] and it has also been reported to bond more easily on the (100) face and most weakly on a (111) face. Based on this, it was not quite clear which oxygen-containing functional groups got dissociated first, but we can predict that they would most likely be those with low residence times. As mentioned before, it has already been shown that oxygen desorbs as CO and/or CO_2 species [125, 134], leaving a relatively etched and rough surface. Raising the temperature of the sample surface was expected to increase substantially the rate of the adsorbed oxygen dissociation(desorption) and therefore lead to the establishment of some sort of oxygen loss mechanism. Ando *et al.* [129] have shown using high resolution EELS (HREELS) that thermal annealing of oxygen pre-treated diamond powders first induces decomposition of the ether (bridge configurations) C-O-C structures while the ketone (ON TOP configuration) decomposes at higher temperatures. Based on this, it is also very likely that this same mechanism would apply to the single crystal oriented diamond surfaces.

Such a desorption process has a strong relationship with the density of states (i.e. electron distribution) and therefore it was in good agreement with the general expectation that the weakly bound species would detach first, as illustrated by the calculated adsorption energies obtained in our DFT calculations for the (111) surface. However, although temperature programmed desorption has been used previously to investigate this phenomenon [134, 138], naturally the desorption of oxygen from diamond surfaces has not received the attention that it deserves, and therefore it would be an interesting subject of research to investigate further which species desorbs first and which one leaves the surface latest. This would probably yield more conclusive results when combined with say LEED and XPS experiments, at various elevated temperatures. Such an endeavour would not only be quite informative especially regarding the specific desorption temperature onset and the corresponding functional groups, but also shed some light on the order in which the desorbed functional groups detach themselves from the polished diamond surfaces.

2.6 Surface states

Valence electrons play a key role in the atomic and molecular bonding of materials, and therefore the study of the charge distribution about them can reveal vital information regarding the bonding process itself, the environment, as well as explaining the strength of the bonds thus formed. This can be achieved by analysing the electronic density of states using either the x-ray beam from the XPS apparatus at low energies or instead the ultraviolet spectroscopy or even EELS. Normally, when two atoms with equal-energy states come close together, the energy levels of the combined system usually have nearby states just above and below the original equal energy. Such states are referred to as bonding (ones at lower energy) and anti-bonding (ones at higher energy states). The

two states thus created (i.e. bonding and anti-bonding) are almost equally separated, below and above, respectively from the original energy. Bonding therefore occurs because matter is in a lower-energy state when electrons fill the bonding levels and fewer of the anti-bonding levels. In this regard, the electron distribution becomes vital in understanding and thus explaining the bonding process. Through the density of states, one gets to know where the electrons are, and whether they are actually in the places where they are supposed to be, i.e. their occupation probability, which is given by the Fermi function.

Using XPS, it was possible to obtain the valence band spectra for the three low index diamond surfaces as shown in figure 2.18. However, since the energy of the x-ray beam may not be reduced to the energies that could only permit the probing of the surface phenomena specifically, some bulk properties (states) were obviously expected to be observed within the valence spectra. In spite of this and also the fear that the more intense bulk states could mask the weak surface states, the observed valence spectra were still useful in giving some vital information about the surfaces, and hence the existing bonding environment between itself and the adsorbates.

In particular, the valence spectra shown in figure 2.18 indicated a small feature slightly above 0eV, which was believed to be due to surface states originating from the adsorbed oxygen atoms, with minimal contributions from the underlying substrate carbon. Already, first principle calculations using the linear muffin-tin orbital (LMTO) approach have confirmed the existence of oxygen induced surface states on the (100) diamond face [108], while our *ab initio* DFT calculations have confirmed this, in the case of the (111) diamond surface. The valence band spectra from all the three low index diamond faces showed an average valence band width of about 20.6eV, which was in agreement with photoemission results that give it as 21.0±0.1 eV [144] and our DFT calculations that show a value of $\simeq$ 21eV. Zheng *et al.* [108] on the other hand obtained

a value of 21.71eV, which compares well with yet another value of 21.63eV for the valence band width [145].

All the valence band spectra were described by a multi-peak structure, with the corresponding VB maxima and minima being shown on the respective plots. Three broad peaks labelled as A, B and C which were centred at around 7.5eV, 14eV and 18eV were observed in all the spectra. A fourth peak centred at around 27eV and labelled as D was observed in only four out of the six cases considered. Those spectra that did not exhibit this fourth peak had a relatively wider valence bandwidth than the others. The peak at 7.5eV was attributed to the O2p electrons while the other two at 14eV and 18eV, as well as the one at 27eV were believed to be due to bulk states of the substrate carbon. This is in approximate agreement with Zheng's [108] observation of the O2p surface state for the on-top oxygen configuration, which he establishes at 6.2eV. In fact, two of the samples that were investigated showed this state occurring at around 6.5eV. However, from Siegbahn's BE tables, the carbon 2p valence electrons' BE is expected at around 7.0 eV which seemingly overlaps with the BE due to the oxygen 2p valence electrons, thus making the peak's interpretation somewhat complex. We further observed bulk-like carbon atom features at 14eV(due to hybridized 2s and 2p states) and 18eV due to the 2s valence states, again being in approximate agreement with the ones reported by Zheng *et al.* [108] at 12eV and 16eV respectively, indicating a shift of about 2eV that could be attributed to sample charging that was not compensated for in these spectra. Reinke *et al.* [146] established a peak at 13.2eV, which was very close to the one that we observed at 14eV, and they indicated that this peak was characteristic of diamond. In fact, the disappearance of the peak at 13.2eV (or 14eV in this case) has been demonstrated to indicate amorphization or graphitization (sp^2 bonding) of the diamond surface, in which case, since this peak was observed in all the spectra, we can conclude that there was no graphitic and or non-diamond

carbon on the samples investigated in this work.

Oxygen termination has also been reported to lead to high density of states at approximately 1.7eV above the valence band maximum [147], and this was reported mainly on fully oxygenated samples. Our study revealed a very weak feature at around 1.2eV above the VBMax for the (100) face as seen from the top right hand side panel of figure 2.18 and 4.8eV for the (110) face as shown in the bottom lower left hand side panel. Our DFT calculations for oxygen and hydroxyl termination on diamond (111) surfaces showed a 2s peak for the adsorbed oxygen atoms at around 22.5eV in most cases, but this was apparently missing for the clean unterminated surfaces.

The VBMin (i.e. the point where emission starts) was further found not to be at a constant value for all the faces. It occurred at 0eV for the (100) faces, while in all the other cases it occurred above 0eV. In particular, three of the cases had it beginning at 3.0eV, 1.5eV (for two of them), and 0.0eV for one sample as show in the respective spectra. Beyond these emission onset values, the emission rate was found to increase quite rapidly in agreement with observations made by Klauser *et al.* [134, 148]. The valence band maximum(VBMax) was not constant either, and it was found to occur between 21.0 & 22.5eV for all the spectra containing the fourth peak labelled as D, while it was found at higher BE of between 25.0 & 26eV for those spectra that did not exhibit this feature. Peak D was attributed to the emission from the oxygen 2s states. Francz *et al.* [149] observed a similar peak to ours at 23eV, which they attributed to oxygen 2s core electrons. Taking into consideration the energy shift of 2eV, this peak corresponded to those that we observed between 25 and 26eV. Its disappearance has been associated with the absence or desorption of oxygen.

Apart from oxygen, hydrogen has also been shown to be the other terminating species for "clean"polished diamond surfaces [150, 94]. It has been reported previously to remove the surface density of states within the band gap [104, 103],

while the clean (111) diamond surface is expected to have both occupied and unoccupied states in the gap. In some of our samples, no states were observed above the valence band maximum, and hence no states within the band gap. As a result, those samples that showed some states above the valence band maximum were assumed to contain less amounts of hydrogen termination, that is, pure C-H bonds, with a majority of their bonds being terminated by either hydroxyl and/or possibly anhydride groups. On the contrary, those that did not show density of states above the valence band maximum may be assumed to contain a large amount of hydrogen termination.

Susana *et al.* [130] reported observing a relatively sharp high-energy peak at approximately 17eV and they indicated that it arose from the electron emission due to negative electron affinity of hydrogen terminated C(100) surface. They further observed emission onset on the C(100) surface at 1.1eV which they said was related to the location of the valence band of diamond. Using Ultraviolet photoelectron spectroscopy (UPS), they also found a "bulk"peak for H terminated surfaces at 8 eV and a smaller peak at 14.5 eV. This peak corresponded to the one that we observed at around 12.5eV in our DFT calculations, and it was attributed to the bulk carbon atoms' strong 2s/2p hybridization. It was similar to the ones that were established at 14eV for most of the valence band spectra in our study. Emission onset was detected at around 1.2eV and 1.3eV, showing some agreement with the findings of Susana et al. [130]. In addition, some of our spectra showed 2s valence state peaks at around 18eV, that were quite close to those observed by Susana *et al.* [130] at 17eV. The peaks at 18eV could well be due to bulk states as pointed out earlier, since the C-C and C-H bonds were normally taken to be the same within the XPS analysis.

2.7 Conclusion

Apart from hydrogen, oxygen was clearly established as the main foreign atom on all the three low index polished diamond surfaces. This, together with the observations of various oxidation states on the diamond faces was consistent with other reported work, as well as *ab initio* calculations on theoretical predictions. Various functional groups were observed on all the three low index diamond surfaces with the C-OH, C-O-C, C=O and COOH being the dominant ones. Minor groups such as O-C-O, O-C=O and C-O-C=O were occasionally indicated, and their existence was attributed to the presence of surface features like steps and edges on the "clean" polished surfaces where more dangling bonds were expected. Except for the dominant polishing grooves, most of the surface features were found to be quite few as confirmed by our Atomic Force Microscopy images that are reported elsewhere in this study.

On the (100) surface, the dominant oxidation states were found to be the C-O-C and C-OH groups, while appreciable amounts of C=O and OH-C=O groups were also found. The (110) face showed the four groups that were observed on the (100) surfaces, but these had almost equal occurrence probabilities, making it difficult to choose the most and least stable of the four. Nevertheless, the C=O and C-OH groups were thought to show some slight dominance over the C-O-C and the OH-C=O groups, although not enough to make a more conclusive observation. However, few samples were considered for this surface, a factor that may have contributed to this apparent inability to establish the stability of the species on the (110) surface. The (111) surface showed the C=O group as the most favoured oxidation state, followed quite closely by the O=C-OH carboxylic group. Significant amounts of the hydroxyl (C-OH) and bridge-bonded (C-O-C) oxygen groups were also established on this face, with the occurrence probabilities of the four main groups established on this face decreasing in the

order that they are listed.

While the existence of large flat areas on the polished diamond surfaces was confirmed by the observations of groups that had been predicted by theoretical models constituted of primarily large and ideally flat areas, observations of the few minor groups seemed to suggest that the faces not only consisted of flat areas but they also exhibited surface features similar to those shown in figure 1.1, such as steps, edges and possibly kinks. These were nonetheless expected to be few, therefore their overall contribution being correspondingly minimal. Around these surface features, more dangling bonds were likely to be found, leading to a greater variety of oxygen functional groups. Increasing the amount of time in which the sample stayed within the UHV system before analysis led to the loss of some of the weakly bound species as confirmed by observations of very low oxygen coverages in some cases. Such species were also believed have had low residence times on the polished surfaces.

Oxygen induced surface states were established on all three low index diamond surfaces. Occasionally, very weak surface states above the valence band maximum were observed, and these occurred within the energy band gap. An average valence bandwidth of about 20.6eV was established for polished (oxygen terminated) diamond surfaces, and the valence band emission rate was found to increase quite rapidly after the respective emission onset values of between 0 and 1.3eV. The valence band widths associated with the carbon atoms was generally broad, indicating the strength of the C-C covalent bonds.

Average oxygen monolayer coverages of 0.47, 0.33 and 0.33 were observed on the (100), (110) and (111) faces of polished diamond surfaces under UHV conditions respectively. These coverages may however decrease to much lower values if the samples stayed for longer periods of time within the UHV chamber as observed by Rebuli *et al.* [97]. The fractional monolayer coverages were in excellent agreement with the earlier work of Rebuli *et al.* [97] and Derry *et al.*

[94] involving oxygen adsorption on polished diamond surfaces, prepared in a similar way as those used in this study.

2.8 Recommendation

It would be of interest to take extra XPS spectra in situ with LEED measurements while annealing the surfaces. This would assist in establishing the species that get desorbed first, those that get desorbed latest, and also the changes occurring in the structure of the surfaces as the temperature is varied. In addition to addressing this problem, these investigations would also complement the temperature programmed desorption studies.

Chapter 3

Carbon Atom Exchange Between The Lubricant And The Diamond Surfaces During Polishing.

3.1 Chapter layout

This chapter explores in detail the process by which atom transfer occurs between the polishing lubricant and diamond surfaces during polishing. The relevant theoretical principles are initially discussed, followed by the experimental procedure, then the results, their discussions and finally conclusions.

3.2 Introduction

The mechanisms by which diamond polishing proceeds are still a matter of debate, in spite of the process having been perfected over a period of more than 50 years [54]. Many theories have been put forward, speculations made and even elaborate experiments done as discussed in chapters 2 and 5, dealing with the (X-ray Photoelectron Spectroscopy) XPS and (Atomic Force Microscopy) AFM studies. Traditionally, a fast moving cast iron wheel impregnated with diamond grit of specified sizes has been used as the tool for carrying out the

polishing process, with the diamond surface getting gradually eroded, following mechanisms that depend on the orientation, polishing direction and probably the surface contact temperature among other factors. In some of their early experiments, Tolansky *et al.* [81] observed that, in spite of the fact that tungsten carbide was considerably softer than diamond, ring cracks developed on the diamond surfaces when spheres made of it were pressed on the diamond using various loads. However, they only observed this effect on the octahedral face of the diamond, and no cracks were obtained on either the cubic nor the dodecahedral faces. In addition, they observed that tungsten carbide balls caused considerable internal disruptions of the diamond compared with synthetic sapphire balls. These experiments formed the early investigations into diamond polishing.

For most materials, surface atoms are normally bound to their neighbours by strong chemical bonds whose average strength is close to 600KJ/mole. This means that the mechanical force needed to remove an atom is in the range of $1x10^{-7}$N to 10 x 10^{-7}N [65], and the external stress applied should be able to overcome this force if the surface atoms are to be detached during polishing. For diamond surface and even for other materials, these values are only averages since the actual contact surface area is determined by the real total contact area of the asperities and the polishing surface as shown in figure 1.4, depending on how flat the surface is. The polishing process does often create dangling bonds on the surface being polished, and these depend on the orientation as shown in figure 3.1.

In general, polished diamond surfaces are usually bulk-like and have carbon atom dangling bonds terminated with hydrogen atoms [150]. Exposure to air or water adds an oxygen submonolayer [97, 151]. The terminating hydrogen atoms are normally thought to be donated by the polishing lubricant which in most cases is olive oil. However, one might argue that the oil molecule shown in

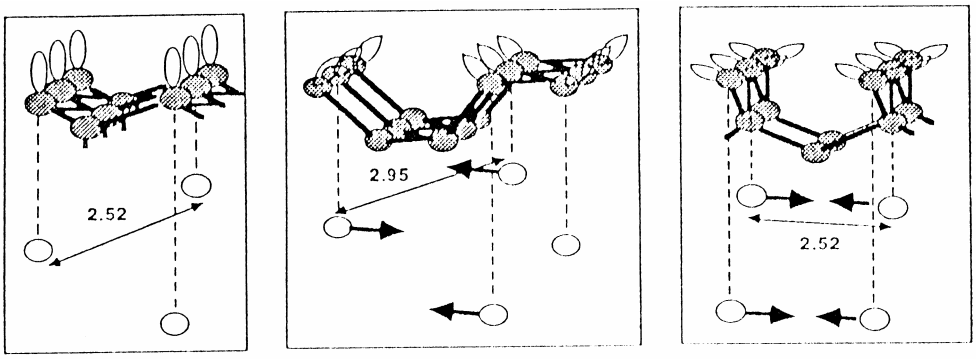


Figure 3.1: Dangling bonds on the three low index diamond surfaces. First panel represents a (111) face, the second a (110) and the last a (100) face. [After Hansen *et al.* [94]]

figure 3.7 is itself short of hydrogen, since it is unsaturated (through its C=C double bond), and therefore might not be expected to give up hydrogen easily in order to facilitate the bonding process. In spite of this, it seems quite logical to imagine that whenever surfaces are polished using a polishing lubricant or any other medium, there is always the possibility of transferring atoms from the lubricant to the surface and vice versa. This has already been alluded to by Franklyn *et al.* [124], where they found contamination of metal surfaces through smearing during polishing. Rao *et al.* [152] on the other hand have also indicated some recent advances in the electrochemistry of diamond, especially for electroanalysis and double layer capacitor applications where the properties of the topmost layers are explained.

The process of atomic transfer from a lubricant to the surface being polished has not been investigated thoroughly up till now, in spite of its obvious importance and the possible consequences that it may have for the eventual use of the surfaces prepared through this way. In particular, polishing diamond surfaces with olive oil may have the consequence that the outer carbon atoms, as well as the hydrogen atoms would come from the oil and not the diamond itself if atomic transfer occurs.

We set out to explore this hypothesis using isotopically labelled olive oil. It was surmised that carbon atoms from the labelled oil molecule would bond with those of the diamond surface in a way that satisfies both its own unsaturated double bond, as well as the diamond surface's dangling bonds that are created while polishing. This possible exchange of atoms between the diamond surface and the lubricant was investigated by the use of the nuclear reaction analysis technique (NRA), where the label on the oil molecule acted as a tracer for the transferred atoms.

3.3 Nuclear reactions

The applications of nuclear reactions are rather varied, and generally range from the desire to have a general understanding of the nuclear and chemical reactions themselves, to understanding the mechanisms of energy release from specific nuclear reactions. Nuclear reactions have also been used quite extensively as tools for studying various material properties because of their versatility. This study utilizes a nuclear reaction of the type A(p,γ)B, commonly referred to as particle-gamma nuclear reactions. Their suitability is enhanced by the fact that the energy of the exciting ion can be chosen in such a way that the nuclear reaction takes place only at the surface, thereby enabling only the surface or near-surface phenomena to be investigated.

3.4 Particle-gamma nuclear reactions ^{x}A(p,γ)^{y}B

When an energetic ion of mass m_1, and energy E, impinges on an atom of mass m_2, it can excite a nuclear reaction if E is greater than the coulomb barrier of the struck atom. In the case of (p,γ) nuclear reactions, the exciting particles are protons whose energy is chosen in such a way that only the desired reaction

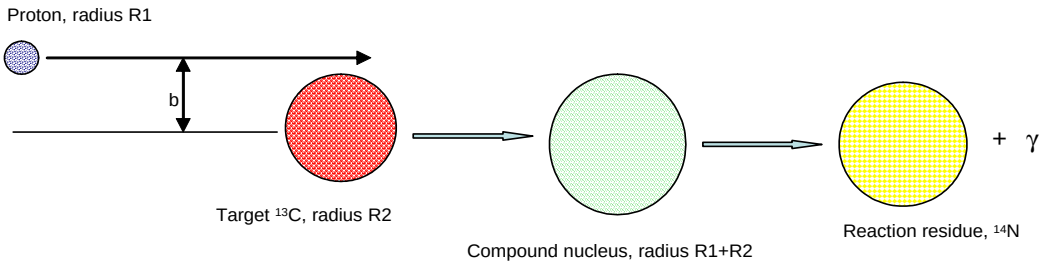


Figure 3.2: A proton of radius R_1 interacting with a target atom of radius R_2. b is the impact parameter.

is excited, and de-excitation is by gamma-ray emission, as illustrated in figure 3.2.

When the proton approaches the target, it interacts with a specific nucleus A, via a two body collision between itself and some nucleon of A. If the proton strikes a particular nucleon within the target nucleus and it doesn't leave the nucleus, another two body collision may occur and eventually the entire kinetic energy of the proton gets distributed between the combination of the nucleons of the target and the proton itself, leading to the formation of a compound nucleus [153].

The compound nucleus thus formed is considered to be in an excited state, and its decay occurs in a rather complex way that depends mainly on the excitation energy and its angular momentum among other factors, and not necessarily the nature of the proton and the target nuclei. If the reaction products are gamma rays and they are detected during the irradiation process, such a reaction is referred to as a prompt gamma emission reaction. At particular energies of the incoming ion, sharp resonances are usually observed, and in order to utilize this resonant state, the resonance energy needs to be well isolated in order to eliminate interferences with other reactions. Analyzing the reaction products of a particular nuclear reaction, yields vital information regarding the

target atom as well as the reaction products themselves. As such, NRA is a technique that is not only sensitive to specific isotopes whose resonant energies are well known, but also the energies of the emitted gamma rays. If the energy of the incoming ion is within the range defined as low to medium, i.e $<$ 1MeV, the ion (in this case proton) doesn't travel deep into the target material, and hence nuclear reaction analysis becomes a very useful surface analysis tool, for those cases where suitable nuclear reactions exists. Nastasi *et al.* [154] have compiled a detailed list of some of the useful nuclear reactions and their reaction products, as well as the corresponding resonance energies.

3.5 Reaction cross-section

Reaction cross-sections normally indicate the probability of a nuclear reaction taking place when an energetic ion hits a target atom with some specific energy. This is clearly demonstrated in figure 3.2, where two spheres of radii R_1 and R_2 collide, representing the incident and target particles respectively in a similar manner as they would in a typical nuclear reaction. This situation closely approaches a first approximation classical case, and the assumption is validated by the fact that when a cloud of particles is held together by the strongly mutually attractive nuclear forces, the spherical shape happens to be the most favoured energetically. The reaction cross-section in such a case would therefore be proportional to $(R_1+R_2)^2$, which is the area of the disc whose radius is R_1+R_2.

Suppose that the colliding balls shown in figure 3.2 are substituted by two real particles interacting in a given nuclear reaction expressed as A(p,γ)B that is initiated by a beam of protons p of intensity I_o particles/sec, incident on to a target A containing M particles, as shown in figure 3.3. The actual number of protons that react with the target then becomes equal to the fraction of the

area q, that is covered by the target nuclei. If the sample contains n atoms/cm^2 of the target nuclei, then the area d that is covered by the target nuclei is n(atoms/cm^2) x q(cm^2) x the effective area subtended by one atom(cm^2/atom), and this area also represents the reaction cross-section, σ for the reaction. The number of γ rays emitted is therefore proportional to the beam I_o and M, where the constant of proportionality is again the reaction cross-section.

However, while the gamma rays resulting from a certain nuclear reaction are emitted through a complete solid angle of 4π steradians, many times one desires to find the number of particles emitted in an element of a solid angle dΩ, in the direction with polar angles (θ,ϕ) with respect to the incident beam, since this could represent the location of the detector. In such a case, the number of particles emitted becomes proportional to dΩ, I_o and M, and the constant of proportionality is now the differential cross-section dσ/dΩ. Owing to the fact that the gamma ray emission is usually quite symmetrical about the direction of the incident beam, the cross-section becomes independent of the azimuthal angle ϕ, and it can then be approximated as,

$$\sigma \approx 2\pi \int_0^{\pi} \frac{d\sigma}{d\Omega} \sin\theta d\theta \tag{3.5.1}$$

Most nuclear reactions involving low to medium energy ions occur via the compound nucleus [155], and in this arrangement, the nuclear excited states of the compound nucleus become unstable against decay by emission of γ rays or other particles, to states of lower energy. This means that, for isolated non-overlapping levels of the compound nucleus, at certain values of the compound nucleus excitation energy, individual levels of the compound nucleus can be excited, and this happens when the excitation energy equals exactly the energy of a given compound nucleus level.

The reaction cross-section σ_{qc} of forming a compound nucleus C, in the resonant state from a pair of nuclei C=p+A at an energy E is proportional

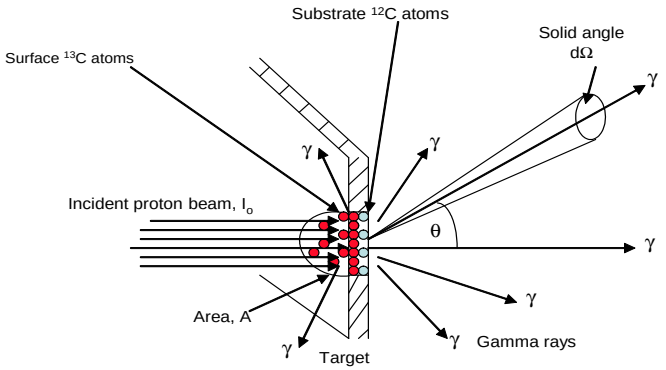


Figure 3.3: A 3 dimensional illustration of a beam of particles I_o hitting a target and producing scattered gamma rays, with some being emitted in an element of a solid angle dΩ. Adapted from G.R. Satchler [155]

to the probability that a resonant state exists in the compound nucleus C at that energy, and that the nucleus decays in some given way. This process could be summarized via the process, a+A→C→b+B, and the reaction cross-section then becomes viz [155],

$$\sigma = \pi D^2 \frac{(2J+1)}{(2J_A+1)(2J_a+1)} \frac{\Gamma_{aA}\Gamma_{bB}}{(E-E_0)^2 + (\Gamma/2)^2} \tag{3.5.2}$$

where j_i is the spin of the ith nucleus, Γ_{aA} and Γ_{bB} are the partial widths of formation of the compound nucleus C through the process a+A, and the decay of C into b+B respectively, and Γ is the total width of the decay, i.e. the Full Width at Half Maximum (FWHM) of the compound nucleus C. D is the compound nucleus's level spacing, E the nuclear excitation energy and E_0 is the resonance energy. The expression shows that in the resonance region, the nuclear phase shift δ_L rises from zero as the energy is increased towards the resonance, passes through $\pi/2$ at the resonance, and finally approaching π asymptotically as the energy increases beyond resonance. The rate of decay of the compound nucleus from its excited state is $\Gamma/\hbar$ [156], which is equal to the sum of the probabilities for decay into the various open channels γ that are

energetically available. That is,

$$\Gamma = \sum_{\gamma} \Gamma_{\gamma}. \tag{3.5.3}$$

with Γ_{γ}=0 for closed channels. Equation 3.5.2 can be rewritten so that the cross-section for a transition from channel p to an open channel γ, that is, the reaction A(p,γ)B going through the compound nucleus becomes,

$$\sigma_{p\gamma} \approx \frac{\Gamma_p \Gamma_{\gamma}}{(E - E_r)^2 + (\Gamma/2)^2} \tag{3.5.4}$$

The reaction cross-section $\sigma_{p\gamma}$, given by equation 3.5.4 readily describes the distribution of the target atoms A in the matrix, and its often referred to as the Breit-Wigner cross-section. When its variation with the solid angle is considered, the differential cross-section is used instead, and this would typically be expressed as viz [157],

$$\frac{d\sigma(E,\theta)}{d\Omega} = \frac{d(E_r,\theta)}{d\Omega} \frac{\Gamma^2}{(E - E_r) + \Gamma^2/4} \tag{3.5.5}$$

3.6 Resonant nuclear reactions.

Resonant nuclear reactions are those that exhibit a sharp increase in the reaction cross-section at some specific reaction energies, known as resonant energies. A resonant nuclear reaction occurs when the energy of the incoming ion matches that of the corresponding energy level of a particular target atom's nuclei. When this happens, the specific energy level gets preferentially populated, and it becomes unstable. This leads to the emission of gamma-ray photons or other charged particles, together with the formation of stable nuclear residues. In other words, if the bombarding energy in a nuclear reaction A(p,γ)B matches the energy E_r of a quasi-stationary quantum state of a compound nucleus, then there will be a resonance [155]. At this energy, the cross-section for the formation of the compound nucleus shows a marked increase as shown in figure

3.4. However, the description of resonant states has continued to intrigue many researchers, leading to them being viewed differently. Sometimes some people assume that at the resonance energy the incident particle gets trapped for a while before it escapes again, while in other cases resonant states are considered to be those where the incident particle's wavefunction assumes a large value within the nucleus compared to its oscillating component at large distances away from it, thus leading to increased nuclear reaction cross-section [156, 158]. In spite of these varied descriptions, they all refer to the same phenomena.

If the energy of the exciting beam of particles such as protons corresponds to the energy of the narrow and sharp resonance E_r, resonance reaction takes place at the target surface. However, if the energy of the ion is greater than the resonant energy of the desired nuclear reaction, it travels through the material matrix, losing its energy through electronic and nuclear processes, until the resonance energy is reached. For light ions, the nuclear energy losses are relatively smaller compared to the electronic losses at energies of the order of 1MeV (as used in the present work), thus the energy loss rate in this ion energy regime is primarily dominated by electronic losses.

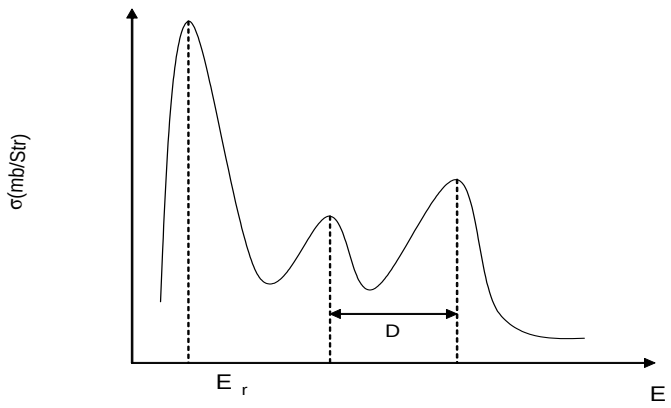


Figure 3.4: Nuclear reaction cross-section, σ as a function of exciting energy. E_r is the resonance energy, and D is the nuclear level spacing

Also known as the stopping power, the energy loss suffered by the incident ion, -dE/dx, in a particular medium gives rise to the energy-to-depth conversion, indicating how far the reacting isotope is located within the material matrix. Compound nuclear reactions are relatively long-lived processes. For level widths of ∼1.0eV, the lifetime of a compound system is $\Gamma/\tau \sim 10^{-15} - 10^{-16}s$ which is indeed very long, especially when compared to the times that are needed for a nucleon to traverse the nucleus, which is $2R/v$ ∼10^{-21}s [156, 158]. As the incident energy approaches and passes through the resonant energy, the cross-section of the channels into which the compound resonant state can decay rises to a maximum value and then falls again. At resonance, the emitted reaction products which in this case include gamma rays are then detected and counted, giving the relevant information about the quantitative amount of the isotope causing the resultant nuclear reaction.

The total gamma ray yield, Y of the nuclear reaction emitted from a thin target layer into an element of a solid angle $\Delta\Omega$ at an angle θ to the proton beam can be expressed as viz [157],

$$Y(E,\theta) = N_p N \frac{d\sigma(E,\theta)}{d\Omega} \Delta\Omega \varepsilon_{instr} \tag{3.6.1}$$

where N_p is the number of the incident particles, which in this case are protons, N is the number of target atoms per unit surface area, $d\sigma/d\Omega$ is the differential cross-section, $\Delta\Omega$ is an element of the solid angle and ε_{inst} is the intrinsic efficiency of the detector system.

Unlike the theoretically predicted sharp and narrow resonances, the experimental width of resonance is normally broadened due to the natural width of the resonance, the energy resolution of the beam and the energy straggling of the particles during energy loss from $E_{bombarding}$ to E_r [154]. For reactions that take place through the compound nucleus, the individual levels are normally fragments of simpler states that have been split by residual interactions, and

hence it is possible that the strength function will show characteristic maxima whenever one of these states is in the region of measurement, or rather corresponds to a resonant state of the compound nucleus. The simplest state is one due to the excitation of a single particle, and since the region of measurement is just above zero, a maximum will be expected in the strength function for nuclei with a single-particle state near the zero of the energy [153]. As such for low energies and also depending on the detector-sample geometry, the s-wave and to a lesser extent the p-wave will contribute to the interaction process, implying that in a majority of the cases, only the effects due to the two states will be detectable.

3.7 Stopping power of protons (H^+) in diamond

In order for charged incident particles above the resonance energy to excite a resonant nuclear reaction at a depth x below the substrate surface, they have to lose the extra energy by suffering energy losses dE/dx, also known as the stopping power S of the target material.

The ion's energy, as well as both the charges of the target atoms and those of the ion play a significant role in the ion and target interactions. At low energies, the ion carries its electrons and becomes neutralized by electron capture. At these low energies [154], elastic collisions with the target nuclei, that is, nuclear energy losses dominate. However, as the ion velocity and thus the bombarding energy increases, the nuclear energy losses diminish as 1/E, where E is the bombarding energy [159].

With increasing ion energies, the electronic energy losses, that is, inelastic collisions with the atomic electrons then become the dominant form of interaction, and at very high velocities, the ion charge state increases and eventually it becomes stripped of all its electrons. Figure 3.5 shows a typical variation of

the stopping cross-section of protons with incident energy on diamond. Nastasi *et al.* [154] have compiled a detailed database of stopping powers/cross-sections of various ions incident on different matrices, together with a corresponding set of graphical representations similar to the one shown in figure 3.5.

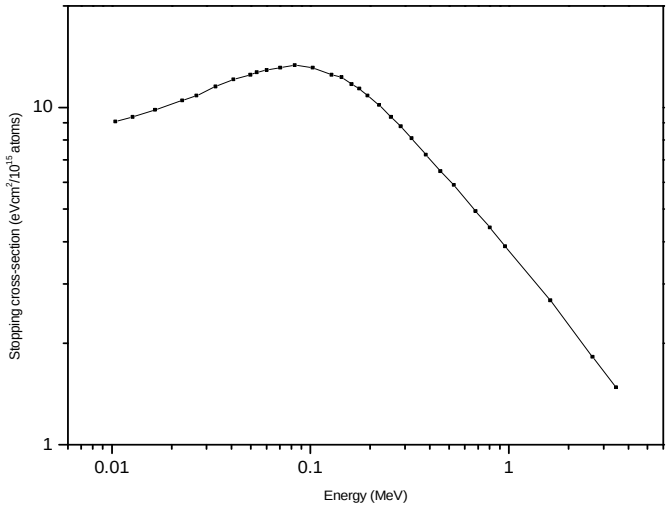


Figure 3.5: Stopping cross-sections of protons incident on diamond at various energies. [Adapted from [154]]

Using empirically determined data, they have also developed a set of relations that can be readily used to calculate the stopping cross-sections for those intermediate energies that are not listed in their databases. However, these parameters can also be obtained through computer simulations using computer codes such as (Transport and Range of Ions in Matter) TRIM98 and its later version SRIM (Stopping and Range of Ions in Matter) [160].

3.8 The 550 keV $^{13}C(p,\gamma)^{14}N$ nuclear reaction

The 550keV $^{13}C(p,\gamma)^{14}N$ resonance nuclear reaction was used to probe for the ^{13}C atoms in this study. It yields two prominent gamma rays; one at 8.06 and the other at 4.11 MeV [154]. The more energetic of the two (8.06MeV) gamma

rays also happens to be the most abundant (80%), and therefore well suited for most nuclear reaction applications. By virtue of their relatively higher energy, the 8.06MeV γ-rays are also well isolated from the interfering low energy background. In addition, the $^{13}C(p,\gamma)^{14}N$ nuclear reaction is also well suited for probing diamond because like all natural carbons, diamond contains a fixed proportion of ^{13}C atoms (1.11$\pm$0.03%) within its bulk [161, 162]. The experiments are therefore self-calibrating. Furthermore, it was ideal for this work because any other adsorbates or near-surface non-diamond species do not show any significant nuclear interactions with protons within the chosen energy window. Those that may occur such as Al or others arising from the presence of non-diamond material, have generally small reaction cross-sections compared to the 1.44mb [154] for the 550keV $^{13}C(p,\gamma)^{14}N$ nuclear reaction, to be able to produce any significant interfering effects. Due to its relatively low excitation energy, the $^{13}C(p,\gamma)^{14}N$ reaction is very well suited for probing surface phenomena, which was the main object of this study. Figure 3.6 shows the energy level transitions leading to the production of the 8.06MeV gamma rays that are used in this study.

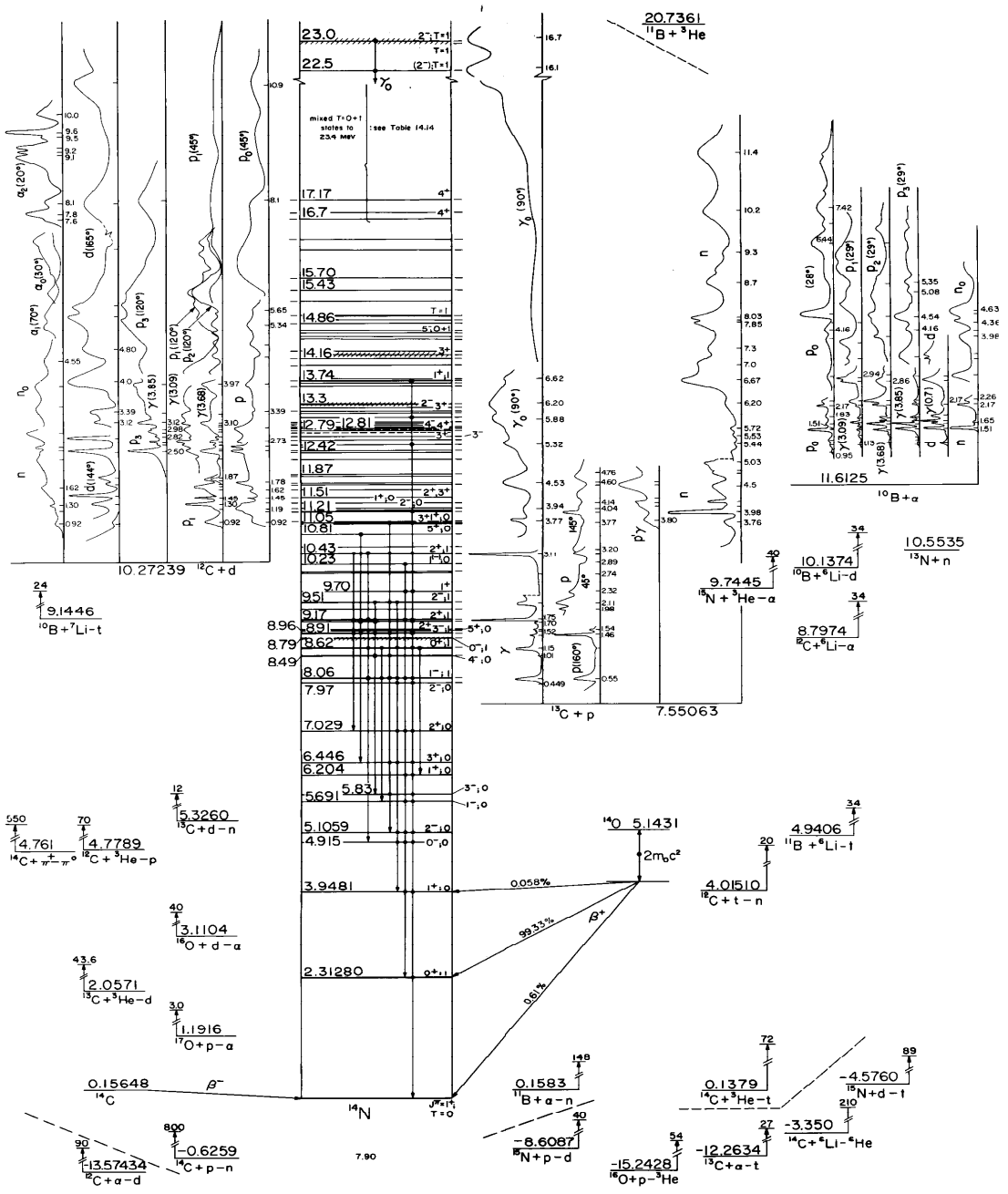


Figure 3.6: Nuclear energy transitions for the production of the 8.06MeV gamma rays from the ^{14}N energy level diagram. (After F. Ajzenberg-Selove [163]).

3.9 The oleic acid molecule.

Olive oil labelled with a high percentage of ^{13}C atoms and whose structure is shown in figure 3.7 was used to polish the diamond surfaces that were to be investigated in this study. It consists of 18 carbon atoms, 34 hydrogen and two oxygen atoms, resulting in a molecular weight of 282.52, and an empirical formula of $C_{18}H_{34}O_2$. Written in a more general way, the oleic acid molecule can be expressed as CH_3-$(CH_2)_6$-CH_2-CH=CH-$(CH_2)_6$-CH_2-COOH and in a more general way as R-$(CH_2)_n$-COOH. The molecule is hydrophobic at the methyl terminated end as seen from figure 3.7 and hydrophilic on the other, which is terminated by a carboxylic group.

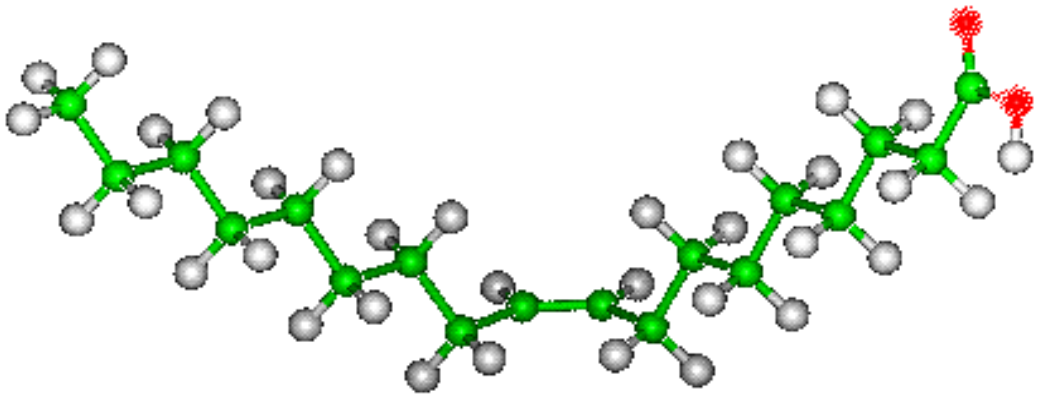


Figure 3.7: The chemical structure of the oleic acid molecule. The green balls are the labelled carbon-13 atoms, the grey ones the hydrogens, and the red ones the oxygen atoms. After [164].

For this reason, it is insoluble in water, since the hydrophobic end makes it non-polar, while the hydrophilic site makes it polar. The double bond further makes it a mono-unsaturated molecule and this leads to the bending of the molecule at its centre as seen in figure 3.7.

The oil used to polish the diamond surfaces for this study was labelled with 99% ^{13}C atoms [165], meaning that all the carbon atoms in its molecule were

usually ^{13}C. It was a colourless and an odourless liquid. A molecule having a high concentration of ^{13}C atoms was especially preferred to polish the diamond surfaces, so as to maximize the probability of transferring the ^{13}C atoms from the oil to the polished diamond surfaces through bonding with the broken diamond surface's carbon-atom dangling bonds, which are created while polishing.

3.10 Interaction of incident gamma rays with the NaI(Tl) detector's active material.

Three dominant processes take place when a detector's active material interacts with gamma rays emitted from a nuclear reaction as shown in figure 3.8. These

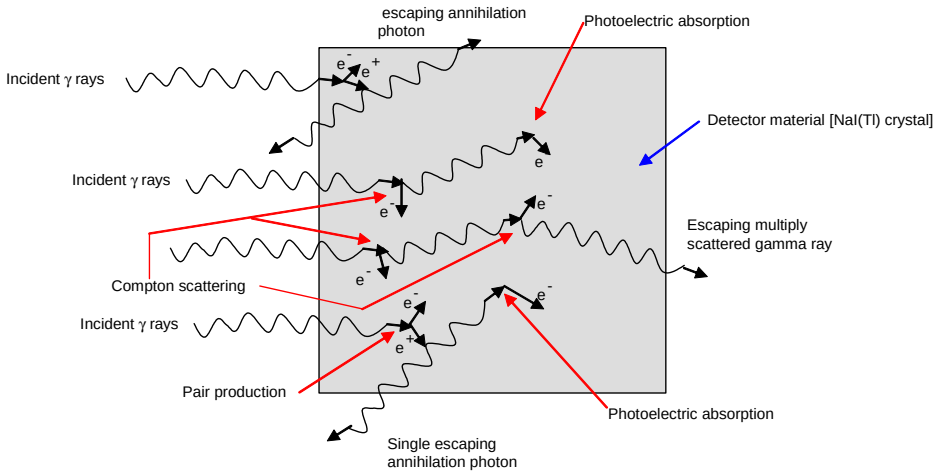


Figure 3.8: Various interaction mechanisms that occur when incident gamma rays interact with the detector's active material.

include Compton scattering, photoelectric effect and pair production. Each of these processes dominates at different gamma ray energies as seen from the graphical representation shown in figure 3.9 for the detector response.

The geometry of the detector with respect to the emitted gamma rays from a given sample is usually a key component towards its efficient performance.

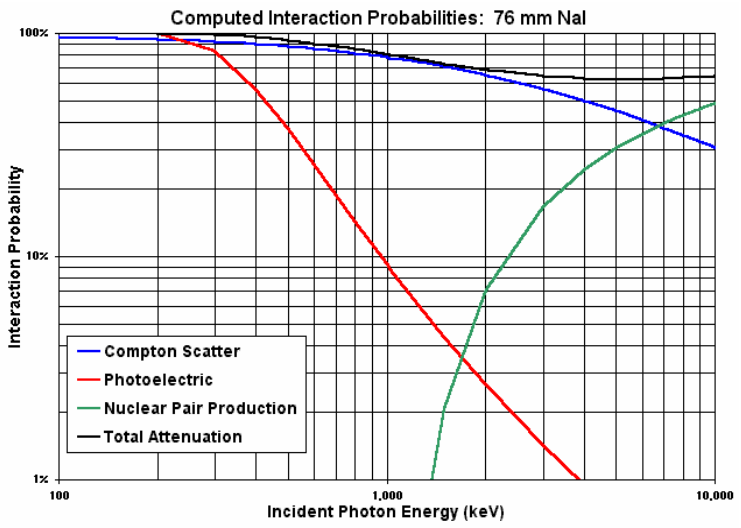


Figure 3.9: Detector interaction response as a function of the incident gamma ray's energy for a 76x76mm NaI(Tl) detector. (After [166])

When coupled with the (large) solid angle subtended, maximum collection efficiency is often guaranteed.

The detector's absolute efficiency ε_{abs}, which is expressed as,

ε_{abs} = (number of counts recorded)/(Activity of source)

and its intrinsic efficiency ε_{int}, defined as,

ε_{int} = (number of pulses recorded)/(number of counts incident on detector),

are linearly related, with the constant of proportionality being the detector's solid angle. These can be expressed as,

$$\varepsilon_{int} = \varepsilon_{abs} \times \Omega, \tag{3.10.1}$$

As such, a large solid angle is always desirable, for improving the detector's intrinsic efficiency and therefore its performance.

In addition, whenever the detector interacts with some radiation, it normally requires a minimum amount of time commonly referred to as dead time to separate and record two pulses distinctly. If the dead time is too long, a true event may be lost when it comes too soon following a preceding one, and

this becomes severe when fast count rates are involved, leading to pulse pile-up. If for example two pulses are sufficiently close to each other so that they are treated as a single pulse by the analysis system, the problem of the dead time becomes significant because this interferes with quantitative measurements based on measuring the area under the full energy peaks, since the area under the peak is no longer the true measure of the total number of full energy events. Luckily, this problem was not encountered in this study because only pulses with low enough count rates that avoided pulse pile-up were involved.

NaI with Thallium atoms added is an exceptionally efficient detector material even when compared with other solid state detectors. This means that the yield of the total light energy output is very close to 1 photon per electron-hole pair originally formed, and therefore the energy transfer to activator sites is extremely efficient for NaI detectors. In most cases, the initial light output (signal) is very small and this normally requires to be amplified, a process that is readily achieved by the use of a photomultiplier (PM), which then enhances it before being passed on to the multi channel analyzer (MCA).

As is the case with all other detectors, the NaI(Tl) detector which was used in this work has a finite energy resolution, that arises from contributions involving separate effects such as charge collection statistics, electronic noise, variations in the detector's response over its active volume, and drifts in operating parameters over the course of the measurement. Fluctuations in the PM tube gain from event to event may also add to the measured resolution in this detector, as well as in other scintillation detectors.

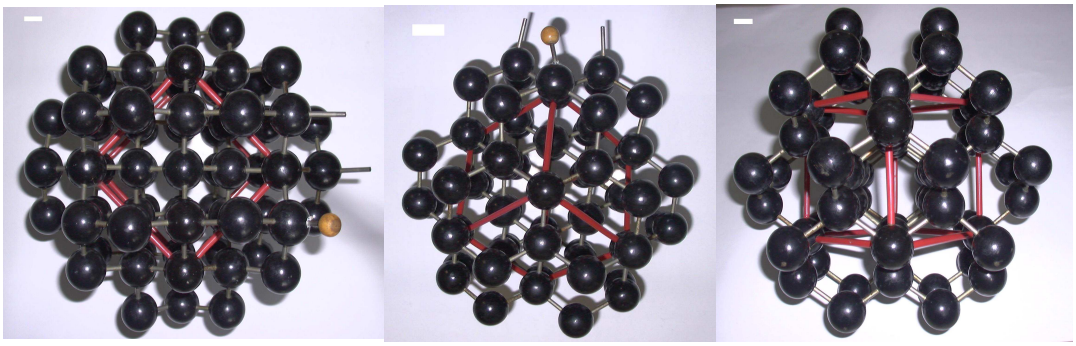


Figure 3.10: Illustrations of the atomic arrangement at each of the three low index diamond faces. The left hand side panel shows a (100) face, the middle a (111) face and the right hand side one, a (110) face. Note the large channels within the (110) face.

3.11 Experimental Procedure

3.11.1 Sample Preparation

The main objective of this study was to investigate the possible transfer of carbon-13 atoms from the polishing lubricant to the "clean" polished diamond surfaces. To realize this, polishing oil labelled with 99% ^{13}C was used, with the ^{13}C atoms acting as tracers for any species that may be transferred onto the surfaces during the polishing. Their presence was then to be detected and quantified using the resonant nuclear reaction analysis technique, that was discussed previously.

In this regard, six natural diamond samples of different sizes ranging from 3mm by 3mm by 1mm and above were used as seen from figure 1.2. These were selected in such a way that they every face was represented by two of each of the three low index families of planes, {100}, {110} and {111}. Figure 3.10 shows models of the atomic arrangement at each of the three low index faces.

The selected faces were first prepolished to within 1° of the desired plane as shown by the Laue pictures presented in figures 4.1, 4.2 and 4.3, following the standard mechanical polishing procedure described in detail within the experimental section of the XPS chapter.

The samples were prepared in such a way that they had two parallel opposite faces polished to the same standard. The polished surfaces were then repolished manually on a highly polished metal block, using 1/4 and 1/10μm diamond pastes and olive oil (principally Olein) labelled with 99% ^{13}C atoms. In this case, the labelled oil acted as both the source of the carbon-13 atoms that may be transferred onto the polished surfaces, as well as a lubricant, and also as a source of the terminating hydrogen atoms in our slow-speed, low-load manual polishing. In the process of polishing, some of the particles of the diamond paste may break down into even smaller ones, thus leading to even better surfaces whose roughness was probably be of the order of the smallest particle size, and hence yielding much smoother and flat surfaces. Each of the manual polishing processes lasted for approximately 30 minutes, and the high ^{13}C concentration in the polishing lubricant ensured that the probability of bonding any broken surface carbon-atom bonds with a ^{13}C atom was maximized.

After the repolishing, each face was thoroughly cleaned in an ultrasonic bath as described in the experimental section of the XPS chapter. A diluted solution of Contrad, which is a surface cleaning detergent also sold under the name "Decon 90"was used. A Pyrex beaker was used in each case, and the initial cleaning and rinsing processes lasted for periods ranging between 3 to 10 minutes. Each surface was ultrasonically rinsed three times using deionised water, and this was expected to yield very "clean"surfaces. To prevent any further contamination, each sample was cleaned and rinsed separately in its own beaker, and plastic tweezers used to handle them, by holding onto those faces that were not repolished. After rinsing, the sample faces were dried by blowing

dry nitrogen over them and/or dried using a special cloth or fine filter paper that did not deposit any fibers onto them, then stored in sterilized polythene bags to avoid any further contaminations as they awaited analysis. As a precautionary measure, the surfaces were not kept for long in the polythene bags before being analyzed, and plastic gloves were always worn during this process to avoid any contamination with body oils.

3.11.2 Experimental set up

The 550keV $^{13}C(p,\gamma)^{14}N$ resonant nuclear reaction was used to probe the surface-bonded ^{13}C atoms. To initiate the nuclear reaction process, the Cockcroft-Walton 1.4MV accelerator based at the Schonland Research Institute [now iThemba LABS (Gauteng)], whose schematic diagram is shown in figure 3.12, was used. This provided the protons needed to probe for the bonded ^{13}C atoms at various energies. In this set up, the initial voltage was generated by a transformer that delivers 100kV, which is then stepped up by a series of rectifiers and capacitors, lined up within the pressurized tank as shown in figure 3.11.

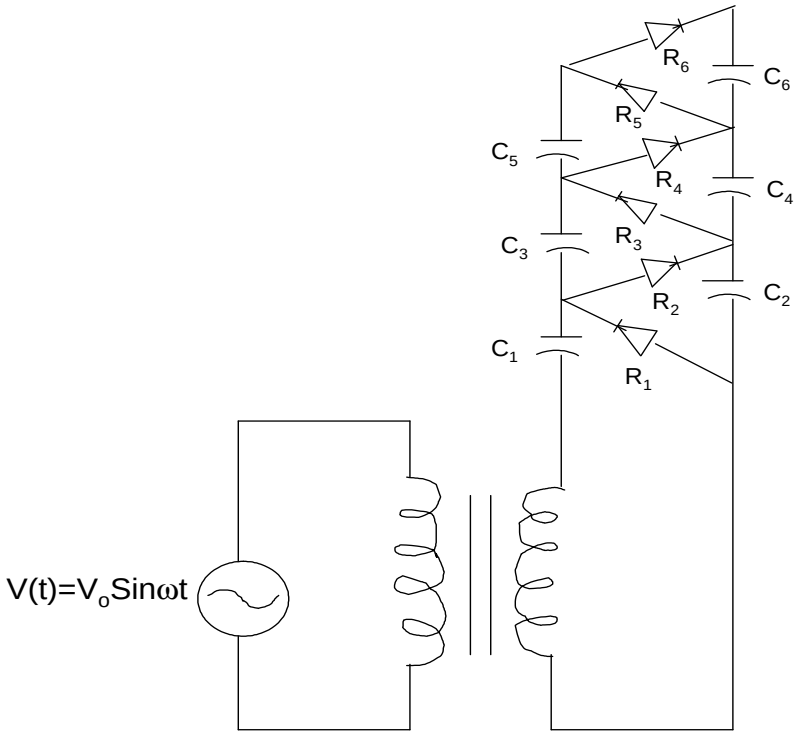


Figure 3.11: Operating principle of the Cockcroft-Walton high voltage Power supply. (After D.B. Rebuli [167])

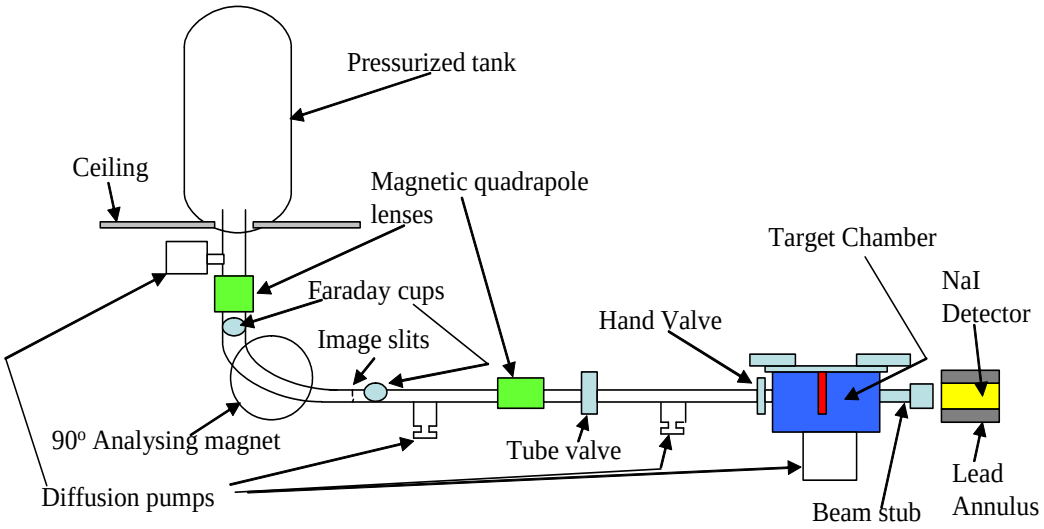


Figure 3.12: Schematic diagram of the 1.4 MV Cockcroft-Walton Proton accelerator. (After R.A. Spits [168])

The accelerator consists of a tank that is fixed above the ceiling of the accelerator building as shown in figure 3.12, pressurized to operating pressures of more than 6 atmospheres with a mixture of dry carbon dioxide and nitrogen gases in proportions of about 1:5. An evacuated beam-line and a target chamber form the remainder of the accelerator set-up. Gas bottles containing the appropriate gases e.g. hydrogen for protons are normally placed at the top of the pressurized tank and ionization of the required particles is initiated by an RF(radio frequency) source fed by one of the gas bottles. The ions are then accelerated vertically downwards from the tank to a magnet that bends them through 90° to a horizontal direction towards the target chamber, which is located at about 5 metres away from the 90° magnet. The magnetic field of the bending magnet is controlled in such a way that only the ions with the desired mass and energy are selected, and hence allowed to proceed to the target chamber. Such an objective is achieved by relating the magnetic flux, B(T) and the proton's energy, E(MeV) as,

$$B = (0.651 \pm 0.001)\sqrt{E} \tag{3.11.1}$$

a relation that is derived empirically using calibration data obtained previously from the accelerator. Since small energy steps were required when varying the proton energy, and also due to the fact that the energy was required to remain relatively constant during any specific irradiation process, both a helipot which controlled the amount of current to the analyzing magnet and a rotating coil magnetic probe that measured the actual magnetic flux were used to ensure that any significant energy fluctuations or drifts were actually monitored, and corrected. The two therefore ensured that the required beam energy was kept in check, to within the errors of the two devices.

Beam focusing was achieved through the adjustments of two pairs of vertical and horizontal quadrapole magnets. Together with these, both vertical and

horizontal beam steerers were also used to control and steer the ions towards the target. Since it was desired to have an intense beam interacting with a specific area of the target, and hence a certain number of ^{13}C atoms on that part of the surface, no beam scanning was attempted.

The pressure within the target chamber as well as the beam line was maintained at better than $5x10^{-6}$ torr, which was sufficient to allow the required mean free paths of the accelerated protons.

3.12 Gamma ray background minimization and sample irradiation analysis.

Within the vicinity of the detector, low energy gamma rays, otherwise referred to as background radiation are often emitted from various sources. These have the unfortunate consequence of being able to interfere with the desired gamma rays that are produced from a given nuclear reaction. For this reason, sufficient measures to minimize this background radiation are often needed, while at the same time maximizing the collection efficiency of the required gamma rays. As mentioned previously, one way of improving the detection system's efficiency is to ensure that it subtends a large solid angle for the emitted gamma rays relative to the detector, an objective that can be realized by minimizing the detector-to-source distance. In our case, the target was placed beyond the normal chamber on a beam stub as shown in figure 3.13. The detector was mounted at 10mm away from the target. This was a very small distance, and it effectively ensured that a large solid angle of nearly 2π steradians was subtended, outside the vacuum. The distance between the target and the detector was critical in determining the solid angle, because the solid angle of a point source located at a distance d along the axis of a cylindrical detector of radius r actually depends

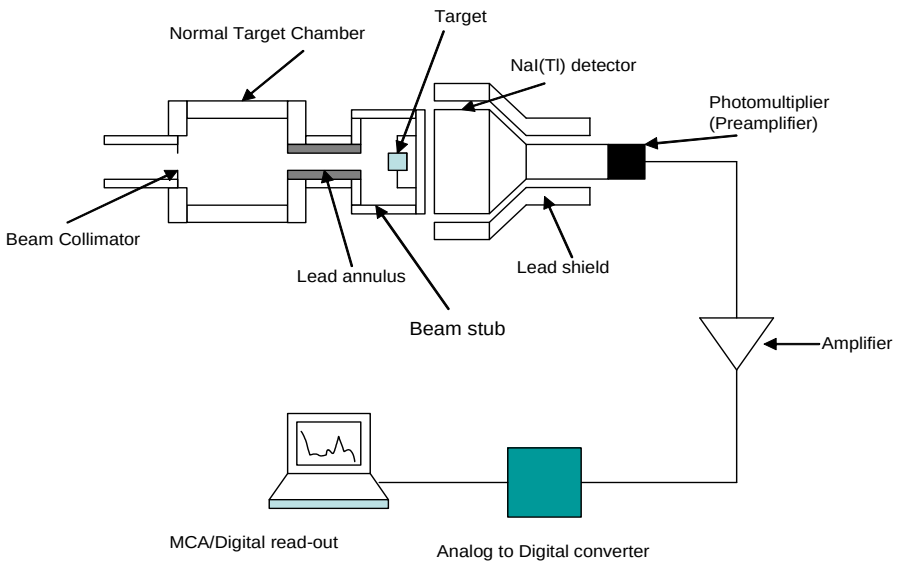


Figure 3.13: Sample - detector - readout arrangement. The dimensions are not drawn to scale.

on it, according to equation 3.14.1.

$$\Omega = 2\pi[1 - \frac{d}{\sqrt{(d^2 + r^2)}}] \tag{3.12.1}$$

From this relation, if the detector radius r is much bigger than the source-to-detector distance d, then the solid angle Ω will approach 2π (about 80% of 2π in our case), which is a rather large value and thus necessary for improving the detector's efficiency as seen from equation 3.10.1 [159]. As one would expect, γ-ray emission is almost isotropic, and therefore absorption by the sample holder is negligible.

In order to cut off the low energy background gamma radiations arising from sources such as building materials, cosmic rays and generally from other sources of low energy γ-rays within its vicinity, the detector was shielded with a lead annulus of thickness close to 6.9cm. In addition to the sources of the background radiation mentioned above, noise from the detector electronics may also contribute to some high background that is registered within the low energy

regime of the gamma ray yield spectrum. Further minimization of the background radiation was achieved by wrapping round the beam stub where the sample was mounted with several 'turns'of lead strips of 1.5mm in thickness.

In order to ensure that only gamma rays arising from the desired nuclear reaction were counted, another lead annulus measuring about 8cm in length by 4.2cm in diameter was used. This had a through 'hole'measuring 0.8cm in diameter which was bored at its center and placed just before the target as shown in figure 3.13. This arrangement ensured that any gamma rays originating from sources such as slits and collimators upstream of the target were strongly attenuated and if possible eliminated completely so that they did not interfere with the required gamma ray signal and hence get erroneously counted.

Together with these measures, data collection times were minimized by using high beam currents. At times, beam currents of up to 500nA were used, and this helped in shortening the exposure times significantly. This was realized by setting the current integrator in such a way that when a total count of $2x10^4$ had been achieved per run, the irradiation process would stop automatically. The number of counts of $2x10^4$ was chosen on the basis of the fact that these were large enough to yield a sufficient number of γ-rays per run for the analysis, and at the same time they also ensured that the surface was not significantly damaged at the end of all the exposures. The beam size (diameter) was verified initially to ensure that it was on the expected area of the target, by irradiating a blue polythene paper that burnt at the point where the beam was hitting, thereby verifying not only the region of the sample where it was falling, but also the actual size for corrections during the quantification process. Through this, the correct position where all the targets were to be placed for the nuclear interaction to take place was established, as well as giving an idea of the size and shape of the beam. From these preliminary experiments, the beam size was found to be $\sim$2mm in diameter, corresponding to the size of the upstream

collimator that was placed near the target. Beam spread was not expected to be a significant factor in this case, because the final collimator and the target were not located too far apart. However, one needs to consider possible changes on the surfaces after long and high beam exposures, because these tend to lead to the deterioration of the surface quality. In addition, the target chamber was also well isolated from the ground, so as to avoid any undesired effects from leakage current. In the process, the whole chamber acted as a Faraday cup for the current integration, which avoided the need for secondary electrons suppression.

3.13 Detector calibration

A 10x10cm Bicron [169] NaI(Tl) scintillation detector with an energy resolution of about 60±10keV FWHM was used to count the (8.06 MeV) gamma rays emitted from the 550keV $^{13}C(p,\gamma)^{14}N$ nuclear reaction. It was positioned outside the vacuum, at 10mm right in front of the beam stub where the target was mounted as shown in figure 3.13, and this arrangement was used for the collection of the gamma rays in all cases. As mentioned before, this ensured a solid angle of about 80% of 2π Steradians was subtended. The detector was operated at a voltage of about 900V and an amplifier gain of 4.4 was used. As mentioned previously, sodium iodide detectors with thallium atoms added are very efficient for the detection of gamma radiation, even when compared with solid state conductivity detectors. They have a much better measuring efficiency particularly at higher energies, although their energy resolution is relatively poor when compared to solid state detectors. However, the poor energy resolution was not a significant factor, since this study did not involve resolution of a large number of peaks. As long as the gamma-rays of interest were recorded, broadening of the peaks became unimportant. On the other

hand, good detector efficiency was required because the study entailed picking out very small amounts of ^{13}C, an objective that made the NaI(Tl) detector more desirable over the others. Since the gamma rays emitted from the 550keV $^{13}C(p,\gamma)^{14}N$ nuclear reaction were rather energetic, a detector having a large NaI(Tl) crystal was required for maintaining a high efficiency. The excellent light yield characteristic of NaI(Tl) detectors (which is related to its efficiency) made them the preferred choice in this study, but their relatively long decay time of 230ns [159] may impact negatively for some fast timings or high count rate applications. This was however not a problem in this study because the count rates were optimized as mentioned previously, through the appropriate choice of collimation and the beam current.

In the case of the 550keV $^{13}C(p,\gamma)^{14}N$, three gamma ray peaks separated by an energy interval equal to $m_o c^2$, where m_o is the rest mass of an electron and c is the speed of light, are always produced as shown in figure 3.15. These correspond to the full energy peak, as well as the single and double escape peaks that arise from processes involving the interaction of the detector's active material and the γ-rays. Additionally, the detector's active material was large enough to interact with the energetic gamma rays appropriately without affecting the accuracy of the results.

In order to establish that only those gamma rays originating from the required nuclear reaction were counted, the multi-channel analyzer (MCA) was first set in such a way that it operated within the correct energy window for the detection of the emitted 8.06MeV gamma rays. The role of the MCA was to place correctly the various gamma rays into the respective channels that corresponded to their energies. The result would then be an output spectrum that consists of a series of peaks, whose number depends on the energies of the γ-rays present from the respective sources.

In this study, two standard gamma ray sources were initially used to set up

the MCA, firstly, as a check for accuracy and two, for correct placement of the resultant gamma rays into the right channels corresponding to their energies. This was achieved by determining the values of the energy per channel for each of the gamma rays emitted by the two standard sources, and then using a linear relationship (scale) to set up the analogue-to-digital (ADC) converter gain, so that the 8.06MeV gamma rays were identified. The use of the two sources also ensured that any ambiguities that may arise from using only a single source were eliminated. The high energy (8.06MeV) gamma rays were conveniently located in a region that was well away from the low energy regime which in itself was an advantage, thus effectively eliminating the problem of low energy background interference. At the same time, the energy window was also chosen in such a way that it took account of the broadening of the detected gamma ray peaks.

The two sources used in the setting up of the MCA were ^{60}Co that produces two gamma rays of energies 1.173MeV and 1.332MeV [169, 170] and ^{137}Cs that produces gamma rays having an energy of 662keV [170]. Each source was placed quite close to the detector ($\approx$ 1cm away), to emulate the actual sample-detector arrangement. The electronics controlling the detector and the signal processing devices such as the amplifier and its gain as well as the ADC and its gain were then adjusted in such a way that the detected gamma rays from the two sources were clearly identified within the desired channels of the collected spectra. Using these as references, it was possible to ensure that the required gamma rays occurred at the channels that would permit the 8.06MeV gamma rays from the 550keV ^{13}C(p,γ)^{14}N nuclear reaction to be observed. This was realized by determining the channel into which the 662keV gamma ray peak from the ^{137}Cs occurred and then by using linear proportionality, establish the channel into which the 8.06MeV gamma rays were expected to occur. By applying a similar procedure for the 1.332MeV gamma ray peak from the ^{60}Co standard

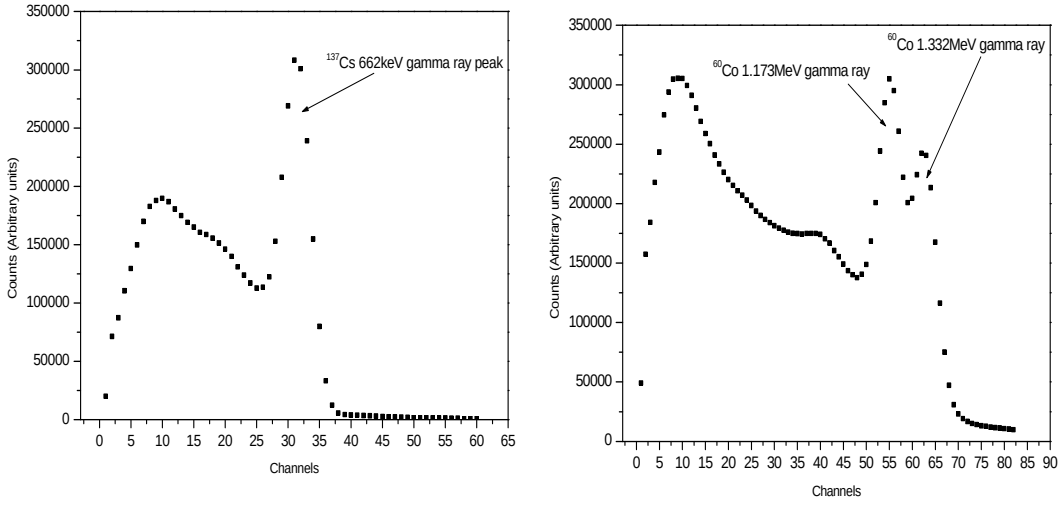


Figure 3.14: Detector calibration peaks using ^{137}Cs and ^{60}Co standard sources.

source, the channel into which the 8.06MeV gamma rays were expected to occur was also determined. These detector settings were then recorded and used for all the subsequent nuclear reactions involving the production and collection of the gamma rays, so as to maintain consistency. Some typical examples of the calibration spectra obtained from the ^{60}Co and ^{137}Cs standard sources are shown in figure 3.14. These spectra gave the resolution for the ^{60}Co 1.332MeV gamma ray peak at the detector settings mentioned previously as 9.1%, while that of the 662keV ^{137}Cs gamma ray line was found to be 10.9% at FWHM of the respective peaks. Energy resolution values are however not constant with energy E, and they are generally better at low energies, with the detector resolution varying as $1/\sqrt{(E)}$ [169].

Natural diamonds have been shown to contain small traces of non-diamond materials [171] such as nickel and aluminium. Unfortunately, Al can produce gamma rays of comparable energy to the 8.06MeV gamma rays from the ^{13}C(p,γ)^{14}N nuclear reaction, especially when the energy of the protons is above 600keV. Luckily, the reaction cross-section of aluminium with protons within this energy regime is quite small [154] compared to that of the ^{13}C atoms being

detected. Additionally, its amounts were expected to be generally small enough that gamma rays from it or any other trace elements would not interfere with the yield from the surface-bonded ^{13}C significantly, especially in situations where relatively large amounts of ^{13}C atoms were residing on the diamond surfaces, as was the case in this study. Furthermore, the Coulomb barrier makes it quite unlikely for the energy of the bombarding ions (protons) to excite nuclear interactions with elements of higher atomic numbers. Spits *et al.* [172] observed that the closest interfering nuclear reaction to 550keV one would originate from ^{30}Si at a resonant energy of 630keV, but its contribution would also be low.

3.14 Quantification of the adsorbed ^{13}C atoms on diamond surfaces.

The number of ^{13}C atoms transferred onto the diamond surfaces through polishing was determined by counting the emitted gamma rays from the 550keV $^{13}C(p,\gamma)^{14}N$ resonant nuclear reaction, since these were considered to be proportional to the number of surface-bonded ^{13}C atoms. The proton energy was varied between 445 and 680keV, that is, quite close to the 550keV resonance energy, using steps of 10keV in the off-resonance region and 5keV in the resonance one. From this, a profile of the gamma ray yield versus the proton energy was obtained. This process was initially done for a graphite sample, using similar energy stepping, and within the same energy range, so as to establish the nature and shape of the ^{13}C yield profiles. Although smaller energy steps may have been more desirable, those below 5keV were not considered useful, nor practical since the accelerator accuracy was about 4keV ($\pm$2keV) [7], thus limiting the step size to this as a minimum. The choice of such a value meant that we were working almost at the highest resolution of the accelerator.

All the samples used in this study were type Ia natural diamonds, and in line with all natural terrestrial carbons, they contained small amounts of ^{13}C

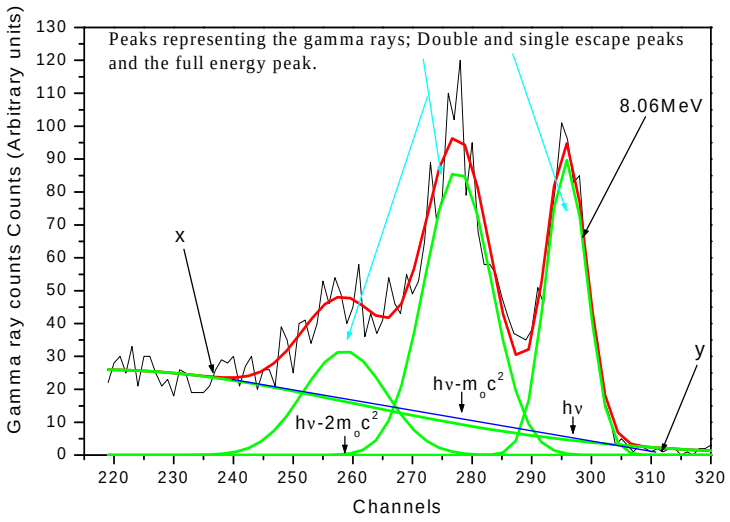


Figure 3.15: Three gamma ray peaks obtained at a specific proton energy, fitted with a Gaussian distribution. The area under them is taken between channels x and y.

corresponding to about 1.11±0.03% of the bulk ^{12}C [161, 162]. Thus, instead of using a different standard sample to calibrate for the ^{13}C atoms transferred onto the diamond surfaces, the small traces of ^{13}C atoms contained in the natural diamonds were used for this purpose, and this makes natural diamonds self-calibrating, with regard to the ^{13}C isotope.

Upon the excitation of the desired nuclear reaction, three gamma ray peaks which were separated by an energy interval equal to m_0c^2 as shown in figure 3.15 were always obtained. The area under these peaks gave the total number of gamma ray counts at the respective proton energies, and from these the corresponding numbers of ^{13}C atoms were computed. The exact area under the peaks was obtained by integrating the counts between the continuum values on either side of the peaks after a linear background subtraction as illustrated in figure 3.15. This area is expressed mathematically as,

$$Peak \quad Area = \sum_{i=x}^{y} C_i - (y-x)\frac{C_x + C_y}{2} \tag{3.14.1}$$

where C_i are the counts in channel i, while C_x and C_y are the counts obtained by

averaging the counts in the four channels about channels x and y respectively. The area was determined by choosing the appropriate region of interest, and then integrating it over the chosen energy channels. For most applications involving the use of a NaI(Tl) detector, a Gaussian curve fit to the points that lie within one standard deviation on either side of the measured photopeak value has been shown to represent adequately the shape of the photopeak for various source geometries and counting conditions [173]. As such, a linear background subtraction was first applied to all the three gamma ray peaks (see figure 3.15), before fitting them with the corresponding Gaussian peaks, and then the area under them was determined as described previously. In figure 3.15, the solid line forming the envelope over the three peaks is their Gaussian fit.

The choice of the exact positions of either channel x or y was not fixed (i.e. was relaxed), and could vary slightly as seen from figure 3.15, depending on the judgment made as to where they began or ended. This gave rise to slightly different peak areas when their extraction was repeated several times (at least 5) at the various x and y values. However, these variations in peak area were generally small, meaning that the repeated values for the area would be pretty much the same. The main cause of the uncertainty in choosing the correct values of channels x and y was the continuum's high and random background especially at the low energy side of the three gamma ray peaks. From the repeated values of the peak areas, the median rather than the mean was considered to represent the correct area. This was especially vital in order to reduce the effects of large areas obtained erroneously affecting the accuracy of the results. The error in the measurements was taken to be one standard deviation of the data obtained from the repeated values of the peak areas. Using the tabulated data of the gamma ray counts (given by the area under the peaks) at every proton energy, line profiles corresponding to the gamma ray yield for the respective diamond faces were plotted.

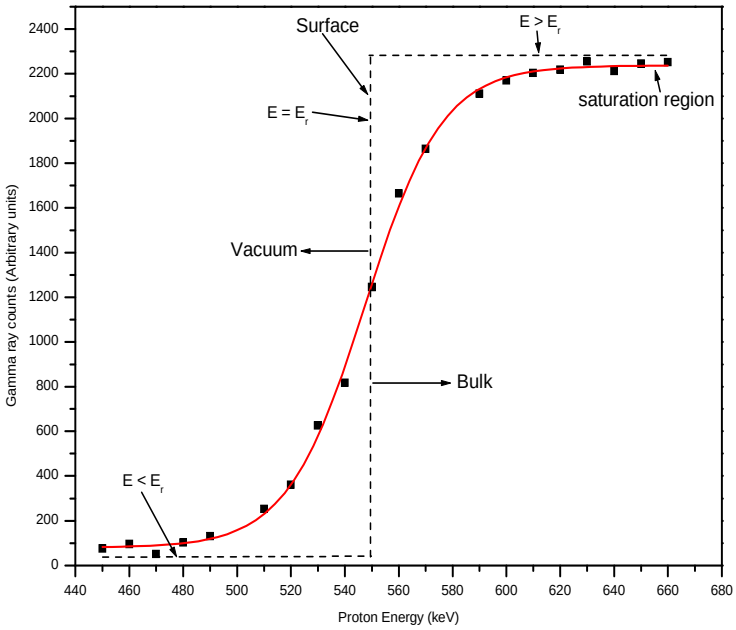


Figure 3.16: A step function illustrating the background spectrum from the 1.11% ^{13}C atoms contained within the bulk of all natural diamond samples. These data were obtained from sample kc5, which was a (111) face.

Their shapes were similar to the one shown in figure 3.16, which was obtained from a diamond sample that was not treated with the ^{13}C-labelled oil, as the proton energy was swept below and above the 550keV resonance energy. This yield profile corresponded ideally to a step function (dashed line) convolved with the resonance width of 25keV. This was taken to represent the calibrating spectrum from the standard samples (originating from the 1.11% ^{13}C atoms contained in the diamond's bulk).

Figure 3.16 is a typical plot from resonant nuclear reactions, due to the relation between the proton energy E, and the nuclear reaction's resonance energy E_r. If $E \ll E_r$, no resonance nuclear reaction takes place, and when $E=E_r$, the reaction takes place at the sample surface. If $E>E_r$, the protons (ions) must lose the extra energy through mainly (the inelastic) electronic stopping, until $E=E_r$ at a depth x, and it is only then that the reaction takes place at

that specific depth. If the bulk contains a fixed amount of the isotope causing the desired nuclear reaction, the gamma ray yield would also become almost constant at some point where E$\gg$E$_r$, implying that the counts reach a point where almost no more increment occurs and this in our case is referred to as the saturation region, as shown in figure 3.16.

For a sample having a thin layer of the relevant isotope at its surface e.g ^{13}C atoms as was the case for the diamond samples used in this study, a surface ^{13}C peak would typically occur at the resonance energy E$_r$. This would be similar to the one shown in figure 3.17, where it appears as a parasitic peak riding on the background, which is represented by the fitted solid line. After subtraction of the background, the parasitic peak gets isolated as a surface peak which is then fitted with the Breit-Wigner (B-W) distribution (solid line) as shown in figure 3.18, which describes the true distribution of the adsorbed atoms. It is also vital to add that, since the ^{13}C surface layer was very thin, the target atom distribution may be thought of as being a delta function to a first approximation. However, due to the finite width of the nuclear reaction as well as the energy spread of the beam and detector response, the surface peak is normally broadened.

Equation 3.14.2 shows the gamma ray yield Y(E), of the extracted surface peak, which is approximated by the B-W relation as,

$$Y(E) = b\frac{\Gamma_p\Gamma_r}{(E_0 - E_r)^2 + \Gamma^2/2} \tag{3.14.2}$$

E$_0$ is the incident proton's energy, E$_r$ the resonance energy, Γ_p and Γ_r the proton and gamma ray's partial widths respectively, Γ the total FWHM, and b a scaling factor.

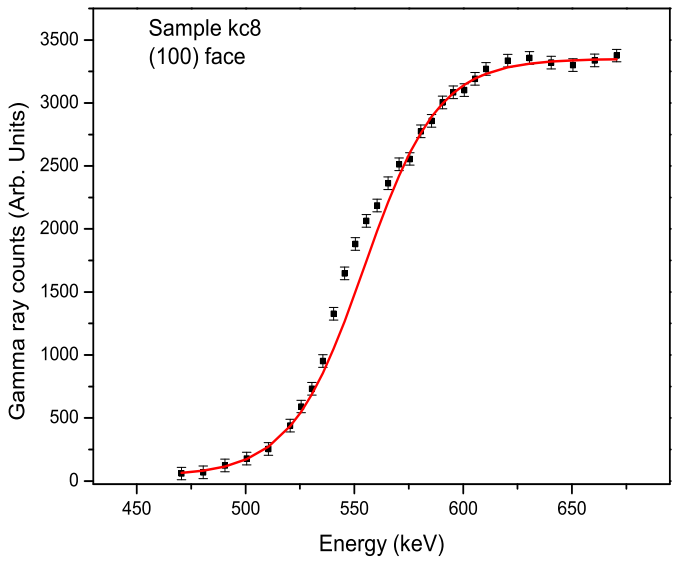


Figure 3.17: A typical ^{13}C peak riding on the background spectrum.

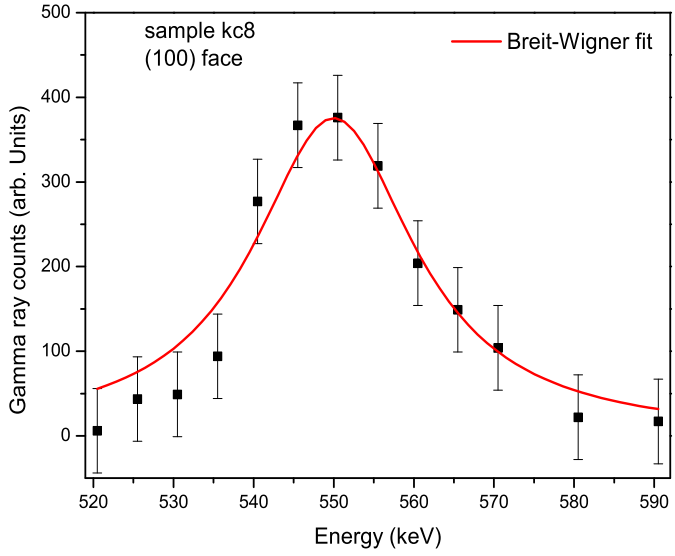


Figure 3.18: An extracted surface peak fitted with the Breit-Wigner distribution.

The extracted data points constituting the surface peaks were fitted with equation 3.14.2, where all the parameters were used as fitting variables except the proton's energy E and the resonance energy E_r. The variables were allowed to vary in turn, until the best least-squares fit to the data was achieved.

The saturated background (see figure 3.16) was proportional to the number of ^{13}C atoms per unit volume in the bulk, which was (1.11% x 1.76x10^{23}) atoms/cm^3, while the integrated area or the total number of counts under each of the surface peaks was taken to be proportional to the number of surface atoms per unit area. The ratio of the two counts gave the areal density of the ^{13}C atoms at the surface as illustrated in the following discussion.

Suppose that the number of gamma ray counts per channel at the saturation region as shown in the background spectrum of figure 3.16, is N_m. If one then considers a small slice of proton energy ΔE within this region, corresponding to an element of depth Δx which contains a specific number of ^{13}C atoms, then Δx can be expressed as,

$$\Delta x = \frac{\Delta E}{(dE/dx)} \tag{3.14.3}$$

where dE/dX is the stopping power of protons in diamond at resonance (since the region chosen varied only slightly from the resonance energy). If the atomic density of diamond, (1.76x10^{23}atoms/cm^3) is taken to be D, the number of carbon atoms per unit area in Δx becomes $D\Delta x$. This means that, the actual number of ^{13}C atoms per unit area originating from the 1.11% bulk ^{13}C in the slice of depth Δx becomes,

$$= \frac{1.11}{100} D\Delta x \tag{3.14.4}$$

This can be stated alternatively as the number of ^{13}C atoms corresponding to the gamma-ray counts per channel within the diamond matrix, previously referred to as N_m, for an equivalent slice of energy ΔE. Using a similar argument,

the number of ^{13}C atoms contributing to a surface peak containing N_s gamma-ray counts per channel becomes,

$$= \frac{N_s}{2N_m}\frac{1.11}{100}D\frac{\Delta E}{dE/dx} \tag{3.14.5}$$

In equation 3.14.5, the term 2 in the denominator comes from the fact that the energy stepping in the resonance region where the surface peak occurs was half of the one in the off-resonance region. Furthermore, in spite of the fact that the layer of ^{13}C atoms was residing on top of the diamond's ^{12}C matrix, it did not offer any significant stopping to the protons since it was extremely thin. Additionally, although the irradiated area was much smaller than 1cm^2, this was normalized when determining the number of counts from the surface-bonded ^{13}C atoms through the ratio N_s/N_m, since both were derived from the same area. Through this, the area of the irradiated region falls out of the equation.

Surface sputtering of the target atoms, was not expected to be significant in this study, according to the TRIM98 [160] computer code and its later version SRIM2003, meaning that the surface-bonded ^{13}C atoms were expected to remain in their respective bonded positions throughout the entire irradiation process. However, surface deterioration through extended periods of beam exposure could cause some changes on the surfaces as mentioned previously. Nonetheless, although some damage was found to occur during the initial preliminary studies at the irradiated regions where the diamonds changed from colourless to dark, this did not change the surface-bonded ^{13}C atom numbers. Furthermore, TRIM simulations showed that most of the damage was occurring at the end of the ion trajectories where most of the particle's energy got deposited, and the low damage at the surfaces was due to the fact that the particles were still too energetic as they approached and passed through the surfaces. The presence of minimal surface damage, may however indicate that

one is not necessarily investigating identically similar surfaces towards the end of a long irradiation process as they were at the beginning. This was however not expected to affect the measured ^{13}C atoms, since if no surface sputtering or long-range atomic displacement occurred, almost the same number of carbon atoms would be excited all the time, up to the end of the irradiation process, the nature of the surface notwithstanding.

3.15 Results

Profiles of the gamma ray yields versus proton energy for diamond surfaces that were not treated with the ^{13}C atoms and those that were treated are shown in figures 3.19 to 3.28. Two different samples were used for the untreated diamond surfaces, and their profiles are shown in figures 3.19 and 3.20. These were taken to represent the background gamma ray counts from the 1.11% ^{13}C contained in all natural diamonds as mentioned before. Figures 3.21 and 3.22 on the other hand show the profiles obtained from the {100} faces that were repolished with the ^{13}C-labelled oil, while figures 3.23, 3.24 and 3.25 show the corresponding profiles obtained from three different {111} faces. Profiles from the ^{13}C-treated {110} diamond faces are shown in figures 3.26, 3.27 and 3.28, with each of the three low index faces being represented by at least two faces, so as to eliminate any ambiguities.

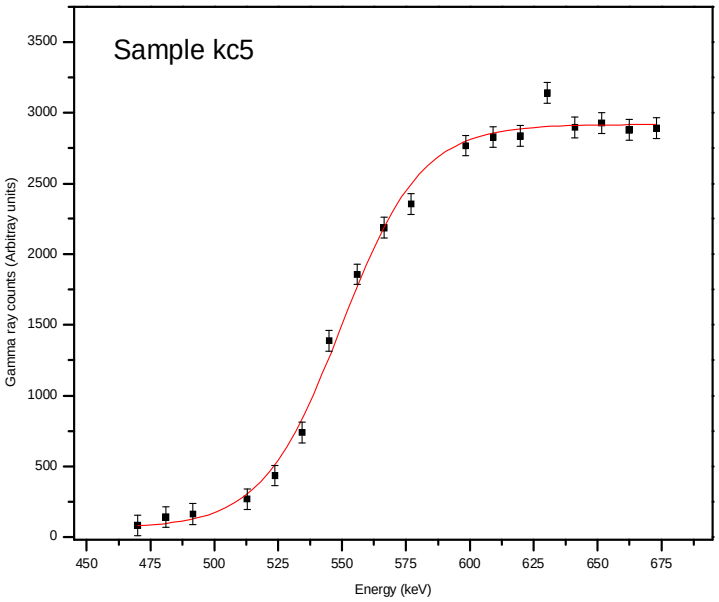


Figure 3.19: Gamma ray profile from sample kc5, which was a (111) surface that was not treated with the ^{13}C-labelled oil. It shows the step function yield of the 1.11% ^{13}C atoms contained in all natural diamonds.

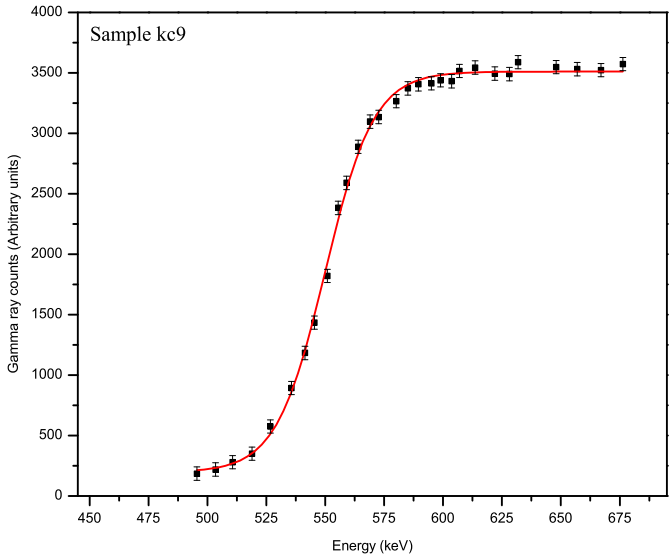


Figure 3.20: Gamma ray profile from sample kc9 which was a (111) surface that was untreated with the ^{13}C-labelled oil. This yield profile corresponds to the 1.11% ^{13}C atoms contained in all natural diamonds.

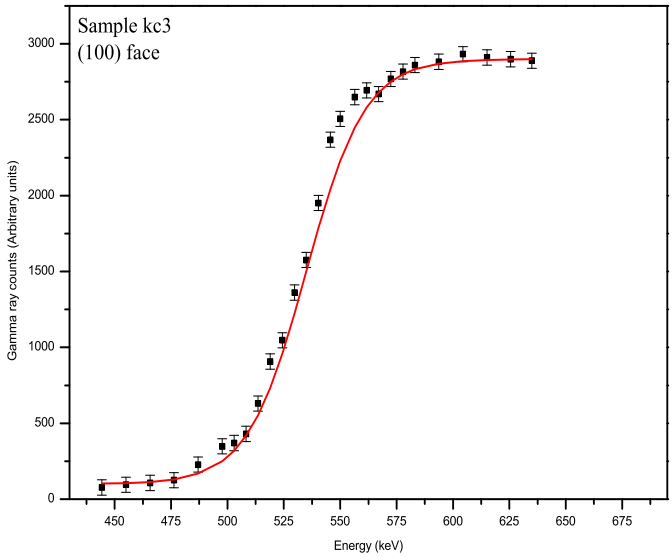


Figure 3.21: A plot of the gamma ray yield profile from sample kc3, which was a (100) surface treated with ^{13}C.

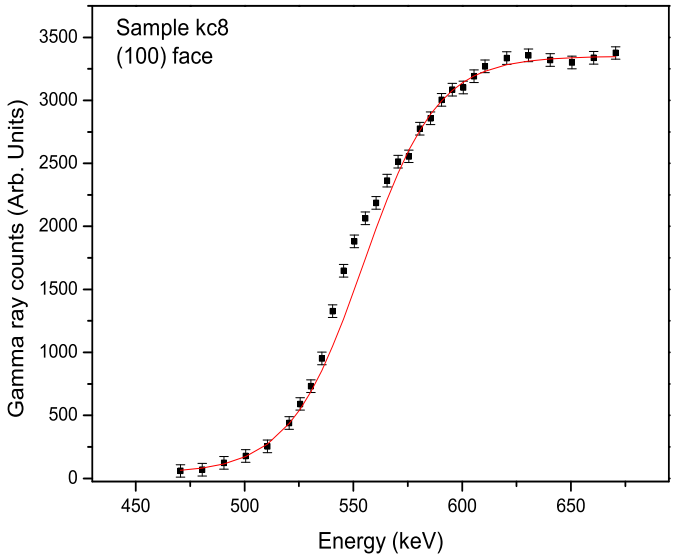


Figure 3.22: Gamma ray yield from sample kc8, which was a another (100) surface treated with ^{13}C.

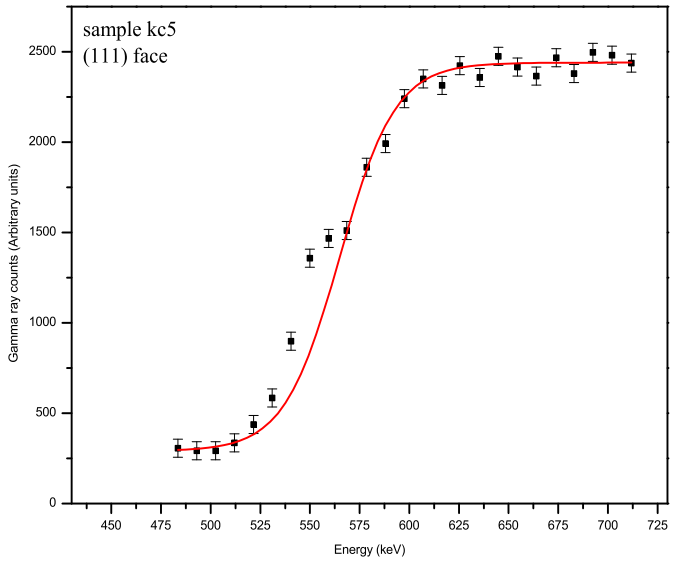


Figure 3.23: Gamma ray yield from sample kc5, which was a (111) surface treated with ^{13}C.

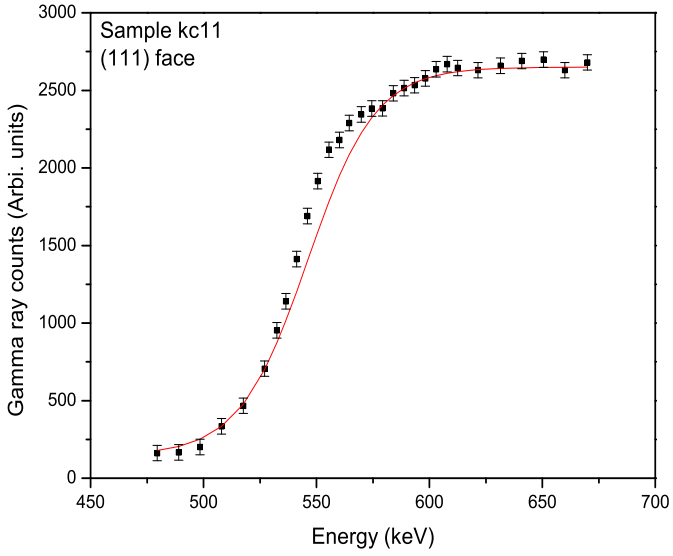


Figure 3.24: Gamma ray yield profile from sample kc11, which was a second (111) surface treated with ^{13}C.

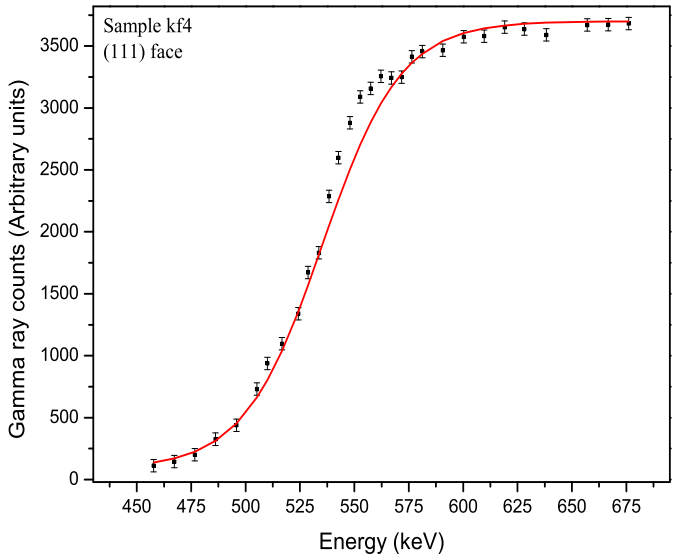


Figure 3.25: Gamma ray yield from sample kf4, which was yet another (111) surface treated with ^{13}C.

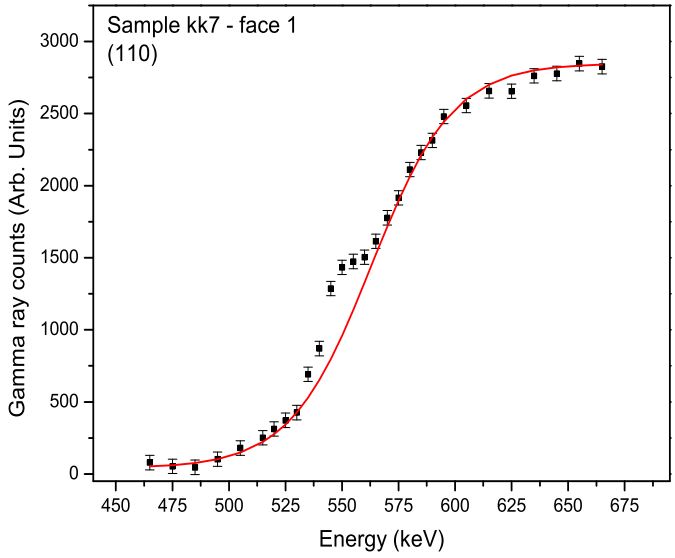


Figure 3.26: Gamma ray yield from sample kk7, which was a (110) surface treated with ^{13}C.

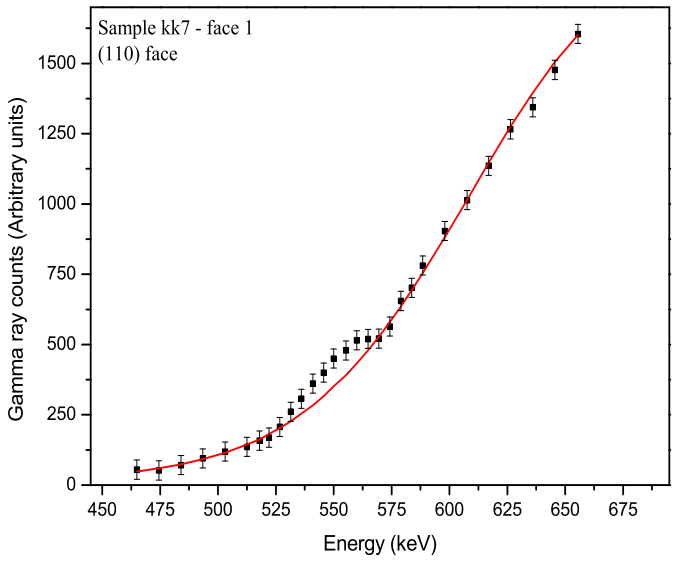


Figure 3.27: Gamma ray yield profile from the opposite side of the (110) surface whose profile is shown in figure 3.26, which was also treated with ^{13}C.

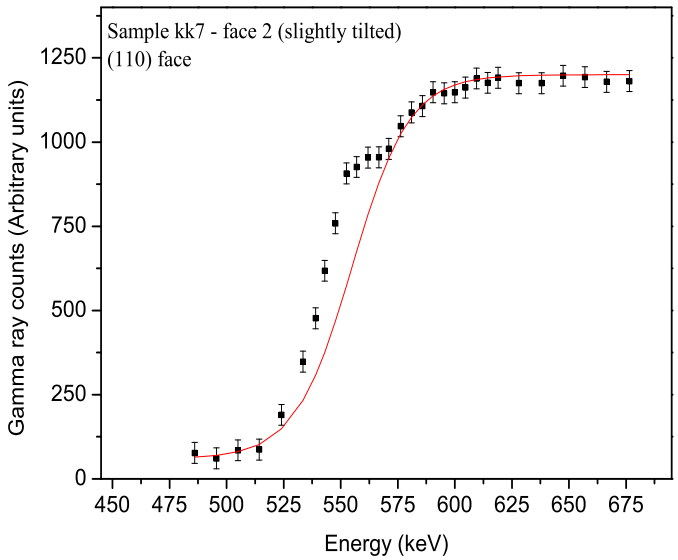


Figure 3.28: Gamma ray yield from the same (110) surface as in figure 3.27 which was treated with ^{13}C, but with the face slightly tilted relative to the proton beam axis.

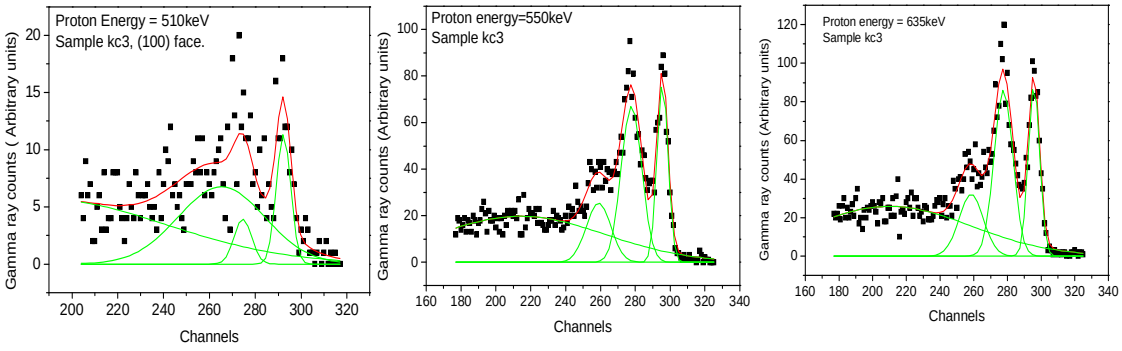


Figure 3.29: Some examples of the three gamma ray peaks obtained as the proton energy was progressively increased. Note the difference in the vertical scale.

All the yield profiles, showed that the gamma ray counts were extremely small at low proton energies, especially below ∼515keV. This was due to the fact that the Coulomb barrier of the nuclear reaction had not yet been overcome. A sharp increase in the gamma ray counts then followed as the resonance energy was approached and passed, reaching a saturation plateau that corresponded to the gamma ray counts from the 1.11% bulk ^{13}C. At high energies, the protons were energetic enough to travel deep into the diamond matrix, thereby exciting nuclear reactions from the bulk ^{13}C atoms. Any further increase in the proton energy was not expected to increase the gamma ray counts, and thus the reason for the saturation plateau which remains more or less constant. Figure 3.29 shows illustrations of some typical gamma ray peaks collected as the proton energy was gradually increased. Owing to the fact that the resonance energy of the nuclear reaction used in this study was clearly known and also well isolated, an initial (narrow) scan within a small energy range very close to the resonance energy was made for some samples. This was intended to verify experimentally whether or not any surface sputtering of the surface-bonded ^{13}C atoms occurred, since earlier TRIM simulations had predicted that no such surface sputtering was expected to occur. If negligible or no sputtering of the bonded surface ^{13}C

atoms occurred, then a repeated scan at the same proton energy was expected to yield similar numbers of gamma ray counts as the previous one. The results, though few, confirmed that no surface sputtering or displacement of the surface-bonded ^{13}C atoms occurred. Lack of proton-induced sputtering on diamond surfaces has also been reported by da Rosa *et al.* [174] and this means that the results are very reliable especially for thin targets involving the first top monolayers of a solid, as well as the near surface region.

After the narrow (short run) scans, complete scans were then made on the respective samples ranging from about 445keV to 680keV at varying energy-step intervals. From these, the nature, shape and size of the gamma ray yield for the ^{13}C-treated diamond surfaces, well below and above the resonance energy of the 550keV $^{13}C(p,\gamma)^{14}N$ nuclear reaction was obtained. Although the number of gamma ray counts at low proton energies was extremely small as seen from the first panel of figure 3.29 and also from the yield profiles shown in figures 3.19 to 3.28, one may be tempted to imagine that the areas under the gamma ray peaks would be characterized by higher errors, but instead the absolute errors were generally small. Following the tabulation of the gamma ray counts against the proton energy, and the plotting of the data points, the Boltzman distribution step function was used to fit these, in order to obtain the desired γ-ray yield profiles. The fit ensured that the error at all the respective energy points was evenly distributed over the entire energy range, which explains why the error bars are all equal in any given spectrun. The size of the error bars was one standard deviation of the values considered at a given proton energy.

3.15.1 Number of ^{13}C atoms transferred onto the polished diamond surfaces.

To determine the number of ^{13}C atoms transferred from the lubricant to each of the polished diamond surfaces or the areal density, the corresponding ^{13}C

Table 3.1: ^{13}C atom coverages on clean diamond surfaces expressed as areal densities and monolayer coverages.

Sample name & Sample Face	Number of ^{13}C atoms(atoms/cm^2)	Expt. areal density of ^{12}C (atoms/cm^2) [94]	Monolayers) (ML)
(kc3)- {100}	1.36 x 10^{15}	1.57x10^{15}	0.9
(kc8)- {100}	1.73 x 10^{15}	1.57x10^{15}	1.1
(kk7-face1) - {110}	2.32 x 10^{15}	2.11x10^{15}	1.1
(kk7-face2) - {110}	1.94 x 10^{15}	2.11x10^{15}	0.9
(kk7-face1) - {110}	0.644 x 10^{15}	2.11x10^{15}	0.3
kc5 - {111}	1.43 x 10^{15}	1.82x10^{15}	0.8
kc11 - {111}	1.89 x 10^{15}	1.82x10^{15}	1.0
kf4 - {111}	1.70 x 10^{15}	1.82x10^{15}	0.9

surface peaks shown in figures 3.30 to 3.37 were extracted from the respective gamma ray profiles shown in figures 3.19 to 3.28. The extracted experimental data was then fitted with the Breit-Wigner distribution function which made it possible to determine the experimental width of the nuclear reaction as well as the distribution of the surface-bonded ^{13}C atoms. The Breit-Wigner fits were made using Origin version 6.1 [175] which is a computer program with various features that are easily adaptable to the fitting process. The same size of error bars used in the γ-ray yield profiles was also applied to the corresponding extracted surface ^{13}C peaks.

Using equation 3.14.5 together with the number of gamma ray counts obtained from the areas under the extracted ^{13}C surface peaks, the number of ^{13}C atoms per unit area (areal density) on each of the respective low index diamond surfaces was determined. These are shown in Table 3.1, wherein they are expressed as both areal density and as monolayers. The monolayer coverages were obtained by comparing the coverages expressed as atoms/cm^2 with the known areal densities of ^{12}C atoms on each of the respective diamond faces, as shown in Table 3.1

A value of 0.1178keV/nm was used for the electronic stopping power of protons in diamond at the resonant energy of 550keV when determining the areal

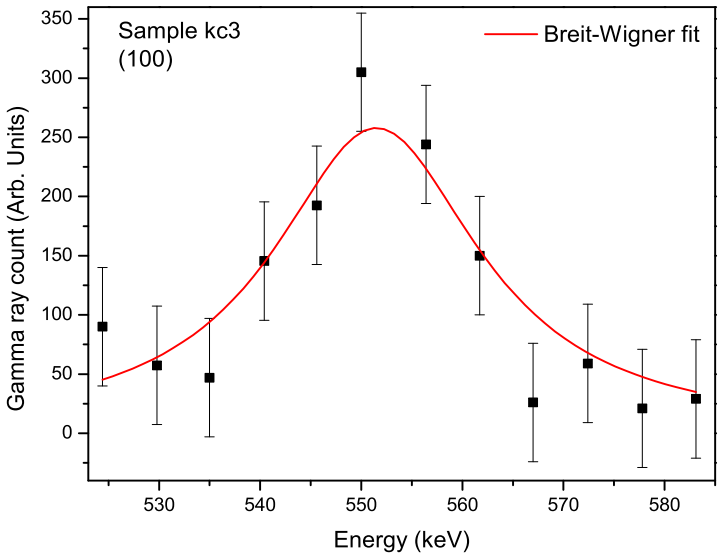


Figure 3.30: Carbon -13 surface peak for a (100) surface, extracted from figure 3.21.

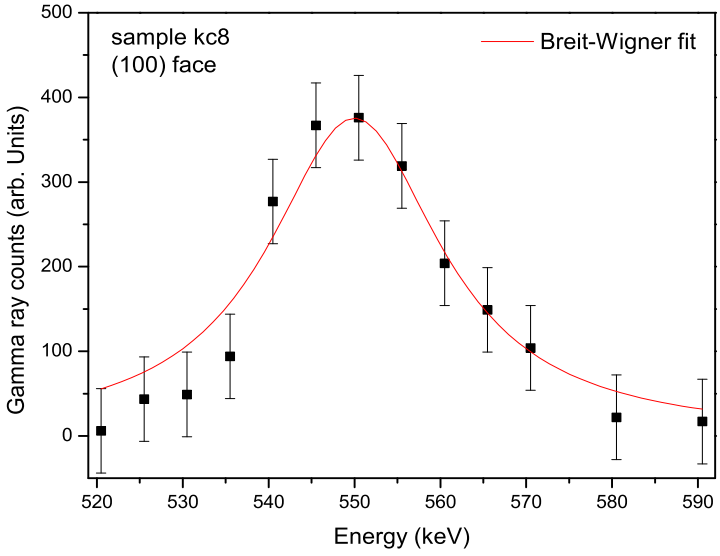


Figure 3.31: Carbon -13 surface peak for a (100) surface, extracted from figure 3.22.

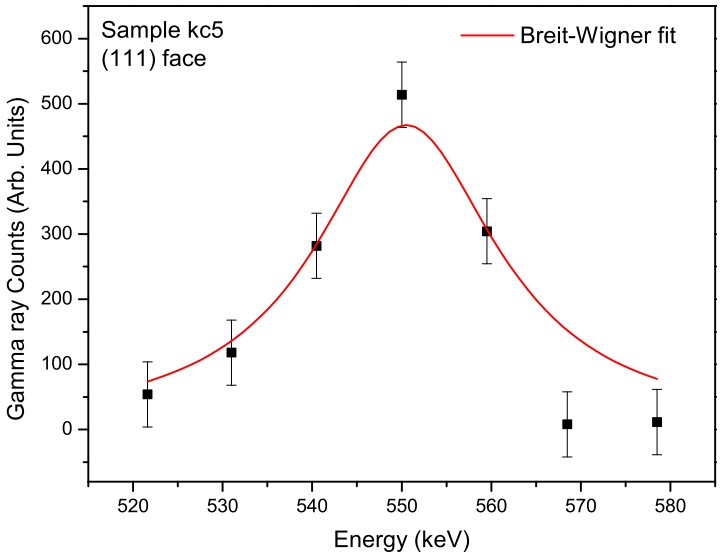


Figure 3.32: Carbon -13 surface peak for a (111) surface, obtained from figure 3.23.

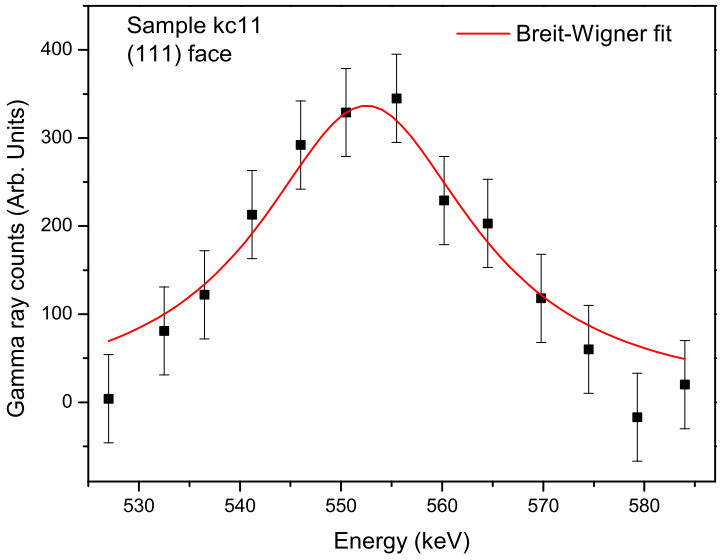


Figure 3.33: Carbon -13 surface peak for a (111) surface, obtained from figure 3.24.

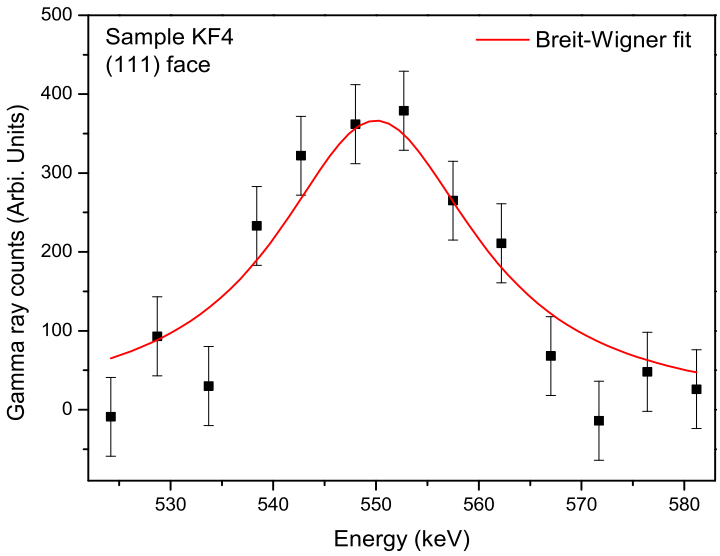


Figure 3.34: Carbon -13 surface peak for a (111) surface, extracted from figure 3.25.

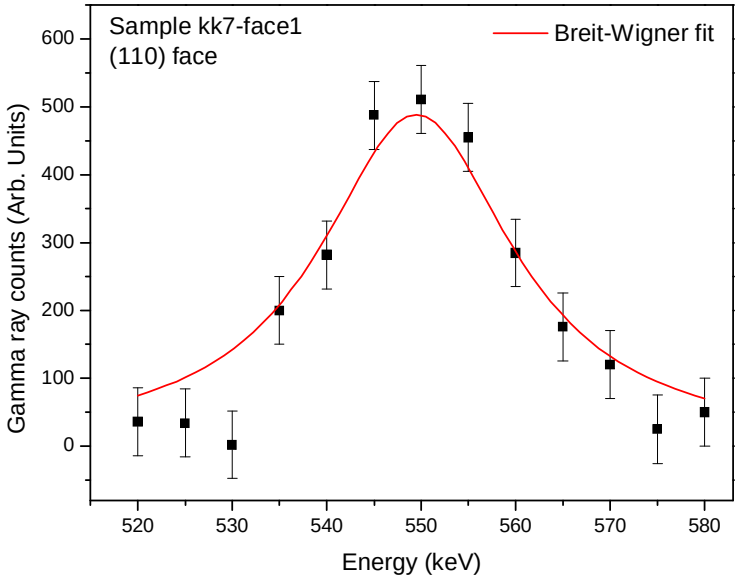


Figure 3.35: Carbon -13 surface peak for a (110) surface, obtained from figure 3.26.

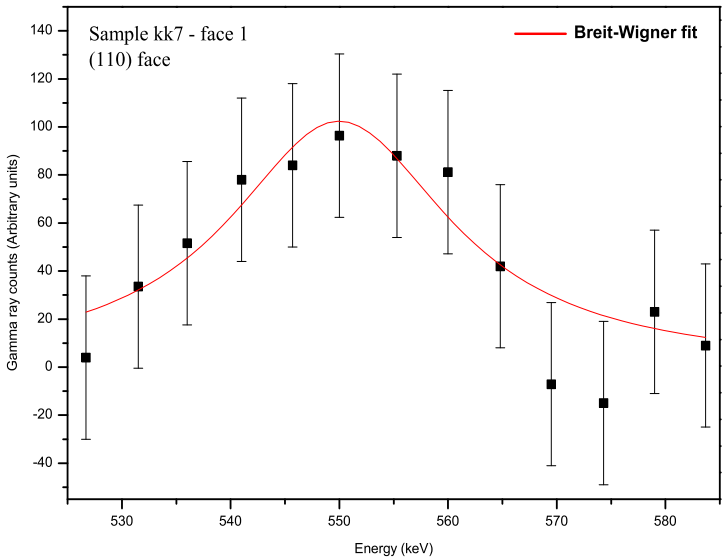


Figure 3.36: Carbon -13 surface peak for a (110) surface, obtained from figure 3.27.

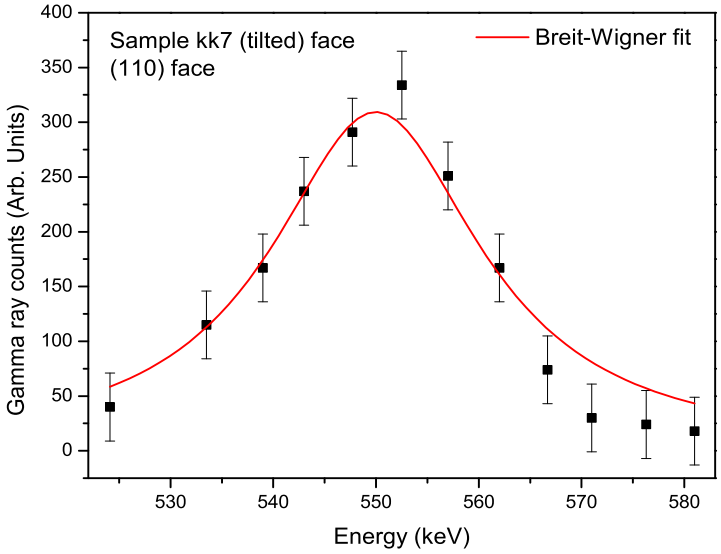


Figure 3.37: Carbon -13 surface peak for a (110) surface, obtained from figure 3.28.

densities. This value was obtained from a TRIM simulation, and it was considered to be generally constant over the small energy range of the experiment, and therefore significantly representative over the desired range of interest. Omitting the smallest value of the monolayer coverage (0.3) shown in Table 3.1, an average value of 0.9±0.1ML was obtained for the number of ^{13}C atoms transferred from the polishing lubricant to the surface. The error in this case was one standard deviation of the values considered when determining the average monolayer coverage.

Table 3.1 further shows that the ^{13}C coverage on most of the faces was close to a monolayer. This was a relatively high coverage, implying that the topmost carbon atom layer was actually constituted of ^{13}C atoms that were derived from the polishing oil and not the diamond. As a result, we postulate that whenever diamond surfaces are polished with oil, transfer of atoms from the lubricant to the diamond surface occurs in such a way that the topmost layer is donated by the polishing lubricant.

In addition, a deconvolution of the Breit-Wigner-fitted surface peaks gave the values of the full width at half maximum (FWHM) of the 550keV ^{13}C(p,γ)^{14}N resonant nuclear reaction, which are shown in Table 3.2 for each of respective low index diamond faces that were investigated. The observation of only a full ML of ^{13}C atoms that was transferred onto the polished diamond surfaces through the procedure described previously confirmed that this constituted probably the thinnest surface layer that can possibly be made. This therefore had the consequence that the experimental width of the nuclear reaction thus obtained was bound to be quite accurate.

Table 3.2: Full width at half maximum (FWHM) values for the 550 keV $^{13}C(p,\gamma)^{14}N$ resonant nuclear reaction.

Sample Face & Sample name	Full Width at Half Maximum(FWHM)
{100}-kc3	25.0
{100}-kc8	24.6
{110}-kk7 face 1	25.0
{110}-kk7 face 1 (repeated)	25.0
{110}-kk7 face 2 (tilted)	25.0
{111}-kc5	25.0
{111}-kf4	24.0
{111}-kc11	26
Average	25±1keV

3.16 Discussion

The tiny parasitic peak that was observed riding on the background spectra close to the resonance energy (550keV) in figures 3.21 to 3.28 was a clear evidence of the transfer of carbon-13 atoms onto each of the three low index diamond surfaces after repolishing with the olive oil labelled with 99% ^{13}C. On subtraction of the background spectra, the tiny peaks gave rise to the surface peaks illustrated in figures 3.30 to 3.37, which was again a clear testimony of the atomic transfer from the lubricant to the repolished diamond surfaces. In addition, it is important to note that, while hydrogen as deuterium has been shown to exchange freely with diamond-like surfaces, carbon does not [176]. Instead we find evidence only of direct bonding during polishing.

This is a rather interesting outcome because the possibility of being able to transfer atoms onto the repolished diamond surfaces has direct consequences to the final applications of such surfaces, and it further shows that there is a high chance of modifying them through bonding with different atoms. Our study suggests that, this can actually be realized by polishing them with a medium containing the desired foreign atoms. The implication of such a finding is that certain surface properties could be altered through this process, suggesting that

immense potential exists as far as many surface applications are concerned [22, 131]. In particular, one might engineer the coverage of a given surface to achieve some intended properties, for example changing the electron affinity, resistance or response to the environmental agents, as well as adhesion to other surfaces such as the already reported adsorbents for blood plasma cleaning on diamond surfaces [177] or even the surface properties of medical devices [178] among many other applications. This becomes even more important when one considers the fact that the operation of most semiconductor devices depends very strongly on the properties and nature of the surface as well as the interface with ohmic contacts. The findings of Koslowksi *et al.* [48] that the morphology of surfaces and interfaces influences quite significantly the resulting properties of devices whose performance is based on multilayers prepared on top of each other, lends more credence to the role of foreign atoms on diamond surface. This is informed from the point of view that their presence on such surfaces or interfaces does modify the devices' response in a number of ways. We therefore propose that novel surfaces or even nanostructures may actually be formed on diamond surfaces, through this way. Already, various authors [179] have observed the attachment of various organic compounds on diamond surfaces, a process which is achieved through different approaches.

However, while such atom transfer may yield benefits in certain aspects of surface applications, the same phenomena could lead to undesired results in others, especially if one is not aware of the fact there is an exchange of atoms taking place between the polishing medium and the surface being polished. Such an eventuality could very easily compromise the performance of many devices. Information regarding the surface preparation, its eventual nature (as discussed in the atomic force and optical microscopy chapters) and other phenomena such as the atom exchange between the surface and the lubricant as mentioned previously is therefore vital. This makes it easier not only to understand the

properties of the devices prepared out of such surfaces, but also to manage and control them better. One could for example choose to eliminate the foreign atoms altogether, or better still, make use of them if they are essential to the application for which the device made is intended.

In some applications, bonding between a coating and the substrate could be greatly enhanced by the presence of the desired surface atoms, while in other cases this could lead to failure if undesired atoms are present on the surfaces. This is especially vital for diamond, because it has lately been used as a heat sink for a number of semiconducting devices, while over the years it has been used traditionally as a hard coating of cutting tools. In both of these applications, better results can only be achieved if the adhesion at the interface is good. On this particular aspect, Caveney [180] points out that if care is not exercised on the interfacial bonding procedure, the benefits of using diamond heat sink can be completely negated. As such, any undesired foreign atoms introduced through polishing and hence existing at the surfaces or interfaces may compromise the mechanical and electrical properties of the device and therefore its overall performance, leading to failure, especially in high-tech, harsh or critical applications. These examples, though not exhaustive allude to the fact that foreign atom transfer onto surfaces during polishing plays an important role, regarding their final applications.

While most surfaces showed coverages that were close to a monolayer, a slight difference between the actual numbers of ^{13}C atoms transferred onto the three low index diamond faces was observed, as seen from figures 3.21 to 3.28, as well as the surface peaks shown in figures 3.30 to 3.37. However, although this variation may just have been statistical, these differences become more significant when one considers them in terms of the areal densities and not monolayers. This is because the experimental error, which is the standard deviation of the values considered in Table 3.1 (omitting the last coverage of

0.3ML from sample kk7) is found to be 3.2×10^{14}atoms/cm^2. Although small, this is a rather significant value with regard to other processes such as the electronic doping of surfaces. It is also interesting to note that even for surfaces having the same orientation, the number of ^{13}C atoms transferred was slightly varied, an observation that can readily be attributed to possible differences arising from the surface preparation procedures for each individual face. Based on this, one can conclude that, although all the surfaces were prepared following the same procedure, it appears that no single surface was exactly identical to another, and probably the wear mechanisms during polishing were also different. An important aspect that may be responsible for these minor differences is that the polishing direction usually remains constant during the mechanical polishing, while in the manual polishing it may alternate between the hard and soft polishing direction due to the difficulties associated with the polishing process itself. This could alter the surface's quality (though marginally), which may in turn translate into the creation of suitable bonding sites for certain species. However, since the areal densities were of the same order of magnitude for most of the faces, these differences were nonetheless expected to be quite small indeed.

For those faces which had the same orientations, these differences (observed in their areal densities) were relatively smaller as compared to those observed on surfaces with different orientations, with the exception of the last {110} face shown in Table 3.1. As such, when the little differences were amplified and then considered in terms of the respective orientations, it was found that both the {100} and {111} faces showed a consistently higher relative areal density, followed quite closely by the {110}. This variation is once more associated with the available bonding sites on each face. In spite of this, with an average value of 0.9 monolayers (or $\sim$1 monolayer) and an experimental error of 0.1 monolayers, the ^{13}C monolayer coverages were practically the same for all the three low index

faces. This coverage was independent of the duration of the polishing when a moderate hand (manual) force was applied between the diamond surface and the polishing metal block. One can thus speculate that the same coverage would be obtained even if a higher force was applied, as was the case in the mechanical polishing, since the bonding was driven by the availability of suitable bonding sites and again no packing of the ^{13}C atoms layers was expected. In addition, it was unlikely for clumping to occur on strongly covalent surfaces, while previous work indicated that there was no free exchange of labelled carbon atoms near diamond surfaces [176]. As a result, distribution in depth was clearly ruled out.

Initial analysis showed that the beam was falling on an irradiated area of 2mm diameter, which was evidently large enough to contain many surface features. In addition, the fact that some faces were easier to polish than others in certain directions seems to support the suggestion that surface features did play a crucial role as far as the number of ^{13}C atoms transferred was concerned. The faces that were easy to polish were expected to have relatively broad and well-oriented terraces with occasional steps. As such, they would generally present fewer surface features, meaning that they were better quality surfaces compared to those obtained through polishing in the hard direction. Couto *et al.* [56] have further shown that surfaces prepared through polishing in the easy directions posses grooves that have smooth bases. Since the steps, slopes and other surface features may have a higher concentration of dangling bonds around them, it follows that faces with less of these would have fewer sites for high dangling bond concentration. As a result, there was a high possibility that the two polishing directions (hard and soft) would give rise to different numbers of transferred ^{13}C atoms, albeit small.

The {110} faces presented the widest variation of the ^{13}C coverages amongst all the three low index faces in spite of the fact that similar surface preparation procedures were applied. This was however not entirely suprising since it was

previously established that the mechanically polished (110) faces and generally most non-(111) surfaces may contain facets having the (111) orientation [178]. This means that strictly speaking, one is not necessarily investigating any one true orientation, but rather surfaces that also had other smaller different facets on them. The development of these is driven mainly by the natural cleavage of diamond along the {111} planes. Pickett *et al.* [181], indeed points out that a (111) polished surface might well contain not only simple steps, but also regions of disordered carbon and microfacets of other low index faces. Our AFM images showed that the (110) faces had wider and sometimes deeper polishing grooves than the other two low index faces, suggesting that the rate of material removal was possibly higher, and therefore the polishing was more effective. The sides of these large grooves could in some way expose other facets.

Based on the prevailing surface thermodynamic processes, it was to be expected that the oleic acid molecule or its fragments would bond preferentially at the favourable sites in such a way that all factors governing its equilibrium position onto the diamond surfaces such as steric hindrance, were adequately fulfilled. Most of the faces showed similar ^{13}C coverages and since it is not easy to diffuse atoms into the diamond bulk [182] the only likely possibility for the interaction between the oleic acid molecule and the diamond's dangling bonds was one whereby, if further adsorption was forced, no more ^{13}C atoms would bond onto the surface. It may therefore be possible that a saturated coverage is achieved when no more dangling bonds are available and this optimum value is maintained since any further bonds that would be broken will be instantaneously saturated by an equal number of ^{13}C atoms. The polishing oil therefore acted as a reservoir for the ^{13}C atoms, and when saturation was achieved, the repulsive force keeping the atoms apart may hinder any further adsorption.

From the principles of particle-solid-interactions, when a light particle like a proton is incident perpendicular to a crystal lattice, it may interact with the

host atoms located at a lattice or an interstitial site, or alternatively, it can pass into the channels between the atomic rows. The (110) surface has the biggest size of the channels between the atomic rows, followed by those of the (111) face and least of all the (100) face, as seen from figure 3.10. The presence of such channels, which are referred to as the <100>, <111> and <110> axial channels herein respectively, means that there is a higher probability of channelling of the proton beam into the (110) face as opposed to the other two low index faces. As a result, since channelling means lower nuclear encounters and hence fewer gamma rays per distance, low bulk gamma ray yields would generally be recorded in those cases where some channelling occurs. This is clearly illustrated in one of the profiles associated with a (110) face, shown in figure 3.27 and its corresponding ^{13}C surface peak shown in figure 3.35. The distance scale in this case depends on the electronic stopping which is almost constant for channelled ions. The channelled protons would then travel deep into the diamond matrix, and excite few ^{13}C atoms, resulting in decreased background. As such the whole gamma ray profile becomes depressed over the desired energy region as shown in figures 3.27 and 3.28. However, the beam can interact with all the surface atoms and so the surface peak should be almost the same size and within the expected position. Exceptions would only occur when the effects of the large channels associated with the material's bulk are extended to its surface.

Owing to the channelling effects, the number of gamma ray counts was found to be consistently lower for two cases involving the (110) surface (figures 3.27 and 3.28), where the bulk 1.11% ^{13}C saturation point was not even achieved at all, as compared to the other surfaces (figure 3.27). It is worth noting that no attempt was made initially to mis-align the surfaces off the perpendicular orientation with the incoming proton beam to avoid effects of channelling for all the spectra shown in figures 3.21 - 3.27, except in the case shown in figure 3.28.

To correct for the channelling effects, a small tilt (<1°) was applied to one of the (110) faces (figure 3.28), relative to the incoming proton beam. However, although the overall number of gamma ray counts improved slightly when compared to those of the other (110) faces (figure 3.27), they were still low, even at the bulk saturation point corresponding to the 1.11% ^{13}C atoms. In addition, although the saturation point was achieved after tilting the sample slightly, the total gamma ray counts at saturation was still relatively lower than those of the other cases involving the (100) and (111) faces, meaning that the effect of channelling may not have been eliminated significantly. This suggested that by tilting the face, we probably only succeeded in moving from axial to planar channelling. Interestingly though, a repeat scan on the opposite face of the same sample which was also a (110) face (figure 3.26) resulted in much higher gamma ray counts, implying that the observed differences could not wholly be generalized to a specific orientation, unless the surfaces were exactly identical, including their mounting onto the sample holder, which may not be too practical.

Nonetheless, it should be noted that a small orientation difference between opposite surfaces could result in a large difference in channelling, especially when one considers the fact that the critical angle for 0.6MeV protons is only 0.7° and below [7].

It may also be important to point out that while investigating oxygen adsorption on polished diamond surfaces as reported in the XPS chapter, one case involving the (110) face was also found to have a significantly lower amount than all the other orientations. Such observations confirm that the nature and even the subtle differences of the surfaces such as the numbers of surface features or defects contained play some role towards this effect. In particular, steps have been said to result in some atomic ordering due to the excess charge that exists at those sites. This, leads to processes such as repulsive interaction, which may

in turn prevent the molecule's atoms from bonding close to each other, and hence possibly resulting in lower coverages than expected [4].

From the yield profiles shown in figures 3.21 to 3.28, it was observed that the parasitic surface peaks did not occur at exactly the same place at the inflection point, especially when considered relative to the saturation counts. Sometimes, their positions occurred closer to the top of the saturation point as seen in figures 3.21, 3.24 and 3.25, while in other cases like those shown in figures 3.22, 3.23, 3.26, 3.27 and 3.28, it was shifted and occurred at a slightly lower value relative to the saturation point.

This apparent shifting was not an artifact, but rather a real effect that was caused by the background counts associated with the bulk ^{13}C atoms contained within all natural diamonds, which are also believed to be randomly distributed within the matrix. In this case, the effect of high background counts was to add on to the actual counts from the surface bonded ^{13}C atoms, resulting in the peak position being shifted much lower than it should be, relative to the step function's saturation point. Using a similar argument, a lower background would result in the peak occurring much closer to the spectrum's saturation point. However, in spite of the shift, it was observed that the surface peak always occurred at about 550keV, which was the resonance energy of the ^{13}C(p,γ)^{14}N nuclear reaction. This confirms that the apparent shift was mainly due to the amount of background that was changing and not necessarily the peak shifting. As mentioned previously, channelling is one of the major factors that can lead to the reduced background.

3.16.1 Full Width At Half Maximum (FWHM) of the 550keV ^{13}C(p,γ)^{14}N resonant nuclear reaction.

Following the fitting of each of the surface peaks with the Breit-Wigner distribution function, an average value of the FWHM was found to be 25$\pm$1 keV

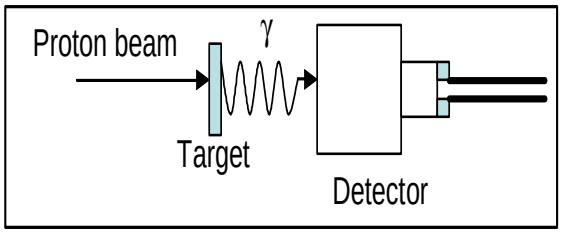


Figure 3.38: Gamma ray detector geometry.

as shown in Table 3.2. This value was in good agreement with the findings of certain others [172, 183], and it also confirms our earlier suggestion that the ^{13}C surface layer was generally thin. The value was however at variance with some others as noted in [184] and the explanations for this are given below.

It was felt that the observed nuclear width was greatly influenced by the way in which the beam of the energetic particles interacted with the target atoms. According to Hodgson *et al.* [153] two waves would be observed if a reaction takes place through the compound nucleus. These are the s and p waves, with the isotropic s-wave being the main contributor to the interaction process, and the p-wave contributing much less according to our sample-detector geometry. Edmund A. Milner [185]on the other hand observes that experiments involving the capture gamma-rays as well as the radiative cascade measurements show that the 8.06MeV level in ^{14}N formed by protons of 0.56MeV is formed by s-wave protons. Figure 3.38 shows the sample-detector geometry that was used in our experiments. From their experiments, Galster *et al.* [183]observed that the width of the nuclear reaction was composed of partial widths that were constituted of the s-wave contribution measuring 26keV and a d-wave contribution of 7keV. Since any effect would only add on to the broadening of the nuclear reaction's width, one would expect that the values that we observed for the nuclear reaction width to be the very minimum, being constituted mainly

of the s-wave, and very little of the p-wave contribution.

3.17 Stereo-chemical bonding of the oil molecule with the diamond surface.

Two possible mechanisms by which the oil molecule bonds with the dangling bonds on the diamond surface are suggested here. These include bonding via the oleic acid molecule's unsaturated double bond or its carboxylic functional group that terminates one end of the molecule as seen from figure 3.39. Both of these are active sites, and therefore are expected to participate and compete in the bonding process.

When the diamond surface's bonds are broken during polishing, the surface can for all practical purposes be considered to behave like an electrophile (i.e a species that seeks out negative centres). As such, this would require an electron to share so that the dangling bonds are saturated, and the obvious donor would be the double bond of the oleic acid molecule. A visualization of this process is illustrated in figure 3.39, where the ^{13}C atoms are depicted with red, C symbols, R is an organic chain $(CH)_n$ and C^+ indicates a dangling bond on the diamond surface. Through this process, the oleic acid molecule saturates its own double bond, as well as the diamond's dangling bonds. A closer look at this bonding process seems to reveal that the oleic acid molecules are not very closely packed on the surface. Additionally, the bonding of the oleic

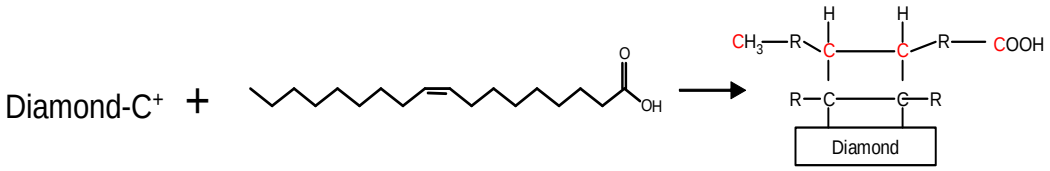


Figure 3.39: Process by which the oil molecule may bond with the diamond surface.

acid molecule onto the diamond surfaces may be achieved either dissociatively or molecularly, depending on the enthalpy of adsorption. However, while this mechanism seems quite likely, it is still not clear whether the molecule bonds onto the surface as a whole entity or breaks down before bonding into smaller units or even whether it bonds as individual atoms. One can still speculate that a combination of all these processes may take place, especially in view of the fact that the pressure and frictional forces existing between the diamond surface, the lubricant, the diamond paste and the metal block as the polishing proceeds could actually lead to the breakdown of the molecule.

Although the pressures developed at the point of contact during the manual polishing do not approach those observed during the mechanical polishing, it is still worth noting that temperatures in excess of about 300°C [54, 186] are routinely developed during mechanical polishing in the soft directions. As such, with a boiling point of 300°C [187], and probably lower chemical breakdown temperature, the oleic acid molecule is likely to experience breakdown at temperatures typical of the mechanical polishing (if it were to be used there), and therefore the break down (or decomposition) of the molecule cannot be ruled out when polishing is done under such conditions. In addition, although no evidence exists, there is no reason not to speculate that the molecule may actually break down during manual polishing too.

On the other hand, although oleic acid is a relatively weak acid, the carboxylic functional group that it carries is also an active site and therefore may be expected to compete favourably for the dangling bonds created on the diamond surfaces, with those of the molecule's unsaturated double bonds. Sappok *et al.* [188] have shown that an oxygen-terminated diamond surface is hydrophilic, and our studies reported in the XPS chapter further showed that diamond surfaces prepared using the technique that was applied in this work were indeed terminated by a fractional monolayer of oxygen. Therefore, if we consider the

participation of the carboxylic site in the bonding process, we can imagine the bonding to proceed via an initial substitution of the hydroxyl hydrogen, in a similar way as it bonds to a polar molecule. Such a bonding process has also been observed when oleic acid molecule bonds onto a water molecule [189]. Through its hydrophilic and hydrophobic ends, the oleic acid molecule bonds onto water in such a way that it sticks upright, since the hydrophilic end gets attached to water while the hydrophobic one does not. Through this process, and also assuming that the dangling bonds on the diamond surface will behave like a strong electrophile, it will attack the nucleophilic oxygen (i.e a species that seeks out positive centres) atom at the carboxylic site of the oleic acid molecule, so that it directly gives a positively charged intermediate which then looses a proton as shown in the equation below, with the acid molecule being represented as RCOOH.

RCOOH+Diamond surface(with dangling bonds acting as strong electrophile)$\longrightarrow$ RCOO-Diamond surface+H^+

The proton then bonds with the oleic acid molecule double bond, or even a dangling bond on the diamond surface. Through such a process, both the diamond's dangling bonds as well as the oleic acid molecule's double bonds get satisfied.

It is also very likely that both these two bonding mechanisms, involving the oleic acid molecule's double bond as well as its active carboxylic site, would participate in the bonding of the oil molecule's atoms onto a diamond surface simultaneously; maybe on an equal basis, slightly or even completely different. Such variations would depend generally on the underlying surface thermodynamics [190], whose role is beyond the scope of this work, but nevertheless is intertwined in the entire bonding process. While considering the bonding process, it is vital to note that the oil molecule contains a relatively large number of hydrogen atoms. If these bonds break during the polishing and at the same

time those of the surface carbon atoms on the diamond surfaces also break, it would be expected that there will be competition to saturate these dangling bonds between the ^{13}C atoms and the hydrogen atoms. Owing to the high affinity of diamond surfaces for hydrogen [150], this competition is bound to be rather severe, especially in view of the fact that the oil molecule is itself short of hydrogen as mentioned before, and hence is not likely to lose its hydrogen atoms easily. This therefore makes it more likely for the ^{13}C atoms to bond onto most of the dangling bonds, and it may therefore explain in part why we find only a ^{13}C coverage of the order of a monolayer, and not more on the polished surfaces.

Strother *et al.* [179] reported a technique in which they were able to attach functionalized organic molecules onto polycrystalline diamond surfaces. In this case, they observed that the C=C group in one of the organic molecules was responsible for the attachment to the surface. They further detailed other cases where organic layers have also been formed via the photochemical reaction of perfluorobutyl iodide multilayers with hydrogen-terminated diamond surfaces, and by the electrochemical reduction of phenyl diazonium salts on diamond electrodes. Recently, close packing of polycyclic aromates was reported by Eremtchenko *et al.* [191] on metal surfaces. Though different structurally, such observations makes the case involving the attachment of the oil molecule onto the polished diamond surfaces even stronger. In a related case, Robert A. Freitas [178] has reviewed the attachment of large molecules on diamond, and in particular the adsorption of proteins on diamond surfaces, where they reported that protein adhesion at the molecular level does take place.

Polished diamond surfaces have also been reported to have a complex web of microcracks below them [192]. Some of these microcracks may even cross with surface cracks that may be created on the diamond surface during polishing. However, assuming that they don't cross with any surface cracks and

owing to the fact that they occur only below the surface, they may not provide any suitable bonding sites for the oil molecule to attach itself there. The fact that they are created in the subsurface region also means that they may not be accessible to the oil molecule at all. Any bonding sites that may be created below the surface via the microcracks in the form of free unsaturated bonds, would therefore be saturated preferentially by electron capture from the diamond's bulk electron cloud, and hence will not be available for the molecule's bonding. This again suggests that the microcracks do not play any role as far as the bonding of the ^{13}C atoms is concerned. This argument is further bolstered by the obvious lack of extremely large amounts of ^{13}C atoms at the surfaces as one would expect, if some oil molecules were to penetrate in to the microcracks, and get buried there.

In addition, the absence of any broadening of the nuclear reaction width (FWHM) arising from the high background from ^{13}C atoms bonded to sites such as microcracks seems to strongly support this view. This becomes even more convincing when one considers the fact that if the proton energy becomes high enough, they have the potential to travel deep into the material matrix and excite reactions from sites that are situated deep below the surface. This would include exciting nuclear reactions due to ^{13}C atoms residing at the microcracks, and hence resulting in excessively high numbers of gamma ray counts that in turn translate into a large number of ^{13}C atoms. This observation was lacking in our findings, and as a result we propose that the oleic acid molecule bonds with dangling bonds on the diamond surface through its unsaturated double bond, and its carboxylic active site, via the mechanisms explained previously. We also note that the oil molecules do not reside in the microcracks, if any.

Furthermore, although large cracks may also occur at the surfaces during their preparation, and hence be able to accommodate large amounts of oil

molecules in the form of non-diamond bonded ^{13}C, no effect of this was observed, meaning that either there were no such cracks on the surfaces being investigated or if any were present, these were extremely few and too small to accommodate any significant amounts of oil. This conclusion is also supported by the view that, if large cracks existed on the surfaces, they could extend and cross with the web of microcracks below the surface, resulting in the polishing oil being trapped in them. This would then result in relatively high gamma ray counts, an observation that was not made here, meaning that neither the surface cracks nor the web of sub-surfaces microcracks contributed to the observed gamma ray yield. As such, the possibility of any buried layer of ^{13}C atoms below the surfaces was effectively ruled out. Additionally, only one out of the six diamond surfaces that were considered showed a surface crack when viewed using an optical microscope at a magnification of 1000. This surface was however not repolished with the ^{13}C-labelled oil so as to eliminate the effects of surface cracks being propagated into the contributions of the observed gamma ray counts.

3.18 Conclusion

A surface ^{13}C peak was observed for every surface finished through repolishing with the labelled olive oil. This means that there was a transfer of carbon atoms from the polishing lubricant to the diamond surface during the repolishing process. The number of ^{13}C atoms recorded on all the three low index faces was found to average at about 0.9 ± 0.1 monolayers (or $\sim$1 monolayer), a value that was relatively large. This suggested that the topmost carbon atom layer on polished diamond surfaces comes from the polishing oil and not the diamond itself. Presumably, the top monolayer on all diamond surfaces, polished with lubricants that are not labelled, comes from the lubricant too.

In spite of the one monolayer coverage observed on most of the repolished diamond surfaces, one of them involving a (110) face showed a significantly low amount of ^{13}C atoms having been transferred on to it through the repolishing. This observation indicated a significant amount of channelling of the protons incident on to this face, and it may also mean that the surface quality was not entirely the same as that of the other surfaces, or alternatively it was generally not too good, after or before the repolishing. However, assuming that the mechanical polishing produced a good surface on account of previous LEED studies [117], then it implies that the repolishing may have either made the surface rougher, or alternatively made the previous grooves larger, wider or deeper, an aspect that is investigated thoroughly in the atomic force microscopy chapter. In spite of the abnormality observed in one of the faces where channelling resulted in depressed counts, we established that within experimental error, the number of ^{13}C atoms on all the three low index faces was effectively constant. However, a closer look at the surfaces seems to suggest that the transfer of the ^{13}C was slightly varied even for surfaces having similar orientations, implying that individual faces responded differently to the bonding of the oil molecule's atoms. This could partly be related to the minor differences occurring in the quality of the individual surfaces. As noted before, surfaces prepared following the procedure explained earlier have been shown to be well ordered with broad terraces containing grooves, and these are crossed by occasional steps, an observation that is confirmed elsewhere in this study by the atomic force microscopy work. Even for exceptionally carefully polished surfaces, Robert A. Freitas reports, that residual asperities of $\sim$5nm are typically observed [178]. Through his review work, he further reports that non-(111) surfaces when mechanically polished will always be rough and will consist of small domains of (111) surface canted at appropriate angles to the microscopic orientation. This appears to suggest that although the surface preparation procedure was often

the same, identical faces cannot simply be achieved, and therefore some sort of small differences will occur in the form of the obvious surface features such as steps, vacancies, terraces, grooves, edges etc. and their varied sizes will always be established. Nonetheless, this study found that their contribution towards the surface properties, and in particular the number of ^{13}C atoms transferred following the repolishing as in this case would be generally small and limited, to a point where they can be ignored in certain applications, although they are quite important in others as mentioned before. In certain instances, the small variations in the number of ^{13}C atoms transferred may actually be only statistical, since the surface sites with more favourable bonding configurations would be formed almost equally on all the three low index faces and hence the attractiveness of the molecule to bond there would also be uniform. This is especially so when one considers the fact that a large size of the sample surface ($\sim$2mm in diameter) was scanned. Additionally, although both the mechanical and manual polishing were done in the soft direction as evident from the polishing lines seen in the optical micrographs of some of the diamond faces presented elsewhere, the manual polishing may occasionally alternate between the soft and hard directions, leading to the formation of more unexpected surface features on the individual faces.

We also established that, while diamond surfaces prepared through mechanical polishing have been shown to contain a web of micro cracks below them, or at times some cracks at the surfaces, there was no evidence of the oil molecule atoms residing within the cracks or even microcracks. Instead, most of the ^{13}C atoms were bonded preferentially onto the diamond surfaces.

This study further showed that the average value of the FWHM of the 550 keV $^{13}C(p,\gamma)^{14}N$ nuclear reaction was 25$\pm$1keV, a value that was in excellent agreement with the findings of others [172, 183, 154]. This confirms that the

^{13}C surface layer was indeed thin, which supports our view that the very topmost layer on polished diamond surfaces was predominantly the foreign atoms donated by the polishing lubricant. The value of the FWHM was however at variance with those obtained by [193, 194, 195, 196, 197], and according to our geometry, it was concluded that the value obtained was mainly due to the isotropic s-wave as reported in Ref. [183]. The only difference between our value and those of other workers was the fact that they were observing contributions from both the s and other waves such as the p and d of the carbon atom. Curiously though, the carbon atom has only empty 3d and higher orbitals, and hence the actual rehybridization taking place wasn't quite clear. Additionally, no evidence of clumping was established in our studies, and therefore distribution in depth was clearly ruled out.

While the stereo-chemical details of the bonding process of the labelled olive oil molecule with the diamond carbon atoms, may not have been fully established, we propose through the arguments presented earlier, that the bonding should occur in such a way that the oil molecule's atoms are bonded in an equilibrium (thermodynamic) state to the diamond surface. This bonding process will most likely be driven by the double bond existing within the oleic acid molecule, and/or its terminating carboxylic group, which are both active sites. Each of the two processes will be governed by the existing surface thermodynamic processes, with the surfaces providing more favourable bonding sites being attractive for the oil molecule atoms to bond there.

The fact that actual atom transfer from the polishing media occurs, should be viewed as both an advantage as well as a disadvantage at times, as far as surface preparation for various applications is concerned. Such an observation means that unwanted foreign atoms could actually be introduced unknowingly onto the surfaces through polishing. On the positive side, novel surfaces including nanostructures could perhaps be prepared in this way. The importance of

such an outcome cannot therefore be overemphasized with regard to the various applications of diamond surfaces. It not only opens up a completely new way of looking at the specific or general surface preparation techniques, but also probably new opportunities for utilizing diamond and its subsequent properties after the polishing. This process of atom donation from the polishing lubricant may not just be unique to diamond surfaces, but could also possibly take place on other hard surfaces prepared through polishing in a similar way to that considered in this work.

3.19 Recommendations

It would be vital to investigate further the samples treated with the ^{13}C-labelled olive oil at elevated temperatures to establish if the ^{13}C monolayer found at room temperature would still be stable at these temperatures. It would also be interesting to remeasure accurately the nuclear width of the 550keV ^{13}C(p,γ)^{14}N resonant nuclear reaction, paying special attention to contributions from not only the s-wave but also the p and d-waves, in order to establish how it would compare with the one obtained from this study. The use of other labelled oils such as fluorinated ones may also be worth considering while repolishing the diamond or other similar surfaces.

Chapter 4

Optical Microscopy studies of the three low index polished diamond surfaces obtained using the Nomarski interference technique.

4.1 Layout of the chapter.

This chapter discusses results of the optical microscopy investigations of the three low index diamond surfaces that were polished mechanically and manually. These were obtained using a Carl Zeiss optical microscope, model Axiotech CL 25 HD at its highest magnification of x1000 [198], which is achieved by setting the objective lens at a magnification of x100 and the eye piece at a magnification of x10. It was fitted with a Carl Zeiss AxioCam (camera) for transferring images to a computer screen. The microscope was based at the School of Process and Materials Engineering, University of the Witwatersrand, and it was also fitted with a Nomarski interference facility that enabled the light rays to travel different distances. In so doing, the depth component of the polishing grooves was greatly enhanced. Before obtaining the optical micrographs, Laue x-ray images were acquired for the purpose of orienting the crystals. These are initially presented in the chapter, followed by discussions on the optical micrographs.

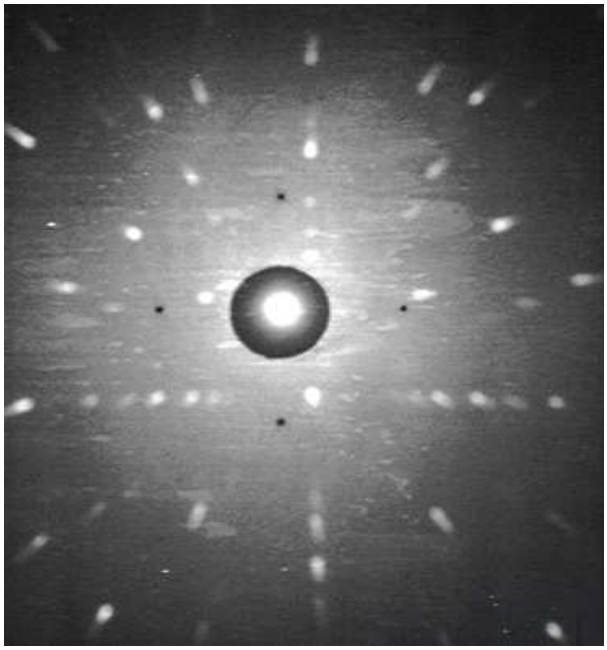


Figure 4.1: Laue x-ray image of a (100) diamond surface polished manually.

4.2 Introduction.

Laue images are often used to determine crystal orientations of various materials [199]. In this study, they were used to establish how close the final polished three low index diamond surfaces were to the expected true orientations. For this reason, three images were obtained, one for each of the three low index faces as shown in figures 4.1, 4.2 and 4.3.

After orienting the crystal surfaces according to the Laue images, optical micrographs for each of the respective three low index diamond faces were obtained as shown in figures 4.4 to 4.8. These were essential in establishing the overall surface quality following the manual polishing, especially at the highest resolution of the microscope, so as to establish whether small roughnesses were introduced or removed following the manual polishing.

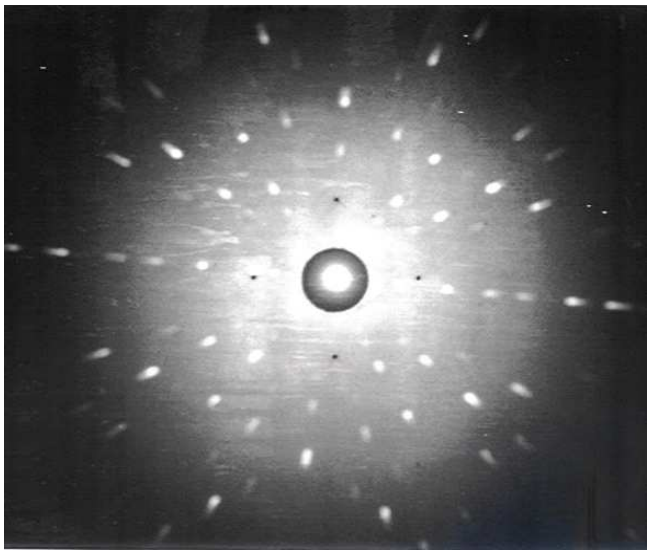


Figure 4.2: Laue x-ray image for a (110) diamond surface polished manually.

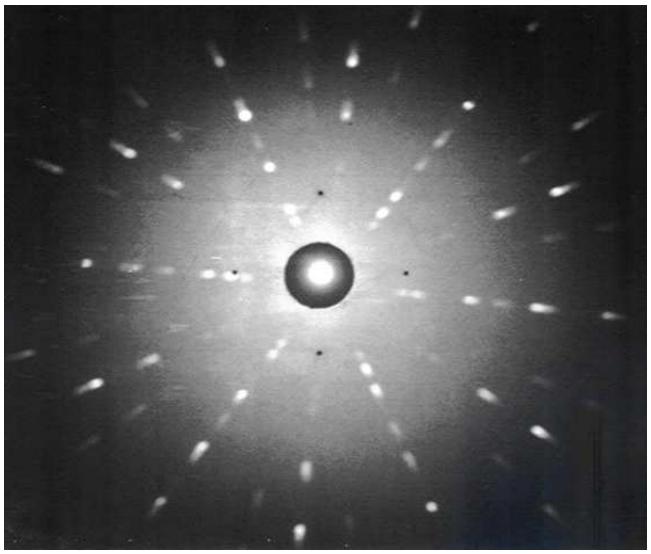


Figure 4.3: Laue x-ray image for a (111) diamond surface polished manually.

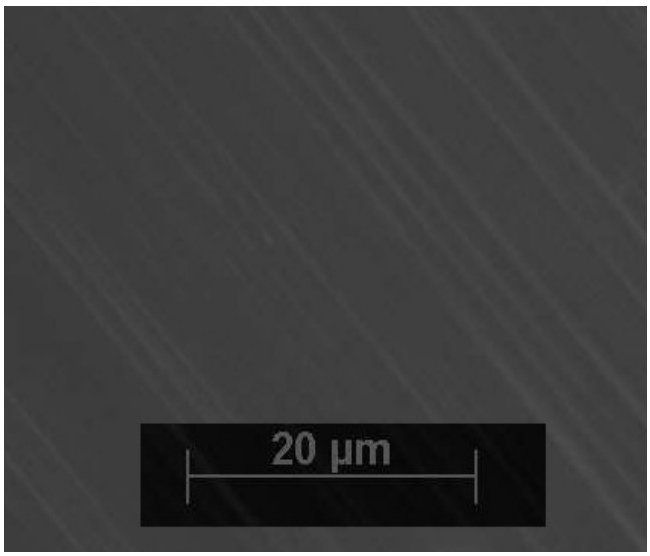


Figure 4.4: Optical microscopy image of a manually polished (100) diamond surface for sample kc3, obtained at a magnification of 1000 times.

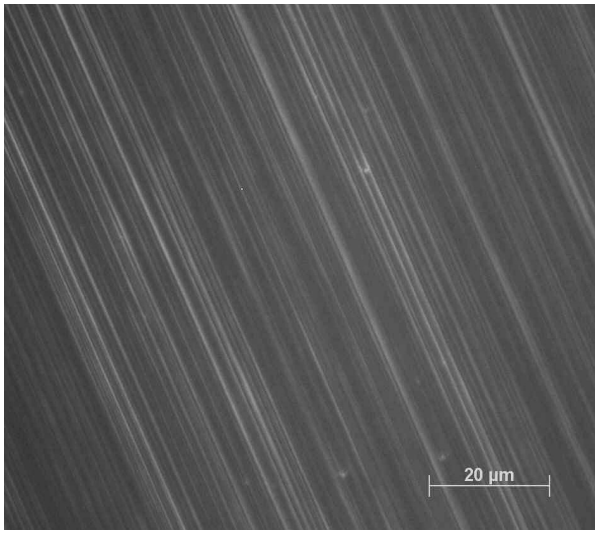


Figure 4.5: Optical microscopy image of a manually polished (110) diamond surface for sample kk7, obtained at magnification of 1000 times.

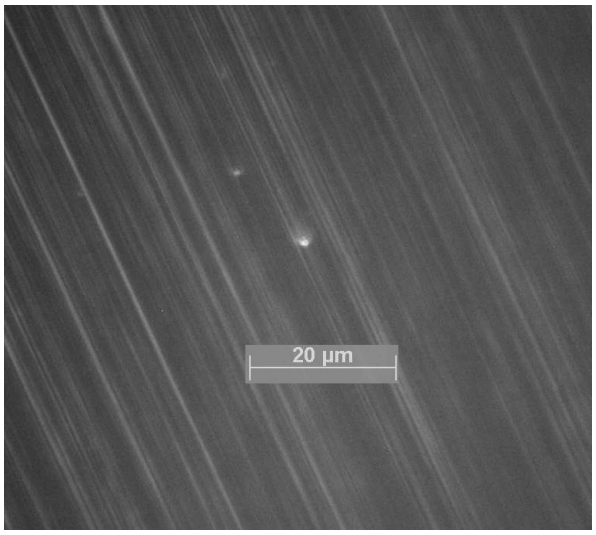


Figure 4.6: Optical microscopy image of another manually polished (110) diamond surface (sample kk7). The image was taken at a magnification of 1000 times.

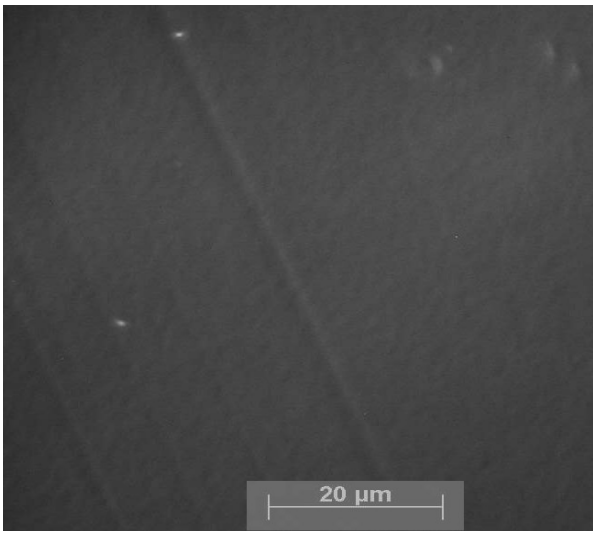


Figure 4.7: Optical microscopy image of a manually polished (111) diamond surface (sample kc11) obtained at a magnification of 1000 times.

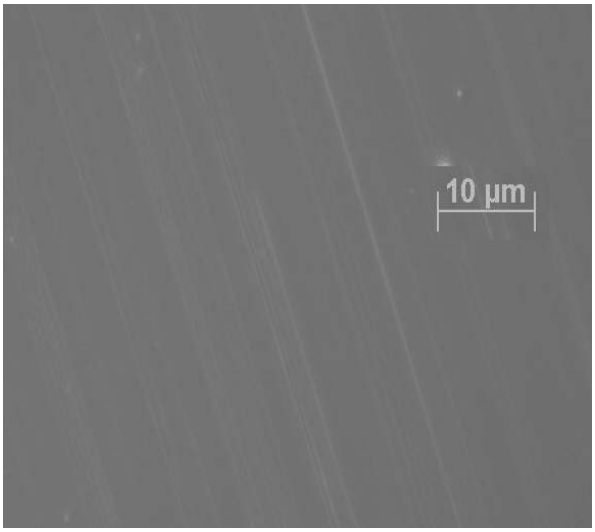


Figure 4.8: Optical microscopy image of another (111) diamond surface polished manually (sample kc11), obtained at a magnification of 1000 times.

4.3 Discussions.

Different materials often have different Laue image patterns depending on the crystal structure. In this particular case, the Laue image shown in figure 4.1 has two bright lines that are constituted of a set of point reflections, indicating quite clearly the fourfold symmetry characteristic of the (100) diamond surface. It was obtained from a manually polished (100) diamond surface, and it shows a slight offset from the true (100) orientation, which arises from the actual crystal orientation during the polishing process. On the other hand, the patterns established in figure 4.2 were typical of the (110) surface whereby a collection of bright spots showing the 2-fold symmetry around the central bright spot were observed. Figure 4.3 was a clear representation of the (111) diamond surface which is associated with its unique 3 fold symmetry. The Laue images shown in figures 4.2 and 4.3, indicated that the (110) and (111) surfaces were both polished quite close ($\sim 1^\circ$ or even less) to their true orientations, unlike the (100) surface whose Laue image had an offset of about 2° as shown in figures

4.1. This offset was however not a feature of all the (100) surfaces considered in this study, and in fact some of them were found to have been polished quite close to their true orientations.

The optical micrograph shown in figure 4.4, and which was obtained from a (100) surface polished manually presented clear evidence of polishing lines with large widths, that were not necessarily equidistant from each other, nor of the order of the polishing diamond grit. Most probably the polishing lines that are observed here as well as in other surfaces originated from the mechanical polishing, since the manual polishing wasn't expected to cause any major visible changes especially at these orders of magnifications. In fact, the optical images from the mechanically and manually polished surfaces did not present any visible differences. Some of the polishing lines were found to be wider than others and also further apart. However, due to the nature of the two dimensional (2D) images, it was not easy to get a feel for their depths. The concentration of the polishing lines at some regions of the surface and not others was again a manifestation of the distribution of the polishing particles on the polishing wheel as illustrated in figure 1.4 of chapter 1 that demonstrates the polishing set up and also in [54].

Figures 4.5 and 4.6, which were obtained from the (110) surfaces polished manually showed more prominent polishing lines that were distributed all over the surface unlike the case of the (100) surface. These appeared wider and seemed to be concentrated more on the raised regions of the surface. It was again not possible to establish the depth of the grooves from the 2D images. Judging from the thicknesses, brightness and/or darkness of the lines, the groove sizes were obviously not the same, and there was some indication of smaller grooves existing inside the larger ones. In addition, some prominent and bright marks were also observed on these surfaces, that were thought of being either polishing debris or dust particles, but clearly not part of the surface features.

Figures 4.7 and 4.8 which were obtained from the (111) surfaces showed fewer polishing lines per given area than those observed on either of the other two faces. These were quite faint and spread relatively further apart. In addition, figure 4.7 which was obtained in the dark view mode of the optical microscope was found to have wider and fairly deep polishing marks. The lack of prominent polishing lines was not too surprising though on the (111) surface, since it is generally known to be hard to polish in all directions [51], although the process shows a three fold symmetry [54] as noted before. This observation also confirms to some extent that the mechanisms of material removal were significantly different from those of the other two low index faces. At the same time, whereas it was generally hard to draw any significant conclusions regarding the surface flatness or smoothness from either of the optical micrographs, a casual look appeared to suggest that the (111) surfaces were smoother and more flat than the other two low index surfaces after the manual polishing, with more prominent polishing features being found on the (110) surface and slightly less visible marks on the cuboid (100) surface. These observation tie in well with those of Thornton and Wilks [60] who observed networks of small irregular lines and sets of parallel light and dark bands of the order of 30nm wide and height variations of the order of 5nm, which ran diagonally across the micrographs, parallel to the directions in which the surfaces were polished. The only difference between our polished surfaces and theirs was that the small irregular lines were missing in our case, but we could not establish precisely the widths or depths of the polishing lines. They further observed that the bands were more visible on the dodecahedron (110) faces, while those on the cuboid and octahedron faces were only discernible on the images of larger prints. This agrees quite well with our findings, although we were further able to establish the polishing lines quite clearly on both the cuboid and octahedron faces unlike in their case.

Carefully prepared and smooth diamond surfaces are critical to their final applications, especially where diamond is used in hard metal cutting tools. In this specific application, Thornton and Wilks [60] observed that when certain aluminium-silicon alloys were turned with diamonds, the metals tended to adhere to the table of the tool if it had not been carefully polished. They explained such a bonding between the diamond and the metal to be due to mechanical keying with the rough surface of diamond. As such, the ultimate performance of a tool may often be limited by the microscopic roughness observed on even well polished diamond surfaces. From their optical micrographs, Bell *et al.* [89] observed that the polishing lines were often straight and continuous, an observation which is clearly confirmed by our studies.

It is important to mention in passing that by focussing the optical beam deep below the polished diamond surfaces, features that appeared like ring cracks were observed in all the three low index diamond faces. These were however not pursued further since they as well as other aspects of the surfaces such as subsurface damage, crack formation and their propagation were beyond the scope of the present study.

4.4 Conclusions

The Laue images gave a clear indication that the diamond surfaces were polished quite close to their true orientations except the (100) surface. However, although small, this offset may actually present some remarkable effects on certain surface analytical techniques such as LEED measurements, whereby some extra erroneous LEED spots would appear on the patterns. This emphasizes the need to orient the crystal surfaces appropriately. In addition, channelling experiments on surfaces that are not properly oriented would often present higher yields than they should, since the beam would not be channelled as it should

if the surfaces were not polished precisely to their true orientation or at least very close. It is therefore critical to polish surfaces as close as possible to their true orientations for better results.

The polishing lines observed on the optical micrographs, confirmed to some extent that the polishing mechanisms taking place on the (100) and (110) surfaces were remarkably different from those taking place within the (111) surface. The (110) surface was found to have wider and probably deeper polishing grooves than those of the other two low index diamond surfaces, implying that higher material removal rates were perhaps taking place on this surface than in the others during both mechanical and manual polishing. The (111) diamond surface was found to have the least number of polishing lines per unit area, which were also further apart and also with some indications of them being shallow. This highlighted the possibility of the existence of differences within the polishing mechanisms between itself and that of the other two low index faces. This in some remote way also confirms the fact that the (111) diamond surface is generally hard to polish through the abrasive wear in all directions, and although not quite conclusive by themselves, the optical micrographs suggested at least to a first approximation that the extra manual polishing that was done after the mechanical polishing achieved relatively much smoother and more flat (111) surfaces, as opposed to the other two low index faces.

Chapter 5

Atomic Force Microscopy investigations of the three low index polished diamond surfaces.

5.1 Introduction

As the quest for obtaining smoother, flat and well characterized diamond surfaces continues, more novel techniques for preparing and analyzing them keep being proposed and tested. These range from the well known mechanical polishing, to exotic ones such as the ion assisted lift-off technique [92], ion polishing itself [48], to the chemically assisted and catalytic processes as well as the tribochemical polishing proposed by Haisma *et al.* [67] among many others. Some of these are specifically surface finishing techniques which follow other surface preparation processes such as the well-known mechanical polishing, with some achieving better results than others.

A key ingredient of all the surface analytic techniques is their ability to operate at the highest possible resolution, even at the atomic level. The AFM technique approaches an upper range magnification of 1,000,000x [200] compared to the optical microscopy's 1000x and therefore ideal for analysing atomically smooth surfaces. This chapter explores atomic force microscopy investigations of the three low index diamond surfaces prepared in two different ways, with

a view to establishing the degree of their effectiveness in creating smoother, and/or alternatively, less rough surfaces after each polishing procedure.

The first method involved polishing the surfaces mechanically on a rotating cast iron disc, a process that is described in more details in the experimental section of the XPS chapter. Different diamond grit sizes were used, ranging from 6 μm down to the finest ones measuring 0.25 μm. The second procedure was a gentle manual polishing, which followed the mechanical polishing. The manual polishing was achieved by pressing and rubbing the diamond surfaces back and forth on a highly polished metal block, using a typical (and at least) constant hand pressure (force) that a person can conveniently apply for a period of about 30 minutes or more. The diamonds were held in a recess made within a soft wooden cork, with the surface to be polished being the only one that was exposed. In this procedure, both 1/4 and 1/10 μm diamond pastes were used, and these were envisaged to achieve finer polishing than that observed in the mechanically polished surfaces. Some of the manually polished surfaces were later annealed, and these are considered separately in section 5.4.4.

Olive oil was used as the lubricant during the manual polishing. Its suitability for the polishing of diamond surfaces with regard to its effects on the lubrication, wear and abrasive processes were previously investigated by Grodzinski *et al.* [87] among other lubricants, where they found it to be an ideal polishing lubricant. Due to its suitability, it has continued to be used in the diamond polishing industry spanning over 600 years [79, 54] up to the present day. Nonetheless, more questions on the role of the oil film with regard to the polishing process are still being asked, and in this regard, Casey *et al.* [78] investigated and reported earlier that an oil layer has no effect on the friction since the adsorbed film only prevents adhesion but does not mask the jagged roughness of the surface. For this reason, they observed that the friction would be less in air than in vacuum, and therefore diamond surfaces prepared under

the two ambient atmospheres, still display their characteristic symmetry.

5.2 Experimental

Following the mechanical and manual polishing as well as the cleaning and rinsing of the diamond surfaces, AFM images measuring between $7\times7\mu$m and $(1\times1)\mu$m were obtained at different regions of each of the three low index diamond surfaces. The AFM images were initially obtained from the mechanically

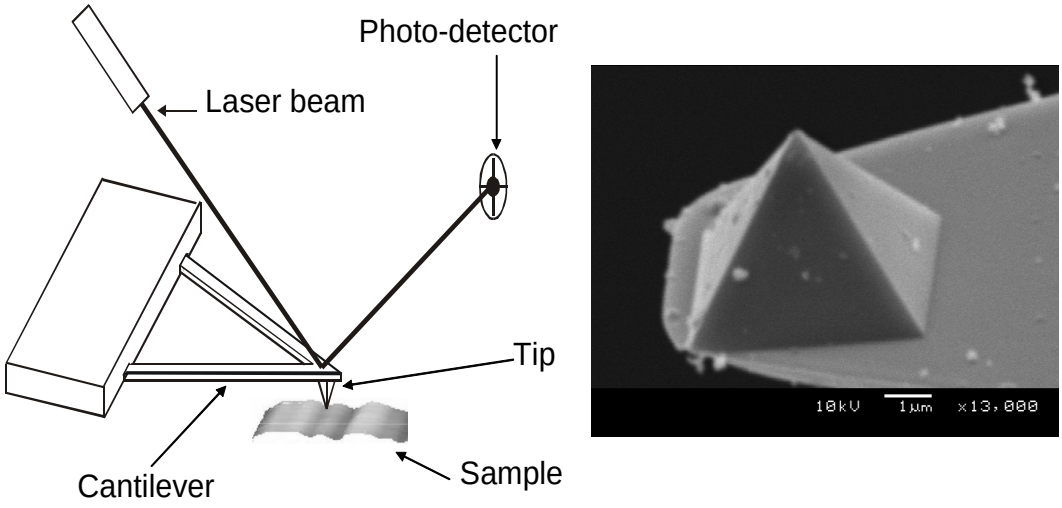


Figure 5.1: Schematic diagram of the AFM equipment showing the cantilever, the tip, photo-detector, laser beam and the sample. On the right hand side is an SEM image of the tip fabricated from Si_3N_4. Note the possible wear and contamination on the tip.

polished surfaces, followed by those of the manually polished ones. These were obtained using a scanning probe microscope based at the University of Pretoria. It was a type TopoMetrix TMX 2000 Discoverer whose key features and the commonly used AFM tip are shown in figure 5.1. D.A. Bonnell [5] has outlined the general principle of the Scanning probe microscopy, while J.C. Vickerman [1] has given the key principles of the AFM process itself. Further details regarding the AFM process are given by Graham J. Leggett quoted in [1], together with

possible artifacts associated with various AFM tips that are commonly used. Taatjes *et al.* [200] has further compared the correlation of tip structure with the rendered images.

Under normal operating conditions, the laser beam is directed onto a cantilever which is connected to the tip that scans the sample surface. The sample is then mounted onto a piezoelectric crystal, which moves laterally in either direction along the x and y-axes, while the cantilever and the tip are kept stationary. The laser light gets reflected as shown in figure 5.1, as the tip passes over different parts of the sample, and the reflected beam is detected by a four-segment photo-detector. Some of the two (horizontal) photo-detectors pick out any frictional forces between the tip and the sample through the torsional forces that are developed in the cantilever. By reconstructing the reflected beam, the surface topography gets mapped out as an AFM image [65], generated via various suitable software such as the (GAFM) computer program used in this study.

The contact mode of the scanning process was used in this study, with a force constant of 0.032N/m being applied and a nominal frequency of 17kHz used. This mode was preferred over the others such as the non-contact one, because it would accurately map out the grooves (which were an important feature in this study) unlike the non-contact mode where smaller surface features such as steps and grooves with sharp edges would only be considered as averages due to the potential between the tip and the respective surface feature. As a result, the height or depth of most features obtained within the non-contact mode would greatly be underestimated, especially when it is noted that the tip wears out over time. Under these conditions, the AFM images would not necessarily be a true reflection of the actual surface nor would the surface features be resolved to the expected atomic size. Coupled with this, the geometry of the tip also has a strong bearing on the observed AFM images [200] since most of the tips tend to have a few of atoms at their ends, instead of the single atom that is

anticipated.

The AFM tip used in this study was a Si_3N_4 pyramidal type, whose base and height were 4mm each, with an aspect ratio of $\sim$ 1:1, and a radius of $<$ 50nm.

Due to the movement of the sample, its height or thickness was of particular importance to the AFM equipment used in this study, with sample sizes of 1cm$\times$1cm$\times$0.4cm being preferred. A thick sample was likely to present artifacts which could otherwise manifest themselves as though the tip was scanning a curved surface as shown in figure 5.2, and in the process either mask true features, or even give rise to features that are not necessarily real, as far as the surface is concerned.

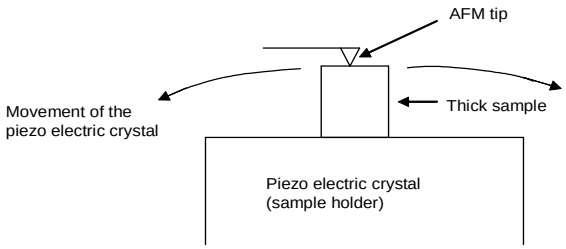


Figure 5.2: Schematic diagram of the AFM tip scanning over a thick sample.

5.3 Results

5.3.1 2D and 3D AFM images, together with their line profiles and the corresponding power spectra.

Some of the 2 and 3 dimensional atomic force microscopy images that were obtained from the three low index diamond surfaces are shown in figures 5.3 and 5.4 for the (100) surface, 5.7 and 5.8 for the (110) surface, as well as 5.11 and 5.12 for the (111) surface. Additional images are given in Appendix C.

The images presented here are mainly those of surfaces that were not annealed, since those of the annealed surfaces are considered separately later on in section 5.4.4. Each surface was represented by at least two sets of images, and in most of the diagrams, the corresponding 2 and 3D images are shown together, so as to be able to compare and extract maximum information from them. They are presented in such a way that they alternate between the mechanically and manually polished surfaces for easier comparison between the two polishing methods. All the surfaces were polished along their correspondingly easy or soft directions as determined by an optical microscope. The horizontal extent of the AFM scans is about 3 orders of magnitude greater than the vertical signal (scale), and hence the surface features are greatly over-emphasized. This implies that these surfaces are actually very smooth and flat.

For some of the 2D images, the directions along which the line profiles were obtained are shown. The lines profiles were obtained perpendicular to the polishing lines (grooves), and also parallel to them, in order to establish the degree of surface roughness/smoothness in each one of them, and also to determine if there were any minor or significant differences. For the purpose of this work, the surface roughness is described in two ways; (a) as the average heights from the peak to valley in the line profiles and (b) as the lengths of the surface features (corrugations, wavelengths or sinusoidal waves) within the line profiles. Previous studies by Couto *et al.* [82, 63] showed that the polishing grooves on diamond surfaces were smooth, while Hird *et al.* [54] observed that they were flat bottomed, an observation which they attributed to the reciprocal polishing between both the surface and the grit particle. They further found that the groove widths for their polished (100) and (110) surfaces were between 20 and 100nm, but we hasten to add that this would depend to some extent on the size of the grit particles. As such, although the groove sizes were not necessarily a direct function of the polishing grit, it will be recalled that a

large grit particle would result in a large damaged region, and consequently larger grooves. Line profiles obtained both parallel and perpendicular to the polishing grooves were therefore vital for two reasons. Firstly, to establish how our manually polished surfaces differed from the mechanically polished ones, and two, to confirm or compare the results obtained from our polished surfaces with the findings of Couto *et al.* [82, 63] and Hird *et al.* [54] or at least to establish whether their observations constituted a general trend, or if they were instead an isolated specific case that applied to their surfaces only. It is nevertheless important to emphasize that some differences may occur due to our special (unique) manual polishing technique for surface finishing, and correlation between their results and ours may only be established for the mechanically polished surfaces since these were prepared in a similar way as theirs.

The regions to investigate on the surfaces were chosen in such a way that they avoided any of the surface features that were otherwise not part of the AFM images, such as dust particles. These were easy to identify since they appeared as strongly bright and hence highly raised features on the AFM images. A plot of the line profiles along the two directions yielded the surface topographies (i.e. ridges, valleys etc.) along the respective directions and faces. It is worth noting that, although some of the x and y-axis scales were different for the mechanically and manually polished surfaces (i.e. some were expressed in nm and others in μm), an idea of the general surface topography from the two polishing techniques was quite easily established by comparing the heights (z-axis component), widths and depths of the features as shown in the respective line profile diagrams. The line profiles give the absolute values of the surface roughnesses, but they tend to ignore any spatial correlation within the surface (such as 3D sloping regions), and as a result, the power spectral densities, which forms the Fourier transforms of the surfaces are often used [201].

The power spectra which are essentially convolutions of the Fourier transform components are usually derived from the line profiles. The Fourier transforms are therefore important in this regard since they identify the scale of the surface roughnesses and especially so the smaller ones that could otherwise not be easily discernible from the AFM images themselves or the corresponding line profiles. The line profiles were in addition useful in identifying the larger roughnesses, meaning that these and the power spectra complemented each other.

In essence, Fourier analysis involves the breaking up of a signal into sine waves of various frequencies, which would then represent different features on the surfaces such as the various sizes of the polishing grooves in our case, where different roughnesses would correspond to different wavelengths. Transformation of the signal results in a set of Fourier coefficients, with each one of them indicating the power (amplitude) of the specific frequency component of the signal. The power spectrum is therefore a simple way of showing the total amplitude at each of the frequencies. It is calculated as the square root of the sum of the squares of the coefficients of the sine and cosine components. For example, figure 5.5 illustrates a set of typical cases of given input signal (line profiles-graphs (a) and (c)) and their corresponding Fourier transform which are in this regard their power spectra (graphs (b) and (d) respectively). However, more often than not the range of the FFT (Fast Fourier Transform) does not contain a complete set of whole number of periods. This means that the discontinuity in the end-points of the signal (waveform) produces a power spectrum that contains high frequency components not necessarily present in the actual input. To avoid this, a correction window is normally used to attenuate the discontinuity and therefore improve on the accuracy. Due the end-point error which is also referred to as leakage, the peak position may not occur exactly at the anticipated frequency, and therefore a phase mismatch would occur unless corrections are made to the signal. The signal, or the time series function is often multiplied

by a window weighting function, before the FFT process is performed. Most window weighting functions attenuate the discontinuity by tapering the signal to zero at both ends of the window, but care needs to be taken so that useful data at the ends of the window is not destroyed by the tapering [202]

With proper corrections, the power spectra make it possible to extract the Fourier components and their amplitudes, thereby establishing whether the surface roughnesses or smoothness improved following both the mechanical and manual polishing. This would manifest itself through the disappearance of certain Fourier components. If new roughnesses are created, these would appear as new Fourier components in the power spectra, and vice versa if they were removed.

For a region of the surface containing N pixels on the AFM images, the root mean square (RMS) roughness were computed from the relation 5.3.1,

$$RMS = \sqrt{\sum_{n=1}^{N}[(z_n - \overline{z})^2 \frac{1}{N-1}]} \tag{5.3.1}$$

where N is the number of pixels, $\overline{z}$ is the average height of the surface profile, and z_n is the surface height at point n.

In each of the 2D images, a bar is shown on the right hand side, which indicates the degree of surface roughness (from peak to valley), with the dark parts representing the deep features while the brighter ones correspond to the raised ones. For example, while the scan areas shown in figures 5.7 and 5.8 were almost the same, the bar on their right hand side shows that the height between the highest and lowest parts of the surface reduced after the manual polishing from 15 to 8nm. In each of the line profiles, the widths and depths of the grooves are shown. These are given in nm and sometimes in μm. For comparison purposes and also in order to appreciate their magnitudes with respect to the expected atomic size roughness, the diameter of one atom is $\approx$0.25nm [1].

In figures 5.5, 5.6, 5.9, 5.10, 5.13 and 5.14 as well as others shown in Appendix C, the top panels show the line profiles (graphs (a)) and their power spectra (graphs (b)) that were obtained perpendicular to the polishing grooves, while the lower two show the corresponding line profiles (graphs (c)) and their power spectra (graphs (d)) that were obtained inside the grooves.

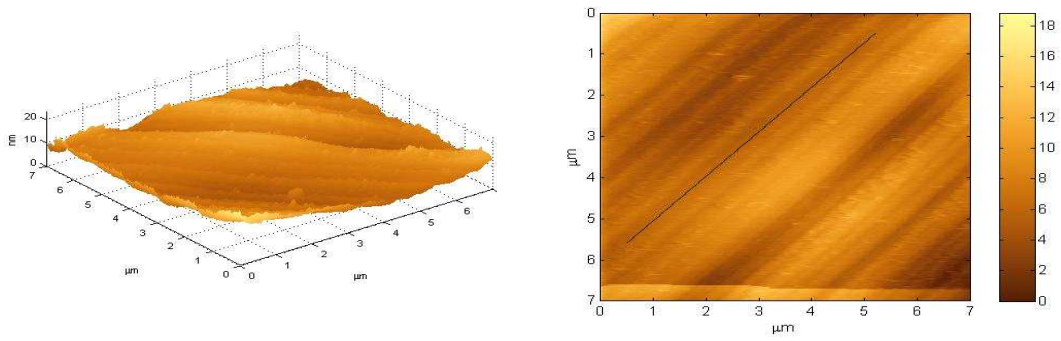


Figure 5.3: Three and two dimensional atomic force microscopy images of a (100) surface polished mechanically (sample kc8), measuring 7×7 μm. Note the dark line used as a guide for the eye to show where data inside the polishing grooves were obtained.

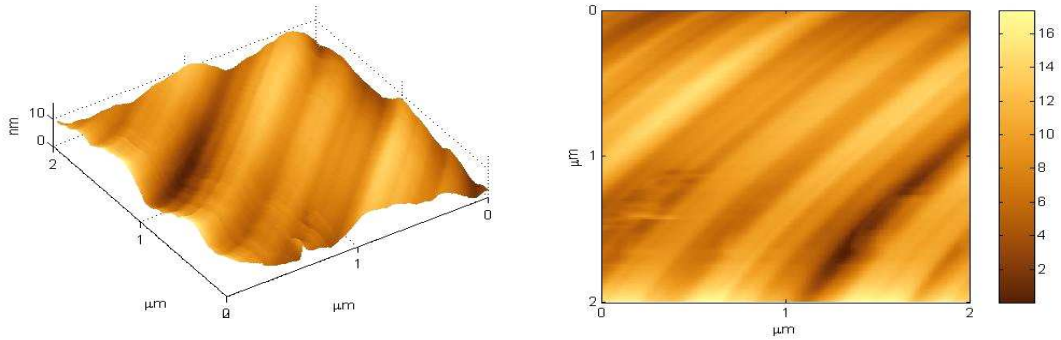


Figure 5.4: Three and two dimensional atomic force microscopy images of a (100) surface polished manually (sample kc8), measuring 2×2 μm.

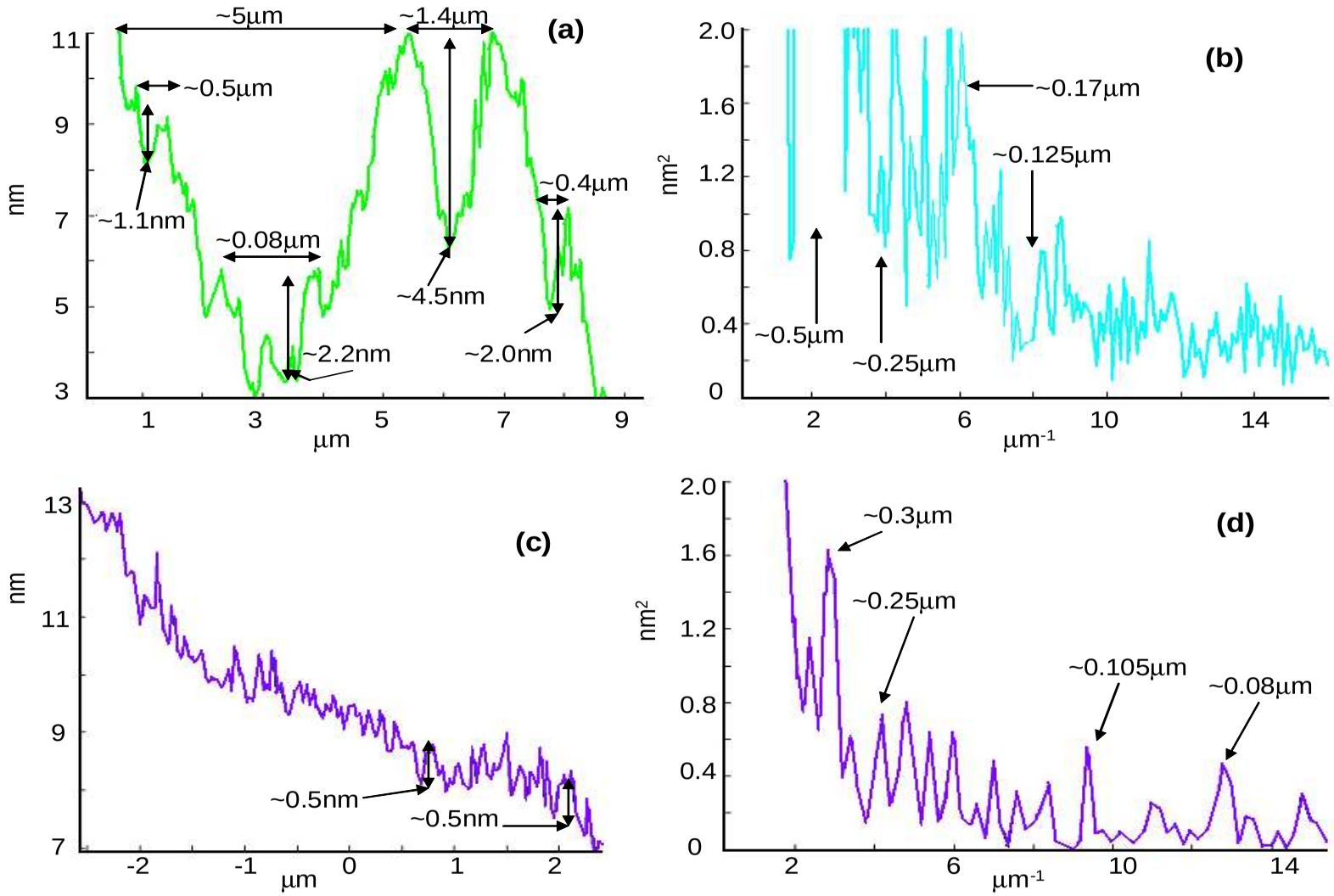


Figure 5.5: Line profiles and power spectra obtained from figure 5.3. These are for a (100) surface (sample kc8) polished mechanically. Graph (a) shows the line profile obtained perpendicular to the polishing grooves, (b) its power spectrum, (c) the line profile obtained inside the polishing grooves, and (d) its corresponding power spectrum. The vertical scale of the power spectra is capped at $2nm^2$ since we wanted to amplify and pick out the smaller roughnesses that were caused by the manual polishing.

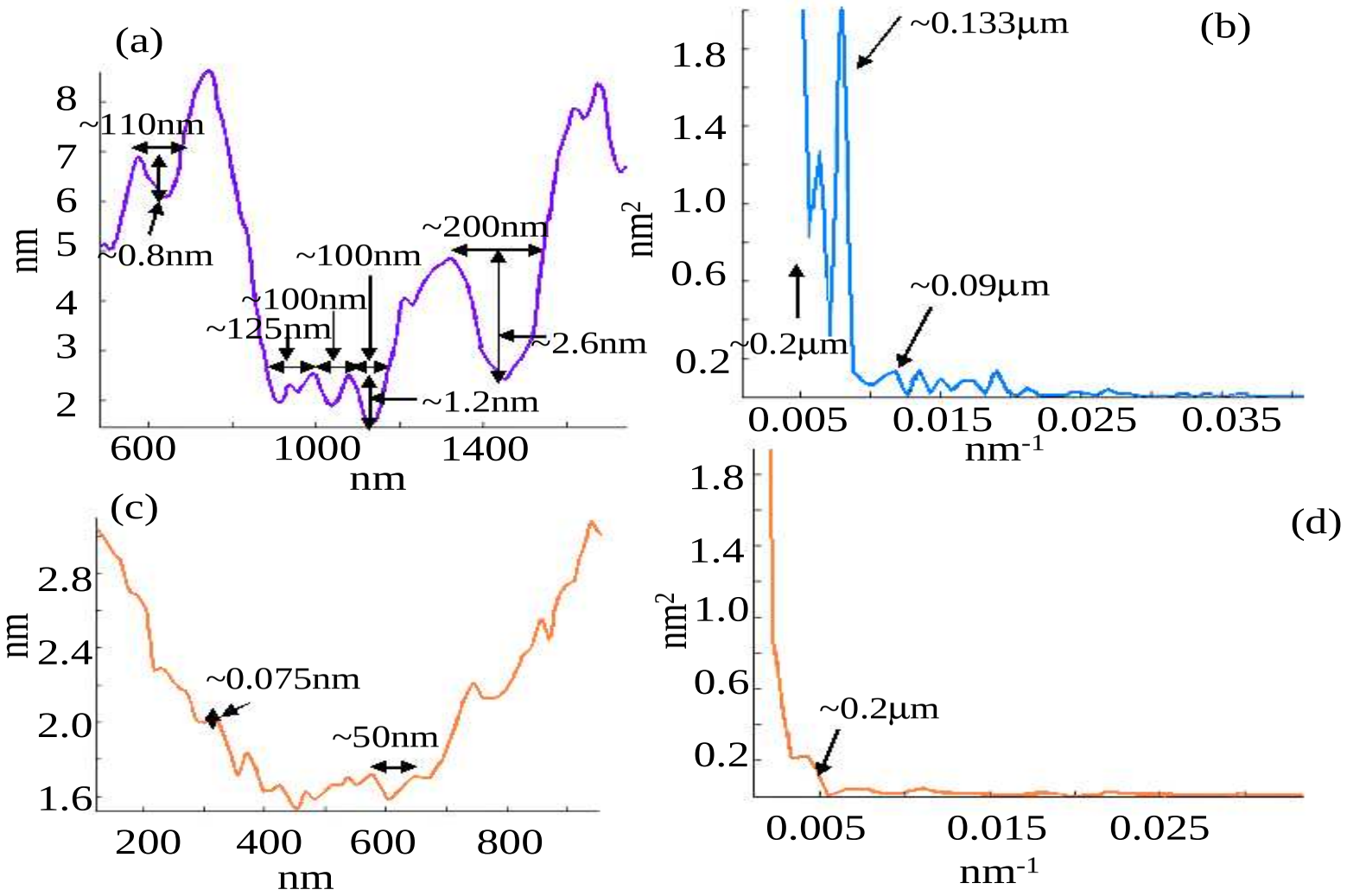


Figure 5.6: Line profiles and power spectra for a (100) surface polished manually, whose AFM image is shown in figure 5.4. Note the shallowing, smoothing and narrowing of the polishing grooves after the manual polishing compared to those of the mechanically polished surfaces (figure 5.5), and also the loss of some high and low frequency Fourier components. Graphs (a), (b), (c) and (d) have similar meanings as those shown in figure 5.5.

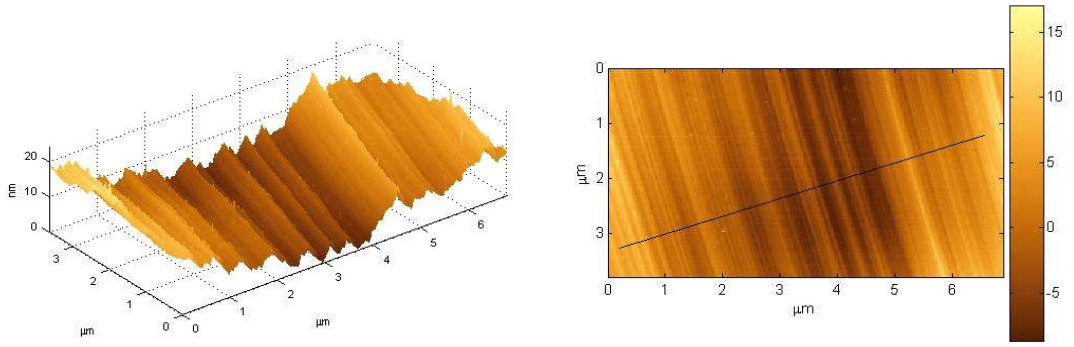


Figure 5.7: Three and two dimensional atomic force microscopy images of a (110) surface polished mechanically (sample kk7), measuring 3.7×6.7 μm.

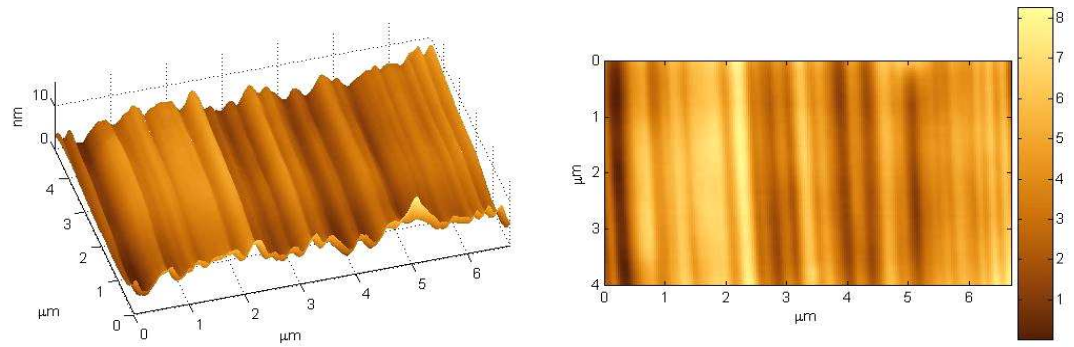


Figure 5.8: Three and two dimensional atomic force microscopy images of a (110) surface polished manually (sample kk7), measuring 4×6.5 μm.

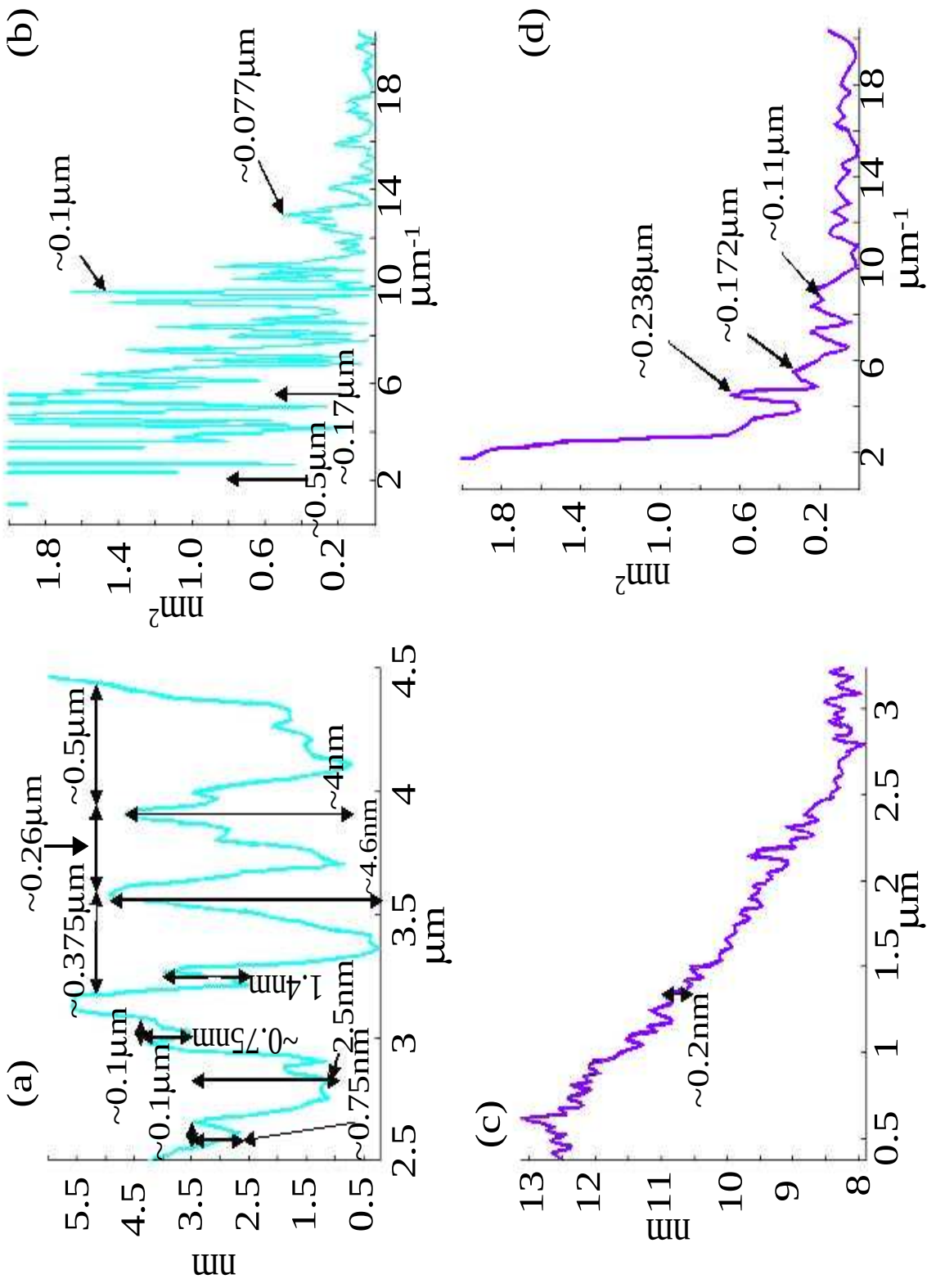


Figure 5.9: Line profiles and power spectra obtained from a mechanically (110) surface, whose AFM image is shown in figure 5.7. Graphs (a), (b), (c) and (d) have similar meanings as those shown in figure 5.5.

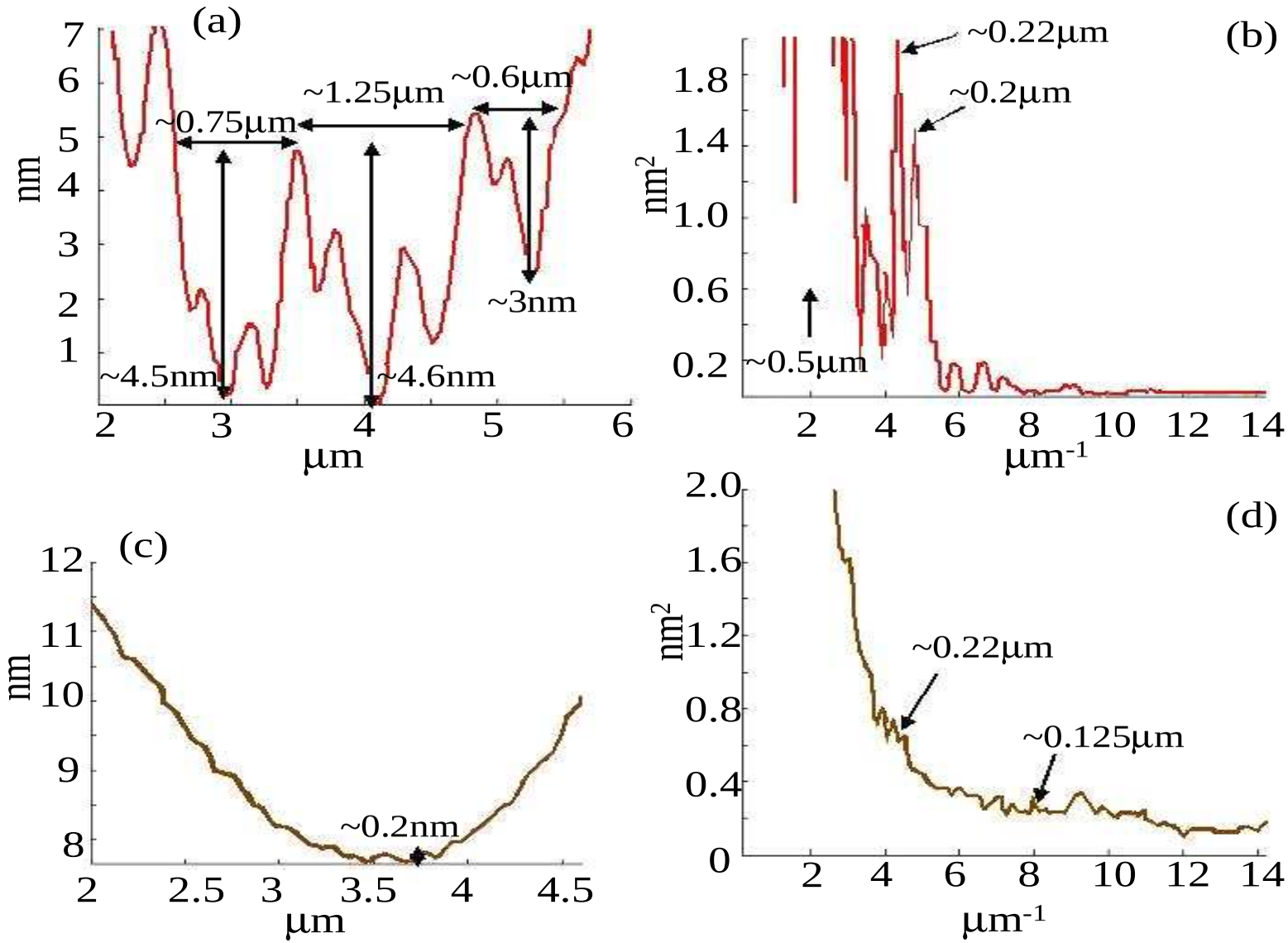


Figure 5.10: Line profile and power spectra for a (110) surface polished manually, whose AFM image is shown in figure 5.8. Note the disappearance of the high frequency components below 0.1μm (graphs (b) and (d)) and the prominence of those above 0.2μm for the spectra obtained perpendicular to the grooves. This is accompanied by the smoothing of the grooves but no noticeable shallowing, compared to the mechanically polished ones. Graphs (a), (b), (c) and (d) have similar meanings as those shown in figure 5.5.

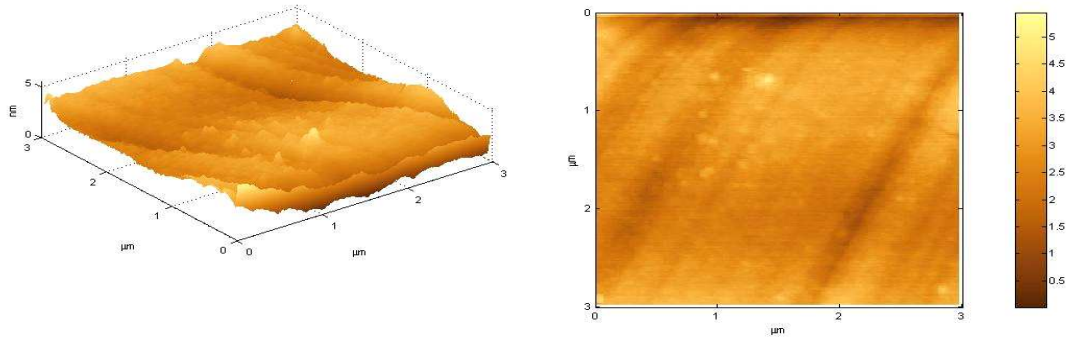


Figure 5.11: Three and two dimensional atomic force microscopy images of a (111) surface polished mechanically (sample kc11).

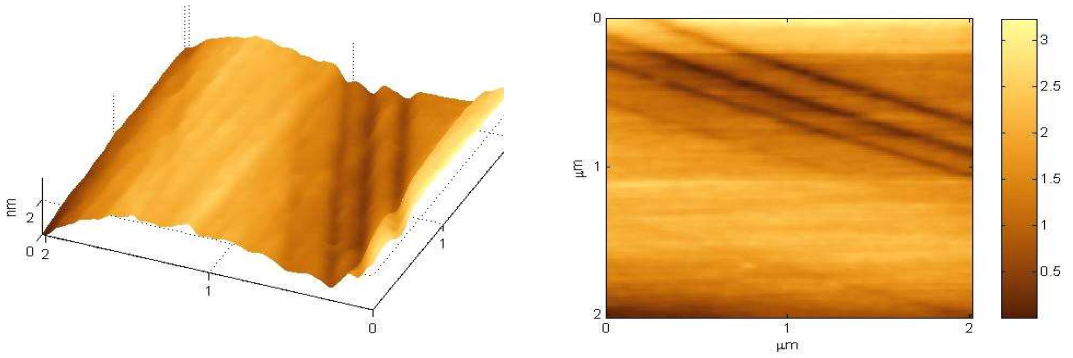


Figure 5.12: Three and two dimensional atomic force microscopy images of a (111) surface polished manually (sample kc11).

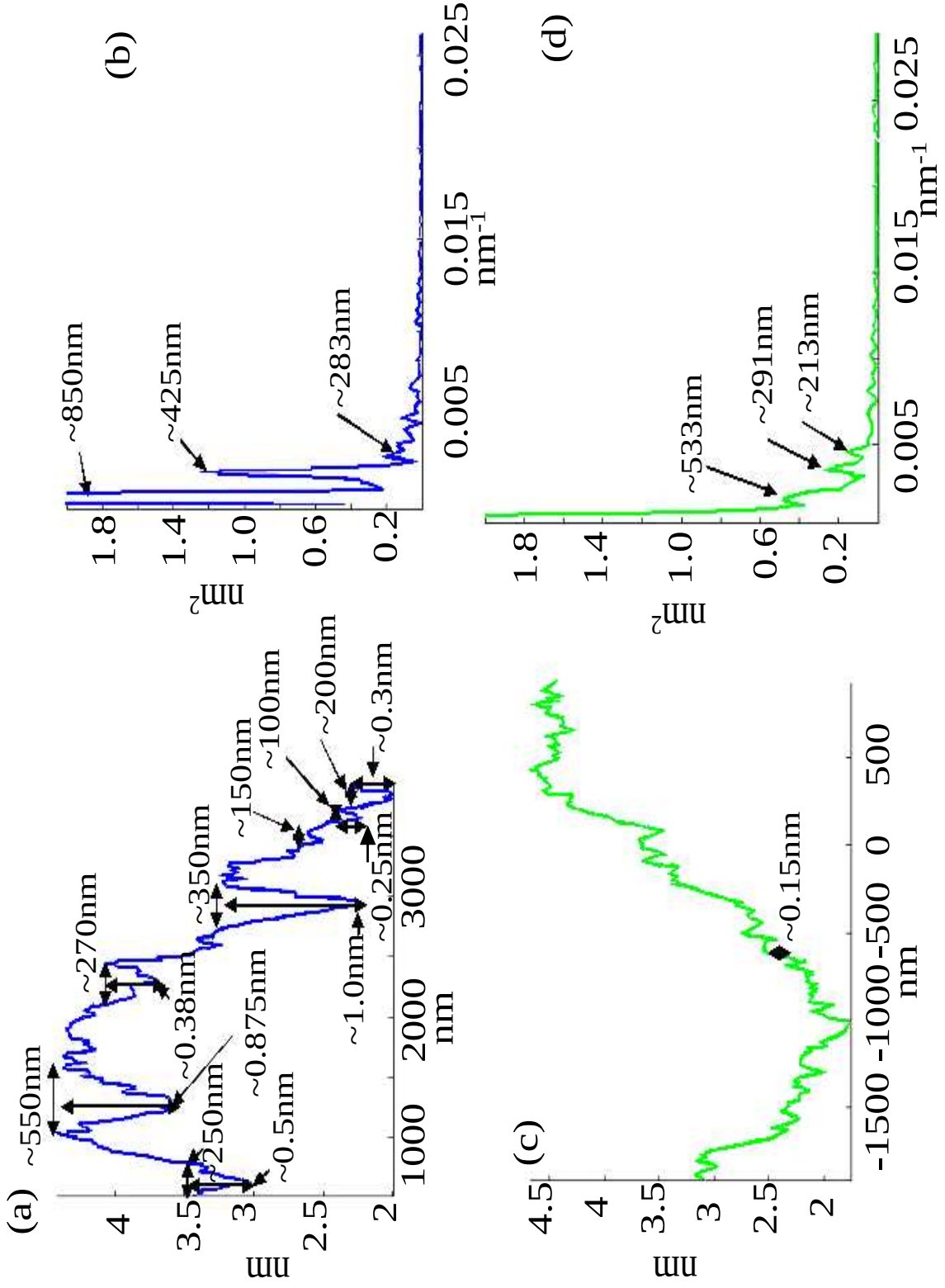


Figure 5.13: Line profiles and power spectra obtained from a mechanically polished (111) surface whose AFM image is shown in figure 5.11. Graphs (a), (b), (c) and (d) have similar meanings as those shown in figure 5.5.

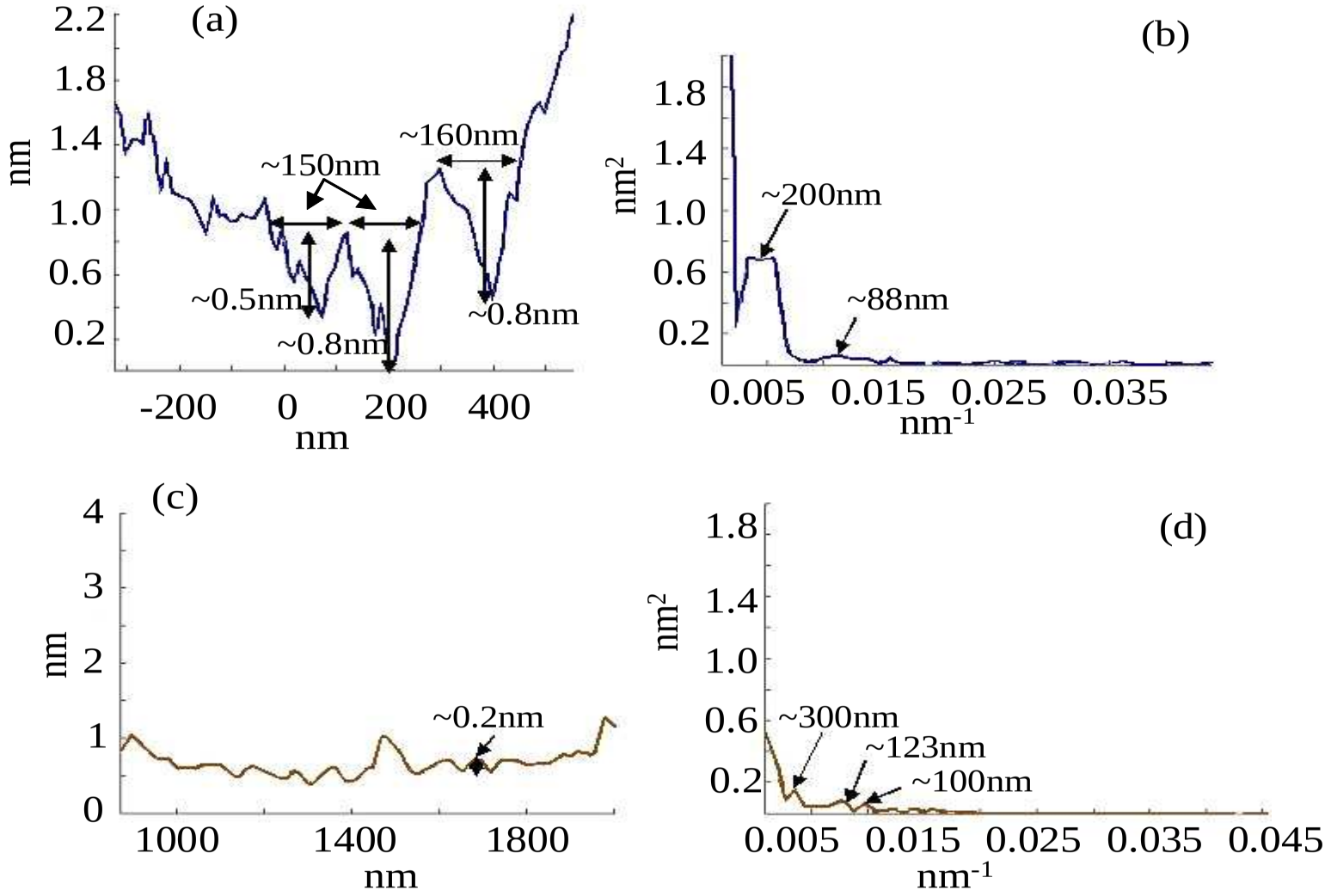


Figure 5.14: Line profiles and power spectra obtained from a manually polished (111) surface, whose AFM image is shown in figure 5.12. Note the disappearance of the high frequency Fourier components in the power spectra, and also those around 0.2μm and the accompanying prominence of the peaks after the manual polishing. The intensity of most components within the polishing grooves is also greatly diminished. Graphs (a), (b), (c) and (d) have similar meanings as those shown in figure 5.5.

5.3.2 Ratios of real areas to the projected ones, and the root mean square roughnesses.

Each of the AFM images was represented by 2D and 3D images, with the 3D images acting more as a guide for eye regarding the general surface roughness or smoothness. However, in order to gauge how the surface roughness changes following the polishing, judging the differences on the AFM images by the naked eye would not be of much help. Instead, the ratio of the real area to the projected one was always obtained as another important measure of the overall surface roughness or smoothness. If the ratio was much greater than unity, it meant that the surface was a bit rugged, and if it was close to one, then the real and projected areas were almost the same, indicating that the surfaces were more smooth and flat. The results obtained from this were plotted as shown in figures 5.15 and 5.17, which gave the relationship between the ratios of the real area to the projected one (scan region), as the scan size was varied. Ideally this should be a non-linear relationship, because there wasn't a one to one correspondence (or proportionality) between the real area and the corresponding projected one, due to the presence of surface asperities. A larger scan region would invariably yield a larger ratio of the real to the projected area, owing to the presence of more surface features, while a smaller area would have a smaller ratio, due to the accompanying decrement of some of the surface features. Nonetheless, this may change if the selected small areas contain more features. As seen from the diagrams, this would approach very close to unity in certain cases as the area was decreased. Since the largest scan size of the AFM images that could be generated by the equipment used in this study was a $7\times7\mu$m, images were taken at different parts of the samples, so as to obtain a true representation of the entire surface.

By integrating over the real scanned area together with its features, the root

mean square roughnesses were also obtained as shown in figures 5.16 and 5.18. Results obtained from a mechanically polished single crystal (100) synthetic diamond were also included, in order to illustrate the comparisons between the quality of its polishing and those of the mechanically and manually polished single crystal natural diamond surfaces.

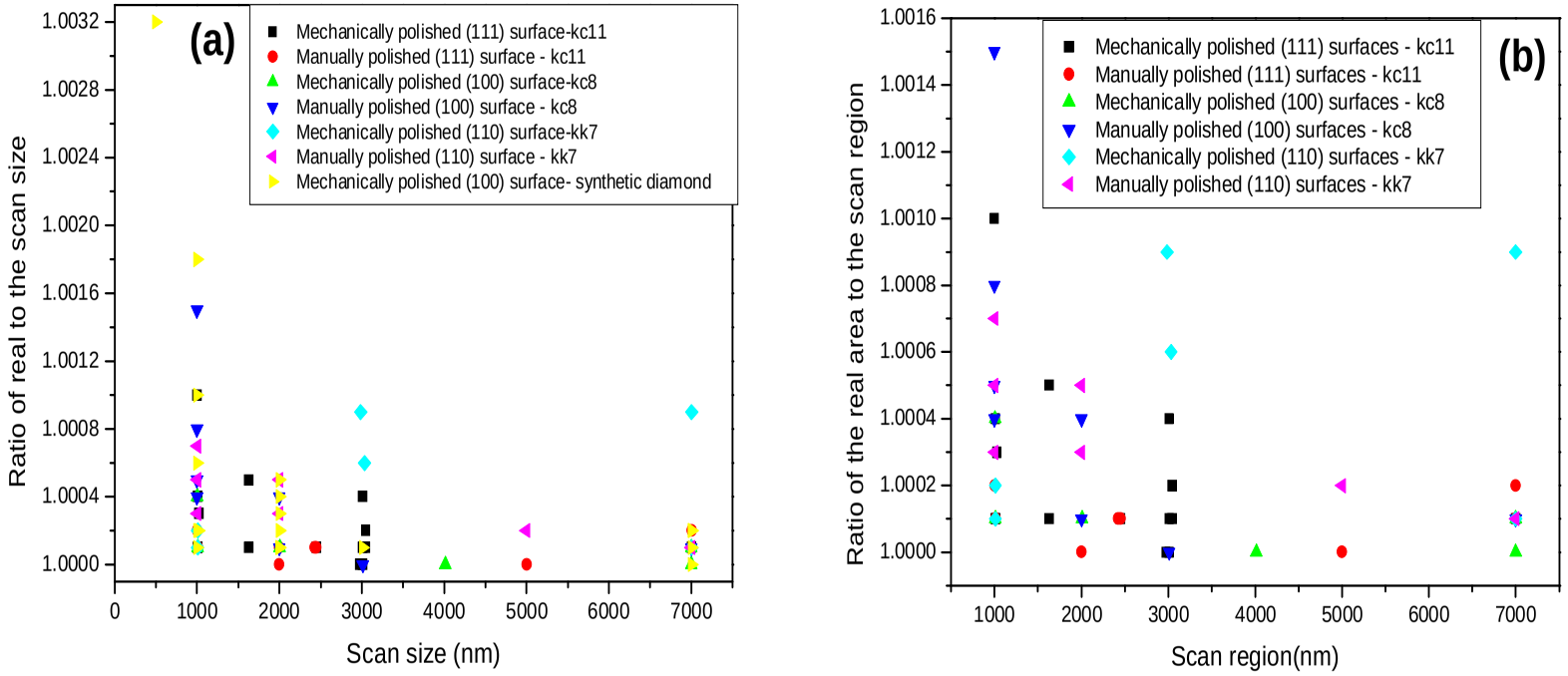


Figure 5.15: Ratio of the real area to the scan size for the three low index diamond surfaces polished both mechanically and manually. Graph (a) includes data for a synthetic diamond sample while (b) doesn't.

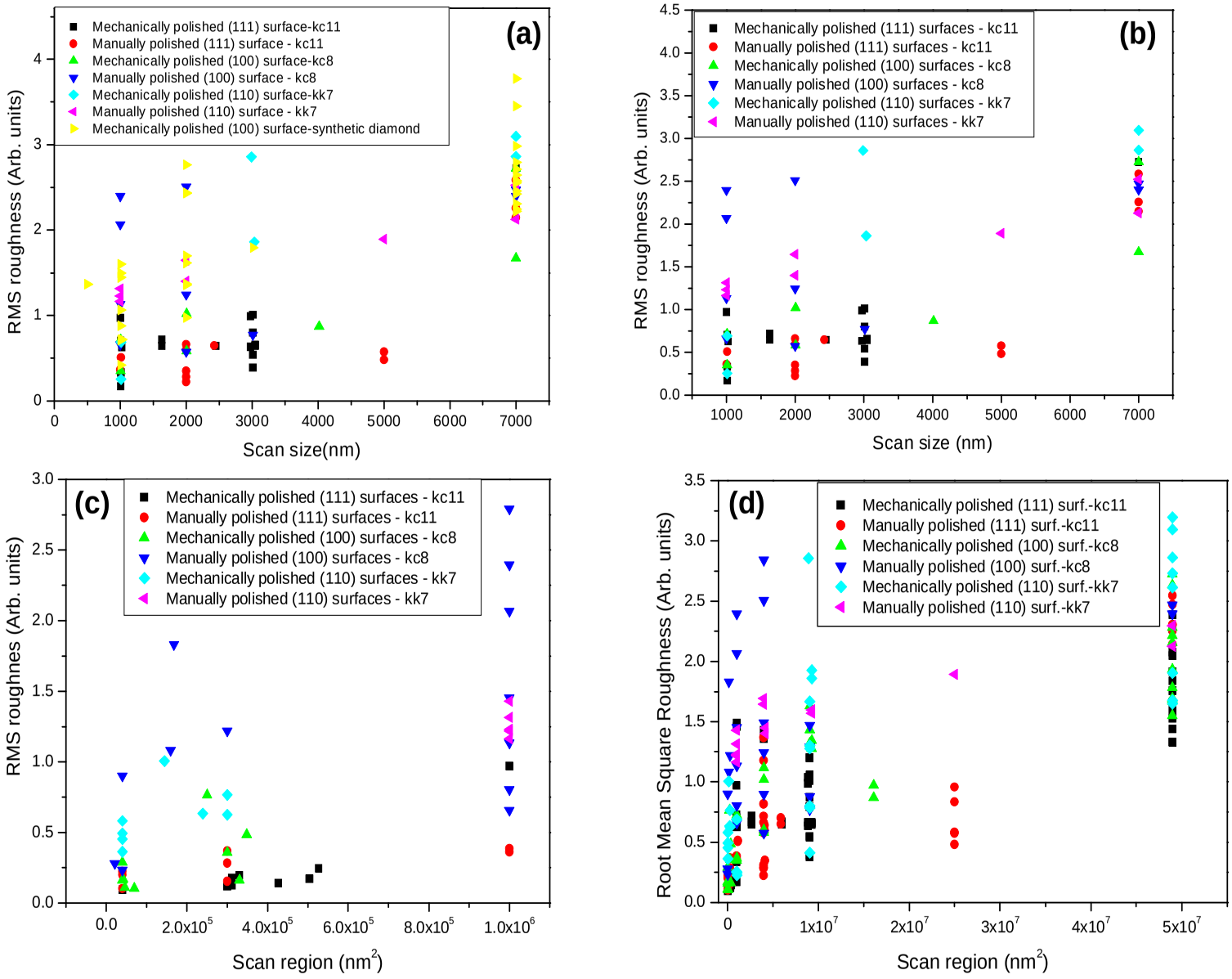


Figure 5.16: Root mean square roughness plotted against the scan sizes. Panels (a) and (b) are for the large scan regions while (c) and (d) are for the smaller ones below 1x1μm. Panel (a) includes data for a mechanically polished (100) synthetic diamond sample.

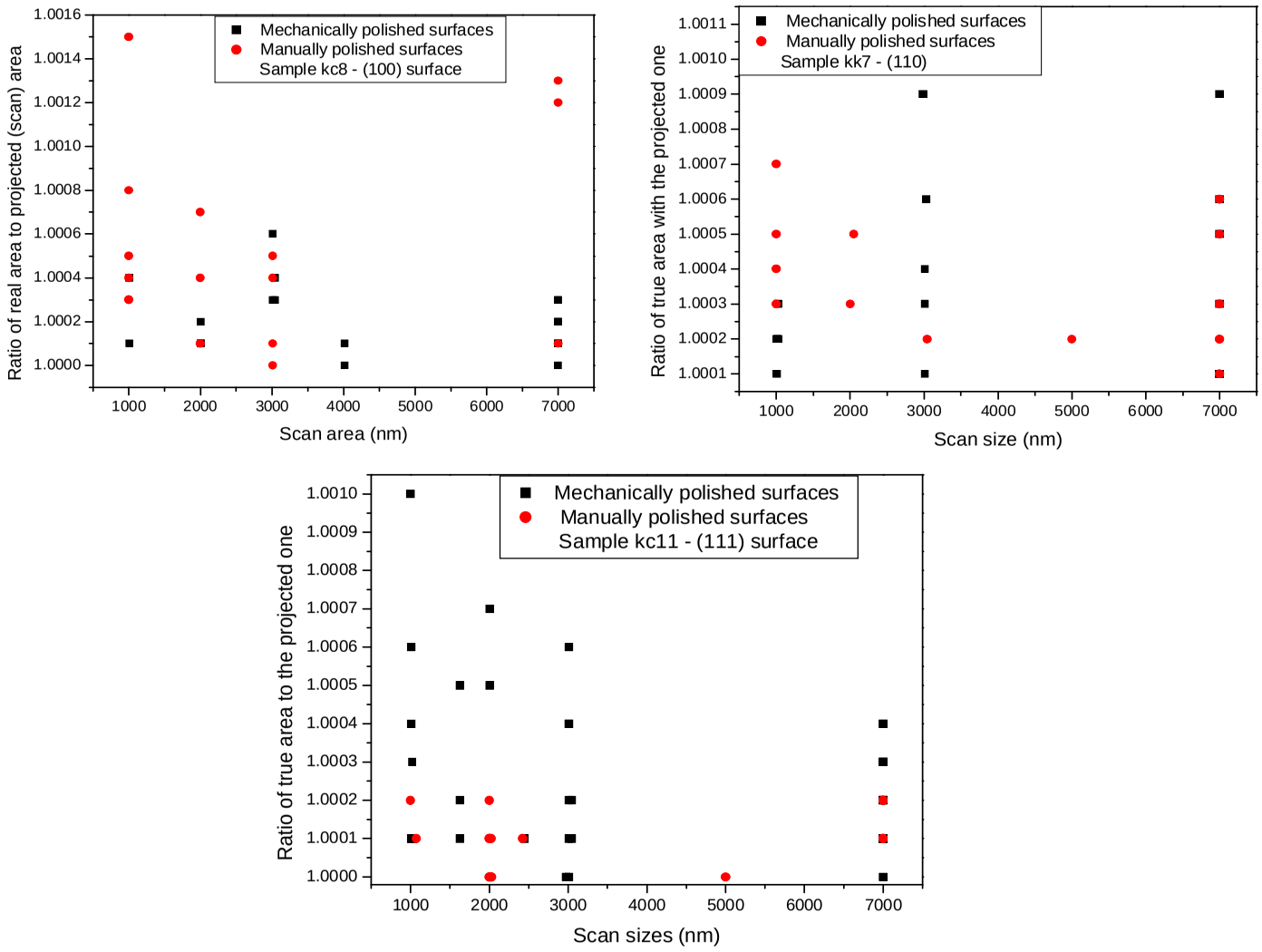


Figure 5.17: Ratio of the true area to the projected one, plotted separately against the scan size for each of the three low index diamond surfaces polished mechanically and manually.

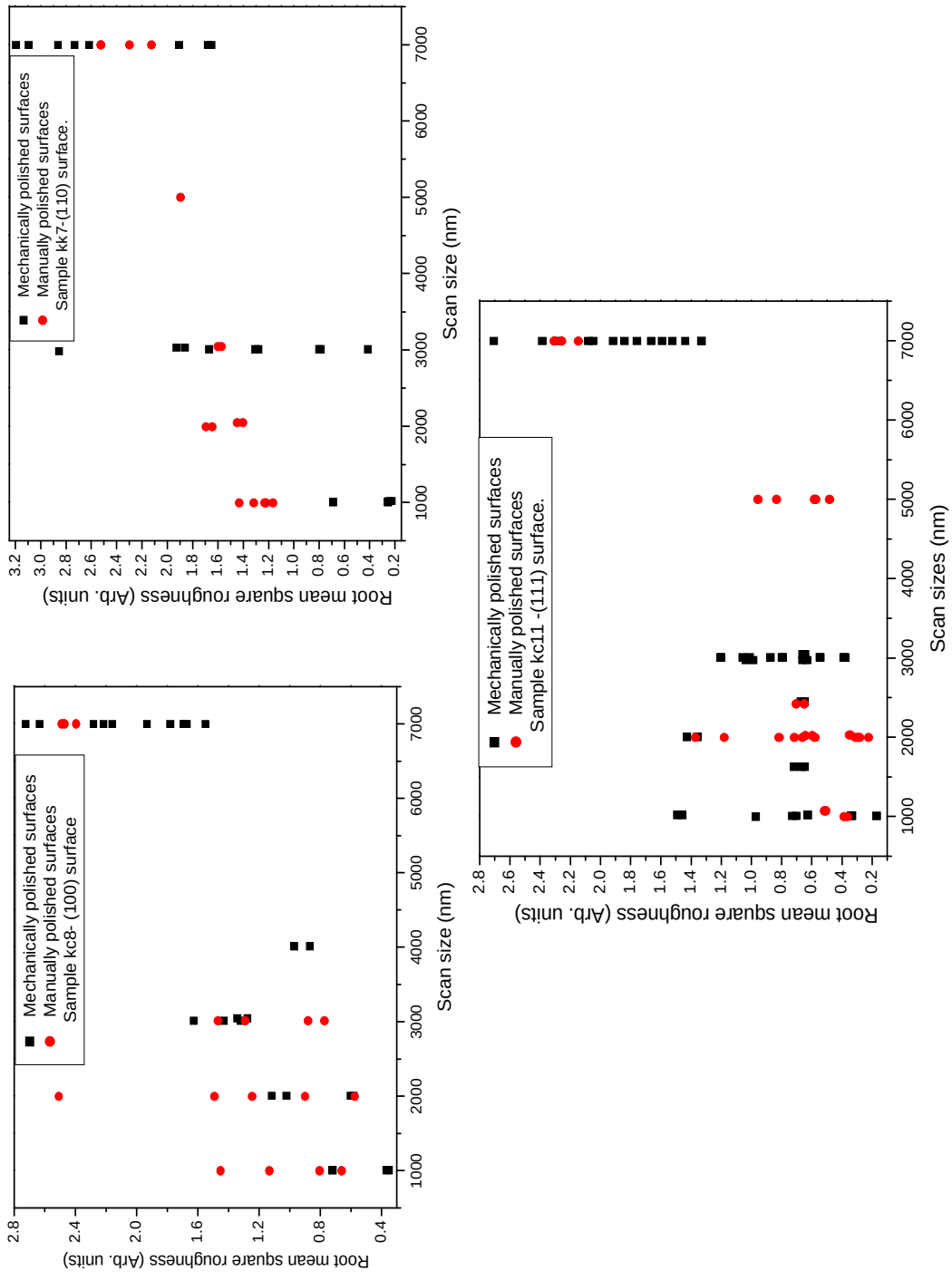


Figure 5.18: Root mean square roughnesses of the three low index diamond surfaces, plotted separately against the scan size. These were polished both mechanically and manually.

5.4 Discussions

The surface roughness was determined in various ways as explained before. Out of these, the line profiles gave the first hints between the surface roughnesses due to the two polishing techniques, where a general variation between the widths and depths of the polishing grooves of the mechanically polished diamond surfaces and those that were given an extra 30 or more minutes of manual polishing were observed. The mechanically polished (100) surfaces were found to exhibit particularly wider grooves than the manually polished ones, and on average the grooves were deeper than those of the manually polished surfaces. On the other hand, the polishing grooves of the mechanically polished (110) surfaces were a bit narrower than those of the manually polished surfaces, and they were also deeper on average than those of manually polished surfaces. The mechanically polished (111) diamond surfaces were found to have wider and shallower grooves than those of the manually polished surfaces. This meant that, the (111) surfaces had grooves that became marginally deeper and smoother after the manual polish. Details of each of the three low index surfaces are given below.

5.4.1 The (100) surface

This is a surface that exhibits a cuboid arrangement of its surface carbon atoms as shown in figure 3.10. A close comparison of its mechanically and manually polished surfaces indicated that the latter appeared generally smoother. From the 2D images (figures 5.3 and 5.4 and others shown in Appendix C), the bar on the right hand side of each image showed that while the general distance between the highest and lowest points (peak to valley) on the surfaces decreased following manual polishing, others showed an increase depending on the size of the images and the asperities present. This indicated that the manual polishing

was actually changing the surfaces by removing and in other cases creating some tiny grooves ($\sim$0.08μm), through the erosion of loosely bound particles. This was accompanied by the removal of particles or debris that were attached at locations which made it easy for them to detach, such as sharp points left behind by the mechanical polishing. The grooves also appeared to become slightly narrower after the manual polishing as seen from figure 5.4 as well as in other AFM images shown in the Appendix (C). Table 5.1 summarizes the range of the widths and depths of the polishing grooves after both mechanical and manual polishing of all the three low index diamond surfaces, while Table 5.2 shows details of the smaller roughnesses. The values shown in the Tables are mainly for the ranges where most of the surface roughnesses were concentrated, but large ones which were also extremely few were observed. These were up to 2.85μm for the mechanically polished surfaces, and up to 1μm for the manually polished ones, and they were observed on all the three low index diamond surfaces. Clearly these large roughnesses were caused by the mechanical and not the manual polishing. The manual polishing only altered them somewhat, resulting in smoother and flat surfaces as discussed in various sections of this work. We need to add here that, we were mostly interested in the smaller roughnesses caused by the manual polishing, and that is why the vertical scale of the power spectra is capped at around 2nm^2 for most of the cases considered here, in order to amply and be able pick these small roughnesses clearly.

Table 5.1: Surface roughness due to the polishing grooves on the three low index diamond surfaces after mechanical and manual polishing.

face	groove widths after mech. polish	groove widths after manual polish	groove depths after mech. polish	groove depths after manual polish
(100)	0.1 to 1.7μm	0.05 to 0.4μm	0.1 to 4.8nm	0.2 to 4.5nm
(110)	0.05 to 0.7μm	0.05 to 1.2μm	0.13 to 7.2nm	0.13 to 5nm
(111)	0.05 to 0.7μm	0.05 to 0.5μm	0.1 to 1.1nm	0.05 to 1nm

The narrowing of the grooves in the case of the (100) surfaces following the

Table 5.2: Smaller surface roughnesses on the three low index faces after mechanical and manual polish.

face	Small roughness widths after mech. polish	Small roughness heights after mech. polish	Small roughness widths after manual polish	Small roughness heights after manual polish
(100)	0.03μm	0.2 to 0.4nm	0.014μm	0.05 to 0.2nm
(110)	0.05μm	0.1 to 0.2nm	0.015μm	0.1 to 0.2nm
(111)	0.05μm	0.1 to 0.2nm	0.03μm	0.05 to 0.2nm

manual polishing was accompanied by the disappearance of some smaller roughness, as seen from the line profiles and the corresponding power spectra shown in figures 5.5 and 5.6, as well as figures C.3 and C.4 (both shown in Appendix C). After the manual polish, some extra smaller and new roughnesses were also observed inside the polishing grooves, which were thought to exist as small indentations caused by the particles as they tumbled through the groove during the polishing process. These are detailed in Table 5.2 for all the three low index surfaces. As such, it is important to appreciate the fact that the high degree of surface smoothness quoted here and in literature does not necessarily imply that the grooves were completely devoid of any features. A majority of the features were 0.2nm in height, which suggested that they were of atomic scale. Some line profiles obtained inside the polishing grooves of the (100) surfaces further showed that they became more curved after the manual polishing, indicating some degree of material removal, and hence smoothing. This was in good agreement with Couto *et al.*'s [82, 63] observations, while others appeared to be flat bottomed as alluded to by Hird *et al.* [54], although not all of them were. However, while this could have been a real effect, it may also have been an artifact caused by the not-so-sharp pyramidal tip as seen in figure 5.1, especially if it was not able to resolve sharp rectangular or v-shaped depressions appropriately. Some AFM images also showed smaller grooves created inside the larger ones. Earlier investigations by Grillo *et al.* [80] indicated that the (100) surfaces polished in the direction of difficult abrasion (the <110>) showed a rough array

of grooves, while those polished in the easy direction (the <100>) exhibited smooth grooves that were often free from indications of fracture. Their findings agree quite well with our observations for (100) surfaces polished manually in the easy direction, where the grooves were found to become generally smooth, with the resultant roughnesses being of the order of those shown in Table 5.1.

Ideally, the line profiles would have had a limitation in providing the required information regarding the surface roughnesses by themselves. These were thus complemented by the power spectra, which further showed that some extra smaller roughnesses which were not easy to observe from the line profiles were introduced after the manual polish. Nonetheless, these had low intensities and were often difficult to observe from the manually polished AFM images. In spite of this, it was still observed in most cases that roughnesses below 0.1μm were often eliminated by the manual polishing. This corresponded to the diamond pastes's particle sizes used in the manual polishing.

Some larger roughnesses of about 0.33μm were occasionally observed inside the grooves of the mechanically polished surfaces, but these too were reduced by the manual polish as seen from the corresponding power spectra. As the smaller roughnesses were removed, the intensity of the remaining longer wavelength roughnesses appeared to increase as seen from the corresponding line profiles and power spectra, which in turn made the root mean square roughness to appear as though it was increasing, while in reality the surfaces were actually getting smoother.

5.4.2 The (111) surface

Not such strikingly noticeable changes were observed in viewing the AFM images of the mechanically and manually polished (111) surfaces, possibly because the (111) diamond surface was generally hard to polish in all directions. These only became apparent after plotting the power spectra and to some extent the

line profiles. It will nonetheless be recalled that the process by which material removal occurs in the (111) surface is different from those of the other two low index diamond surfaces. However, many instances showed some improvement of the surface quality after the manual polish. The polishing grooves did not appear as smooth as those observed in the (100) surface, probably due to the process by which material removal occurs on this surface as opposed to that of the (100) and (110) surfaces. We can therefore postulate that the manual polishing occurred through the erosion of tiny groups of atoms as suggested previously by Couto *et al.* [82, 63], which in turn resulted in the removal of the surface asperities, and therefore reorganizing the surface carbon atoms. This improvement of the surface quality was also in agreement with the earlier findings of Derry *et al.* [117], who reported an improvement of the LEED patterns from their (111) surfaces with the lowering of the electron beam energy, after manual polishing. They concluded this to imply a general improvement of the surface smoothness, which is now confirmed by our AFM work reported in this study.

The line profiles obtained inside the polishing grooves of the (111) surface showed smaller features or roughnesses whose height was between 0.1 and 0.2nm, which were clearly of atomic size as shown in Table 5.2. The widths of the polishing grooves of the manually polished (111) surfaces were comparable to those observed in the manually polished (100) surface, but were narrower than those of the mechanically polished (100) surfaces as summarized in Table 5.1. The values shown in the table are the ranges where most of the surface roughnesses were concentrated. A majority of these had their roughness heights in the lower end of the range, around 0.1 and 0.4nm. However, although the range of the depths of the polishing grooves for the mechanically and manually polished (111) surfaces were almost similar, the manual polishing resulted in slightly deeper grooves on average.

From the line profiles, there was no evidence of flat-bottomed grooves on this surface in most cases (figures 5.13 and 5.14 and others shown in Appendix C) as reported earlier by Couto *et al.* [82, 63, 56] and Hird *et al.* [54] in the case of (100) and (110) surfaces, and also the grooves were less curved than those observed in the (100) surface as seen from figure 5.14 and C.12 (shown in Appendix C).This may have been due to the fact that there was minimal polishing (material removal) taking place on this surface as opposed to either the (100) or the (110) surfaces, and also because the polishing process proceeded differently. These observations were well corroborated by the corresponding power spectra, which showed the disappearance of the high frequency components after the manual polishing.

The power spectra obtained inside the polishing grooves showed that the grooves were devoid of many small bumps (asperities) though not completely, and thus the surfaces were smoother. However, some higher frequency roughnesses were typically observed for the larger scan sizes, and these decreased with scan sizes as shown in the additional images shown in Appendix C. All the power spectra, showed that the intensity of the Fourier components decreased with increasing frequency, meaning that the high frequency (small roughnesses) were becoming less with the manual polishing. Smaller roughnesses of up to 0.05μm were occasionally observed in the mechanically polished surfaces, which decreased to below 0.03μm after the manual polishing (see Table 5.2), and their intensities were always equally small. All the (111) surfaces had comparatively similar amounts of roughnesses in the neighbourhood of 0.1μm after both mechanical and manual polishing. However, slightly more intense (low frequency) Fourier components were observed after the manual polishing, suggesting that although the general surface smoothness improved through the elimination of the tiny roughnesses, the larger wavelength roughnesses became more well defined and therefore intense. It was evident from the line profiles and the power

spectra that the process of material removal from the (111) surface was one of fracture of small groups of atoms, leading to the erosion and reorganization of the surface carbon atoms, as alluded to earlier by other workers, resulting in the smoothing and flattening of the (111) surfaces after manual polishing.

5.4.3 The (110) surface

AFM images obtained from the (110) surface showed deeper, much closer and even more prominent grooves than those of the other two surfaces. This was probably an indication that both mechanical and manual polishing were more effective on this surface. The corresponding line profiles and power spectra shown in figures 5.9 and 5.10 as well as figures C.7 and C.8 (all shown in Appendix C) indicated quite clearly the disappearance of some high frequency components after the manual polish, which was accompanied by a decrease in the intensity of the other components. The line profiles obtained from within the grooves showed very tiny roughness heights of the order of 0.1-0.2nm for both the mechanically and manually polished surfaces (see Table 5.2), which were clearly of atomic size. The line profiles obtained from the manually polished surfaces appeared more curved than the corresponding ones obtained after mechanical polishing, except in a few isolated cases mostly on the smaller scan regions.

The corresponding power spectra not only confirmed these observations, but also showed that more lower frequency (longer wavelength) components were predominantly found on the manually polished surfaces than on the mechanically polished ones, following the disappearance of the high frequency components. Fourier components obtained from within the polishing grooves of both the mechanically and manually polished surfaces, indicated the existence of some bumpy regions as the grit particles tumbled along, while eroding the loosely bound asperities such as those at the raised sharp points, as well as loosely positioned particles or debris left behind by the mechanical polishing.

Through this process, some of polishing grooves became generally wider and fairly smooth after the manual polishing stage as confirmed by the line profiles and the power spectra shown in figures C.7 and C.8 both of which are shown in Appendix C. The mechanically polished surfaces had slightly narrower polishing grooves than the manually polished ones, but these were deeper than those of the manually polished surfaces. Some new grooves were found to develop on the edges/slopes of the wider ones, making them even wider. There was some remote evidence of the grooves becoming flat-bottomed on this surface after the mechanical polishing, but upon the manual polishing, some extra smaller polishing lines were introduced at the bottoms and even sides of the grooves. This could explain why in some instances the overall root mean square roughness appeared to increase after the manual polishing on this surface.

The groove widths and depths are summarized in Table 5.1 where the distinction between the roughnesses of the mechanically and manually polished surfaces is quite evident. The creation of newer and smaller roughnesses on the edges of some of the wider grooves were confirmed by the corresponding power spectra. In this case, it was established that some high frequency (short wavelength) roughnesses between 0.1 and 0.2μm as seen in figures 5.9 (b) and 5.10 (b) were eliminated (or at least diminished) after the manual polishing, leading to the widening of the existing grooves. This resulted in the low frequency components becoming more clearly defined and therefore dominant (see figures 5.7 and 5.8 together with their line profiles and power spectra).

On the other hand, figures C.7 and C.8 (both shown in Appendix C) indicated the disappearance of some high frequency components below 0.1μm after manual polishing, which was accompanied by the creation of a few but marginally intense and well defined new high frequency components whose widths lay between 42 and 62.5nm. These were lacking in the mechanically

polished surfaces, and their creation was accompanied by the low frequency components (bigger roughnesses) becoming more pronounced, intense and clearly defined. One notices almost instantly that the sizes of the grooves were not of the order of the polishing grit particles, suggesting that the polishing was caused by either smaller particles, or by a collection of these as the debris got eroded. Both the line profiles and power spectra showed that, although the groove widths ranged between 0.05 and 1.2μm, on average most of the roughnesses were concentrated between 0.05 and 0.5μm for both the manually and mechanically polished surfaces, with the lower frequency components again showing a marginal increase in their intensities after the manual polishing. As opposed to the grooves associated with the (111) surfaces which were generally fairly flat (i.e. not curved), those from the manually polished (110) surface were mostly curved, which again was an indication of the effectiveness of the manual polishing on the (110) surfaces. The improvement of the quality of the (110) surfaces after the manual polishing arises from the overall changes within the groove widths since this surface had the deepest ones even after the mechanical polish. The bond distortion theory which involves the conversion to non-diamond carbon material seems unlikely here because the forces due to manual (hand) polishing may not have been sufficient to initiate the process. Instead, any surface changes were believed to be due to the rubbing and scratching of the surfaces gently, thereby resulting in the removal of a few atoms or groups of atoms, which led to the observed changes in the surface topography.

Smaller roughnesses of the order of $\sim$0.015μm were observed on the manually polished (110) surfaces, but these were often thought to be too small for the technique's resolution, especially with the tip not being of atomic size, as expected.

The intensities of the smaller roughnesses (i.e. high frequency components) were always quite small on all the three low index surfaces, to the extent that

they could easily have been thought of being errors in the measurements. These were however real, and in approximate agreement with those observed by Couto *et al.* [82, 63], ranging between 20 and 100nm.

5.4.4 Annealed surfaces

Following the manual polishing, the surfaces were annealed under vacuum ($< 10^{-6}$Torr) up to 250°C and again up to 750°C for about 10 minutes each, and then cooled down under similar vacuum conditions to room temperature. AFM images were then obtained from each of the annealed surfaces, where it was found that the overall surface roughness changed quite somewhat from what it was before the annealing, especially at 750°C. AFM images obtained after the annealing process are shown in figures 5.19 and 5.20 for the (100) surface, 5.23 and 5.24 for the (111) surface, as well as 5.27 and 5.28 for the (110) surface, while additional images are shown in Appendix C. Each set of AFM images is followed by their corresponding line profiles and power spectra, for ease of comparison between their smoothness. In figures 5.21, 5.22, 5.25, 5.26, 5.29 and 5.30, the top panels represent the line profiles and power spectra obtained perpendicular to the polishing grooves respectively, while the lower panels show the line profiles and power spectra that were obtained along the polishing grooves.

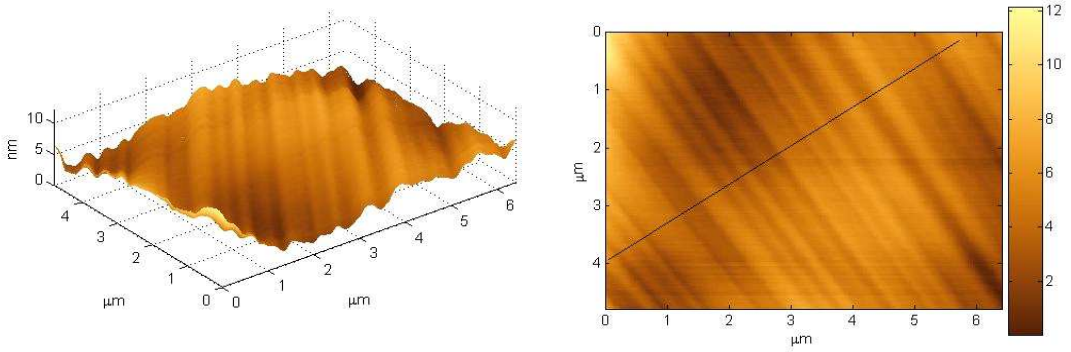


Figure 5.19: Three and two dimensional atomic force microscopy images of a (100) surface annealed to 250°C after manual polishing (sample kc8).

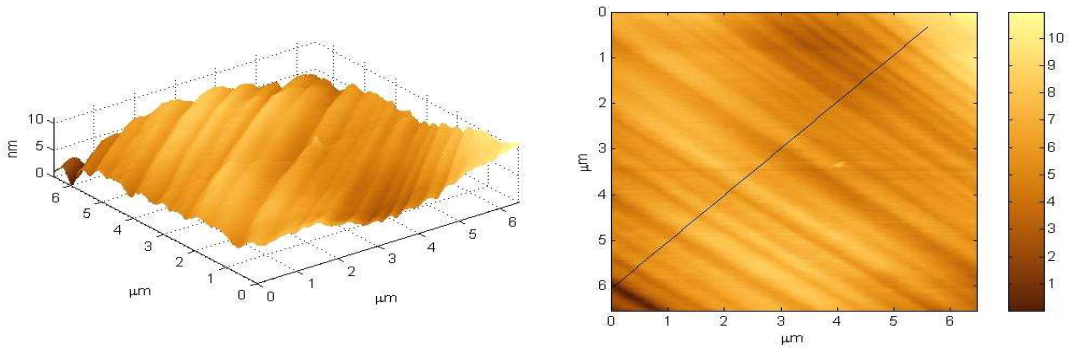


Figure 5.20: Three and two dimensional atomic force microscopy images of a (100) surface annealed to 750°C after manual polishing (sample kc8). The bar on the RHS shows a marginal decrease of 2nm in the peak-to-valley distance after the 750°C anneal compared to the 250°C anneal shown in figure 5.19.

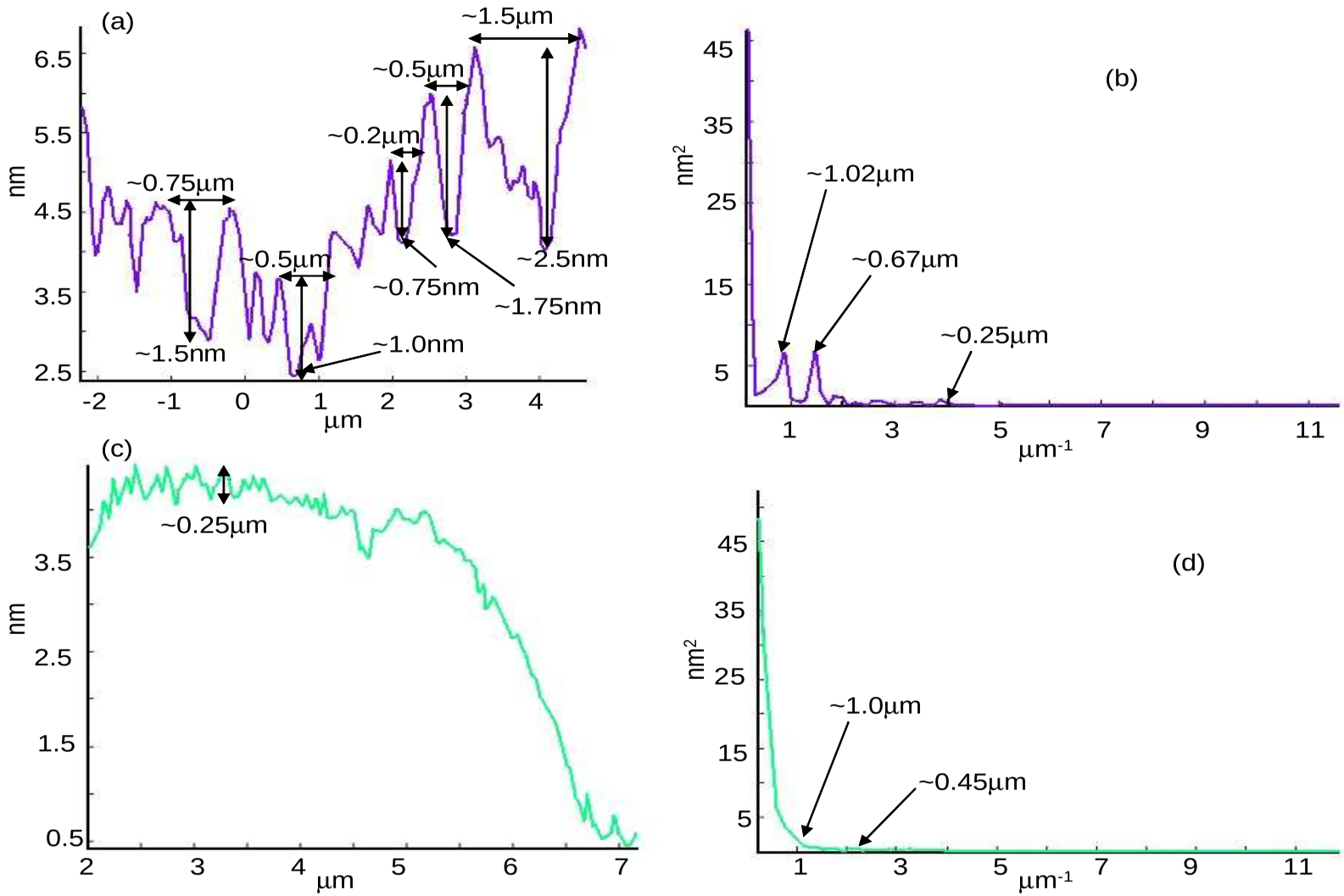


Figure 5.21: Line profiles and power spectra for the (100) surface whose AFM image is shown in figure 5.19. This was polished manually, and then annealed in vacuum upto 250°C. Graph (a) shows the line profile obtained perpendicular to the polishing grooves, while (b) is its corresponding power spectra. Graph (c) is the line profile obtained inside the polishing grooves, while (d) is its power spectra.

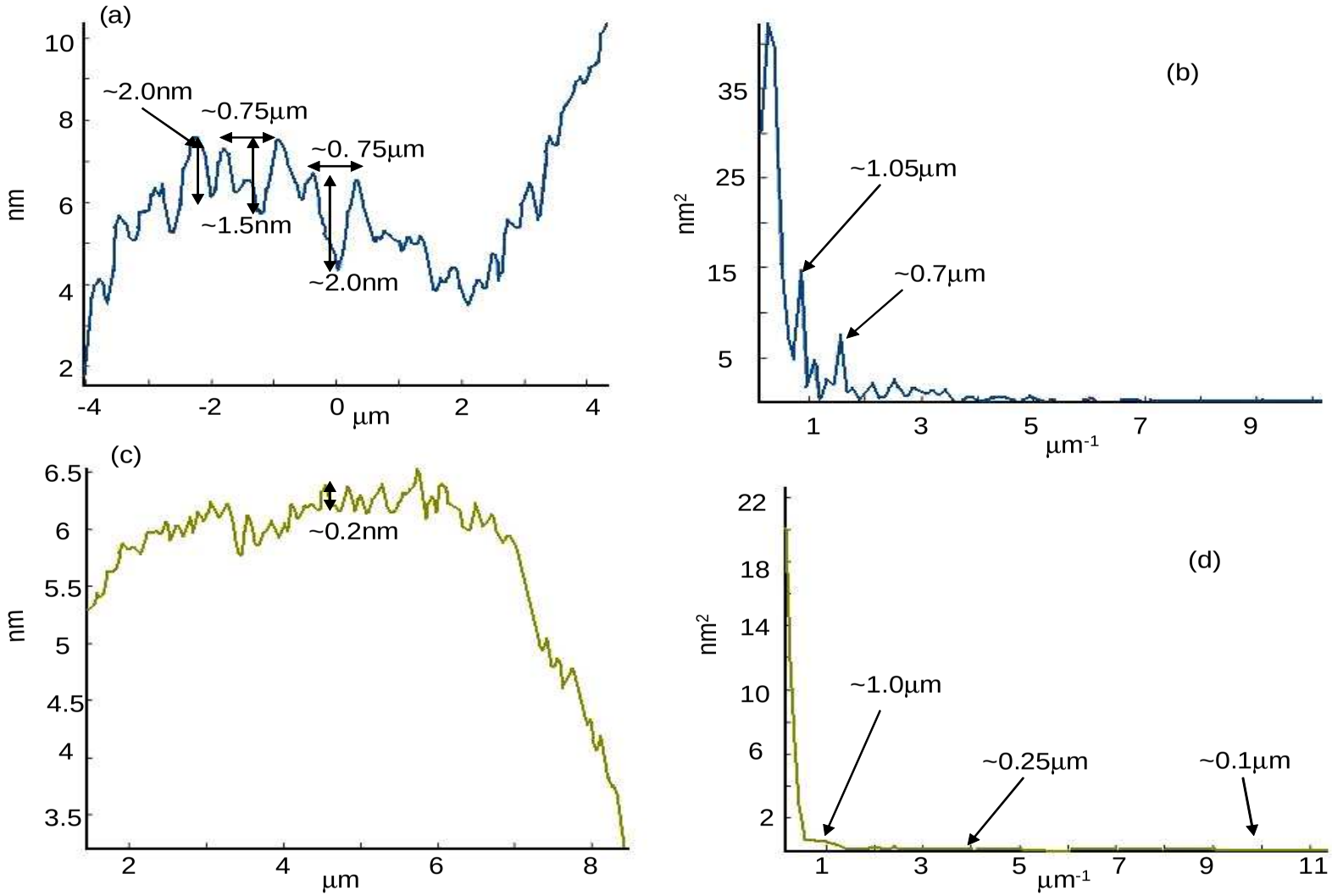


Figure 5.22: Line profiles and power spectra for the (100) surface whose AFM image is shown in figure 5.20. This surface was polished manually and then annealed upto 750°C. Graphs (a), (b), (c) and (d) are similar to those described in figure 5.21. Note the marginal shallowing after the 750°C anneal (figures 5.21 (a) and 5.22 (a) obtained from AFM images of almost equal size).

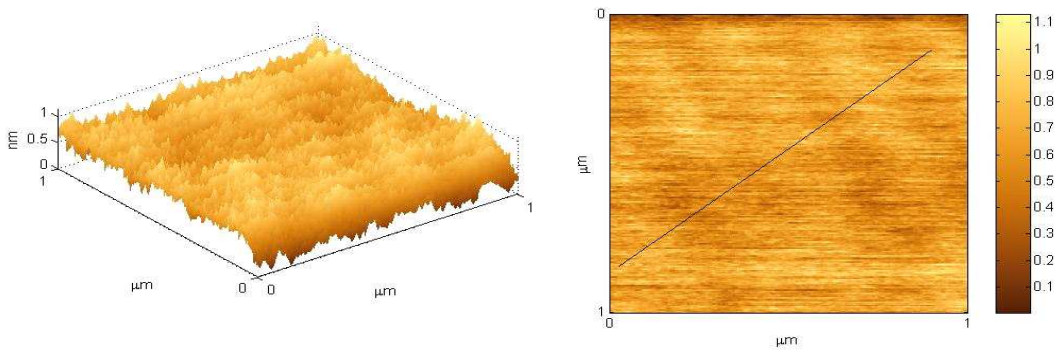


Figure 5.23: Three and two dimensional atomic force microscopy images of a (111) surface annealed to 250°C after manual polishing (sample kc11).

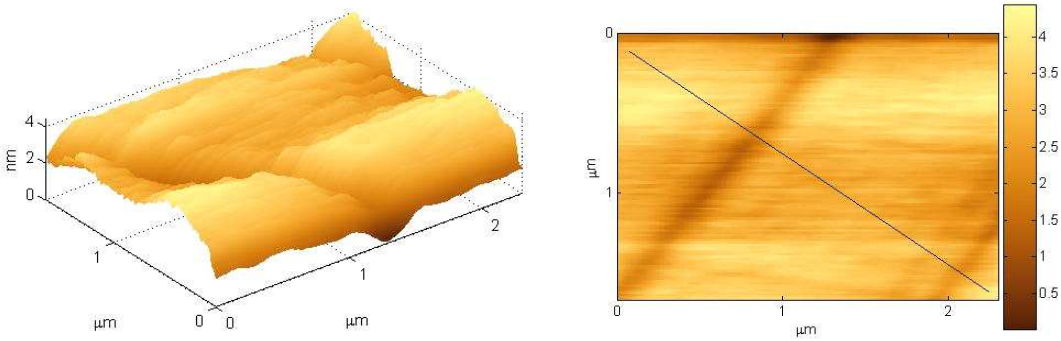


Figure 5.24: Three and two dimensional atomic force microscopy images of a (111) surface annealed to 750°C after manual polishing (sample kc11).

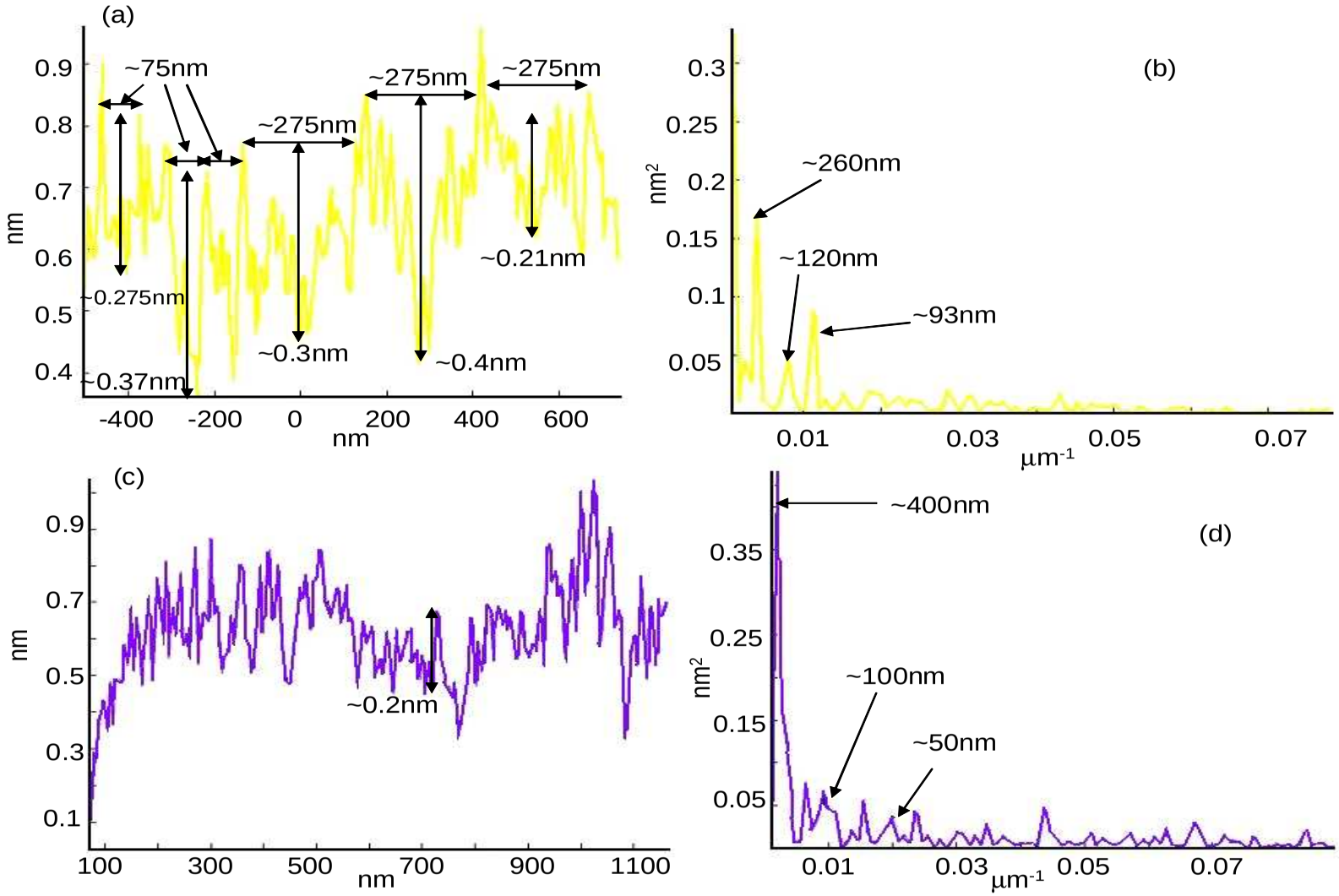


Figure 5.25: Line profiles and power spectra for the (111) surface whose AFM image is shown in figure 5.23. This was polished manually and then annealed under vacuum upto 250°C. Graphs (a), (b), (c) and (d) are similar to those described in figure 5.21.

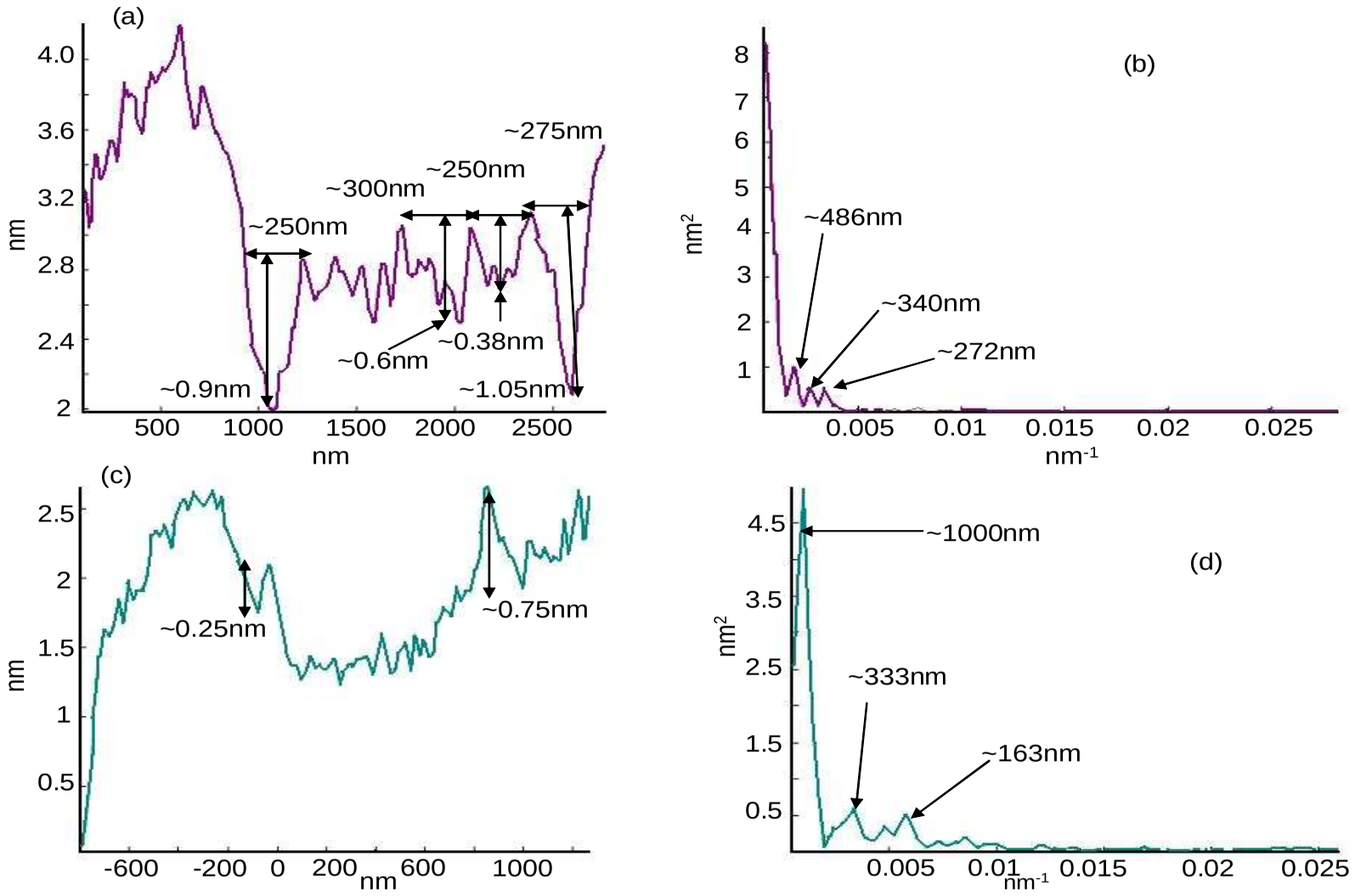


Figure 5.26: Line profiles and power spectra for the (111) surface whose AFM image is shown in figure 5.24, which was polished manually and then annealed upto 750°C. Graphs (a), (b), (c) and (d) are similar to those described in figure 5.21. Note the loss of some roughnesses and the deepening of the grooves after the 750°C anneal (figures 5.25 (a) and 5.26 (a)), which is corroborated by the power spectra where components above 0.27μm became fairly prominent and more intense.

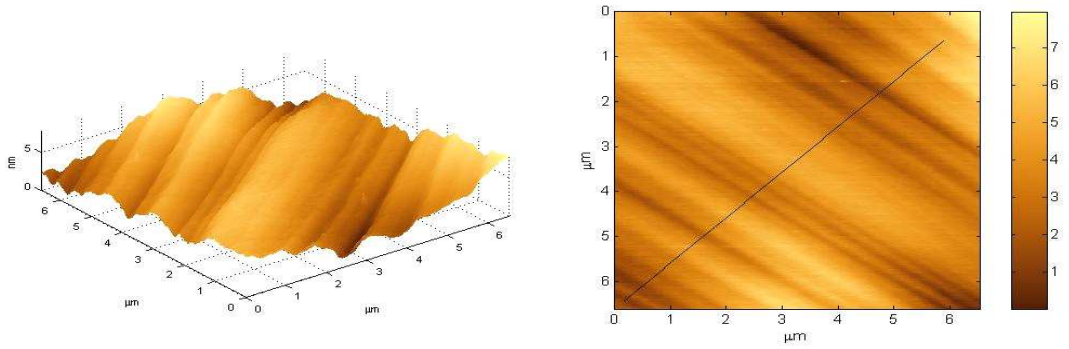


Figure 5.27: Three and two dimensional atomic force microscopy images of a (110) surface annealed to 250°C after manual polishing (sample kk7).

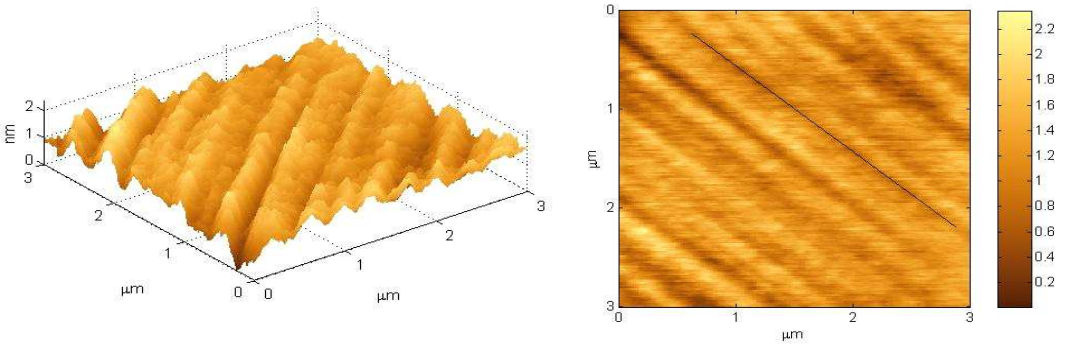


Figure 5.28: Three and two dimensional atomic force microscopy images of a (110) surface annealed to 750°C after manual polishing (sample kk7).

Annealing the surfaces under vacuum up to 250°C did not result in much changes within the surface roughness of all the three low index faces, but this became more pronounced when the temperature was raised to 750°C as seen from the respective AFM images. Such results were interpreted to mean that annealing up to 250°C possibly only got rid of the physisorbed and loosely bound species that were not expected to change the surface topography significantly, whereas annealing to 750°C resulted in the dissociation of the adsorbed species, which in the process left the surfaces rougher and etched out as observed by Bobrov *et al.* [143, 125]. However, although the vacuum conditions above the annealed diamond surfaces was not so high, it was expected that the desorption

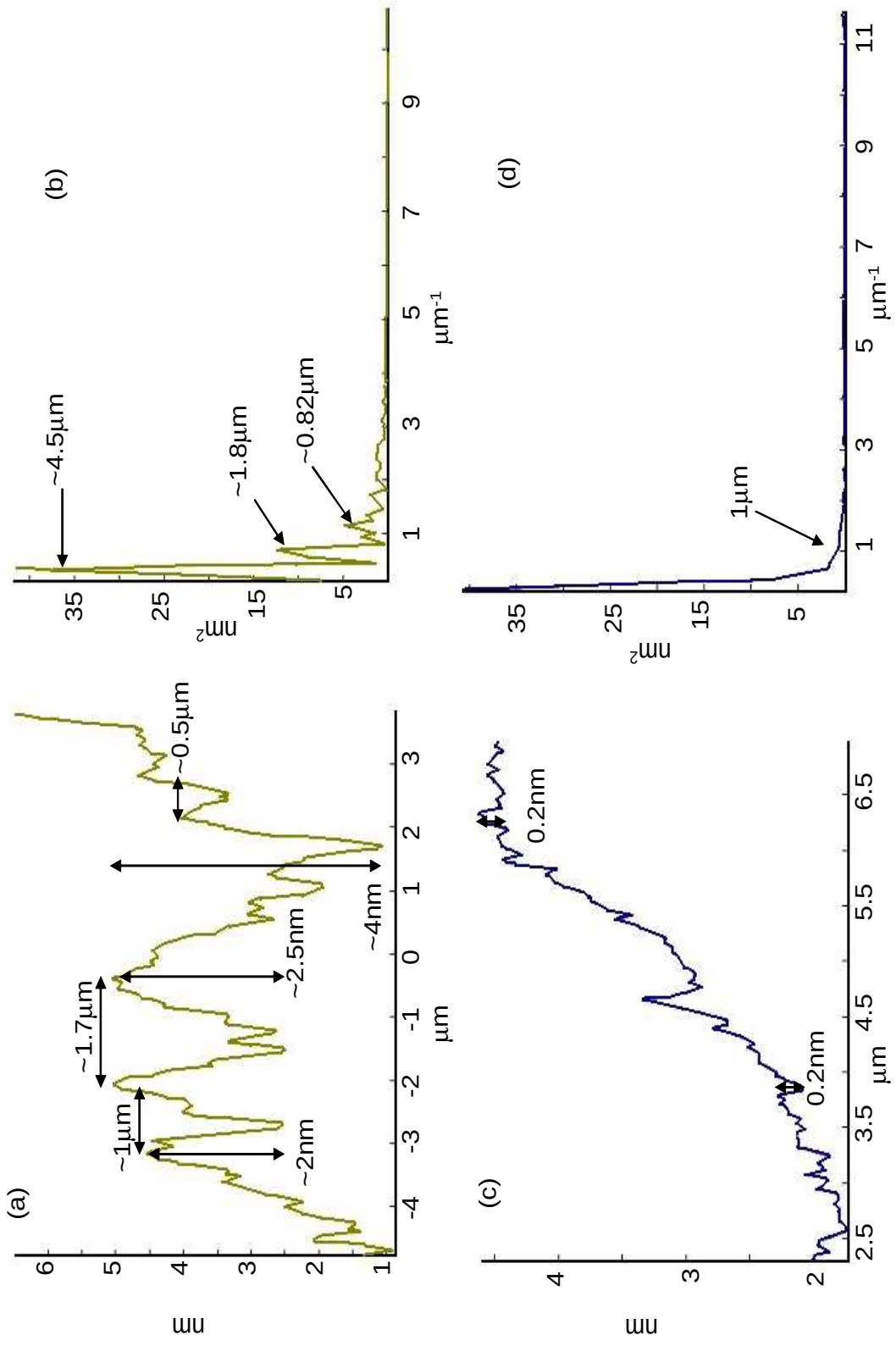


Figure 5.29: Line profiles and power spectra for the (110) surface whose AFM image is shown in figure 5.27. This surface was polished manually and then annealed under vacuum upto 250°C. Graphs (a), (b), (c) and (d) are similar to those described in figure 5.21.

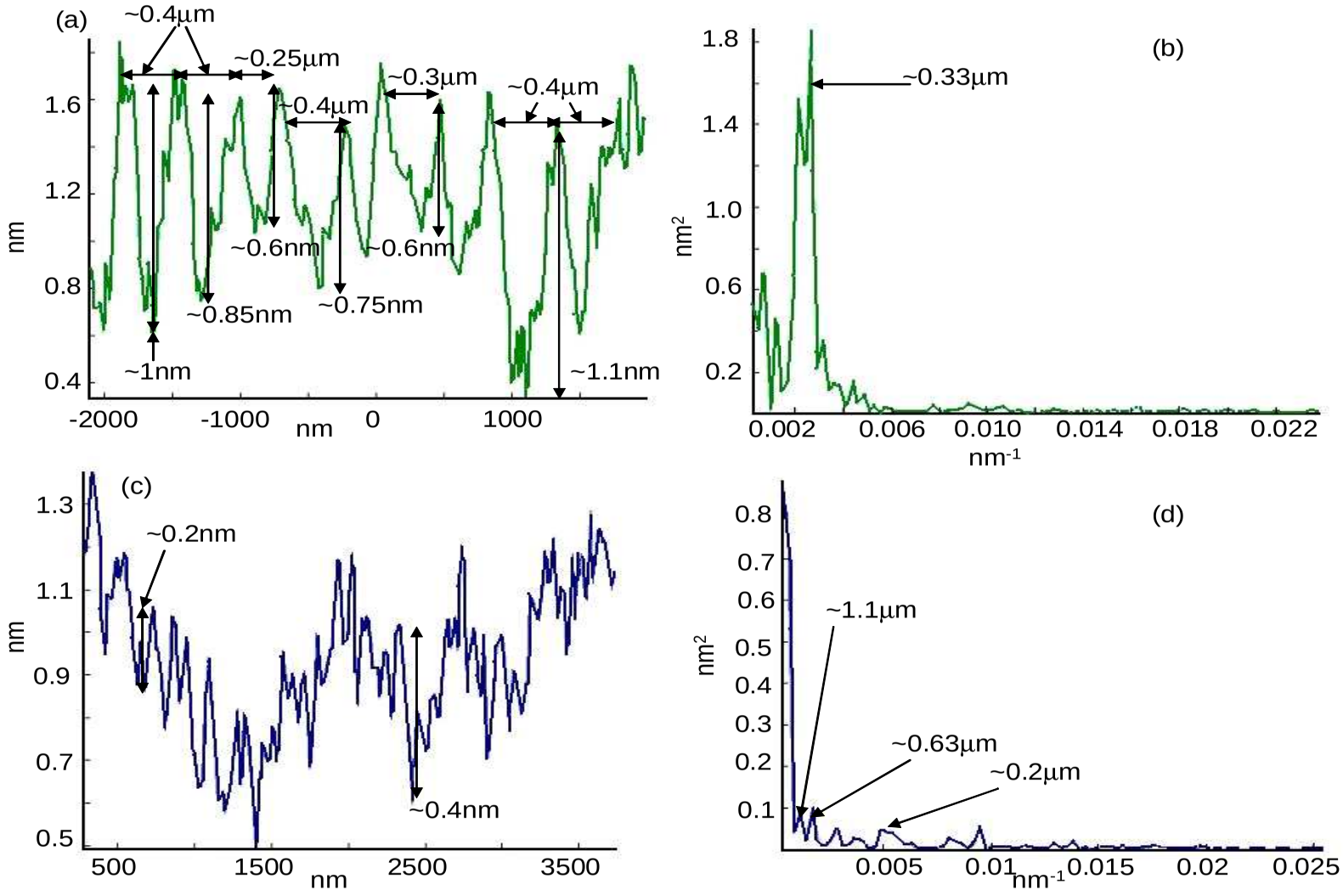


Figure 5.30: Line profile and power spectra for the (110) surface whose AFM image is shown in figure 5.28. The surface was polished manually and then annealed upto 750°C. Graphs (a), (b), (c) and (d) are similar to those described in figure 5.21. Note the prominence of the grooves after the 750°C anneal (figures 5.29 (a) and 5.30 (a)), just like in the AFM images themselves (figures 5.27 and 5.28), accompanied by shallowing and narrowing of the grooves.

rate would be low since Derry *et al.* [94] observed previously that oxygen on diamond surfaces desorbs slowly in ultra high vacuum conditions, and rapidly on warming.

The surfaces were only annealed up to 750°C, since this temperature was not expected to induce any graphitization on them, because in addition to damaging the surface, if this happened, the hard Si_3N_4 AFM tip would have left other unwanted scratch marks on the soft graphitic layer as it scanned along the surface. Although long known, Derry *et al.* [94] noted that graphitization of diamond occurs in oxygen atmospheres at temperatures higher than 800K, but in our case the surfaces were annealed under vacuum ($\approx 10^{-6}$Torr) up to 250 and 750°C, and for these reasons, no graphitization was expected. This temperature was nonetheless sufficient to lead to the desorption of the adsorbed oxygen and possible hydroxyl groups, thus resulting in an etched surface. Baumann *et al.* [203] found that the annealing of diamond (100) surfaces to 500°C did not affect significantly the Auger electron spectroscopy peak, and a LEED measurement showed a bulk terminated (1×1) pattern. For this reason, our annealing to 250°C was not expected to have much effect on the adsorbed oxygen, but this heating was still vital in establishing and confirming what happens under these relatively low temperature conditions. According to Baumann *et al.* [203] annealing the (100) surface to 1150°C results in the disappearance of the oxygen feature, and a (2×1) reconstructed clean surface is observed. For both the (110) and (111) diamond surfaces, they observed that the adsorbates were completely desorbed at 1150°C.

AFM images obtained from the (100) surfaces together with their corresponding line profiles and power spectra showed a remarkable difference between annealing to 250 and 750°C. The polishing grooves apparently became more pronounced following the 750°C anneal than they were at 250°C according to figures C.13, C.14 and C.15 (shown in Appendix C). The widths and depths

of the polishing lines following annealing up to the two temperatures are shown in Table 5.3. For the (100) surface, the groove depths were apparently slightly

Table 5.3: Surface roughness due to polishing grooves on the three low index faces polished manually and then annealed to 250° and 750°C.

face	250°C Groove width	250°C Groove depth	750° Groove width	750°C Groove depth
(100)	0.1 to 1.5μm	0.1 to 2.5nm	0.08 to 1.0μm	0.2 to 2.5nm
(110)	0.08 to 1.2μm	0.25 to 2.5nm	0.08 to 0.6μm	0.2 to 1.2nm
(111)	0.06 to 0.4μm	0.1 to 0.4nm	0.1 to 0.35μm	0.2 to 1.4nm

shallower after the 750°C anneal, but wider than they were after the manual polishing and no annealing as shown in Table 5.1. On average the grooves on the (100) surfaces became narrower after the 750°C vacuum anneal than they were at 250°C. Incidentally the widths of the polishing grooves for the 250°C compared well with those of the mechanically polished surfaces but were wider than those of the manually polished surfaces. Their depths also compared quite well with those of the mechanically and manually polished surfaces, except for a few cases where large depths of 4.8 and 4.5nm were observed for the unannealed but mechanically and manually polished surfaces respectively. Following the 750°C vacuum anneal, the low frequency (long wavelength) components became slightly more and also well defined, meaning that the high frequency (short wavelength or small roughnesses) were removed. The corresponding line profiles obtained inside the polishing grooves of the annealed surfaces (upto 250 and 750°C) showed atomic-scale roughnesses whose heights were between 0.1nm and 0.25nm. These compared quite well with those observed previously for the unannealed surfaces, meaning that not much change occurred here, or in this range. It could also mean that since these roughnesses were at the highest resolution of the technique, they could not get any lower than this. Some of the (100) surfaces had some small depressions on the larger polishing grooves which occurred as new grooves or steps on the edges/slopes (see for example

figure C.15 shown in Appendix C), suggesting evidence of grit particles rubbing and eroding material from them.

The power spectra on the other hand showed similar results to the AFM images themselves and the line profiles, where the low frequency components below 0.5μm become more intense and broader after annealing to 750°C than they were at 250°C. However, figure C.17 (shown in Appendix C) which was obtained from a (100) surface that was annealed to 750°C showed some extra high frequency components compared to those observed in figure C.16 (also shown in Appendix C and annealed to 250°C), although their intensities were greatly reduced. In addition, the power spectra obtained inside the corresponding polishing grooves showed that some of the high and even low frequency components were removed after annealing to 750°C corroborating the broadening of some peaks (roughnesses) noted in the power spectrum obtained perpendicular to them. Figure C.16 (obtained from figure C.13) which represented results from a (100) surface annealed to 250°C showed extremely few components inside the grooves, suggesting a smoothing of the grooves. In general, the line profiles and power obtained inside the polishing grooves as shown in figures C.16, C.17 and C.18 (all shown Appendix C) revealed that the (100) surfaces did not develop any more high frequency roughness after annealing to 750°C, than at 250°C anneal, except the narrowing of the grooves as summarized in Table 5.3.

Annealing the (111) surfaces to both 250 and 750°C, did not reveal much difference between the two temperature regimes as is evident from a casual look at the AFM images themselves as shown in figures 5.23, 5.24, C.19 and C.20, except that the roughness bars next to the respective 2D images shows a difference of about 3nm from peak-to-valley after the 750°C anneal. What was undoubtedly clear though was that annealing seemed to have had a small effect on the (111) surfaces as opposed to the other two low index faces, with the surface appearing fairly smoother. This could have been an indication that

the surface atoms as well as the adsorbates on them were strongly bonded on this surface and hence desorption would be hard, implying that etching through annealing would also be correspondingly minimal. The widths and depths of the grooves on this surface [(111)] after annealing to 250 and 750°C are summarized in Table 5.3. These were in principle the same when quoted to one significant figure, while the depths varied quite significantly between the two temperature regimes. In the case of the 750°C anneal, most of the roughness widths lay around 0.2μm, although the entire range spanned between 0.06 and 0.4μm. As such, the widths of the polishing lines from the 250°C anneal were comparatively similar to those at 750°C but were generally shallower than those of the 750°C anneal and those of the mechanically polished surfaces. Their widths also compared with those of the manually polished surfaces but they were a bit shallower than those of the manually polished surfaces.

Figure 5.26 showed that the smaller roughnesses which were observed at 250°C disappeared after annealing to 750°C, and only components above $\sim$0.3μm were more visible. The intensities of the components observed at 250°C anneal were also very small. A similar observation was also made in figures C.21 and C.22 which are shown in Appendix C, where some of the faint (low intensity) high frequency components which were observed in the case of the 250°C anneal disappeared after annealing to 750°C. This was accompanied by the low frequency components above 0.272μm becoming somewhat more intense and well defined, which possibly suggested the broadening of the same.

The line profiles obtained inside the polishing grooves showed roughness heights in the range of 0.1 and 0.2nm for the surfaces annealed to 250°C, and predominantly 0.25nm for those annealed to 750°C, although the groove bottoms appeared rather rugged, and fairly flat (i.e less curved), with some smaller roughnesses being eliminated at 750°C. This was in agreement with the corresponding power spectra, where it was established that newer roughnesses were

introduced below 0.16μm after annealing the (111) surface to 750°C as seen in figure 5.26, while those that were observed around 0.1μm as seen in figure 5.25 for the 250°C anneal diminished. The same behaviour was observed in figures C.21 and C.22 shown in Appendix C, where new components around 0.54 and 0.27μm became slightly more prominent than they were after 250°C anneal. The number of components inside the polishing grooves were also few and less intense. High frequency components were seldom found, either at 250°C or 750°C on the (111) surfaces. Figure 5.26 on the other hand, which represents a (111) surface that was annealed to 750°C indicated the appearance of smaller roughnesses at 0.33 and 0.16μm which were apparently lacking in the corresponding surface annealed to 250°C (figure 5.25). In addition, the power spectra that were obtained inside the polishing grooves showed that although quite small, the roughnesses that were observed at around 0.01nm^{-1} (0.1μm) for the surface annealed to 250° C disappeared after annealing to 750°C. In general, the (111) surfaces appeared to become only somewhat rougher when annealed to 750°C than they were at 250°C anneal, and in the process, the low frequency components became well defined. These may have the consequence of increasing the root mean square roughnesses.

The annealing process seemed to have had a more pronounced effect on the (110) surface after the 750°C anneal than it was for the 250°C anneal, possibly because it had the deepest grooves even before the annealing process commenced. The polishing grooves became more prominent after annealing to 750°C than they were at 250°C and the line profiles also showed varying degrees of widths and depths for the polishing grooves as shown in Table 5.3. From the AFM images themselves, the widths of the grooves appeared more regular after annealing to 750°C than they were at 250°C as seen in figures 5.27 and 5.28 as well as in figures C.37 and C.35 (both shown in Appendix C) respectively, and others shown in Appendix C too. The 250°C anneal resulted in slightly wider

polishing grooves than the mechanically polished and unannealed ones, but almost similar to those that were polished manually. This was not unexpected because the 250°C anneal did not change the surface roughness much than it was after the manual polishing. The polishing grooves from the 250°C anneal were also shallower than those of the mechanically and manually polished surfaces on average (see Table 5.1) but they were slightly wider than those of the 750°C anneal, and on average the depths of the polishing grooves were comparatively deeper for the 250 than 750°C anneal. The corresponding line profiles obtained inside the polishing grooves showed roughness heights of between 0.2 and 0.4nm for the surfaces annealed to 750°C and therefore being a bit rugged and rougher, compared to roughnesses that were predominantly 0.2nm for the (110) surfaces that were annealed up to only 250°C. This behaviour was nonetheless not unique to the (110) surfaces but was also witnessed across all the three low index faces. In some cases, a few smaller roughnesses were observed inside the wider grooves or on their edges, while in other cases, grooves whose widths were of the order of the polishing diamond pastes's particle sizes used in the manual polishing (0.1 and 0.25μm) were also observed.

The power spectra obtained perpendicular to the polishing grooves showed low frequency components at $\sim$1.0μm (figure 5.29) for surfaces annealed to 250°C thereby showing good agreement with the line profiles. Those obtained from surfaces annealed to 750°C showed components at around 0.33μm (figure 5.30), which also had an extremely low intensity compared to the ones seen in the surfaces annealed to 250°C. Clearly the high temperature anneal had a remarkable effect within the (110) surface as opposed to the other two low index faces. Power spectra obtained inside the polishing grooves as seen from figures 5.29 and 5.30 showed a similar trend, where low frequency components were observed above $1(\mu\text{m})^{-1}$ for surfaces annealed to 250°C, while these diminished quite significantly for surfaces annealed to 750°C. This was quite intriguing, and

an indication of some of the grooves actually getting etched out and becoming smoother at high temperatures, with a regular array of roughnesses (polishing grooves) following the removal of some of the components. Nonetheless, not all (110) surfaces showed this improvement in quality with the high temperature vacuum anneal.

Lack of major surface etching and roughening in all the three low index diamond surfaces following the 750°C anneal was a possible indication that some of the adsorbed species were not completely desorbed at this temperature, which was consistent with earlier explanations.

5.4.5 Root mean square roughnesses of the polished surfaces and ratios of the real area to the scan size; for unannealed and annealed surfaces.

Just like the line profiles and the power spectra and even the AFM images themselves, the ratios of the real areas to the projected ones, as well as the root mean square roughnesses were an important measure of the surface quality, regarding the overall roughness and smoothness. As mentioned before, by comparing the real surface areas to the scan regions as shown in figures 5.15 and 5.17 (for surfaces that were not annealed), it was possible to establish whether new roughnesses were created or not after the manual polishing. This complemented the results already obtained in the line profiles and power spectra. Any new roughnesses were expected to manifest themselves through the increment of the real area, and therefore the ratio of the true area to the projected one too. Nonetheless, the polished surfaces are already known to be quite smooth, and therefore the changes anticipated from the manual polishing were likely to be extremely small. This would effectively make the ratios of the areas to be quite close to 1.0, but obviously greater than or equal to this value due to the

presence of the surface features, such as the rugged polishing grooves among others. In spite of this though, some differences between the mechanically and manually polished surfaces were still observed.

At a glance, the mechanically polished (111) surfaces were seen to be a bit rougher than their corresponding manually polished surfaces, based on the ratios of the areas. The evidence of surface improvement with manual polishing was not outrightly clear for the manually polished (100) surfaces as shown in figures 5.15 and 5.17.

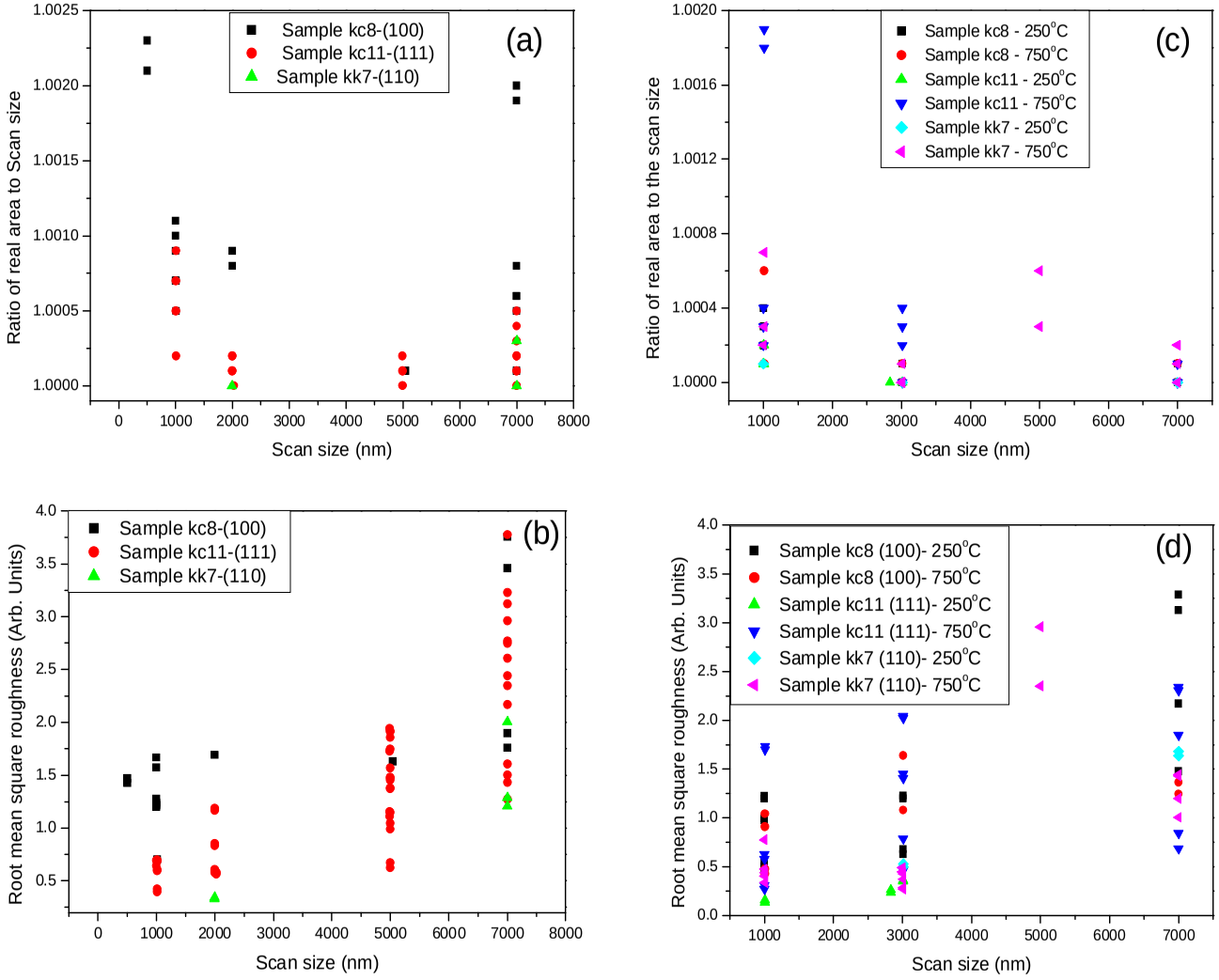


Figure 5.31: Ratios of the real area to the scan size as well as the corresponding RMS roughness for diamond surfaces annealed up to 250 and 750°C (panels (c) and (d)) and those of surfaces polished manually for about an hour (panels (a) and (b)).

However, in some cases (for example figure 5.18), there was some evidence of modest improvement in the surface quality through decreased RMS roughnesses, especially when one considers the intermediate and larger scan sizes. At the same time, the manually polished (110) surfaces were clearly better than the mechanically polished ones, meaning that the manually polished surfaces were generally more flat than the corresponding mechanically polished ones. However, on comparing these with a mechanically polished (100) synthetic diamond surface, it was found that the synthetic diamond was rougher than all the polished natural diamond samples, whether mechanically or manually polished (see figures 5.15 & 5.16). It was only the mechanically polished (110) surface that appeared slightly worse than these, especially at larger scan regions. This result of the quality of the synthetic diamond's surface being worse was however not wholly unexpected because the natural diamond surfaces had undergone several cycles of mechanical and manual repolishing when they were used for other studies previously, unlike the synthetic diamond. This suggests that repeated polishing and repolishing using finer grades of diamond grit particles would eventually result in much smoother and better quality diamond surfaces. In fact figure 5.31 (a) which was obtained from surfaces that were polished manually for about an hour confirmed this, except in only a few cases involving the (100) surfaces. In this case, the maximum ratio of the areas was 1.0032 when data for the synthetic (100) diamond sample was included, decreasing to below 1.0022 for the manually polished single crystal natural diamonds. Most of the surfaces showed some slight improvement in their overall surface smoothness with the extra manual polishing. These findings were consistent with most of the corresponding root mean square roughnesses shown in figure 5.31 (b), where it was again found that the RMS roughnesses reduced slightly with the extra manual polishing.

Regarding the RMS roughnesses of the respective faces, the manually polished (100) surfaces were only better than the mechanically polished synthetic (100) diamond surfaces, but worse than those of the mechanically polished (111) surfaces. This was followed by the mechanically and manually polished (110) surfaces, together with the manually polished (111) surfaces. These had the ratios of their areas being approximately equal to 1.0 which was confirmed by the corresponding RMS roughnesses. It is worth emphasizing though that the changes observed in the ratios of the areas and hence the corresponding roughness had to be complemented by the observations made within the line profiles, as well as the power spectra, in order for them to be considered conclusive. This was particularly important because it may happen that after the manual polishing, the surfaces became more curved after removing or introducing the smaller roughnesses as seen from the curvature of the line profiles, thereby increasing the true surface area, but certainly not necessarily making the surfaces rougher. As such, both the ratios of the true and projected areas, the line profiles, and the power spectra had to show some common agreement for the findings to be convincing.

While they may not have been entirely a true measure of the quality of the surface smoothness on their own, the root mean square roughnesses were still vital parameters for gauging the flatness of surfaces polished in the two different ways. These confirmed that the mechanically polished synthetic diamond was much rougher than all the others as seen from figure 5.16 (a), followed by the mechanically polished (110) and (111) surfaces, then the manually polished (100) surfaces. It should be noted that the sort of roughnesses that are considered at these resolutions are very small indeed, being at least three orders of magnitude smaller than the x and y-axis scales of the 3D AFM images. Apart from the ambiguities noted in some of the manually polished (100) surfaces, a general improvement of the surface roughness was observed for most of the

manually polished surfaces.

The changes observed in the RMS roughnesses implied that either newer small roughnesses were introduced by the manual polishing or that the surfaces became smoother with the low frequency (or long wavelength) components dominating, which led to the general increase in the values of the RMS roughnesses. It is however important to emphasize that, although the same polishing direction used in the mechanical polish was maintained for the manual polish, there were instances where attendant difficulties made it unlikely to always maintain this direction during the entire manual polishing period, and in the process, possibly introducing newer roughnesses that were not parallel to the polishing direction. However, lines crossing the polishing grooves were not observed here nor in the optical micrographs, except in some occasional small-angle branching of the grooves, but this was not to rule out the possibility of introducing such crossing polishing lines entirely, if at all the direction of polishing changes.

A plot of the root mean square roughness with the scan size for smaller scan regions as shown in figures 5.16 (c) and (d) showed large differences between the mechanically and manually polished (100) surfaces, especially at the larger scan sizes due to the presence of many surface features.

In addition, although some scatter was observed in the RMS roughness of the manually and mechanically polished surfaces in almost all cases, both the manually polished (111) and (110) surfaces appeared much better than those polished mechanically. Average RMS values of below $\sim$3nm were observed for the manually polished (100) surfaces, while these were on average below 2.0nm for the (111) and (110) surfaces. One notices from the onset that the roughnesses were extremely small, and even a tiny change in the surface topography could have had a significant effect on the overall RMS value. On the other hand, the ratio of the true area to the scan size also confirmed the observations made earlier in the RMS values, where it was established that the manually polished

surfaces were generally better (see figure 5.17) except the (100) surface where the evidence was rather ambiguous. Furthermore, a plot of the root mean square roughness of each individual face with the scan size as shown in figure 5.18 revealed that the manually polished (111) surfaces were clearly better than the mechanically polished ones. This was a clear indication that the manual polishing was indeed changing the surface topography in a way that made them smoother as confirmed earlier by the line profiles and the power spectra and even the ratios of the areas (see figure 5.17). Again, for larger scan regions, features that were not necessarily part of the surfaces such as dust particles attached to the surface or contributions from the AFM tip may have had an affect on the root mean square roughness. Besides, from a fundamental point of view of the way in which the RMS roughnesses were obtained, one clearly notices that a few big wave-like (sinusoidal) features or roughnesses may actually have the same RMS value as that of many small ones. This is why we allude to the fact that the RMS values could not be used as a measure of the surface roughness on their own, and can only be considered credible if they showed agreement with the line profiles as well as the power spectra, and if possible the AFM images themselves and the ratios of the areas. Looking at both the ratios of the true area to the projected one as shown in figure 5.17, both the manually polished (111) and (110) surfaces appeared quite smooth with average values of $\sim$1.0001 and 1.0005 respectively, compared to the expected value of 1.000. This was further confirmed by the RMS roughnesses shown in figure 5.18, where the corresponding RMS values for the two surfaces decreased on average to about 0.8 and 1.6nm respectively, while their maximum RMS roughnesses were 2.7nm and 3.1nm respectively.

Judging from the ratios of the areas and the RMS values, it was very likely that greater regions of the surfaces were dominated by the low frequency (i.e. long wavelength) components after the manual polishing, while only a few other

regions had the high frequency components (smaller roughnesses). Such an observation was made previously in some of the optical micrographs, where certain regions were found to consist of thick dark and bright bands while others had closely packed dark and bright thin bands, which represented the deep (grooves) and raised regions of the surfaces respectively. The corresponding power spectra however seemed to rule out the existence of many high frequency components on the surfaces after manual polishing, instead favouring the low frequency undulating roughnesses and hence confirming the smoothing of the surfaces. In particular, the power spectra together with the AFM images (of equal scan sizes such as figures 5.7, 5.8, 5.9 and 5.10) and the corresponding line profiles showed that the surfaces became generally smoother with the manual polishing, and the reason for the high values of the RMS values were due to a combination of the resultant large smooth grooves and the raised features that were left behind by the manual polishing. This observation was further confirmed by the plot of the ratio of the true area to the projected scan size. In spite of this though, the smaller scan regions appeared generally better than the larger ones because of the obvious lack of many surface features.

Again, it is important to emphasize here that a change in the RMS value did not necessarily indicate a worsening of the surface quality but rather, suggests that the original wave form (surface topography) has changed, implying that the average roughness i.e. RMS roughness changes too, in a way that actually leads to the reduction of the overall surface roughness as confirmed by the line profiles and the accompanying power spectra. Such finding tied in well with the earlier results of Derry *et al.* [117], emanating from their LEED measurements for diamond surfaces that were polished in a similar way to those described in this study, as mentioned before.

Surfaces polished for more than 30 minutes (1hour) showed a slight improvement in their overall roughnesses as seen from figure 5.31 (a) and (b).

Absolute average root mean square roughness values of below 2nm were typically observed over those that were polished for only 30 minutes which were below 2.6nm for all the three low index surfaces. This was especially so for scan sizes below 5×5μm, increasing somewhat to below 3.8nm for the larger sizes.

The RMS roughnesses for surfaces annealed to both 250°C and 750°C ranged between 0.25 and 3.5nm, as seen in figure 5.31 (d), which were only marginally lower than those of surfaces polished for longer periods. In addition, figures 5.31 (a) and (c) which shows the ratios of the areas for the unannealed and annealed surfaces, revealed that the absolute values of the ratios were much smaller after annealing, being below ∼1.0025 before the annealing, and below 1.0020 after the 250 and 750°C anneals. This could imply smoothing of some of the surfaces after the annealing. It was further found that with the exception of the (100) surfaces, the RMS roughnesses of some of the (110) and (111) surfaces increased somewhat after the 750°C than they were at 250°C, as seen in figure 5.31. This could again imply that the surface features such as the polishing grooves became more prominent with the higher temperature annealing as seen from some of the AFM images, therefore making the RMS values to increase modestly. Nonetheless, while not in all cases, annealing to 750°C appears to have reduced the overall RMS surface roughnesses comparatively in some instances, especially the (100) and (111) surfaces when compared to the unannealed surfaces, whereas in other cases it showed some slight increase due to the possible unequal etching effects.

5.5 Conclusions

A significant amount of surface improvement in terms of roughness was observed after the 30 minutes manual polishing on the (111) diamond surfaces, together with the (110) surfaces when compared to those surfaces that were polished

mechanically only. This also applied to the (100) surfaces, but to a lesser extent. Surfaces polished manually for more than 30 minutes showed a marginal improvement in their overall roughness except some cases involving the (100) surface.

Following both the mechanical and manual polishing, the groove widths and heights (which essentially determined the surface roughnesses) were found to vary as summarized in Tables 5.1 and 5.2. Incidentally, most of these grooves appeared wider than those observed by Couto *et al.* [82] on their polished (100) and (111) surfaces, where they established these to be between 20 and 100nm. It was only at the lowest end of our surfaces's grooves widths that showed some agreement with their values of 100nm. These differences could possibly be accounted for on the basis of the differences in their surface finishing techniques as opposed to ours.

After the manual polishing, the surface topography was found to change from that observed in the mechanically polished surfaces. In particular, the grooves became narrow and shallower in some cases while in others they became wider, implying some sort of changes occurring on the respective surfaces albeit on a small scale in some cases. This provided the first evidence of the fact that there was a significant amount of material removal, and especially so regarding some of the smaller roughnesses that were residing inside the wider grooves, following the manual polishing. This resulted in making the surfaces relatively smoother as observed from the corresponding line profiles and even the AFM images themselves. Some grooves even indicated a remote evidence of being flat bottomed, thereby agreeing with the earlier observations of Hird *et al.* [54], although these were very few. Polishing grooves on the (111) surfaces were found to become narrower but not shallower after manual polishing. In some other very exceptional cases, smaller roughnesses of around 20nm and even down to 14nm were observed, but with very small intensities according to the

power spectra and the line profiles. Most of the surfaces were found to be very much better in terms of their smoothness (roughness heights) than those of the mechanically polished HPHT (100) diamonds observed by Kumagai *et al.* [204] whose roughnesses were between 3.40, 2.63 and 1.19nm and peak-to-valley distances of 20nm. These values were even worse than those of some of our mechanically polished surfaces, as observed before.

While the line profiles across the grooves gave an idea of their widths and heights/depths, those along the grooves were used to give an idea regarding their smoothness. Most of the grooves became smoother and more curved after the manual polishing than they were after the mechanical polishing. This indicated that erosion of some particles within the grooves took place, with the average roughnesses inside the grooves ranging between 0.2 and 0.1nm which was clearly of atomic scale. Only the mechanically polished (100) diamond surfaces had some occasional larger roughness heights of about 0.5nm, which decreased to between $\sim$0.1 and 0.2nm following the manual polishing, just like in most of the other cases.

Overall, it was established that although an observable change occurred within all the three low index diamond surfaces, the narrowest and shallowest grooves after the manual polish were found in the (111) surfaces, and the deepest in the (110) surface. This surface also had some of the widest polishing grooves, probably due to the widening caused by the ones formed on their edges/slopes after the manual polishing. The (100) surface also had a few wider grooves after the manual polishing which were clearly caused by the preceding mechanical polishing, but most of its grooves had widths that were comparable to those of the manually polished (111) surfaces, as seen in Table 5.1.

The changes observed in the polishing grooves following the manual polishing were therefore sufficient to conclude that the manual polishing method was a reliable and effective surface finishing technique, thereby giving rise to diamond

surfaces that are smoother, flat and hence of superior quality.

Previous studies conducted by Haisma *et al.* [67] using Atomic Force Microscopy, revealed some differences between their mechanically and tribochemically polished surfaces, where they observed that although the mechanically polished surfaces had a high geometric precision and were optically smooth, they were subjected to both surface and subsurface damage. On the contrary, their tribochemically polished surfaces had smooth surfaces and damage-free subsurfaces, but their surface geometric precision was often poor at the submicron level. They did not however mention whether the tribochemically polished surfaces were initially polished mechanically or not, since mechanical polishing is known to cause some minor subsurface damage [67, 68]. On the other hand, Thornton and Wilks [60] suggested that a good way of obtaining smoother surfaces was the use of chemical action to attack the peaks of the asperities.

Clearly, the efforts of these workers as well as those of others mentioned previously in the introductory section of this chapter suggests an almost desperate need of creating well characterized and smooth diamond surfaces for various applications. However, although many techniques have so far been proposed, mechanical polishing still remains the most widely used and well understood method for preparing good quality diamond surfaces for various applications. This therefore means that a technique that puts more emphasis on improving the mechanically polished surfaces would be a most viable alternative to others already proposed in literature. For this reason, the manual polishing which was used as a surface finishing technique in this work appears to be quite attractive in this regard.

While investigating defects in the surface region of polished diamond surfaces, Baumann *et al.* [101] observed that these may result from the polishing procedure itself or they could be intrinsic to the natural diamond crystals. This aspect was however not pursued by the AFM investigations of this study, but

the question of subsurface damage still remains one that continues to attract some controversy since Rutherford Backscattering Spectrometry (RBS), has been used previously to show that a large number of atoms is displaced in the subsurface layer during polishing [67], while Derry *et al.* [68] on the other hand, and still using RBS found that very little subsurface damage occurred, with only one or two atom layers being disordered. Clearly further investigations are needed to verify and if possible reconcile the two observations.

The RMS roughnesses and the ratios of the real to the projected areas for some of the (100) surfaces indicated as though the surfaces or some sections of them were experiencing some slight deterioration in quality after the manual polish. A visual inspection/analysis of the AFM images themselves showed that the polishing grooves for these surfaces were only getting more curved after the manual polishing, accompanied by widening of the same (grooves). This had the consequence of increasing the two parameters, and not necessarily resulting in extra roughening of the surfaces. Nonetheless, perhaps some of the difficulties associated with maintaining a constant direction of polish could have been partly responsible for the observed changes in the RMS values and ratios of the areas. In certain directions, it was occasionally felt as though the diamond was actually "digging"into the polishing metal block, accompanied by difficulties in the sliding process. When the diamond was tilted to the correct polishing direction, the sliding (polishing) proceeded well without the feeling of the diamond "digging"and getting stuck into the polishing metal block. Most of the surfaces showed parallel polishing grooves that were oriented towards the polishing direction, with some being narrower and others deeper.

The changes observed in the ratios of the real area to the projected one revealed how the surface topography changed with the polishing, but these could still not be used on their own. They instead needed to be considered collectively with other complementary findings such as the root mean square

roughness and the accompanying line profiles. It will be recalled that the real area is an integration of all features on the surface, some of which may not actually be part of the surface as alluded to previously. As such, the results of the ratios of the areas were quite interesting, because when polished on the soft planes, it was expected that the surface quality would improve, owing to the higher material removal rates than in the case of the (111) surface. However, the high material erosion rate due to the manual polishing on the (100) and (110) surfaces appears to have resulted in either new roughnesses being introduced following the manual polish, or alternatively the overall surface roughness improved, with the higher frequency (short wavelength) components or small roughnesses diminishing, both in number and intensity. Analysis of the Fourier transforms of the surfaces revealed the latter to be the case, although some few new high frequency roughnesses were seen in certain cases, with very small intensities.

This was further confirmed by the line profiles that were obtained perpendicular to the polishing grooves, with roughnesses of the order of $\sim$ 0.05nm being observed on the mechanically polished surfaces. For the (110) surfaces, these were of the order of $\sim$0.015μm, while for the (111) surfaces they were $\sim$0.04μm. These decreased to $\sim$0.03μm for the (111) surfaces following the manual polishing on the (111) surface. Similarly smaller roughnesses were observed in the (100) surfaces ranging between $\sim$0.03μm and $\sim$0.014μm for the mechanically and manually polished surfaces respectively. These were nonetheless few and their intensities were also very small, and one may at first have been tempted to conclude these to be instrumental, especially if they only appeared in the mechanically polished surfaces. However, their occurrence in the manually polished surfaces and even being much narrower, confirmed that the smaller roughnesses may not have been caused by instrumental errors, but were indeed a real effect.

The inability of maintaining a precisely constant direction of polish throughout the entire manual polishing period was again cited here as one of the factors contributing to the deterioration of the surface quality for some cases. This, together with a significant amount of material removal in the soft directions for the surfaces ((100) and (111)) may have led to the introduction of extra polishing lines crossing the actual polishing lines, thereby leading to the observed changes in the overall surface quality. The crossing lines were however not seen in this work, but it is quite likely that if the direction of polish was kept constant, the quality of the surface finish would be greatly improved.

From the 2D images of the (100) and (110) surfaces, it was observed that the manually polished surfaces had darker grooves than their corresponding mechanically polished ones (e.g. in figures C.1 and C.2 shown in Appendix C) implying that their grooves became deeper following the manual polishing. These observations were further confirmed by the curvature seen in the line profiles that were obtained inside the polishing grooves after the manual polish, and the grooves appeared to also be getting smoother than they were after the mechanical polish. The deepening of the grooves was again confirmed by the bars shown on the RHS of each of the 2D images (figures C.1 and C.2 shown in Appendix C). This meant that the manual polishing not only resulted in the erosion of loosely bound atoms (species) but also sharp points in the form of surface asperities that were oriented in positions that made it preferentially suitable for them to be easily eroded. This process can be thought of being quite close to the preferential easy polishing orientation of the grit particles embedded in the polishing wheel as alluded to by Hird *et al.* [54]. The deepening of the grooves especially on the (100) surface was responsible for increasing the real area of the surface, and hence the overall ratio of the true to the projected one and also the root mean square roughnesses.

Since it has already been established that the wear of diamond in the soft

direction is not produced by abrasion, the grooves thus formed suggested that small fragments of loosely bound atoms were swept away during the manual polishing.

Upon annealing to 250°C, it was found that there was a minimal change within the surface quality compared to those of the unannealed surfaces. Annealing to 250°C is therefore thought to have resulted in the removal of probably the physisorbed and any loosely bound species. This explains why few noticeable changes were observed when annealing was done up to this temperature. However, after annealing to 750°C, significant changes were noted on all the three low index surfaces, where the grooves became quite prominent. In spite of this though, the (111) surfaces showed smaller changes from the annealing process, followed by the (100) surfaces and the largest changes were observed in the (110) surfaces. The changes observed in the surface quality after annealing were a clear testimony of surface etching through the desorption of the adsorbed species. Derry *et al.* [7] observed previously some damage associated with polished diamond surfaces, which they noted to improve by annealing. This again confirms that annealing does indeed change the polished diamond surfaces. Some surfaces also appeared to be getting smoother with the elevated temperatures, especially the (110) and (111) surfaces.

Overall, manual polishing resulted in a fair amount of improvement in the general surface quality (smoothness), except in some few isolated cases involving the (100) surfaces where the evidence wasn't too clear. This apparent change in roughness was attributed to some roughnesses being eliminated and new ones being created, according to the line profiles, the power spectra, the ratio of the real area to the projected one, and the RMS roughnesses. This tended to present the surfaces as though they were getting rougher while others were getting smoother, but in reality they were all actually improving as observed previously by Derry *et al.* [117] in their LEED studies of diamond surfaces

that were polished manually as those described in this work. Based on these findings, we conclude that the low-speed low-load manual polishing resulted in better (111) and (110) surfaces than those observed after the mechanical polishing. This is believed to be driven by the erosion of loosely bound atoms or groups of atoms or smaller surface asperities, leading to the reorganization of the surface carbon atoms. However, since the technique was quite labour intensive, we propose that it could be improved and be made more accessible, attractive and controllable by designing a polishing machine which mimics the actual manual polishing parameters. These include low linear polish speeds of between 0.2 and 1.0ms^{-1} and normal hand polish pressures. This would thus eliminate some of the difficulties associated with the manual polishing, such as problems in maintaining a constant direction of polish, as well as a constant load. This is envisaged to endear the process to many diamond polishers, which would ultimately guarantee smoother surfaces for the ever increasing demand for such surfaces in various applications. Due to the low loads, the manual polishing was further expected to be more advantageous by not causing or aggravating any surface or subsurface damage. Indeed there is no doubt that low speed sliding (0.1mms^{-1}) does cause some polishing as observed previously by Couto *et al.* [56], and also by Casey and Wilks [78].

Hird *et al.* [79] have nonetheless investigated the wear mechanism for diamond polishing where they reported lack of any significant wear at low velocities and pressures. However, our manual polishing technique is only recommended as a surface finishing technique for those surfaces that have already been polished mechanically and not as a complete polishing technique on its own. This is the reason why we suggest that if the wear rate is to be based on the mass lost from the surface per unit distance slid in time as was the case with Hird *et al's* [79] work, it would definitely appear as though the manual polishing was not achieving any polishing, since no significant amounts of material that can be

detected and measured is removed. It is actually due to the very same reasons of insignificant amounts of material removal from the manual polishing that we had to employ other sensitive techniques such as deconvolving the roughnesses from the AFM images into their power spectra. This enabled us to establish any form of changes occurring on the surfaces, that could otherwise not easily be discernible from the images themselves, or even the line profiles.

The question of polishing at low loads in air using oil was initially investigated by Casey and Wilks [78] where they noted that at first it may seem as though measurements of friction (polishing) at low loads in air would give little information on the nature of diamond surface, as it is protected by the contaminant film, and therefore has no direct interaction with the other sliding surface. Nonetheless, they pointed out that it was already known that even under low loads in air, the friction for sliding (100) and (110) planes showed the characteristic symmetry of the underlying diamond surface according to Seal [205, 206], meaning that some form of polishing did take place even at the low loads in air. This means that our low-speed, low-load manual polishing has already been vindicated and proven to be an ideal surface finishing technique by the earlier works of Casey and Wilks [78], and the later work of Couto *et al.* [56].

Our findings of the broadening of the polishing grooves after manual polishing in some certain cases concur with those of Hird *et al.* [79], where they reported that low velocity polishing resulted in smooth grooves that were wider and more clearly defined than those produced at normal polishing speeds, although their polishing speeds were still much higher than ours. They further noted that the grooves observed after relatively high polishing velocities were both narrower and shallower than those produced at lower velocities. This is nonetheless a rather general statement since our findings show some dependence of the sizes of the grooves (widths and depths) to the respective orientations,

which is quite understandable due to the different polishing mechanisms taking place on each of the three low index diamond surfaces. Our manual polishing in particular resulted in grooves of varied widths and depths between the mechanically and manually polished surfaces as summarized in Tables 5.1 and 5.2, depending on the orientation being investigated. An important observation made from the AFM images as well as the optical micrographs was that the polished diamond surfaces were made up of a series of polishing grooves of different sizes, with some smaller ones of nanometer scale being observed inside the larger ones. This array of grooves was found on all the regions of the entire surfaces, since images were taken at different places.

Results of this study further revealed that the manual polishing was more effective on both the (111) and (110) surfaces and probably least on the (100) surface. By controlling the direction of polish as well as the applied load over the period of the 30 or more minutes of manual polishing, this study suggested that the manual polishing process would ultimately yield much better surfaces with superior smoothness than those polished mechanically only, as well as many others reported in literature. This again confirms rather convincingly that the gentle manual polishing presented and discussed in this work was indeed an effective surface finishing technique for those diamond surfaces prepared through mechanical polishing.

Appendix A

A.1 Papers published in refereed journals.

N. W. Makau and T. E. Derry, *Surf. Review. and Lett.*, **10** Nos. 2&3, 2003, 295-301.

N.W. Makau and T.E. Derry, *Nucl. Instr. Meth. A.*, **555**, 2005, 31-35.

T.E. Derry and N.W. Makau, *Diam. & Related Materials.*, **15**, 2006, 160-163.

T.E. Derry and N.W. Makau, in: Y. Ballim, A.G. Avery, S. Luyckx, D.C. Levendis (Eds.), *Proceedings of the 2nd International Conference of the African Materials Research Society.* Johannesburg, South Africa, 8-11 December 2003, University of the Witwatersrand (ISBN:0-620-31513-X), 195-196.

N.W. Makau and T.E. Derry, in: Y. Ballim, A.G. Avery, S. Luyckx, D.C. Levendis (Eds.), *Proceedings of the 2nd International Conference of the African Materials Research Society.* Johannesburg, South Africa, 8-11 December 2003, University of the Witwatersrand (ISBN:0-620-31513-X), 255-256.

A.2 Paper to be submitted to a refereed journal.

N.W. Makau, Nic van der Berg and T.E. Derry, *Diam. & Related Materials.*

A.3 Papers presented at international conferences

N.W. Makau and T.E. Derry, *The 7th intern. Conf. on the Structure of Surfaces (ICSOS7)*, Newcastle, Australia, 21-26 July 2002. (Published in Surf. Rev & Lett.)

T.E. Derry and N.W. Makau, *The 2nd International Conference of the African Materials Research Society.* Johannesburg, South Africa, 8-11 December 2003, University of the Witwatersrand.

N.W. Makau and T.E. Derry, *The 2nd International Conference of the African Materials Research Society.* Johannesburg, South Africa, 8-11 December 2003, University of the Witwatersrand.

T.E. Derry and N.W. Makau, *The 55th Diamond Conference*, University of Warwick, UK, 2004.

A.4 Papers presented at local conferences

N.W. Makau and T.E. Derry, *The 46th South African Institute of Physics Annual Conference.* Durban, South Africa, July 2001.

T.E. Derry and N.W. Makau, *The 48th South African Institute of Physics Annual Conference.* Bloemfontein, South Africa, 2003.

T.E. Derry and N.W. Makau, *The 49th South African Institute of Physics Annual Conference.* Stellenbosch, South Africa, July 2004.

N.W. Makau and T.E. Derry, *The 50th South African Institute of Physics Annual Conference.* Pretoria, South Africa, July 2005.

Appendix B

This section gives the appendices for the XPS work.

B.1 Correction for XPS oxygen monolayer coverage.

B.1.1 Contribution from oxygen on the molybdenum (Mo) sample holder, for spectra obtained using the VG Scientific spectrometer.

$$= \frac{Area \quad of \quad Mo \quad on \quad XPS \quad spectrum}{Total \quad Mo \quad area \quad on \quad holder} \times Amount \quad of \quad Oxygen \quad on \quad holder$$

$$= \frac{Molybdenum \quad area \quad observed \quad on \quad diamond \quad spectrum}{4009.3} \times 833$$

$$= 0.207756578 \times Molybdenum \quad area(counts) \quad observed \quad on \quad diamond \quad (XPS) spectrum.$$

B.1.2 Oxygen atoms coverage σ, per cm^2 on polished diamond surfaces.

NB: Subscript C represents a carbon atom, while O stands for an oxygen atom and RSF, the Relative Atomic Sensitivity Factors.

$$\sigma = \frac{\frac{A_O}{RSF_O}}{\frac{A_C}{RSF_C}} \frac{N \cos\phi \mu_C \rho_C \lambda}{\mu_O M_C} \tag{B.1.1}$$

where N=6.023×10^{23} RSF_O=0.733(For quantum 2000)

μ_C=1 RSF_O=0.711(For VG Scientific)

μ_O=2.92 RSF_C=0.314(For Quantum 2000)

ρ_C=3.52g/cm^3 RSF_C=0.296(For VG Scientific)

M_C=12.01g ϕ=45°(Quantum 2000)

λ=10×10^{-8}cm ϕ=25°(VG Scientific)

A_O = Area under the O peak A_C = Area under the C peak

$$\therefore \sigma_{VGScientific} = \frac{A_O}{A_C} \times 2.281011577 \times 10^{15} \tag{B.1.2}$$

and

$$\therefore \sigma_{Quantum2000} = \frac{A_O}{A_C} \times 1.831219243 \times 10^{15} \tag{B.1.3}$$

Number of carbon atoms per cm^2 on diamond surfaces for:-

(100)=1.57×10^{15}

(110)=2.22×10^{15}

(111)=1.82×10^{15}

B.1.3 Oxygen monolayer coverage

$$= \frac{Calculated\ \ No.\ \ of\ \ oxygen\ \ atoms\ \ per\ \ cm^2, \sigma}{No.\ \ of\ \ carbon\ \ atoms\ \ per\ \ cm^2\ \ on\ \ the\ \ respective\ \ diamond\ \ surface}$$

Table B.1: Functional groups on the respective diamond faces investigated together with their corresponding binding energies (eV).

(100)	C-O-C	C=O	COOH	C-C,C-H	C-OH	C-O-C	C=O	OH-C=**O**	**O**H-C=O	H_2O	C-OH
Sample-kc8	286.1	288.63	288.63	284.78	286.1	532.87					531.97
Sample-kc8	286.42			284.87	286.42	532.98	531.24	531.24		534.87	
Sample-kc3	286.42	288.66	288.66	284.79	286.42	533.14			533.14		532.19
Sample-kc3	286.33	288.8	288.8	284.8	286.33						
Average	286.3	288.7	288.7	284.8	286.3	533.0	531.5	531.5	533.14	534.9	532.2
(111)	C-O-C	C=O	COOH	C-C,C-H	C-OH	C-O-C	C=O	OH-C=**O**	**O**H-C=O	H_2O	C-OH
Sample-kf4	286.5	289.18	289.18	284.86	286.5	533.7			533.7		532.32
Sample-kf4		288.77	288.77	284.74			531.07				532.01
Sample-kc9				284.72			531.68	531.68			532.62
Sample-kf4							531.61	531.61			
Sample-kc11	286.38	289.4	289.4	284.85	286.38		531.21	531.21		534.05	532.65
Sample-kc11				284.80		533.41	531.55	531.55	533.41	535.33	
Average	286.4	289.0	289.0	284.7	286.4	533.5	531.4	531.5	533.5	534.7	532.3
110	C-O-C	C=O	COOH	C-C,C-H	C-OH	C-O-C	C=O	OH-C=**O**	**O**H-C=O	H_2O	C-OH
Sample-kk7	286.56	289.17	289.17	284.86	286.56	533.67			533.67		532.32
Sample-kk7				284.81			530.94	530.94			532.56
Sample-kk7				284.73		533.15	531.67	531.67	533.15		
Average	286.6	289.2	289.2	284.8	286.6	533.4	531.3	531.3	533.4		532.4

Appendix C

This section presents additional AFM images obtained in this study. These are presented together with their corresponding line profiles and Fourier transforms, for those cases where this applies. They are also presented according to the respective orientations, starting with the (100) surface, then the (110) and finally the (111) surface. Images are shown for surfaces that were not annealed as well as those that were annealed to 250° and 750°C.

In figures C.3, C.4, C.7, C.8, C.11, C.12, C.16, C.17, C.18, C.21 and C.22 the top panel represents the line profiles and power spectra obtained perpendicular to the polishing grooves, while the lower panels represent the line profiles and the power spectra obtained from inside the polishing grooves.

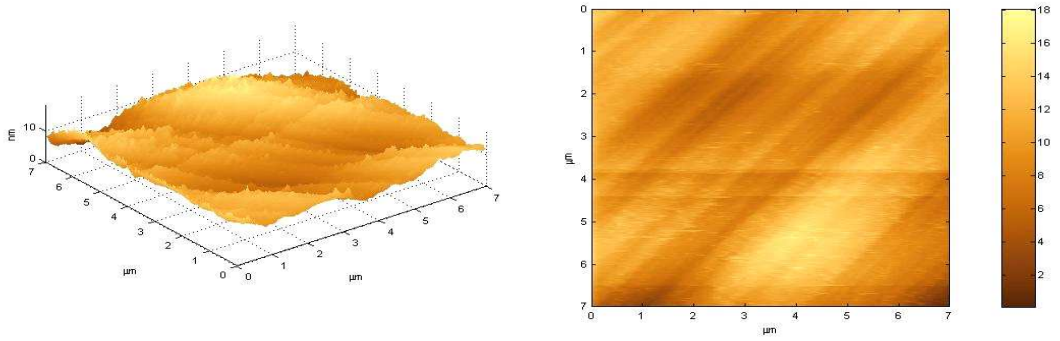


Figure C.1: Three and two dimensional atomic force microscopy images of a (100) surface polished mechanically (sample kc8), measuring 7×7μm.

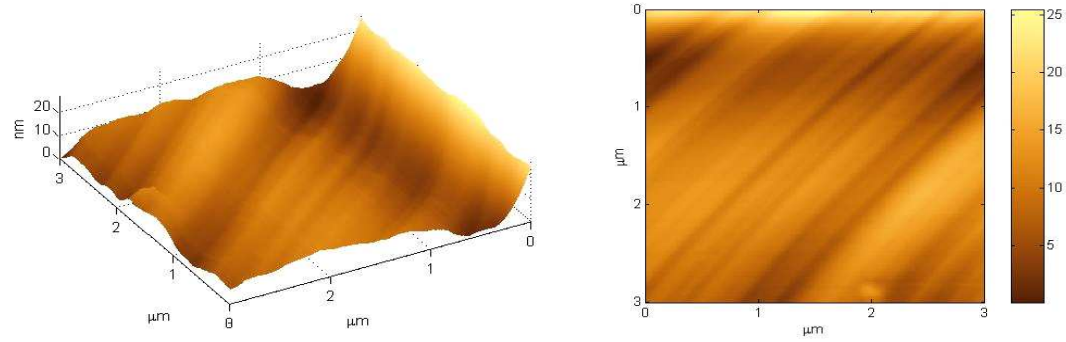


Figure C.2: Three and two dimensional atomic force microscopy images of a (100) surface polished manually (sample kc8), measuring 3×3μm.

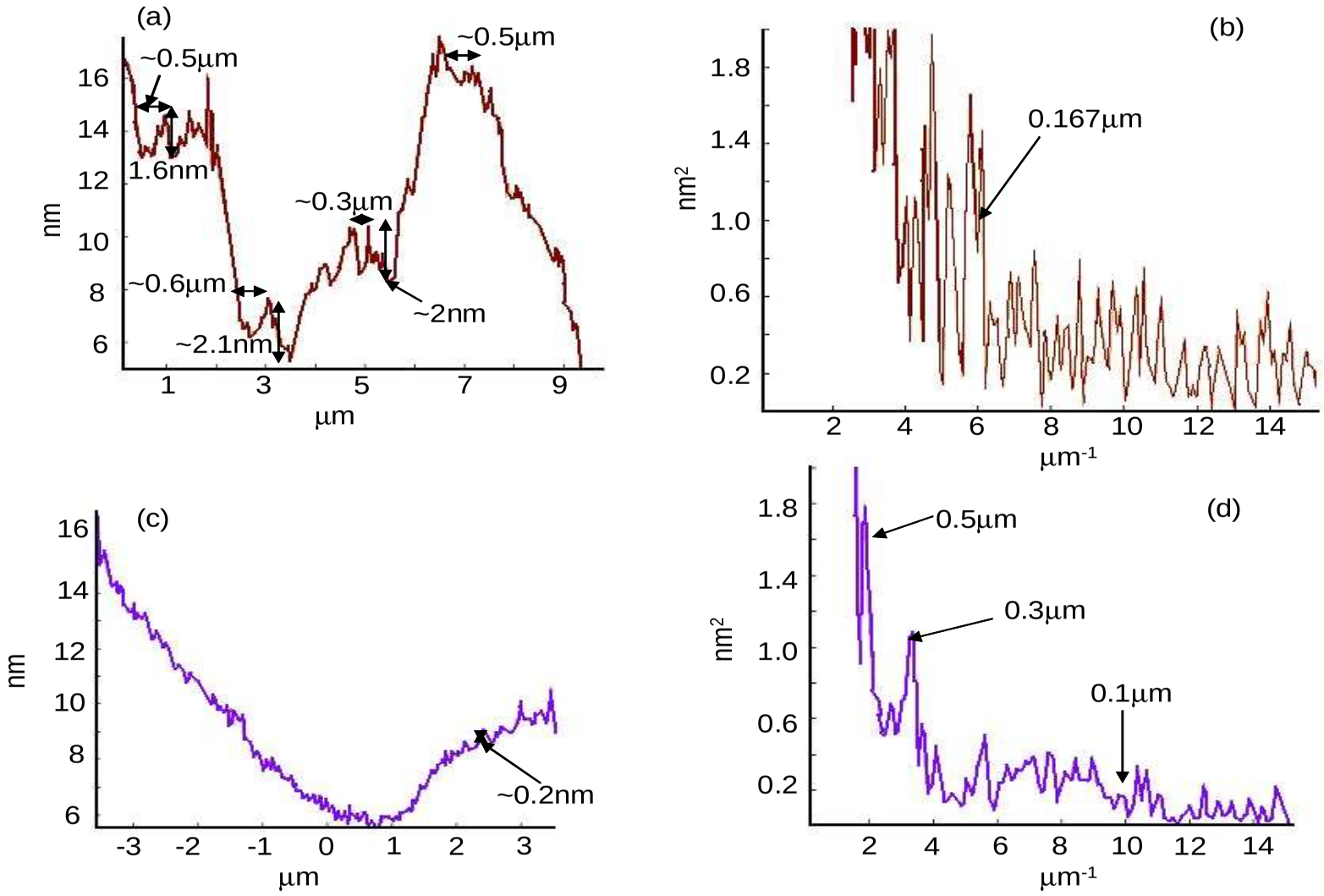


Figure C.3: Line profiles and power spectra for a (100) surface polished mechanically, which were obtained from the AFM image shown in figure C.1. Graph (a) shows the line profile obtained perpendicular to the polishing grooves, (b) its power spectra, (c) the line profile obtained inside the polishing grooves, and (d) its corresponding power spectra.

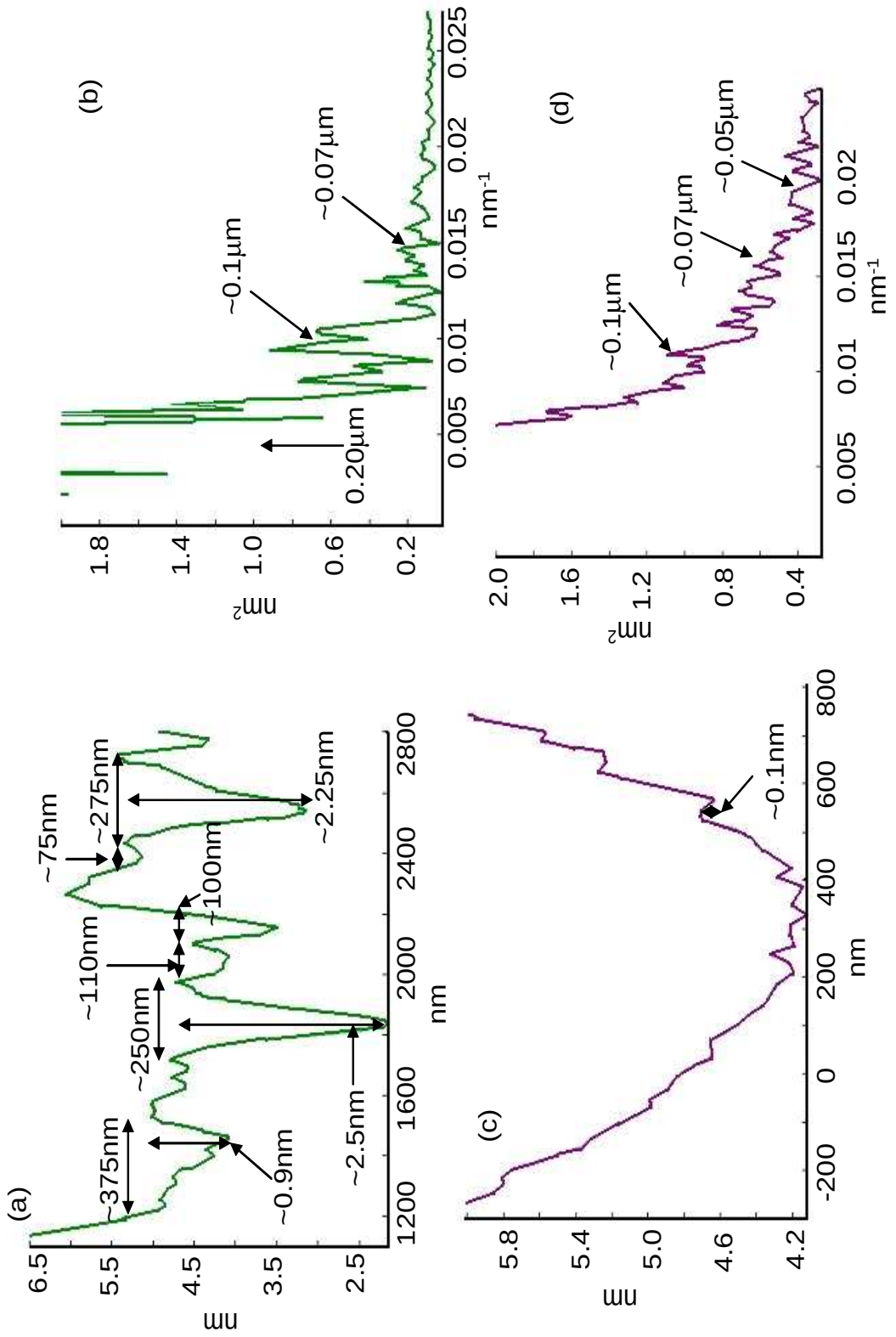


Figure C.4: Line profiles and power spectra for the (100) surface polished manually, which was obtained from the AFM image shown in figure C.2. Graphs (a), (b), (c) and (d) are as described in figure C.3.

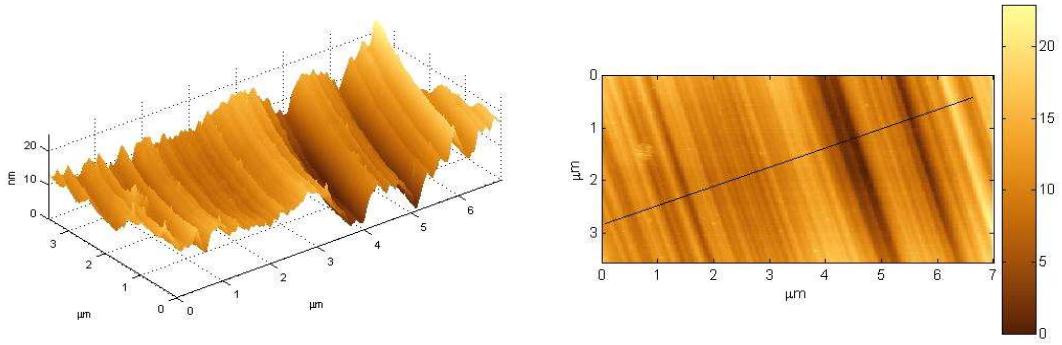


Figure C.5: Three and two dimensional atomic force microscopy images of a (110) surface polished mechanically (sample kk7), measuring 7×3.5μm.

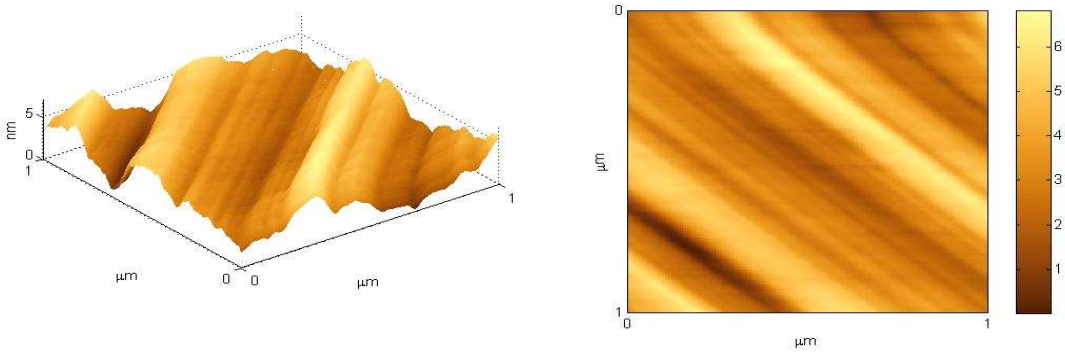


Figure C.6: Three and two dimensional atomic force microscopy images measuring 1×1μm, for a (110) surface polished manually (sample kk7).

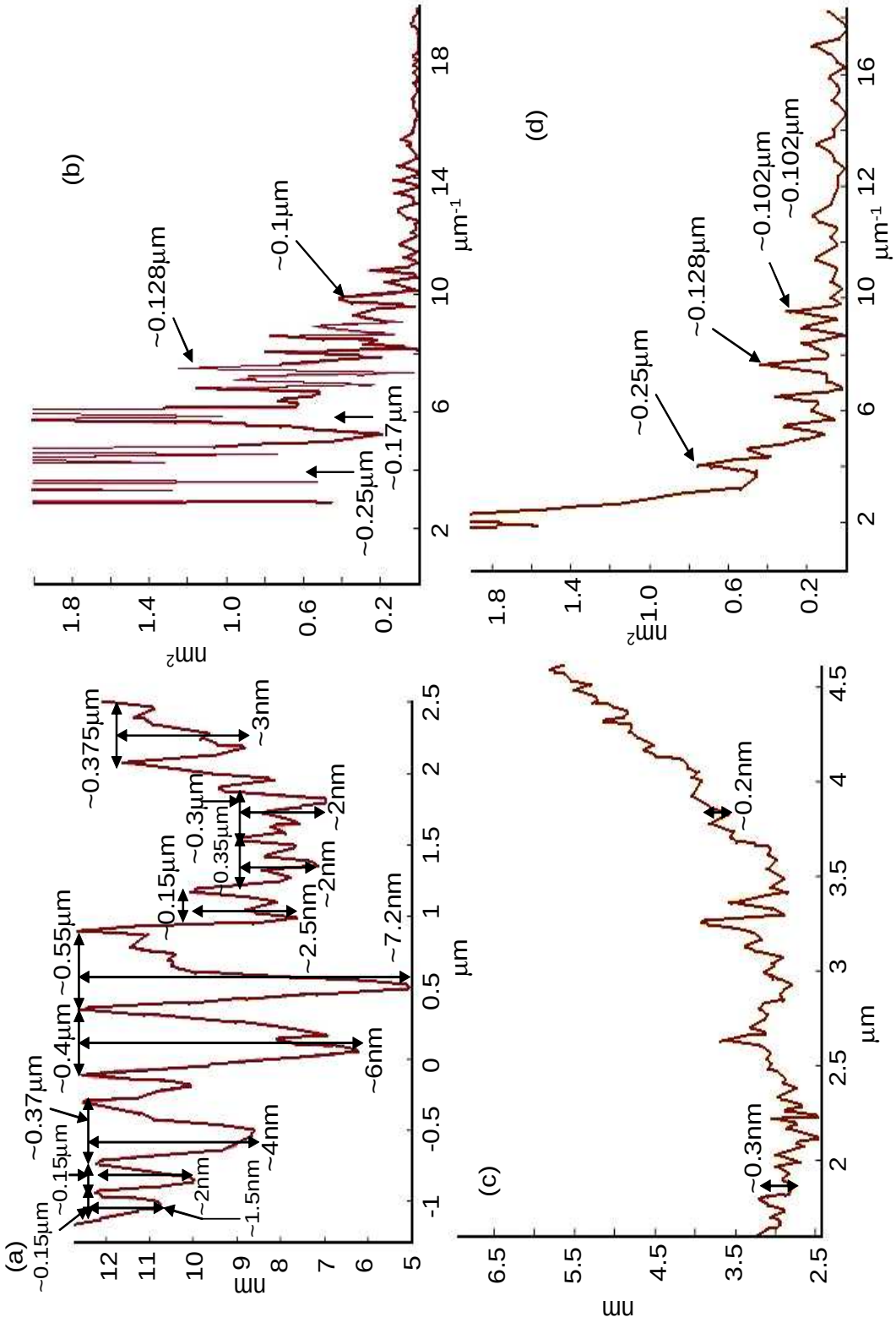


Figure C.7: Line profiles and power spectra for a (110) surface polished mechanically, which were obtained from the AFM image shown in figure C.5. Graphs (a), (b), (c) and (d) are as described in figure C.3.

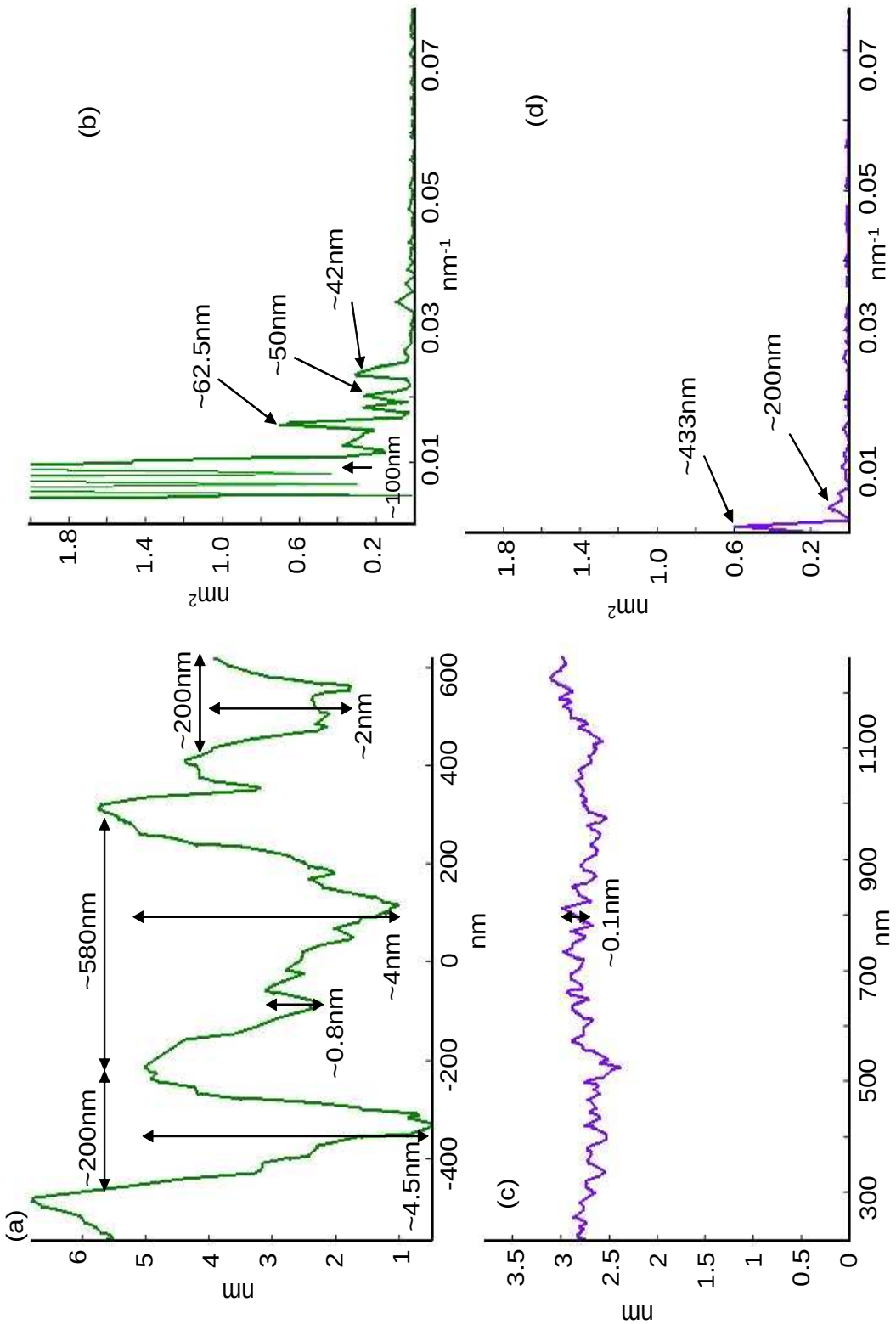


Figure C.8: Line profiles and power spectra for a (110) surface polished manually, which were obtained from the AFM image shown in figure C.6. Graphs (a), (b), (c) and (d) are as described in figure C.3.

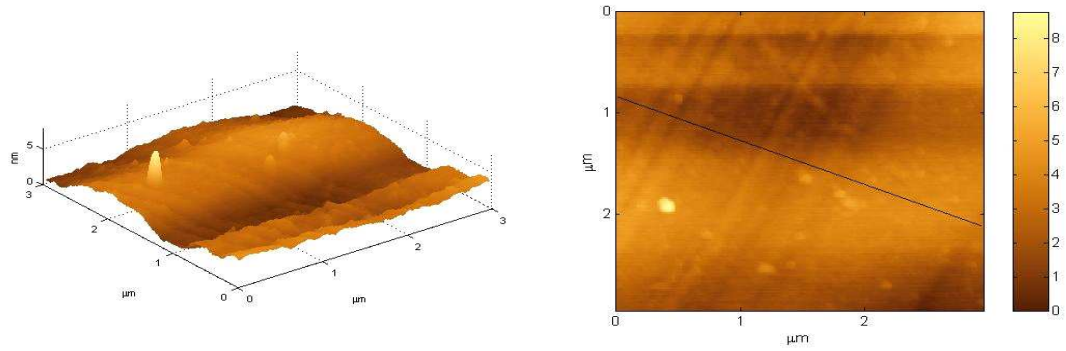


Figure C.9: Three and two dimensional atomic force microscopy images of a (111) surface polished mechanically (sample kc11).

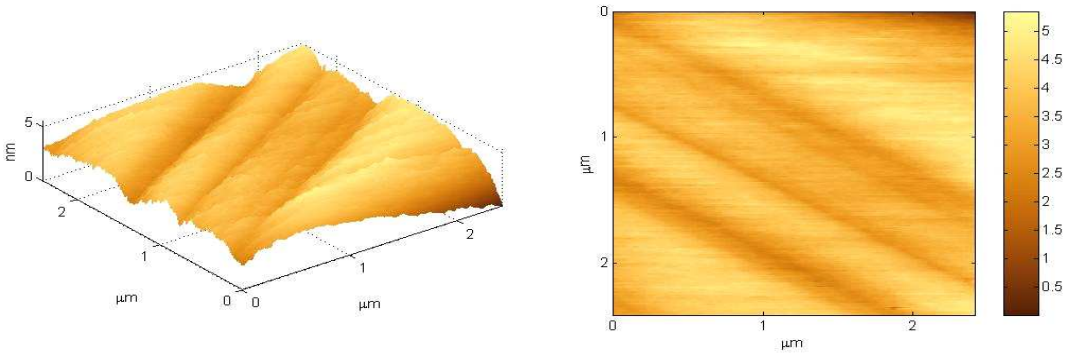


Figure C.10: Three and two dimensional atomic force microscopy images of a (111) surface polished manually (sample kc11).

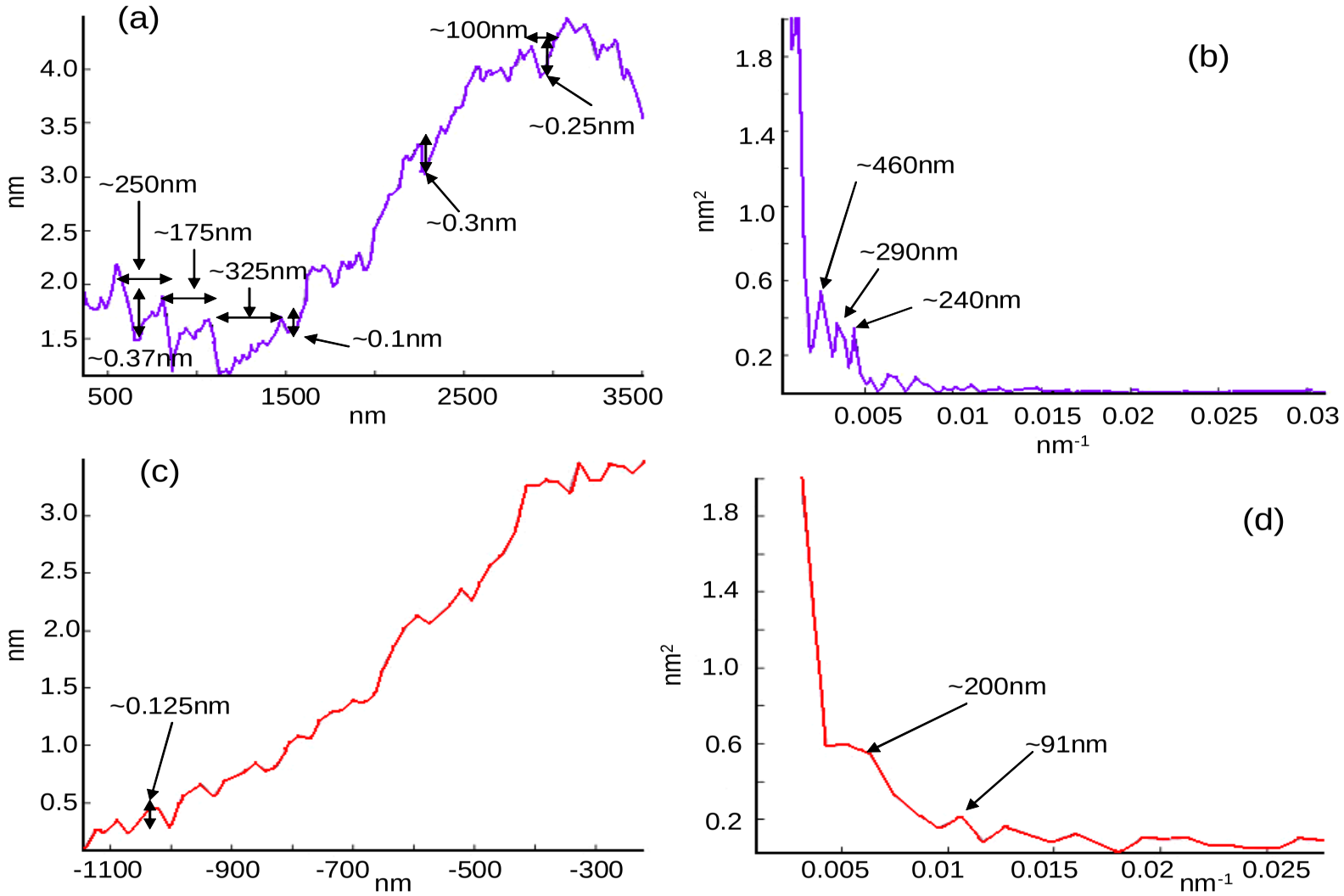


Figure C.11: Line profiles and power spectra for a (111) surface polished mechanically, that were obtained from the AFM image shown in figure C.9. Graphs (a), (b), (c) and (d) are as described in figure C.3.

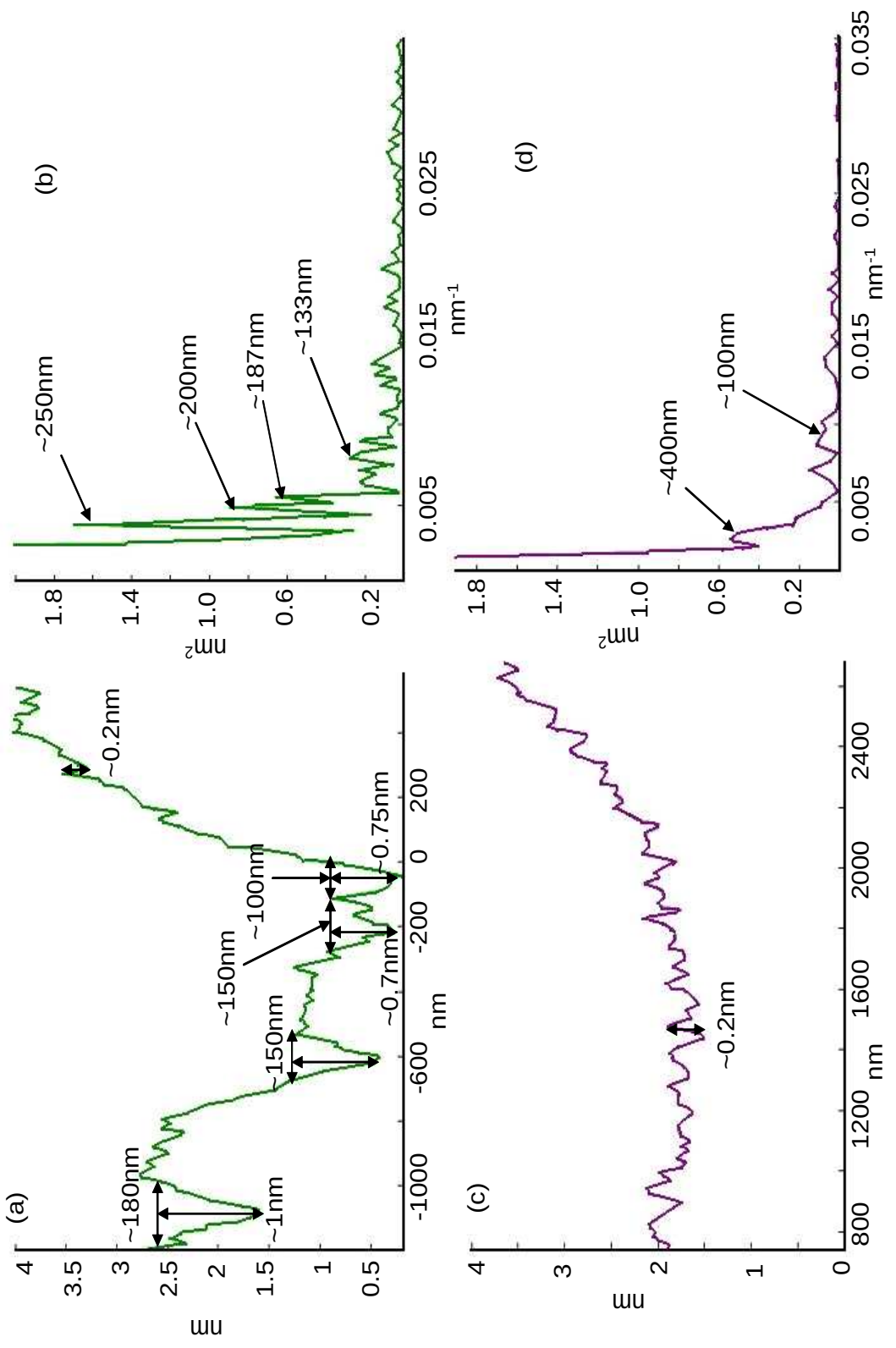


Figure C.12: Line profiles and power spectra for a (111) surface polished manually, which were obtained from the AFM image shown in figure C.10. Graphs (a), (b), (c) and (d) are as described in figure C.3.

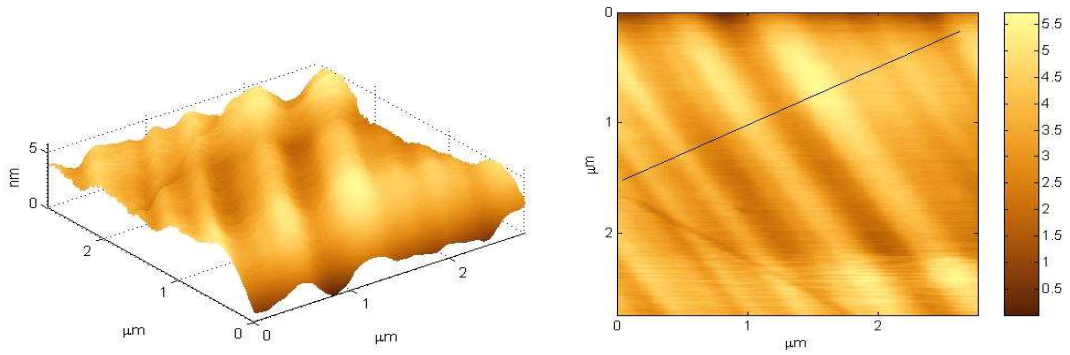


Figure C.13: Three and two dimensional atomic force microscopy images of a (100) surface annealed up to 250°C after manual polishing (sample kc8).

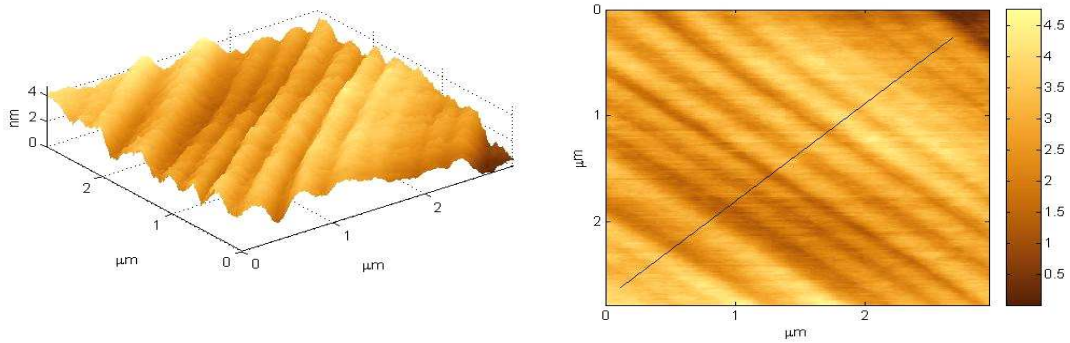


Figure C.14: Three and two dimensional atomic force microscopy images of a (100) surface annealed up to 750°C after manual polishing (sample kc8).

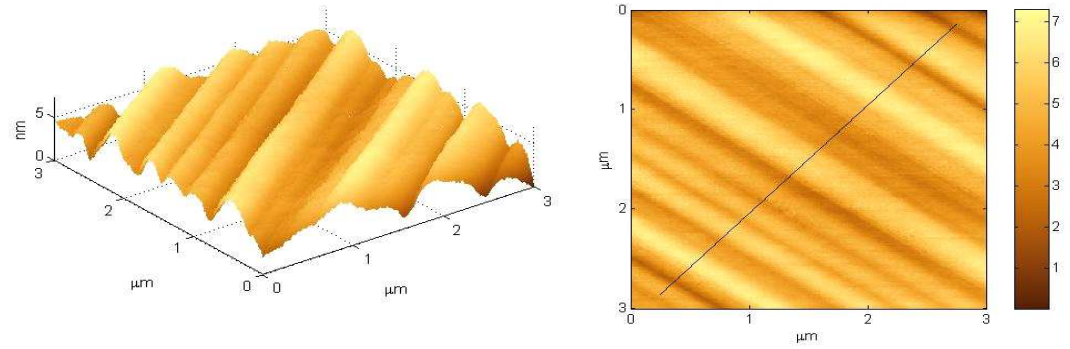


Figure C.15: Three and two dimensional atomic force microscopy images of a (100) surface annealed up to 750°C after manual polishing (sample kc8).

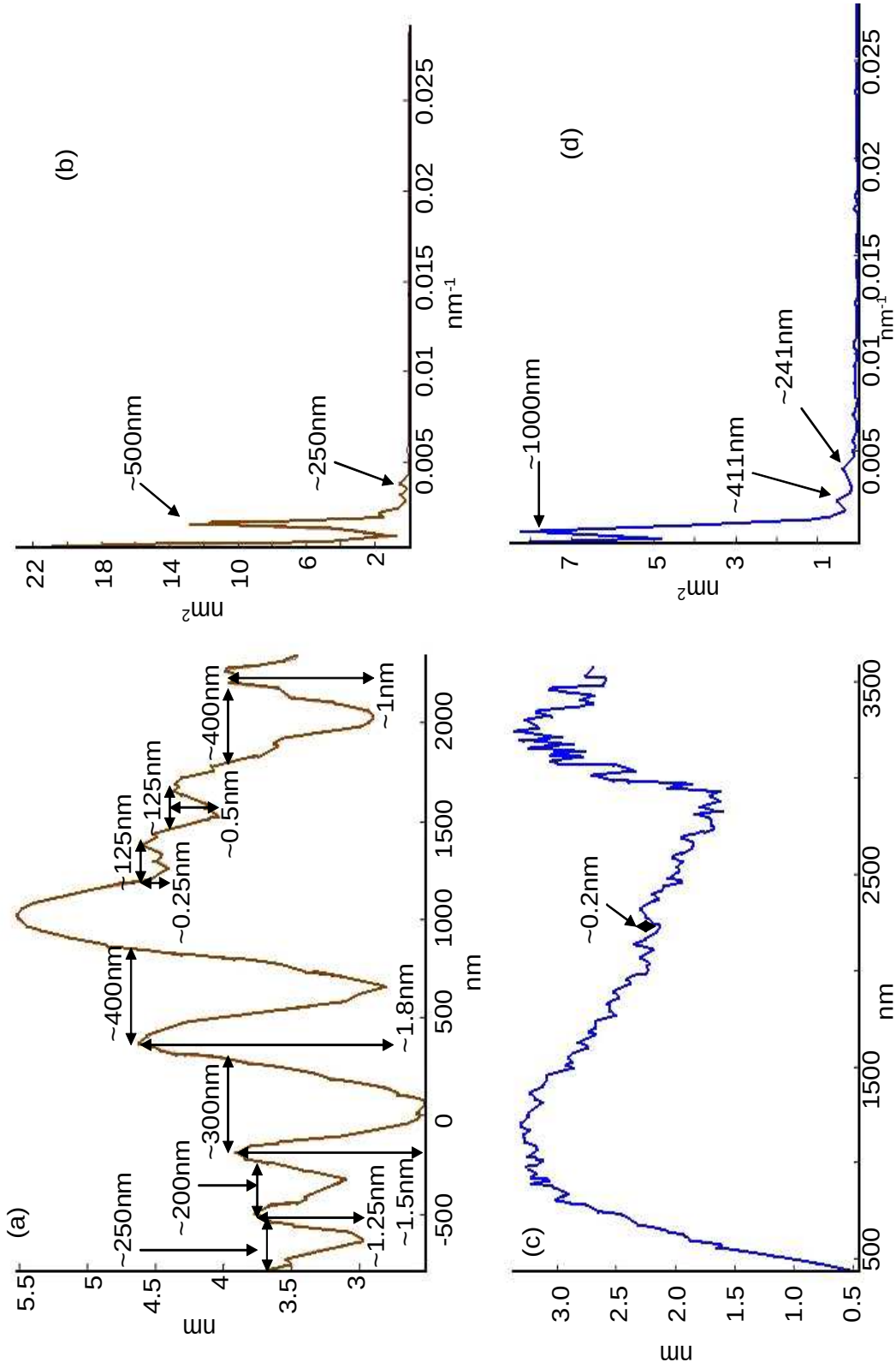


Figure C.16: Line profiles and power spectra for a (100) surface annealed to 250°C after manual polishing, which were obtained from the AFM image shown in figure C.13. Graphs (a), (b), (c) and (d) are as described in figure C.3.

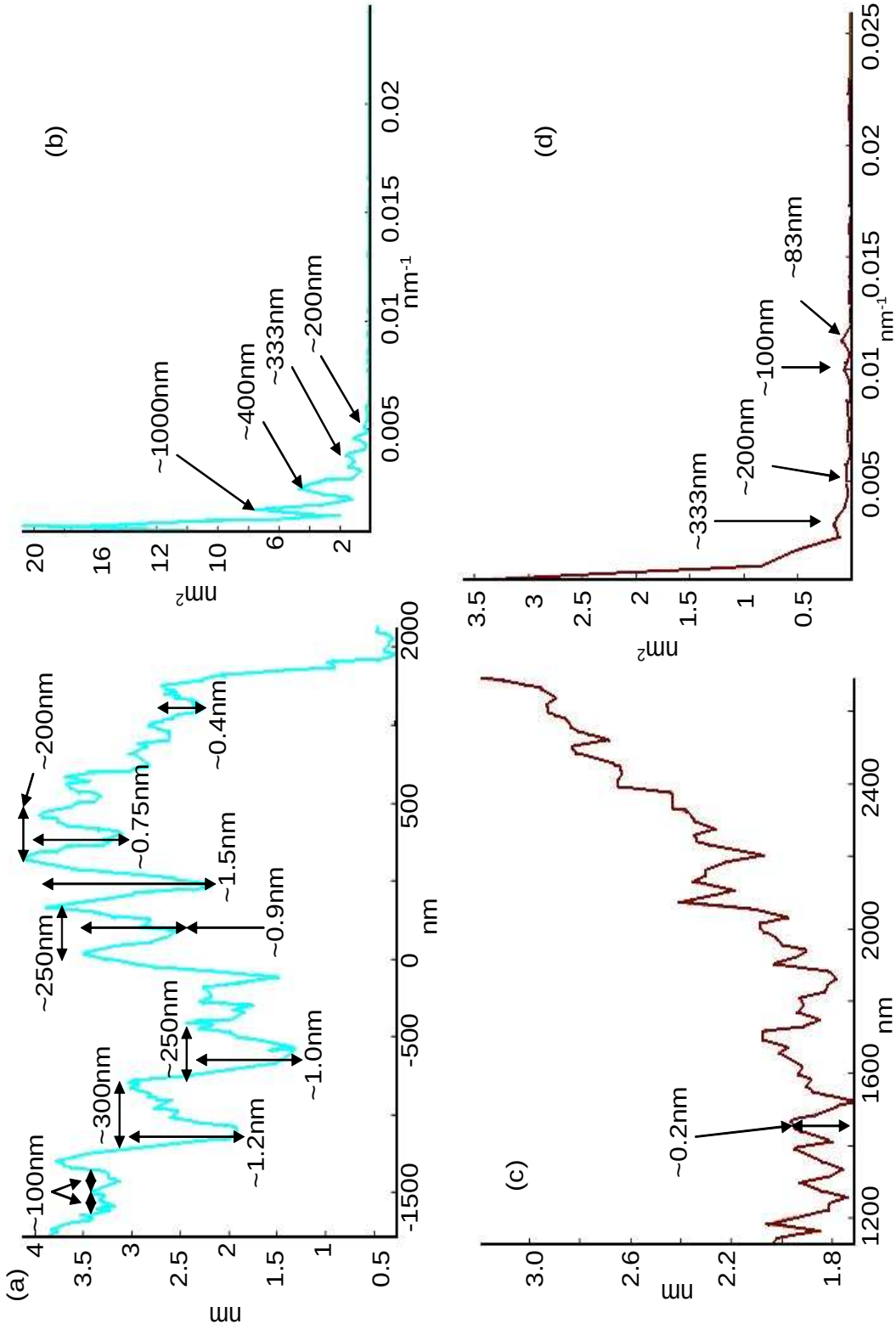


Figure C.17: Line profiles and power spectra for a (100) surface annealed to 750°C after manual polishing, which were obtained from the AFM image shown in figure C.14. Graphs (a), (b), (c) and (d) are as described in figure C.3.

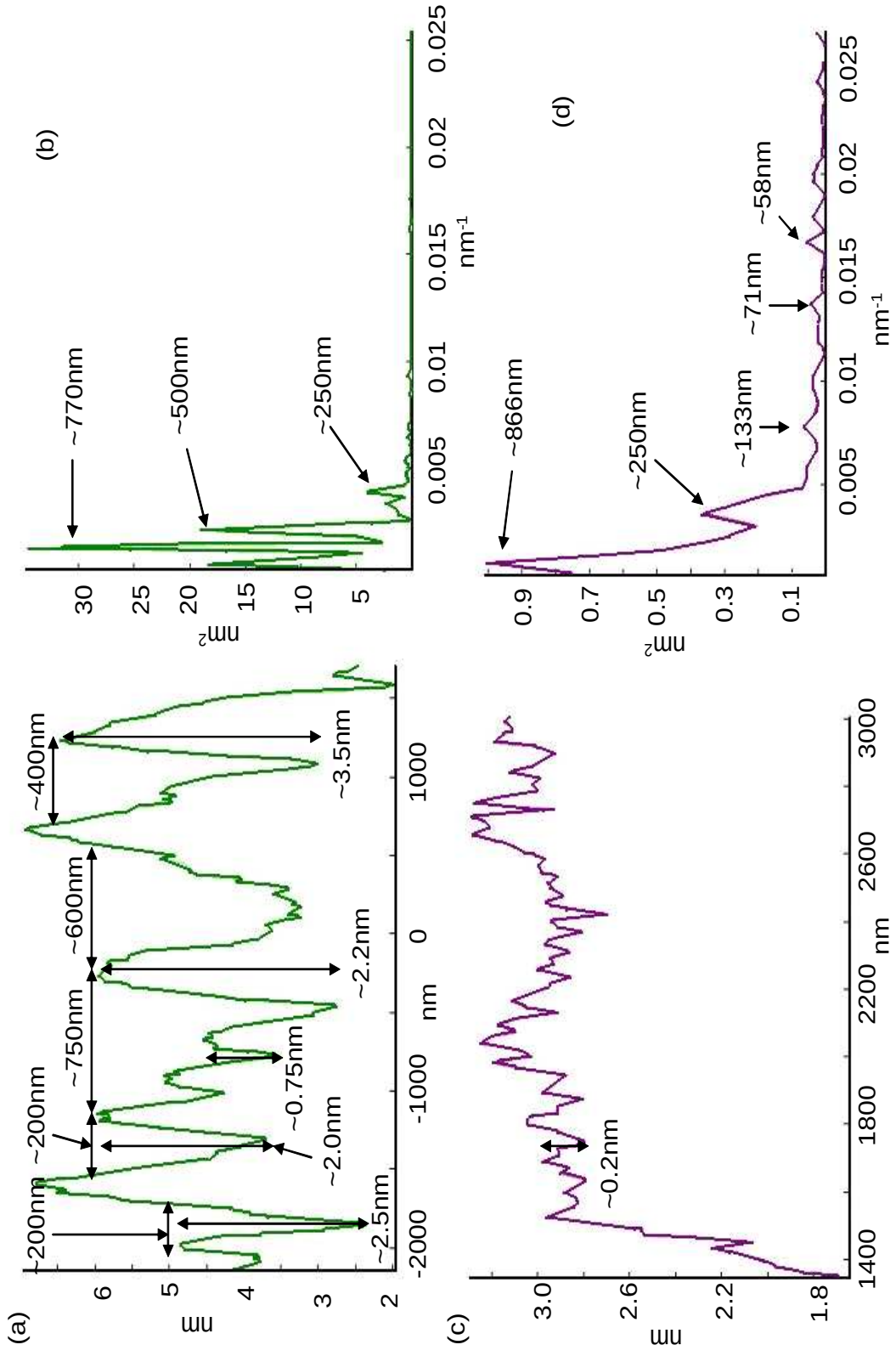


Figure C.18: Line profiles and power spectra for a (100) surface annealed to 750°C after manual polishing, which were obtained from the AFM image shown in figure C.15. Graphs (a), (b), (c) and (d) are as described in figure C.3.

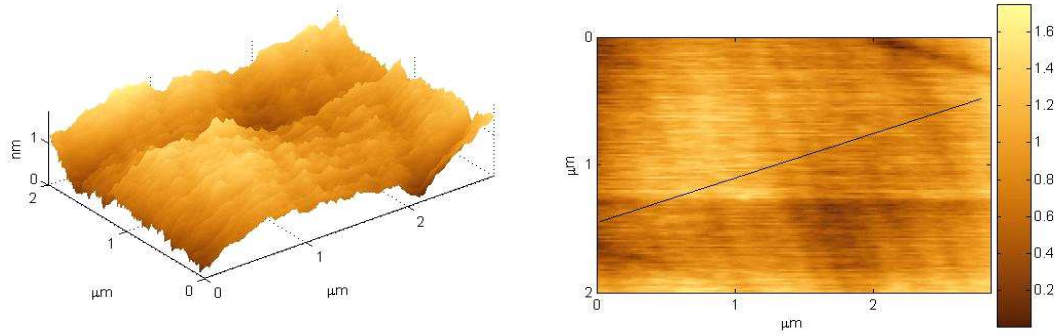


Figure C.19: Three and two dimensional atomic force microscopy images of a (111) surface annealed to 250°C after manual polishing (sample kc11).

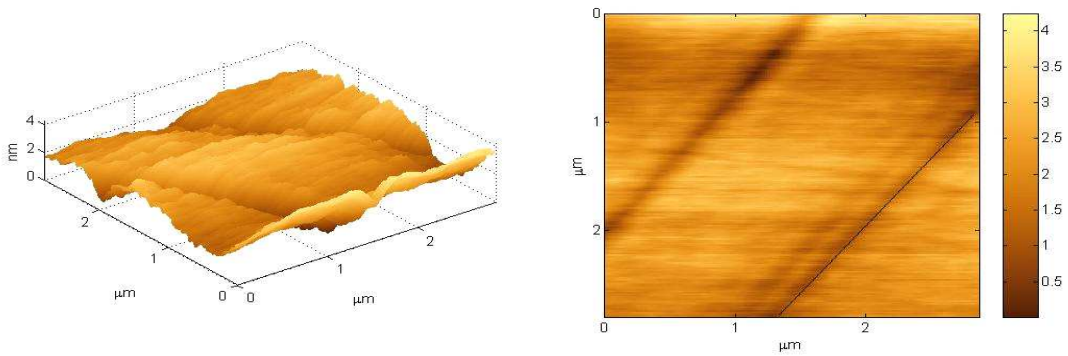


Figure C.20: Three and two dimensional atomic force microscopy images of a (111) surface annealed to 750°C after manual polishing (sample kc11).

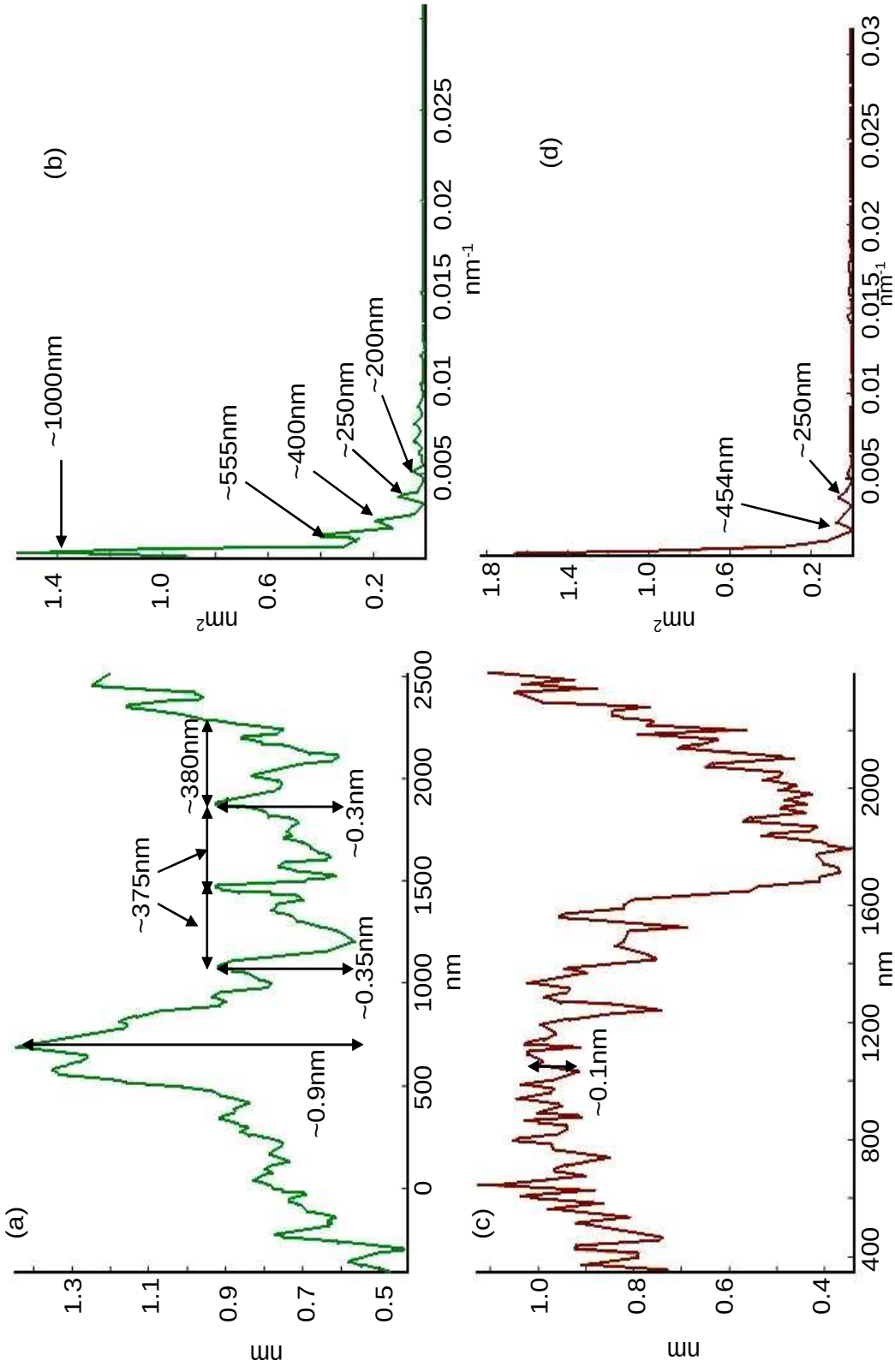


Figure C.21: Line profiles and power spectra for a (111) surface annealed to 250°C after manual polishing, that were obtained from the AFM image shown in figure C.19. Graphs (a), (b), (c) and (d) are as described in figure C.3.

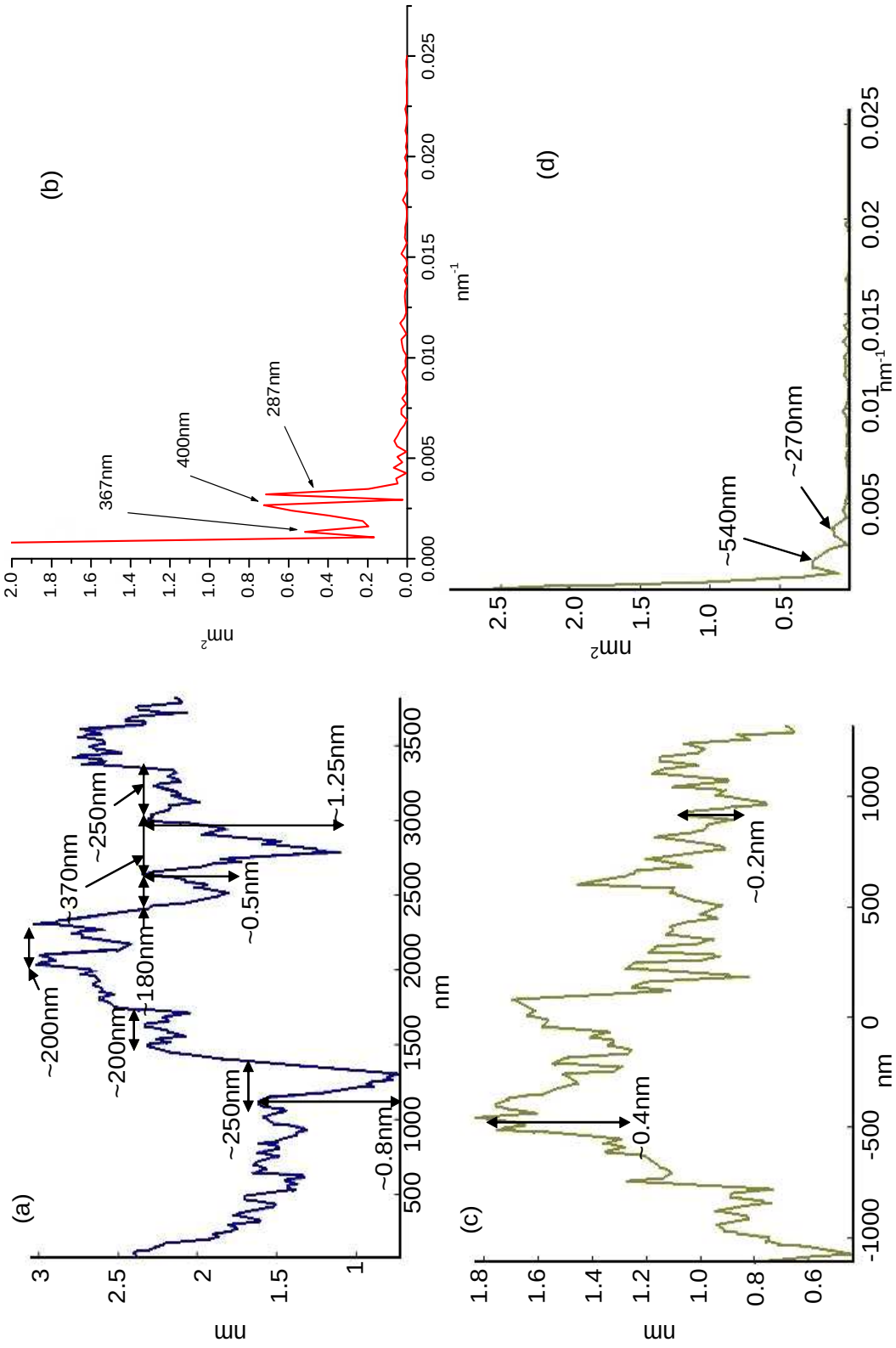


Figure C.22: Line profiles and power spectra for a (111) surface annealed to 750° after manual polishing, which were obtained from the AFM image shown in figure C.20. Graphs (a), (b), (c) and (d) are as described in figure C.3.

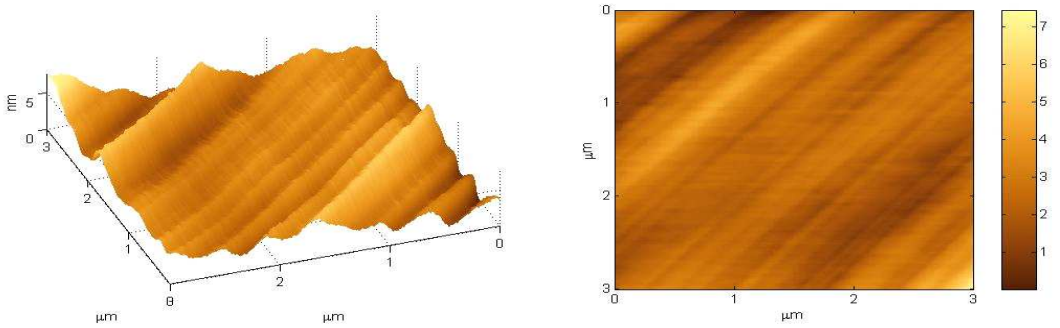


Figure C.23: Three and two dimensional atomic force microscopy images of a (100) surface polished manually (sample kc8), measuring 3×3μm.

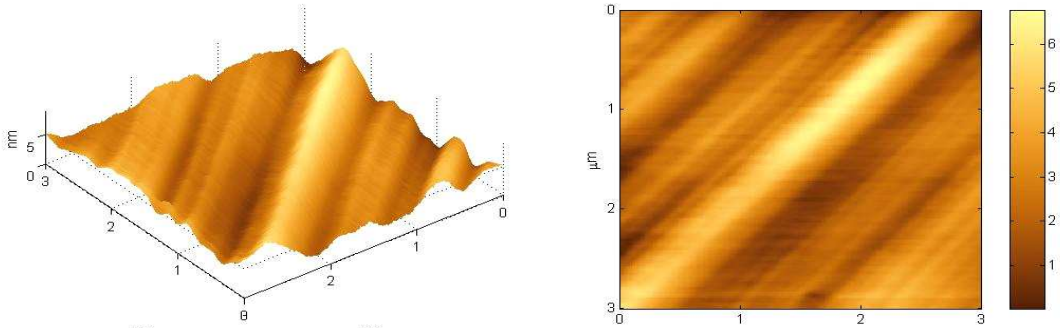


Figure C.24: Three and two dimensional atomic force microscopy images of another (100) surface polished manually (sample kc8), measuring 3×3μm.

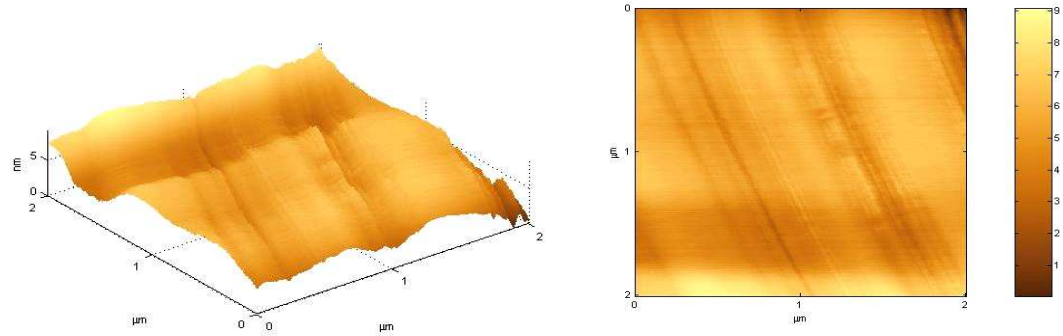


Figure C.25: Three and two dimensional atomic force microscopy images of a (100) surface polished mechanically for sample kc8, measuring 2×2μm.

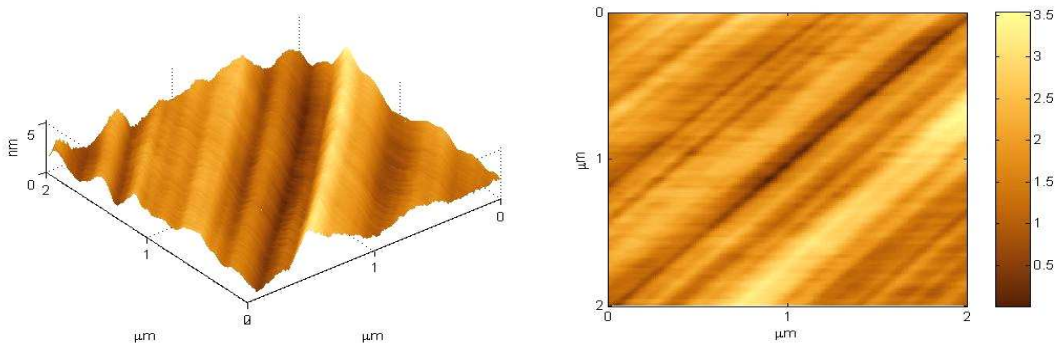


Figure C.26: Three and two dimensional atomic force microscopy images of a (100) surface polished manually (sample kc8), measuring $2\times2\mu$m.

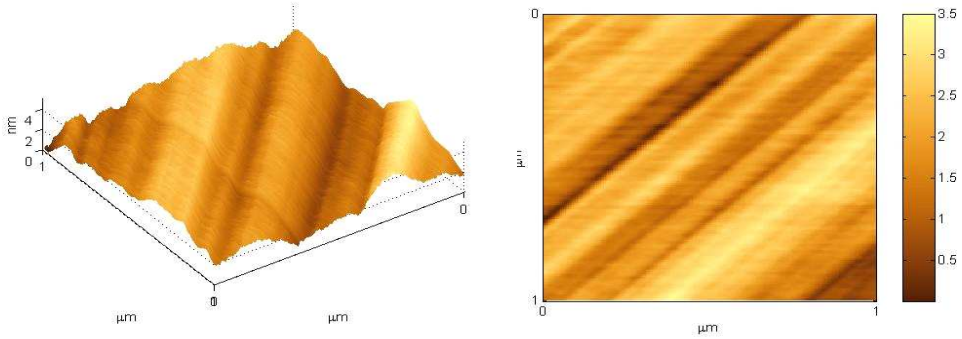


Figure C.27: Three and two dimensional atomic force microscopy images of a (100) surface polished manually (sample kc8), measuring $1\times1\mu$m.

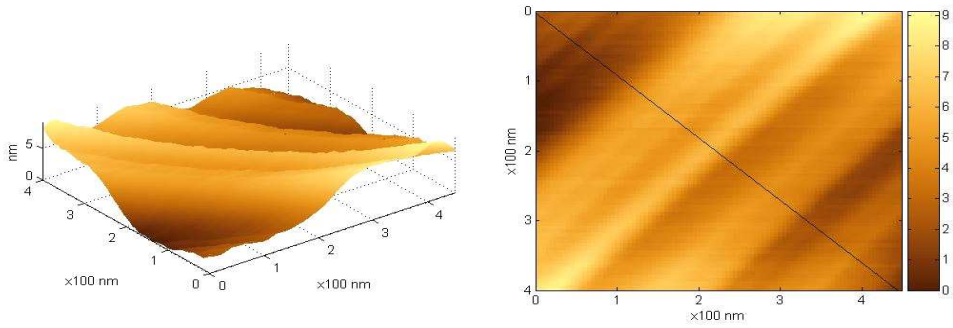


Figure C.28: Three and two dimensional atomic force microscopy images of a (100) surface polished manually (sample kc8), measuring 400×420 nanometers.

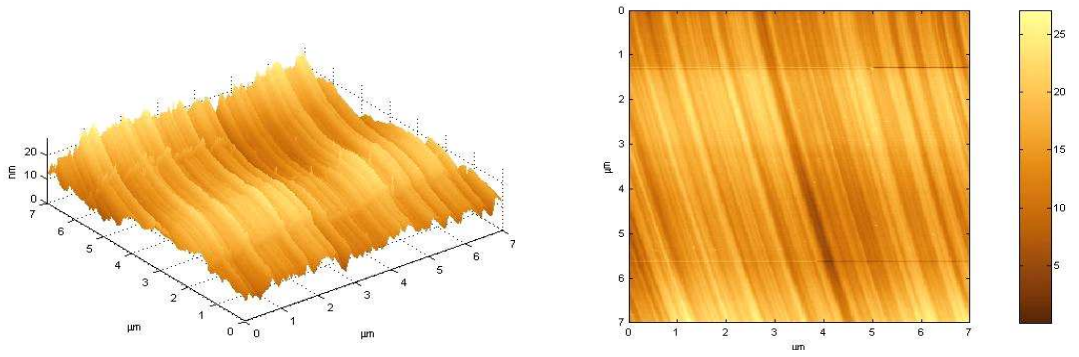


Figure C.29: Three and two dimensional atomic force microscopy images of a (110) surface polished mechanically (sample kk7), measuring $7\times7\mu$m.

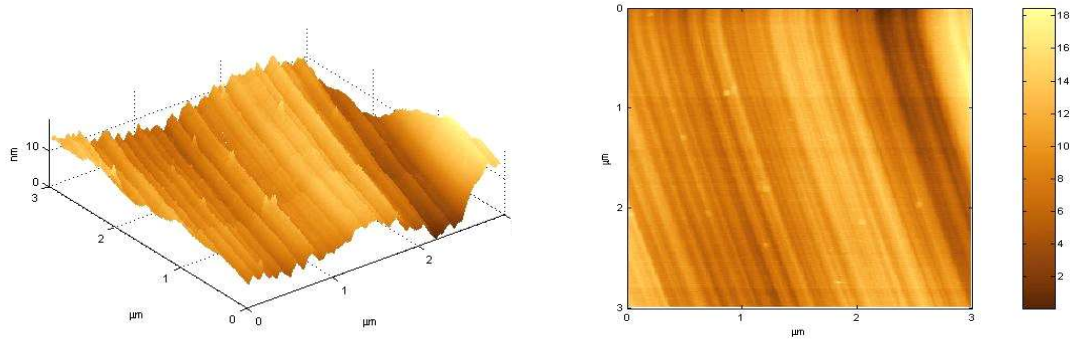


Figure C.30: Three and two dimensional atomic force microscopy images of a (110) surface polished mechanically (sample kk7), measuring $3\times3\mu$m.

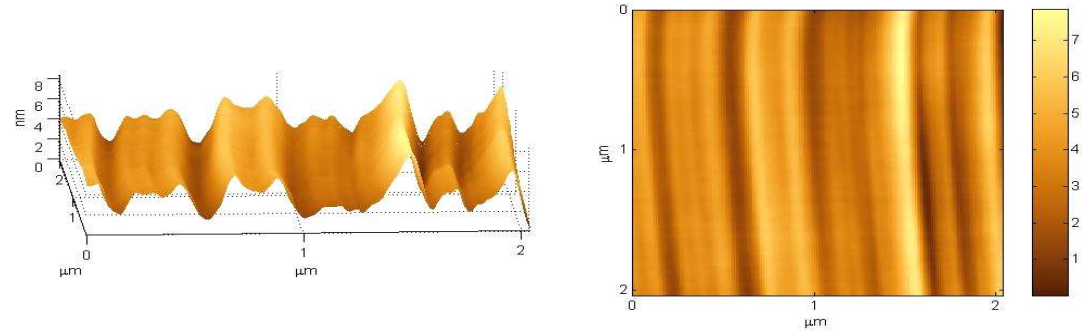


Figure C.31: Three and two dimensional atomic force microscopy images of a (110) surface polished manually (sample kk7), measuring $2\times2\mu$m.

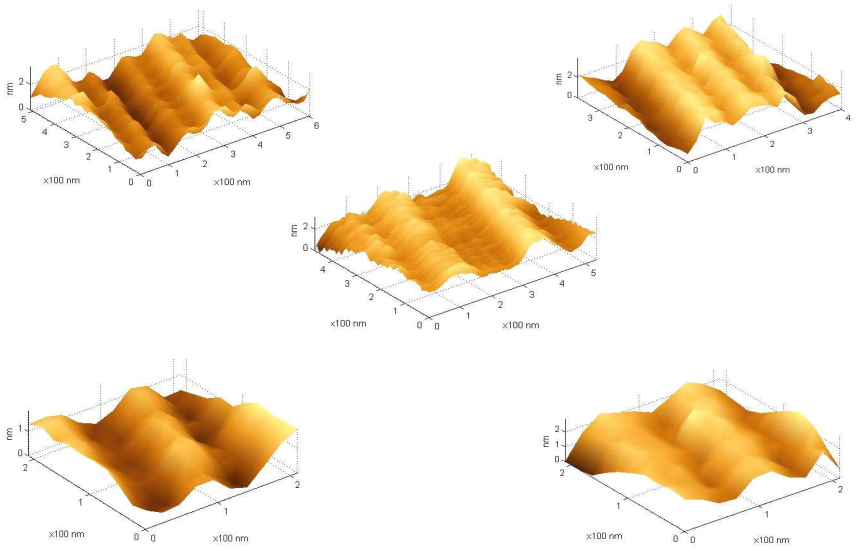


Figure C.32: Three dimensional atomic force microscopy images of (110) surfaces polished mechanically (sample kk7). The images show different but small sizes of scan areas, all expressed in nanometers in order to amplify the polishing grooves.

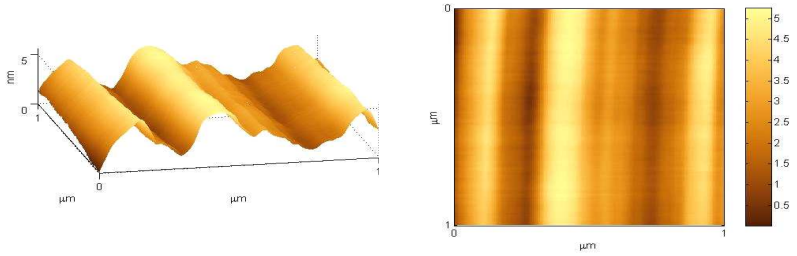


Figure C.33: Three and two dimensional atomic force microscopy images of a (110) surface polished manually (sample kk7), measuring $1\times1\mu$m.

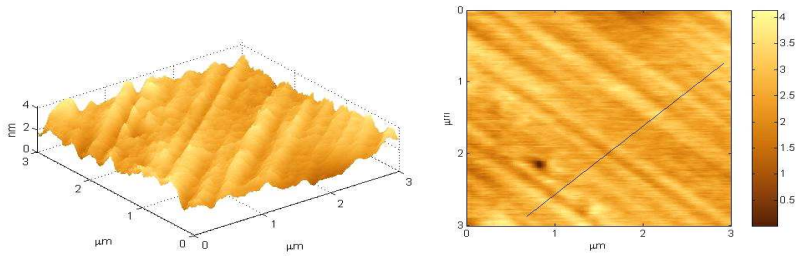


Figure C.34: Three and two dimensional atomic force microscopy images of a (110) surface annealed to 750°C after manual polishing (sample kk7).

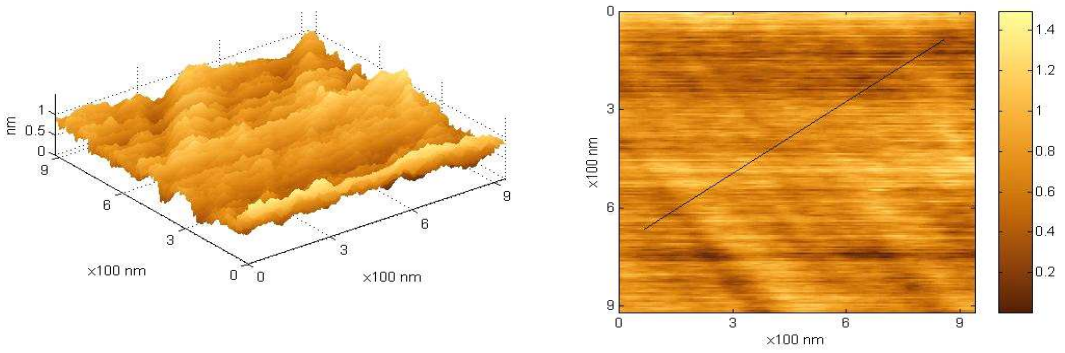


Figure C.35: Three and two dimensional atomic force microscopy images of a (110) surface annealed to 250°C after manual polishing (sample kk7).

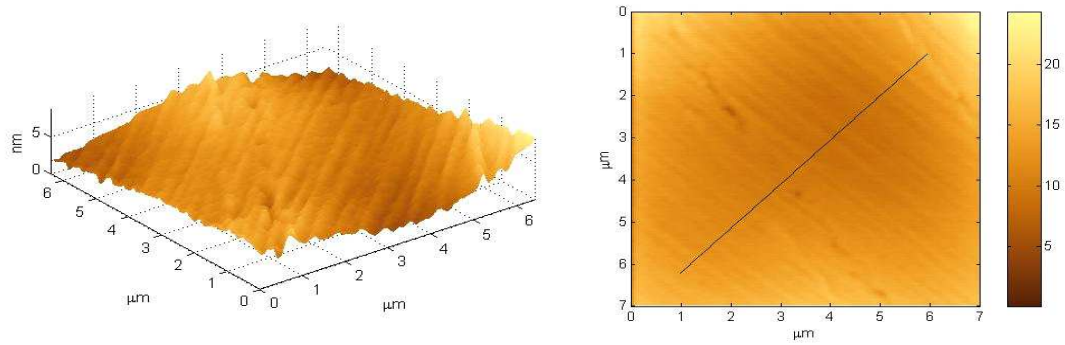


Figure C.36: Three and two dimensional atomic force microscopy images of a (110) surface annealed to 750°C after manual polishing (sample kk7).

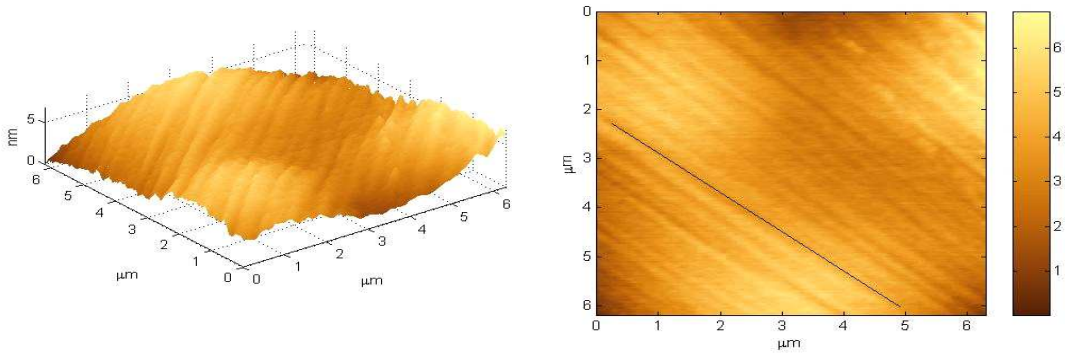


Figure C.37: Three and two dimensional atomic force microscopy images of a (110) surface annealed to 750°C after manual polishing (sample kk7).

References

[1] J. C. Vickerman (Edt.), *Surface Analysis: The Principal Techniques.*, John Wiley & Sons, New York, 1997, pp. 1 – 93, 395–444.

[2] Martin Prutton, *Introduction to Surface Physics*, Clarendon Press, New York, 1994, pp. 1–138.

[3] D. R. Randell and W. Neagle (Edts.), *Surface Analysis Techniques and Applications, Proc. of the Roy. Soc. Of Chem. U.M.I.S.T.*, Thomas Graham House, The Science Park, Cambridge, Manchester, UK, 1989, p. 1.

[4] Gabor A. Somorjai (Edt.), *Introduction to Surface Chemistry and Catalysis.*, John Wiley & Sons Inc., New York, 1994, pp. 54 –60 and 596–617.

[5] Dawn Bonnell (Edt.), *Scanning Probe Microscopy and Spectroscopy:Theory, Techniques and Applications, 2nd Ed.*, Wiley-VCH, New York, 2001, pp. 14–141.

[6] Niel Coville (Edt.). *Materials analysis course notes.* University of the Witwatersrand, Johannesburg, South Africa, 2001.

[7] T.E.Derry, *PhD. Thesis*, University of the Witwatersrand, Johannesburg, South Africa, 1978, pp. 60, 79, 164.

[8] J.E.Field (Edt.), *The Properties of Natural and Synthetic Diamond.*, Academic Press, Harcourt Brace Jovanovich, London, 1992, pp. 677–684.

[9] A. K. Ramdas, *in Properties and Growth of Diamond, (Edt.) Gordon Davies.*, Emis Datareview Series No.9, INSPEC., Short Run Press Ltd. Exeter, London, United Kingdom, 1994, p. 13.

[10] Eunja Kim and Chang Feng Chen, Physics Letts., **A 326** pp. 442–448, 2004.

[11] M.H. Grimsditch and A.K. Ramdas, Phys. Rev B, **11** pp. 3139–3148, 1975.

[12] A. R. Lang, *in Properties and Growth of Diamond, (Edt.) Gordon Davies.*, Emis Datareview Series No.9, INSPEC., Short Run Press Ltd. Exeter, London, United Kingdom, 1994, pp. 106–109.

[13] J.E. Field, *in Properties and Growth of Diamond, (Edt.) Gordon Davies.*, Emis Datareview Series No.9, INSPEC., Short Run Press Ltd. Exeter, London, United Kingdom, 1994, pp. 52–56.

[14] J. E. Field. *in diamond and diamond-like coatings.* In Robert E. Clausing, Linda L. Horton, John C. Angus, and Peter Koidl, editors, *Nato ASI Series B: Physics*, volume 266, pp. 17–35, New York, 1990. Plenum Publishing Company.

[15] R. Berman, *in Properties and Growth of Diamond, (Edt.) Gordon Davies.*, Emis Datareview Series No.9, INSPEC., Short Run Press Ltd. Exeter, London, United Kingdom, 1994, pp. 23–25.

[16] J. W. Vandersande, *in Properties and Growth of Diamond, (Edt.) Gordon Davies.*, Emis Datareview Series No.9, INSPEC., Short Run Press Ltd. Exeter, London, United Kingdom, 1994, p. 33.

[17] S Walter, J.Bernhardt, U. Starke, K.Heinz, F.Maier, J.Ristein, and L.Ley, J.Phys.: Condens. Matter, **14** pp. 3085–3092, 2002.

[18] A.T. Collins, *in Properties and Growth of Diamond, (Edt.) Gordon Davies.*, Emis Datareview Series No.9, INSPEC., Short Run Press Ltd. Exeter, London, United Kingdom, 1994, pp. 263–288.

[19] Nazare M. H. and Neves A. J. (Edt.), *in Prop. Growth and Applications of diamond.*, INSPEC, The Institution of Electrical Engineers., London, UK, 2001.

[20] Alexander M. Zaitsev (Edt.), *Optical Properties of Diamond: A Data Handbook.*, Springer-Verlag, Berlin, Germany, 2001.

[21] Driscoll W. G and Vaughan W. (Edt.), *Handbook of Optics.*, McGraw-Hill, New York, 1970.

[22] M . J. Rutter and J. Robertson, Computational Mater. Sci., **10** pp. 330–333, 1998.

[23] P. Ransten, C. Ribbing, C. Strandman, and L. Smith B. Hök, Sensors and Actuators, **82 Nos 1-3** pp. 24–29, 2000.

[24] K. Lmimouni, C. Legrand, C. Dufour, A. Chapoton, and C. Belouet, Appl. Phys. Letts., **78 (17)** pp. 2437–2439, 2001.

[25] C. E. Nebel, C. R. Miskys, J. A. Garrido, M. Hermann, O. Ambacher, M. Eickhoff, and M. Stutzmann, Diam & Relatd. Mater., **12 (10-11)** pp. 1873 – 1876, 2003.

[26] M. Joachim Lindblom, J. Holsa, H. Papunen, H. Hakkanen, and J. Mukanen, Optical Materials., **24** pp. 243–251., 2003.

[27] A. T Collins, *Optical Properties of Diamond: A Data Handbook.(Edt.) A.M. Zaitsev*, Springer-Verlag, Berlin, Germany, 2001, p. foreword.

[28] H. Kanda and T. Sekine, *in Properties and Growth of Diamond, (Edt.) Gordon Davies.*, Emis Datareview Series No.9, INSPEC., Short Run Press Ltd. Exeter, London, United Kingdom, 1994, pp. 403–426.

[29] R. Gat and J.C. Angus, *in Properties and Growth of Diamond, (Edt.) Gordon Davies.*, Emis Datareview Series No.9, INSPEC., Short Run Press Ltd. Exeter, London, United Kingdom, 1994, pp. 325–335.

[30] R. Haubner and B. Lux, *in Properties and Growth of Diamond, (Edt.) Gordon Davies.*, Emis Datareview Series No.9, INSPEC., Short Run Press Ltd. Exeter, London, United Kingdom, 1994, pp. 336–348.

[31] P.K. Bachman, *in Properties and Growth of Diamond, (Edt.) Gordon Davies.*, Emis Datareview Series No.9, INSPEC., Short Run Press Ltd. Exeter, London, United Kingdom, 1994, pp. 349–367.

[32] P.W. Morrisson jr. and J.T. Glass, *in Properties and Growth of Diamond, (Edt.) Gordon Davies.*, Emis Datareview Series No.9, INSPEC., Short Run Press Ltd. Exeter, London, United Kingdom, 1994, pp. 368–397.

[33] J. Isberg, J. Hammersberg, D.J. Twitchen, and A. J. Whitehead, Diam. & Reltd. Mater., **13** pp. 320–324., 2004.

[34] Filip De Weerdt and Jef Van Royen, Diam. & Reltd. Mater., **10** pp. 474–479., 2001.

[35] L.S. Hounsome, R.Jones, A.T.Blumenau, T.Frauenheim, P.R. Briddon, and S. Öberg, *The 55th Diamond Conference.*, Warwick, UK, 2004.

[36] F. De Weerdt and A.T. Collins, *The 55th Diamond Conference*, Warwick, UK, 2004.

[37] R. Berman, P.R.W Hudson, and M. Martinez, J. Phys. C., **8 L430** pp. 474–479., 2001.

[38] W. Kaiser and W. L. Bond, Phys. Rev., **115** pp. 857–63, 1959.

[39] W. V. Smith, P. P. Sorokin, I.L. Gelles, and G. J. Lasher, Phys. Rev., **115** pp. 1546–1550, 1959.

[40] J. Chavallier, B. Theys, A. Lusson, and C. Grattepain, Phys. Rev. B, **58 No.12** p. 7966, 1998.

[41] J. Isberg, J. Hammersberg, E. Johansson, T. Wikstrom, D.J. Twitchen, A.J. Whitehead, S.E. Coe, and G.A Scarsbrook, Science, **297** pp. 1670–1672, 2002.

[42] M. H. Nazaré, *in Properties and Growth of Diamond, (Edt.) Gordon Davies.*, Emis Datareview Series No.9, INSPEC., Short Run Press Ltd. Exeter, London, United Kingdom, 1994, pp. 85–87.

[43] K. Nassau, *in Diamond films and Coatings. (Edt.) Davis R.F.*, Noyes publishers, Park Ridge, NJ, 1993, p. 31.

[44] G. Jansen, W. Vollenberg, J. Giling, W.J.P. Van Enckervort, J.J.D. Schaminee, and M. Seal, Surf. Coat. Technl., **47** p. 113, 1991.

[45] J. Wilks and E. M. Wilks, *in Properties of Diamond, (Edt.) J.E. Field*, Academic Press, London, 1979, pp. 351–382.

[46] S. Evans and J.E. Field, *in Properties and Growth of Diamond, (Edt.) Gordon Davies.*, Emis Datareview Series No.9, INSPEC., Short Run Press Ltd. Exeter, London, United Kingdom, 1994, pp. 59–78.

[47] F. M. van Bouwelen and W.J.P. van Enckervort, Diam. & Reltd. Mater., **8** pp. 840–844 and refs. therein, 1999.

[48] B. Koslowski, S. Strobel, and P. Ziemann, Diam. & Reltd. Mater., **9** pp. 1159–1163 and refs. therein, 2000.

[49] S. E. Grillo and J. E. Field, J. Phys. D: Appli. Phys., **30** pp. 202–209 and refs. therein, 1997.

[50] F. M. van Bouwelen, Diam. & Reltd. Mater., **9** pp. 925–928 and refs. therein, 2000.

[51] W.J.P van Enckevort and H.J. van Halewijn, *in Properties and Growth of Diamond, (Edt.) Gordon Davies.*, Emis Datareview Series No.9, INSPEC., Short Run Press Ltd. Exeter, London, United Kingdom, 1994, pp. 293–300.

[52] J.E Field, *in Properties and Growth of Diamond, (Edt.) Gordon Davies.*, Emis Datareview Series No.9, INSPEC., Short Run Press Ltd. Exeter, London, United Kingdom, 1994, pp. 36–51.

[53] A. M. Zaitsev, *in Handbook of Diamond Technology, 8-11, (Edt.), W. R. Fahrner*, Trans. Tech. Publications Ltd., (Uetikona a. S), Switzerland, 2000, pp. 317– 357.

[54] J.R. Hird and J.E. Field, *in Procd. of R. Soc. (A).*, volume 460, London, United Kingdom., 2004, pp. 3547–3568.

[55] J.E Field, *in Properties and Growth of Diamond, (Edt.) Gordon Davies.*, Emis Datareview Series No.9, INSPEC., Short Run Press Ltd. Exeter, London, United Kingdom, 1994, pp. 70–76.

[56] M.S. Couto, W.J.P Van Enckevort, and M. Seal., Diam. & Relatd. Mater., **6** pp. 975–982 and refs. therein, 1997.

[57] Y. Yarnitsky, J.P.F. Sellschop, M. Rebak, and S. Bartolucci Luyckx, Mat. Sci. & Engin., **A105/106** pp. 565–569., 1988.

[58] Mik Rebak. 2004. Private Communication.

[59] M. P. Hitchiner, E.M. Wilks, and J. Wilks, Wear, **94** pp. 103–120, 1984.

[60] A.G. Thornton and J.Wilks, J.Phys. D:Appl. Phys., **9** pp. 27–35, 1976.

[61] E.M. Wilks and J. Wilks, *in Properties and Applications of Diamond*, Kluwer, Dordrecht, 1992, p. 348.

[62] A. G. Thornton and J. Wilks, Diamond Research, Suppliment. Indust. Diam. Rev., (UK)., pp. 39–42, 1979.

[63] M. S. Couto, W.J.P. Enkevort, B. Wichman, and M. Seal, Appl. Surf. Sci., **62** p. 263, 1992.

[64] M. S. Couto, W.J.P. Enkevort, and M. Seal, Phil. Mag., **B69** pp. 621–641, 1994.

[65] Gabor A. Somorjai (Edt.), *Introduction to Surface Chemistry and Catalysis.*, John Wiley & Sons, Inc., New York, 1994, pp. 600–604.

[66] N.W. Makau and T.E. Derry, *The 55th Diamond Conference*, Warwick, UK, 2004.

[67] Jan Haisma, Frank J.H.M. van der Kruis, Bert A.C.M. Spierings, Jo M. Oomen, and Fons M.J.G. Fey, Prec. Engin., **14** pp. 20–27, 1992.

[68] T.E.Derry and J.P.F. Sellschop, CSIR/NFNL-WNWR, ISBN:07988 24174, Pretoria, South Africa, 1981, pp. 31–37.

[69] M. Casey, A.G.Lewis, A.G.Thornton, and J.Wilks, J.Phys. D:Appl.Phys., **10** pp. 1877–1881, 1997.

[70] M. R. Jarvis, Ruben Perez, F. M. van Bouwelen, and M. C. Payne, Phys. Rev. Lett., **80 No. 16** pp. 3428–3431, 1998.

[71] E.M. Wilks and J. Wilks, *in Physical Properties of Diamond, (Edt.) R. Berman*, Clarendon, Oxford, UK, 1965, pp. 221–250.

[72] E.M. Wilks and J. Wilks, Wear, **81** pp. 329–346, 1982.

[73] C. D. Ollison, W. D. Brown, A. P. Malshe, H. A. Naseem, and S.S. Ang, Diam. & Reltd. Mater., **8** pp. 1083–1090, 1999.

[74] C. Tang, A. J Neves, A.J. Fernandes, J. Taniguchi, N. Ohno, S. Takeda, I. Miyamoto, and M. Komuro, J. Vac. Sci. Tech., **B16** p. 2506, 1998.

[75] E.M. Wilks and J. Wilks, J.Phys. D:Appl.Phys., **5** p. 1900, 1972.

[76] I.J. Ford, J.Phys. D:Appl. Phys., **26** pp. 2219 – 2225, 1993.

[77] Z.Feng, Y.Tzeng, and J.E. Field, J.Phys. D:Appl. Phys., **25** pp. 1418 – 1424, 1992.

[78] M.Casey and J. Wilks, J.Phys. D:Appl. Phys., **6** pp. 1772–1781, 1973.

[79] J.R.Hird and J.E.Field, Wear, **258** pp. 18–25, 2005.

[80] S.E.Grillo, J.E.Field, and F.M van Bouwelen, J.Phys. D:Appl. Phys., **33** pp. 985–990, 2000.

[81] S.Tolansky and V.R.Howes, volume 70, PT. 5-B, Royal Halloway College, University of London, Eghan, Surrey, 1956, pp. 521–526.

[82] M.S. Couto, W.J.P Van Enckervort, and M. Seal., J. Hard Mater., **64 No.5** p. 31 and references therein, 1994.

[83] D. Tabor, *in Properties of Diamond, (Edt.) J.E. Field*, Academic Press, London, 1979, pp. 325–350.

[84] E. M. Wilks and J. Wilks, *The properties of diamond*, Butterworth-Heinemann, Oxford, UK, 1991, p. 251.

[85] D. Tabor and J.E. Field, *in The properties of Natural and Synthetic diamonds, (Edt.) J.E. Field*, Academic Press, London, 1992, pp. 547–571.

[86] Minyoung Lee, William G. Morris, Andrew K. Han, and Francis Kennedy, Mat. Scien. & Engi., **A209** pp. 60–67, 1996.

[87] P. Grodzinski, British Journal of appli. Phys., pp. 86 – 90, 1950.

[88] V.R.Howes, in Proc. Phys. Soc., **80** pp. 78–80, 1962.

[89] J.G.Bell, M.E. Stuivinga, A.G.Thornton, and J. Wilks, J.Phys. D:Appl. Phys., **10** pp. 1379–1386, 1977.

[90] C. J. Tang, A. J. Neves, A.J.S. Fernandes, J. Grácio, and N. Ali, Diam. & Reltd. Mater., **12** pp. 1411–1416, 2003.

[91] P.E.Russel, T. J. Stakk, D.P. Griffis, J. R. Philips, and K.F. Karausch, J. Vac. Sci. Tech., **B16** p. 2494, 1998.

[92] P.F. Lai, S. Prawer, and L.A. Bursil, Diam & Reltd. Mat., **10** pp. 82–86, 2001.

[93] S. Skokov, B. Weiner, and M. Frenklach, Phys. Rev. B, **56** p. 4203, 1997.

[94] T.E.Derry, J.O.Hansen, P.E.Harris, R.G.Copperthwaite, and J.P.F.Sellschop, *In The Structure of Surfaces II: Proc. of 2nd Intern. Conf. on the Structure of Surfaces (ICSOSII), Amsterdam, June 1987; (Edts.) J.F.Van der Veen and H.A. Van Hove*, Springer Series in Surface Sciences 11, Berlin, 1988, p. 384.

[95] B.B. Pate, Surf. Sci., **165** pp. 83–142, 1986.

[96] T. Tachibana, J.T. Glass, and R.J. Nemanich, J. Appl. Phys., **73** p. 835, 1993.

[97] D. B. Rebuli, T. E. Derry, E. Sideras-Haddad, B. P Doyle, R. D. Maclear, S. H. Connell, and J. P. F. Sellschop., Diam. & Relatd. Matr., **8** p. 1620, 1999.

[98] D.R.Rebuli, J.E. Butler, P. Aggerholm, S.H.Conell, T.E.Derry, B.P. Doyle, E.Sideras-Haddad, and J.F.P.Sellschop, Nucl. Instr. Meth. B, **158** p. 701, 1999.

[99] P.E. Pehrsson and T.W. Mercer, Surf. Scie., **460** p. 49, 2000.

[100] Y.M. Wang, K.W. Wong, S.T. Lee, M. Nishitani-Gamo, I. Sakaguchi, K.P. Loh, and T. Ando, Diam. & Relatd. Mater., **9** p. 1582, 2000.

[101] P.K.Baumann and R.J.Nemanich, Surf. Scie., **409** pp. 320–335, 1998.

[102] M.J.Rutter and J.Robertson, Phys. Rev. B, **57** pp. 9241–9245, 1998.

[103] G.Kern, J.Hafner, and G.Kresse, Surf. Scie., **366** pp. 445–463, 1996.

[104] B.N. Davidson and W.E. Pickett, Phys. Rev B, **49** pp. 11253–11267, 1994.

[105] R. Graupner, J. Ristien, and L. Ley Ch. Jung, Phys. Rev B, **60** pp. 17023 – 17029, 1999.

[106] J. van der Weide and R.J. Nemanich, Appl. Phys. Lett., **62** pp. 1878–1880, 1993.

[107] G. Kern and J. Hafner, Phys. Rev. B., **56** pp. 4203–4210, 1997.

[108] J.C.Zheng, X.N.Xie, A.T.S.Wee, and Kian Ping Loh, Diam. & Reltd. Mater., **10** pp. 500–505, 2001, and refs. therein.

[109] Kian Ping Loh, X.N.Xie, S.W.Wang, J.S.Pan, and P.Wu, Diam. & Relatd. Mater., **11** pp. 1379–1384, 2002.

[110] M. Yokoyama and T. Ito, Appl. Surf. Sci., **162-163** pp. 457–463, 2000.

[111] P.E. Pehrsson and T.W. Mercer, Surf. Scie., **460** pp. 74–90, 2000.

[112] Hiroyuki Tamura, Hui Zhou, Kiyoshi Sugisako, Yasuto Yokoi, Seiichi Takamaki, Momoji Kubo, Kazuo Teraishi, Akira Miyamoto, Akira Imamura, Mikka N.-Gamo, and Toshihiro Ando, Phys. Rev. B., **61** p. 11025, 2000.

[113] Gabor A. Somorjai (Edt.), *Introduction to Surface Chemistry and Catalysis.*, John Wiley & Sons Inc., New York, 1994, pp. 400–436.

[114] *Twin anode XR3E2 X-ray Source Operating Manual, issue 1.* West Sussex, England, 2003. URL `http://www.VGScientific.com or www.thermo.com`.

[115] *Physical Electronics Manual.* Ismaning, Germany, 2000. URL `http://www.phi.com`.

[116] J.van der Weide and R.J.Nemanich, Phys. Rev. B., **49** p. 13629, 1994.

[117] L.Smit, T.E.Derry, and J.F.van der Veen, Surf. Scie., **167** pp. 502–518, 1986.

[118] D. Briggs and M.P. Seah (Edts.), *Practical Surface Analysis by Auger and X-ray Photoelectron Spectroscopy.*, John Wiley & Sons, New York, 1983, pp. 484–525.

[119] B. Vincent Christ, *HandBook of Monochromatic XPS spectra; The Elements and Native Oxides (for Ag - Au)*, XPS International Inc., Kawasaki, Japan, 1999, p. xxxii.

[120] *VG Scientific Manual.* London, Britain, 1980. URL `http://www.VGScientific.com or www.thermo.com`.

[121] Mike Preuss. *Private Communication.* VG Scientific Sales Dept., 2006.

[122] R. Benoit, Y. Durand, B. Narjoux, G. Quintana, and Y. Georges. *Thermo Electron Corporation.* Les Mimosas, France, 2002. URL `http://www.lasurface.com`.

[123] M.W. Roberts, *Advances in Catalysis., (Edts.) D.D. Eley and H.Pines and P.B. Weisz*, volume 29, Academic Press, New York, 1980, p. 55.

[124] C.B. Franklyn and R.K.W. Merkle, Nucl. Instr. & Meth. B, **181** pp. 140–144, 2001.

[125] K.Bobrov, H.Shechter, A.Hoffman, and M.Folman, Appli. Surf. Scie., **196** pp. 173–180, 2002.

[126] J. van der Weide, Z. Zhang, P.K. Baumann, M.G. Wensell, J. Bernholc, and R.J. Nemanich, Phys. Rev. B, **50** p. 5803, 1994.

[127] S. Skokov, B. Weiner, and M. Frenklach, Phys. Rev. B, **49** p. 11374, 1994.

[128] S. Skokov, B. Weiner, and M. Frenklach, Phys. Rev. B, **55** p. 1895, 1997.

[129] T. Ando, K. Yamamoto, M. Ishii, M. Kamo, and Y. Sato, J. Chem. Soc. Faraday Trans., **89** p. 3635, 1993.

[130] Susana Petrick and Carsten Benndorf, Diam & Reltd. Mat., **10** pp. 519–525, 2001.

[131] R.J. Nemanich, P.K. Baumann, M.C. Benjamin, O.-H. Nam, A.T. Sowers, B.L. Ward, H. Ade, and R.F. Davis, Appl. Surf. Sci., **130-132** pp. 698–703, 1998.

[132] R.E. Thomas, R.A. Rudder, and R.J. Markunas, J.Vac.Sci.Tech., **A10** p. 2451, 1992.

[133] R.J. Nemanich, P.K.Baumann, M.C. Benjamin, O.-H. Nam, A.T. Sowers, B.L. Ward, H. Ade, and R.F. Davis, Appli. Surf. Scie., **130-132** pp. 694–703, 1998.

[134] R. Klauser, Jin-Ming Chen, T.J. Chuang, L.M. Chem, M.C. Smith, and J.C-. Lin, Surf. Scie., **356** pp. L410–416, 1996.

[135] M. Frenklach, D. Huang, R.E. Thomas, R.A. Rudder, and R.J. Markunas, Appl. Phys. Lett., **63** p. 3090, 1993.

[136] P.G. Lurie and J.M. Wilson, Surf. Sci., **65** p. 453, 1977.

[137] R. Sappok and H. Boehm, Carbon, **6** pp. 283–295, 1968.

[138] Kian Ping Loh, X.N.Xie, S.W.Wang, and J.C.Zheng, J. Phys. Chem. B, **106** pp. 5230–5240, 2002.

[139] X.M.Zheng and P.W.Smith, Surf. Scie., **262** p. 219, 1992.

[140] Andrew Freedman and Charter D. Stinesspring, Appl. Phys. Lett., **57** pp. 1194–1197, 1990.

[141] J.L. Whitten, P. Cremaschi, R.E. Thomas, R.A. Rudder, and R.J. Markunas, Appl. Surf. Sci., **75** p. 45, 1994.

[142] T.E. Beerling and C.R. Helms, Appl. Phy. Lett., **65** pp. 1912–1914, 1994.

[143] K. Bobrov, G. Comtet, G. Dujardin, L. Hellner, P. Bergonzo, and C. Mer, Phys. Rev. B, **63** p. 165421, 2001.

[144] F.J.Himpsel, J.F. van der Veen, and D.E.Eastman, Phys. Rev. B., **22** p. 1967, 1980.

[145] C.Y.Fong and B.M.Klein, *Electronic and vibrational properties of bulk diamond in Diamond: Electronic Properties and Applications. (Edts.) L.S.Pan and D.R.Kania*, Kluwer., Dordrecht, 1995.

[146] P. Reinke, G. Francz, and P. Oelhafen, Phys. Rev. B, **54** pp. 7067–7073, 1996.

[147] A. Denisenko, A. Aleksov, and E. Kohn, Diam & Reltd. Mat., **10** pp. 667–672, 2001.

[148] T. Gora, R. Staley, J.D. Rimstidt, and J. Sharma, Phys. Rev. B, **5** pp. 2309–2314, 1972.

[149] G.Francz and P.Oelhafen, Diam. & Reltd. Mater., **4** pp. 539–543, 1995.

[150] H. Kawarada, Surf. Sci Rep., **26** p. 205, 1996.

[151] N. W. Makau and T. E. Derry, Surf. Revie. and Lett., **10 Nos. 2&3** pp. 295–301, 2003.

[152] T.N. Rao and A. Fujishima, Diam & Relatd. Mat., **9** pp. 384–389, 2000.

[153] P.E. Hodgson (Edt.), *Nuclear Reactions and Nuclear Structure*, Clarendon Press, Oxford, United Kingdom, 1971, pp. 195–319.

[154] Michael Nastasi and Joseph R. Tesmer (Edts.), *Handbook of Ion Beam Materials Analysis. (Edts.) Michael Nastasi and Joseph R. Tesmer.*, Materials Research Society, Pittsburg, Pennyslvania, 1995, pp. 139–204, 385–609 and refs. therein.

[155] G.R. Satchler, *Introduction to Nuclear Reactions*, The Macmillan Press Ltd., London, 1980, pp. 1–272.

[156] Daphne F. Jackson, *Nuclear Reactions*, Nederlandse Boekbruk Industrie N. V., Netherlands, 1970, pp. 96–109.

[157] C. Tsartsarakos, P. Misaelides, and A. Katsanos, Nucl. Instr. & Meth. in Phys. Research, **B45** pp. 33–35, 1990.

[158] Kenneth S. Krane, *Introduction to Nuclear Physics*, John Willey & Sons, New York, 1988, pp. 378–443.

[159] Glenn F. knoll (Edt.), *Radi. Detec. and Measrnt.*, New York, 3rd. edition, 2000, p. 118 and 235.

[160] J.F. Zeigler (Edt.). *The Stopping and Range of Ions in Matter*, volume 5. Pergamon Press, New York, 1980. URL `http://www.SRIM.com`.

[161] *CRC Handbook of Chemistry and Physics, 71st edition, (Edt.) D.R. Lide*, CRC Press, Boston, USA., 1992, pp. 9–1,9–2,11–34,11–37.

[162] H.J. Rösler and H. Lange (Edts.), *Geochemical Tables*, Elsevier Publishing Company, Amsterdam, 1972, p. 405.

[163] F. Ajzenberg-Selove, Nucl. Phys., **A449** pp. 1–86, 1986.

[164] Antonio Zamora. *Oleic acids.* 2005. URL `http://www.scientificpsychic.com/fitness/fattyacids.html`.

[165] *Aldrich Chemical Company Inc., Stable Isotopes Catalog.* Milwaukee, USA., 2003. URL `http://www.Aldrich.com`.

[166] *Computed probabilities of detector response*, Amptek Inc., 14 De Angelo Drive, Bedford, MA. U.S.A., 2005.

[167] D.B. Rebuli, *MSc. Thesis*, University of the Witwatersrand, Johannesburg, South Africa, 1999, pp. 26–27.

[168] R.A. Spits, *MSc. Thesis*, University of the Witwatersrand, Johannesburg, South Africa, 1991, p. 31.

[169] *Scintillation Detector Operating Manual*, Bicron, Newbury, Ohio, USA, 2000, pp. 1–12.

[170] C.H. Wang and David L. Willis, *Radiotracer Methodology in Biological Sciences*, Prentice-Hall Inc., Engelwood Cliffs, New Jersey, 1965, p. 92.

[171] W.L. Griffin, S. Rege, R. M. Davies, S. Jackson, and S.Y. O'Reilly, *The 55th Diamond Conference*, Warwick, UK, 2004.

[172] R. A. Spits, W. Baloyi, and T. E. Derry, Phys. Rev. C., **41 No. 5** pp. 2429–2431, 1990.

[173] C.F.G. Delaney and E.C. Finch, Nucl. Instr. Meth., **215** p. 219, 1983.

[174] E.B.O. da Rosa, C. Krug, F.C. Stedile, J. Morais, and I.J.R. Baumvol, Nucl. Instr. Meth., **190** pp. 538–542, 2002.

[175] *OriginLab Corporation.* One Roundhouse Plaza, Northampton, MA O1060, USA., 2004. URL `http://www.OriginLab.com`.

[176] J. Perrière, A. Laurent, and J.P. Enard, Mater. Sci. & Eng., **B11** p. 327, 1992.

[177] G. P. Bogatyreva and M.A. Marinich, Surf. Engin., **19** pp. 65–66, 2003.

[178] Robert A. Freitas jr., *Nanomedicine: Biocompatibility*, volume IIA, Landes Bioscience, 2003.

[179] T. Strother, T. Knickerbocker, J.N. Russell Jr., and J.E. Butler, Langmur, **18** pp. 968–971, 2002.

[180] R.J. Caveney, *in Properties of Diamond.(Edt. J.E.Field).*, Academic Press, Harcourt Brace Jovanovich, London, 1979, pp. 619–639.

[181] W.E. Pickett, M.R. Pederson, and B.N. Davidson, Nanotechnology, **5** pp. 172–178, 1994.

[182] R. Kalish, *in Properties and Growth of Diamond, (Edt.) Gordon Davies.*, Emis Datareview Series No.9, INSPEC., Short Run Press Ltd. Exeter, London, United Kingdom, 1994, pp. 191–203.

[183] W. Galster, P. Leleux, I. Licot, E. Lienard, P. Lipnik, D. Mertens, P. Decrock, M. Huyse, P. van Duppen, and P. Duhamel *et al.*, Phys. Rev. C., **44 No. 6** p. 2776, 1991.

[184] N.W. Makau and T.E. Derry, Nucl. Instr. Meth. A., **555** pp. 31–35, 2005.

[185] Edmund A. Milne, Phys. Rev., **93** pp. 762–767, 1954.

[186] J.R. Hird, A. Chakravarty, and J.E. Field, *The 55th Diamond Conference.*, Warwick, UK, 2004.

[187] *Chemical profiles*. Canadian Centre for Occupational Health and Safety, Hamilton, Ontario, 2004. URL `http://www.ccohs.ca`.

[188] R. Sappok and H. Boehm, Carbon, **6** p. 573, 1968.

[189] Mike Horton. *Oleic acid on water*. Michigan, U.S.A., 2003. URL `http://Chem.lapeer.org/chem1docs/OleicAcidlab.html`.

[190] A. Mainwood, S.K. Estreicher, M. Sanati, and J.P. Goss, *The 55th Diamond Conference*, Warwick, UK, 2004.

[191] M. Eremtchenko, D. Bauer, J.A. Schaefer, and F.S. Tautz, New J. Phys., **6** p. 4, 2004.

[192] J. W. Vandersande, Phys. Rev B., **13** p. 4560, 1976.

[193] J.D.King, R. E. Azuma, J.B. Vise, J. Görres, C. Rolfs, H. P. Trautvetter, and A. E. Vlieks, Nuclear Physics A, **567** pp. 354–376, 1994.

[194] W.A. Fowler, C.C. Lauritsen, and T. Lauritsen, Rev. Mod. Phys., **20** p. 236, 1948.

[195] C. M. Mahaux, Nucl. Phys., **71** p. 241, 1965.

[196] W. A. Fowler, G. R. Caughlan, and B. A. Zimmermann, Ann. Rev. Astrophysics., **5** p. 525, 1967.

[197] C. R. Brune and R. W. Kavanagh, Phys. Rev. C., **44 No. 4** pp. 1665–1667, 1991.

[198] *Optical Microscopy Bronchure*. 2005. URL `http://www.Zeiss.com`.

[199] N.W. Ashcroft and N.D. Mermin. *Solid State Physics*. Saunders College, Philadelphia, 1981.

[200] D.J. Taatjes, A.S. Quinn, M.R. Lewis, and E.G. Bovill, Micros. Res. and Tech., **44** pp. 312–326, 1999.

[201] David Courtney. *Introduction To Spectrum Analysis*. 1992. URL `http://chandrakantha.com/articles/spectrum/spectrum.html`.

[202] Melissa R. Weimer. *Waveform Analysis Using The Fourier Transform*. DATAQ Instruments, Inc., 2005. URL `http://www.dataq.com/applicat/articles/an11.htm`.

[203] P.K.Baumann and R.J.Nemanich, Phys. Rev. B, **58** pp. 1643–1654, 1998.

[204] N. Kumagai, S. Yamasaki, and H. Okushi, Diam. & Reltd. Mater., **13** pp. 2092–2095., 2004.

[205] M. Seal, Proc. R. Soc., **A 248** pp. 379–393, 1958.

[206] M. Seal, *Science of Technology of Industrial Diamonds, (Edt.) J. Burls*, volume 1:Science, Industrial Diamond Information Bureau, London, 1966, p. 145.